OPTICAL PARAMETRIC OSCILLATORS PUMPED BY EXCIMER LASERS

Majid Ebrahimzadeh

A Thesis Submitted for the Degree of PhD
at the
University of St Andrews

1990

http://hdl.handle.net/10023/14164

Optical Parametric Oscillators Pumped by Excimer Lasers

A thesis presented by

MAJID EBRAHIMZADEH, BSc, MSc

to the

University of St. Andrews

in application for the degree of

Doctor of Philosophy

October 1989

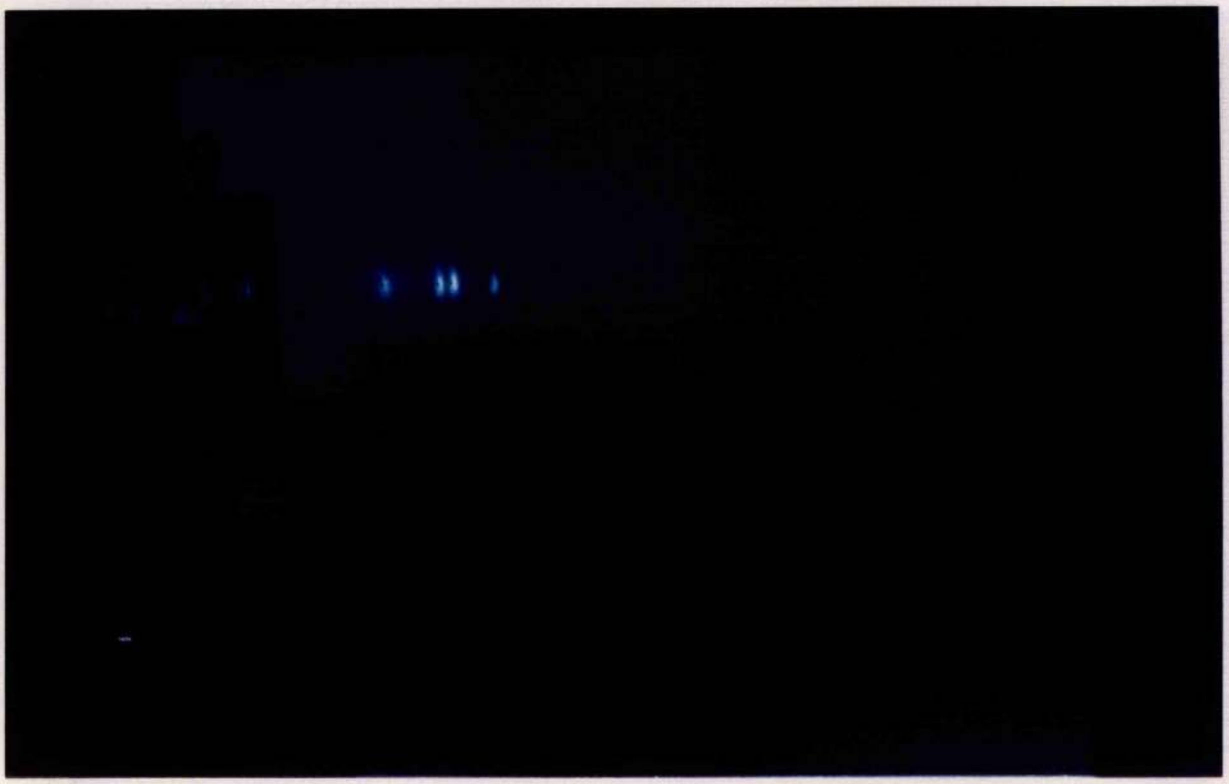

Multiple-exposure photographs of the output from the pulsed singly-resonant β-BaB_2O_4 optical parametric oscillator, pumped at 308nm by an injection-seeded XeCl excimer laser. The photographs show the visible portion of the tuning range from approximately 400nm to 800nm, out of the total available tuning bandwidth of 354nm–2.37µm.

DECLARATION

I hereby certify that this thesis has been composed by myself, that it is a record of my own work, and that it has not been accepted in partial or complete fulfilment of any other degree or professional qualification.

This research was carried out in the J. F. Allen Physics Research Laboratories in the Physics Department of the University of St. Andrews, under the supervision of Dr. M. H. Dunn.

M. Ebrahimzadeh

CERTIFICATE

I hereby certify that the candidate has spent nine terms of research work towards the Degree of Doctor of Philosophy in the J. F. Allen Physics Research Laboratories of St. Salvator's College, at the University of St. Andrews, under my supervision, that he has fulfilled the conditions of Ordinance General No. 12 (St. Andrews), and that he is qualified to submit the following thesis in application for the degree of Doctor of Philosophy.

M. H. Dunn

Research Supervisor

CAREER

The author was born in Tehran, Iran, on May 5, 1962. He attended the United World College of the Atlantic, South Glamorgan, Wales, where he received his International Baccalaureate in 1980. He obtained the degree of BSc. in Physics and Electronics and the degree of MSc. in Optoelectronic and Laser Devices from the University of St. Andrews in 1984 and 1985, respectively. His postgraduate research studies towards the degree of PhD commenced in October 1985 in the Physics Department at St. Andrews University, on the project described in this thesis. Since October 1988, he has been employed as a Research Assistant in the same department, continuing his research activities in the field of broadly tunable excimer-pumped optical parametric oscillators and related non-linear devices.

ACKNOWLEDGEMENTS

The success of this work is a result of the combined efforts of several individuals. I would like to thank my supervisor Dr. Malcolm H. Dunn for his guidance, enthusiasm, encouragement, and invaluable advice during the course of this project. I also wish to express my thanks to Frits Akerboom for the growth and preparation of some of the crystals used during this study, and for his assistance in other areas of the work. The initial success of this work is largely due to his efforts. It is also a pleasure to acknowledge the technical assistance of members of the mechanical workshop in the Physics Department, under the direction of Mr. Ron McCraw. In particular, I would like to thank Myles White for the fabrication of many of the pump laser components, as well as Jim Clark, Bill Brown, George Cunningham, and Willie Smith for their skills and efforts in fabricating the various OPO components. My special thanks to Kate for her support and understanding over the past few years, and for her patience during the concluding stages of this work. Finally, I would like to thank Angus Henderson for helpful discussions regarding the OPO oscillation threshold and for providing some of the relevant theoretical data.

PUBLICATIONS AND PAPERS

Publications and papers by the author on topics discussed in this thesis :

- M. Ebrahimzadeh and M. H. Dunn, "A visible optical parametric oscillator pumped by an excimer laser," in *Postdeadline Papers, Conf. Lasers Electro-Opt.,* Opt. Soc. Amer., Washington, DC, 1988, paper PD30.
- M. Ebrahimzadeh and M. H. Dunn, "Optical parametric fluorescence and oscillation in urea using an excimer laser," *Opt. Commun.,* vol. 69, pp. 161-165, 1988.
- M. Ebrahimzadeh and M. H. Dunn, "Optical parametric oscillators pumped by excimer lasers," in *Tech. Dig., Conf. Lasers Electro-Opt.,* Opt. Soc. Amer., Washington, DC, 1989, paper FK1.
- M. Ebrahimzadeh, M. H. Dunn, and F. Akerboom, "Highly efficient visible urea optical parametric oscillator pumped by a XeCl excimer laser," *Opt. Lett.,* vol. 14, pp. 560-562, 1989.
- M. Ebrahimzadeh, A. J. Henderson, and M. H. Dunn, "An excimer-pumped β-BaB_2O_4 optical parametric oscillator tunable from 354nm to 2.370μm," *IEEE J. Quantum. Electron.* (submitted, August 1989).
- A. J. Henderson, M. Ebrahimzadeh, and M. H. Dunn, "Optical parametric oscillators pumped by excimer lasers," in *Tech. Dig., The Ninth National Quantum Electron. Conf.,* Oxford, UK, 1989, paper 180.
- A. J. Henderson, M. Ebrahimzadeh, and M. H. Dunn, "Characterisation of urea optical parametric oscillators pumped by excimer lasers," *J. Opt. Soc. Amer. B* (submitted, October 1989).

ABSTRACT

This thesis describes the development of a new generation of pulsed optical parametric oscillators (OPO's) based on two new non-linear materials, urea and β-BaB_2O_4 (or BBO), and pumped by a new class of laser pump sources, namely, excimer lasers, to provide broadly tunable coherent radiation in new regions of the electromagnetic spectrum, particularly in the ultraviolet and the visible, which have previously been inaccessible.

The laser pump source used during this work was a pulsed ultraviolet XeCl excimer laser operating at 308nm. Because of the stringent demands on the pump beam quality (with regard to both spatial and spectral coherence) for successful operation of OPO's, the pump laser was designed and constructed as an injection-seeded system, to provide a narrow-linewidth, near-diffraction-limited output beam, with sufficiently high peak powers to enable OPO operation. In this way, we were able to obtain an output beam with a linewidth $\leq 0.2cm^{-1}$, and a full-angle of divergence as low as $60\mu R$ (~3 times the diffraction limit). The maximum energy available from the pump laser was 30mJ, in pulses measuring typically 10ns in duration. The output beam was also linearly polarised to better than 95%, and the pulse repetition rate was 1 Hz.

In the early part of this work, we used the constructed pump laser to investigate spontaneous parametric fluorescence in a home-grown urea sample, in order to characterise the crystal, and to compare the observed spectrum with the calculated OPO tuning curves. The results of these experiments were found to be in good agreement with the theoretical predictions. The main thrust of the project, however, was the development of an OPO based on urea as the non-linear medium and pumped at 308nm

by the narrowband XeCl excimer laser. We were successful in constructing such an OPO, using an 8-mm-long, home-grown crystal, and were able to generate continuously tunable output from 572 to 667nm, with a 2.5% energy conversion efficiency. The tuning range of the device was later extended to 537-720nm, by utilising a 15-mm-long, home-grown urea sample, and its conversion efficiency was improved to as high as 37% at 90° phase-matching, with ≥ 10% efficiency over a 100-nm range in the visible (from 570 to 670nm). Finally, in an effort to achieve even higher efficiencies, we performed experiments in a 25-mm-long commercial urea crystal, and demonstrated exceptionally high external energy conversion efficiencies of up to 66%, with evidence of even higher levels of pump depletion (as high as 85%) at 90° phase-matching.

The latter part of the project was concerned with the design and development of a similar device based on the new non-linear material, β-BaB_2O_4, to provide continuously tunable radiation over a much broader tuning range, particularly in the blue and the near ultraviolet, not accessed by the urea OPO. We used a 12-mm-long commercially available β-BaB_2O_4 crystal to construct this OPO, and successfully operated this device over the entire wavelength range from 354nm in the near ultraviolet, throughout the visible, to 2.37μm in the near infrared, with an energy conversion efficiency in excess of 10% over the range 450-960 nm. The constructed OPO's were also characterised with regard to several operating parameters, including oscillation threshold, spectral linewidth, as well as spatial and temporal variation and, where appropriate, the experimental results were compared with the predictions of theory.

To My Parents

"God does not care about our
mathematical difficulties.
He integrates empirically."

Albert Einstein 1897-1955

(in *L. infeld Quest* 1942; London: Golancz)

TABLE OF CONTENTS

1 INTRODUCTION 1

2 THEORY OF PARAMETRIC INTERACTIONS 19

3 THE PUMP LASER 52

Introduction

1.0 INTRODUCTION

Since the invention of the laser in 1960, considerable effort has been devoted to the development of frequency-variable sources of coherent radiation. Many applications require tunable laser radiation of high intensity and narrow bandwidth in different regions of the electromagnetic spectrum. In recent years, various physical principles have been successfully employed to produce such radiation. Following the demonstration of second harmonic generation of light, and hence the existence of substantial non-linear optical coefficients, by Franken *et al.* [1] in 1961, many experiments in non-linear optics were performed. These experiments were made possible due to the significant increase in the spectral intensity provided by the laser radiation. Soon after, optical parametric amplification and oscillation were recognised as convenient techniques for generation of widely tunable coherent radiation in different spectral regions. Many of the basic ideas of parametric amplification and oscillation had been extensively explored in the microwave frequency region. The development of parametric devices in the microwave region was well under way, when Kingston [2], Kroll [3], Akhmanov and Khokhlov [4], and Armstrong *et al.* [5] proposed the extension of parametric interactions to optical frequencies. Since then, much progress has been reported in the development of optical parametric amplifiers and oscillators and these devices have been extensively studied by several investigators. The main attraction of these devices compared with the other more widely-established tunable lasers (e.g. dye lasers, colour centre lasers, semiconductor lasers, alexandrite and Ti: sapphire lasers) is the exceptionally broad tuning bandwidth and the ability to cover those wavelength regions that are not accessible by the other tunable lasers (see Fig. 1.1). In addition, these devices can be made very compact, are potentially long-lived and efficient, and above all, remarkably easy to operate. In this chapter, we discuss the basic operating principles of an optical parametric oscillator and present a brief historical overview of the practical devices constructed to date. We also outline the important merits of excimer lasers for use as pump sources for these devices, which is the subject of this thesis.

1.1 THE OPTICAL PARAMETRIC OSCILLATOR

In its simplest form, the optical parametric oscillator (OPO) consists of a non-linear crystal enclosed by an optical resonator, similar to that used in a traditional laser, and irradiated by an intense optical pump field at ω_p, as shown in Fig. 1.2. The pump field gives rise to a pair of signal and idler fields at ω_s and ω_i, such that

$$\omega_p = \omega_s + \omega_i \qquad \textbf{(1-1)}$$

The excited fields at ω_s and ω_i can be simultaneously amplified as they propagate through the non-linear crystal, provided the *phase-match* condition is satisfied, that is

$$k_p = k_s + k_i \qquad \textbf{(1-2)}$$

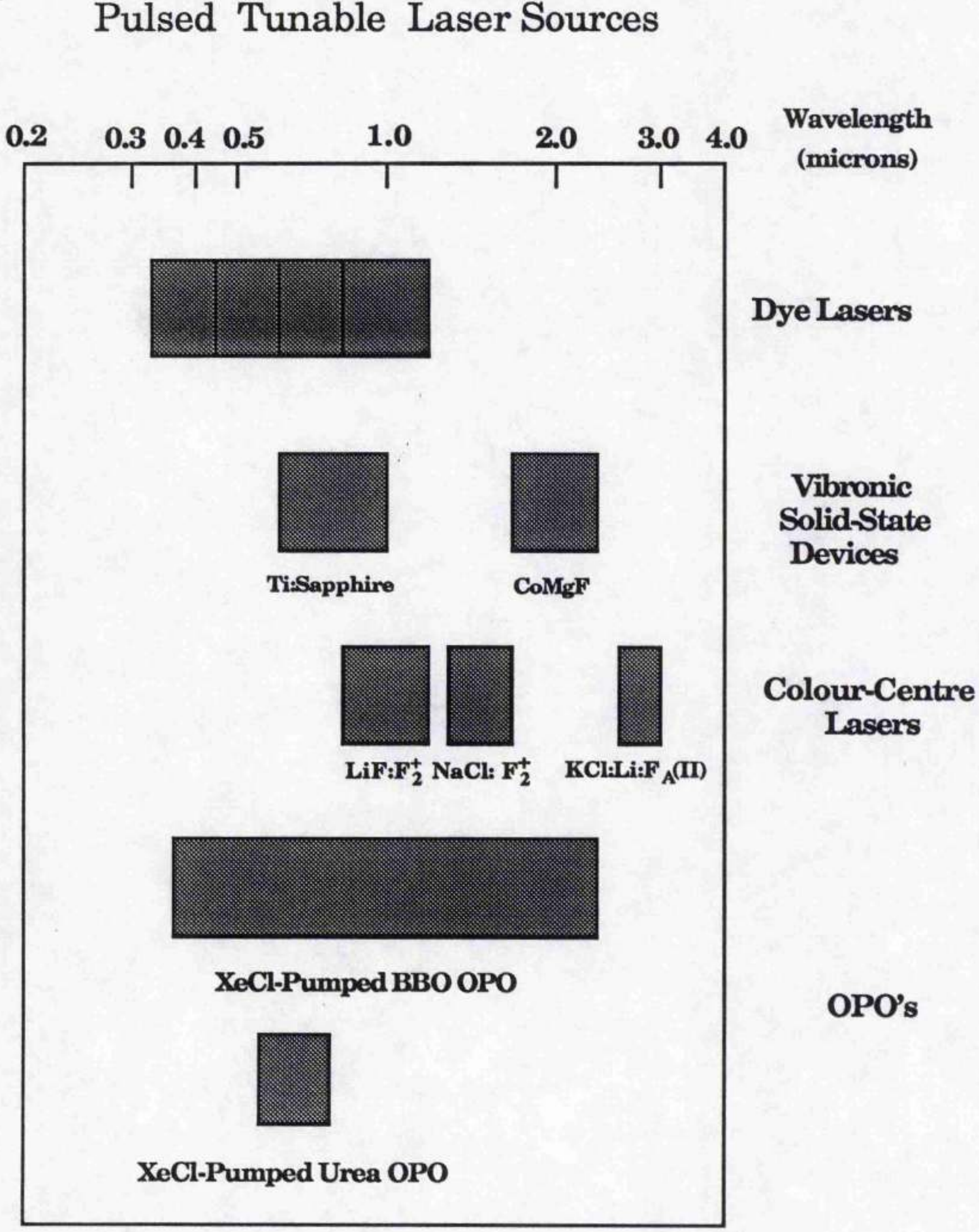

Fig. 1.1. Wavelength coverage of a number of pulsed tunable laser sources.

where k is the wavevector within the material. Gain at ω_s and ω_i is provided through parametric interaction of the three optical fields within the non-linear medium. This interaction is a result of the non-linear polarisation exhibited by the material, which must lack inversion symmetry in its crystalline structure. Equations (1-1) and (1-2) may also be regarded as statements of conservation of energy and momentum, respectively.

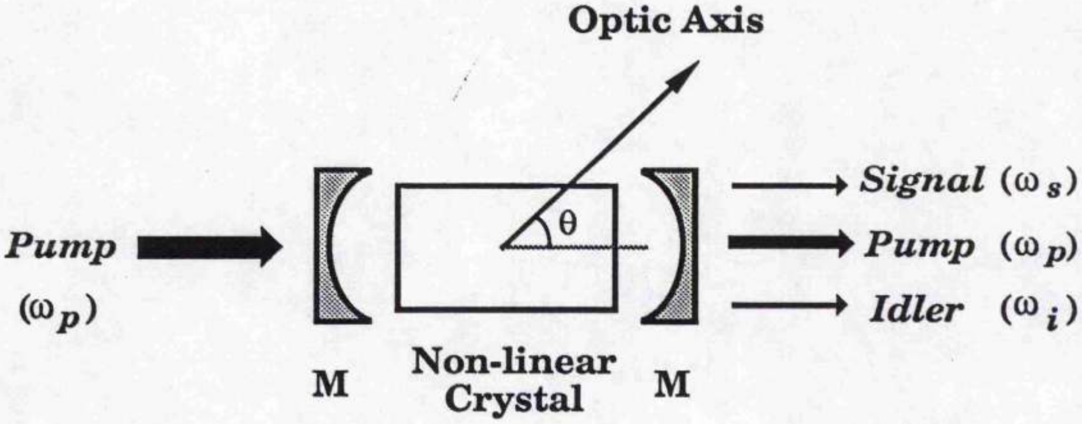

$$\omega_p = \omega_s + \omega_i \, , \; k_p = k_s + k_i$$

Fig. 1.2. The Optical Parametric Oscillator.

For a given pump frequency ω_p and wavevector k_p, the parametric process selects, out of an infinite number of possible combinations allowed by $\omega_p = \omega_s + \omega_i$, a single pair of frequencies satisfying the phase-match condition $k_p = k_s + k_i$ which is determined by the dispersive properties of the medium. The pair of frequencies ω_s and ω_i may be varied by changing the refractive indices of the crystal along the direction of propagation. This is most commonly achieved by either altering the crystal temperature (temperature tuning) or its orientation with respect to the pump beam (angle tuning). In this way, ω_s and ω_i can be tuned over broad spectral ranges with relative ease and simplicity. The optical cavity may provide feedback for either the signal or the idler waves or both. In the case where the feedback is provided for both the signal and the idler, the oscillator is called a *Doubly-Resonant Oscillator* (*DRO*). In the case where the cavity is resonant for either the signal or the idler, but not both, the oscillator is referred to as a *Singly-Resonant Oscillator* (*SRO*). In either form of oscillator, *DRO* or *SRO*, there is an oscillation threshold at which the parametric gain will cause oscillation at either of the signal or idler frequencies ω_s or ω_i, or both. The threshold condition is defined by the requirement that the round-trip parametric gain experienced by the resonated wave(s) just balances the total resonator loss. Below threshold, there is a small amount of spontaneous parametric emission (see chapter 4), while above threshold the resonated wave(s) experience a *net* round-trip gain and can grow to the point where the magnitudes of the fields are comparable to that of the pump, and useful coherent output can be extracted from the oscillator. This is the underlying principle of the optical parametric oscillator. The practical importance of the device derives from its ability to convert the pump power at a fixed frequency ω_p, to power at the signal and idler frequencies ω_s and ω_i, which are continuously tunable over broad spectral regions.

1.2 PARAMETRIC OSCILLATOR DEVICES

The first successful operation of an OPO was reported by Giordmaine and Miller as early as 1965 [6]. The non-linear crystal used in that experiment was $LiNbO_3$ and the OPO was pumped by a frequency-doubled Nd^{3+}: $CaWO_4$ laser at 529nm. The oscillator provided tunable output over a limited range in the near infrared from 970nm to 1.15μm. Since then, many oscillators have been constructed and extensive tuning ranges throughout the optical spectrum have been demonstrated using a variety of non-linear crystals and pump sources. Table 1.I summarises the principal characteristics of a number of practical OPO devices constructed since 1965. It is seen from the table that operation of OPO's has, in the past, been confined primarily to the infrared spectral regions. The extension of the tuning range of these devices into the visible and ultraviolet spectral regions has been difficult because of two major practical problems. The first has been a lack of suitable non-linear materials of desirable properties, most notably a large effective non-linear coefficient, d_{eff}, and a high optical damage threshold. The latter constraint is particularly severe at the pump wavelengths of interest in the visible and ultraviolet spectral regions. The second obstacle has been an absence of pump sources of high spectral and spatial coherence in the ultraviolet spectral regions. This requirement is particularly important, since OPO devices are much more demanding on the quality of the pump radiation than is the case with laser gain media utilising population inversions, because of the need to maintain a definite phase relation between the interacting fields for macroscopic growth of the parametric waves. Due to these difficulties, there has previously been a limited interest in the OPO for generation of tunable laser radiation in the visible and near ultraviolet spectral regions and other more practical options have been favoured. Recently, however, because of the introduction of new non-linear materials such as urea, β-BaB_2O_4 (BBO), and most recently Lithium tri-Borate (LBO), which exhibit a reasonably large d_{eff} coupled with a high optical damage threshold, wide transparency range, and adequately large birefringence, as well as laser pump sources of improved spatial and spectral coherence particularly in the near ultraviolet spectral regions, operation of visible, ultraviolet, and near infrared OPO's has been made possible.

Table 1.1. Summary of a number of parametric oscillator experiments performed to date.

Pump Laser	Crystal	Tuning Range	O/P Power	Efficiency	Refs.
2x $CaWO_4:Nd^{+3}$ (0.529μm)	$LiNbO_3$	0.97-1.15μm	15W	~0.1%	[6]
2x Nd^{+3}:Glass (o.530μm)	KDP	0.96-1.18μm	5kW	–	[7]
2x $CaWO_4:Nd^{+3}$ (0.529μm)	$LiNbO_3$	0.73-1.93μm	1kW	1%	[8]
2x Nd^{+3}:Glass (o.530μm)	$LiNbO_3$	0.68-2.36μm	50W	0.1%	[9]
Ruby (0.694μm)	$LiNbO_3$	1-1.08μm	38kW (peak power)	1.2%	[10]
2x Nd^{+3}:YAG (0.532μm)	$Ba_2NaNb_5O_{15}$	0.98-1.16μm	3mW	1%	[11]
Ruby (0.694μm)	$LiNbO_3$	1.04μm & 2.08μm	–	22%	[12]
2x Nd^{+3}:Glass (0.530μm)	$LiNbO_3$	0.96μm & 1.18μm	–	36%	[13]
Argon (0.514μm)	$LiNbO_3$	0.68-0.71μm 1.90-2.11μm	3mW	–	[14]
Ruby (0.694μm)	$LiNbO_3$	0.98-1.04μm 2.38-2.08μm	250kW (peak power)	28%	[15]
2x Nd^{+3}:YAG (0.532μm)	$Ba_2NaNb_5O_{15}$	0.95-1.06μm 1.07-1.21μm	60mW (average power)	0.1%	[16]
2x Nd^{+3}:Glass (0.530μm)	ADP	–	100kW (peak power)	1%	[17]
Ruby (0.694μm)	$LiNbO_3$	1.05-1.19μm	340kW (peak power)	45%	[18]
Nd^{+3}:YAG (1.064μm)	$LiNbO_3$	1.95-2.35μm	170W (peak) 17mW (average)	8.5%	[19]
2x Nd^{+3}:Glass (0.530μm)	KDP	–	3-5MW	7%	[20]
Argon (0.514μm)	$LiNbO_3$	0.66-0.70μm (*signal*) ~2μm (*idler*)	–	60% (depletion)	[21]
Ruby (0.694μm)	$LiNbO_3$	1.064μm & 2μm	100kW (peak power)	3%	[22]

Table 1.I. continued

Pump Laser	Crystal	Tuning Range	O/P Power	Efficiency	Refs.
Ruby (0.694μm)	$LiNbO_3$	1.015μm & 2.22μm	–	–	[23]
Nd^{+3}:YAG (1.064μm)	$LiNbO_3$	2.13μm	–	–	[24]
Nd^{+3}:YAG (1.064μm)	Ag_3AsS_3	~2.1μm	–	–	[25]
Ruby (0.694μm)	$LiIO_3$	0.84-0.96μm (*signal*) 4-2.5μm (*idler*)	2kW –	1% –	[26]
2x Nd^{+3}:YAG (0.532μm)	$LiNbO_3$	0.55-3.65μm	105mW (average power)	67% (depletion)	[27]
Nd^{+3}:YAG (1.064μm)	$LiNbO_3$	~2μm	350mW (average power)	75% (depletion)	[28]
Argon (0.488μm)	$Ba_2NaNb_5O_{15}$	0.64-0.66μm 2.05-1.87μm	7mW	1%	[29]
Nd^{+3}:YAG (1.064μm)	Ag_3AsS_3	1.82-2.56μm	1kW (peak power)	1%	[30]
Nd^{+3}:YAG (1.833μm)	CdSe	2.23-2.25μm 9.8-1.04μm	–	40%	[31]
Nd^{+3}:YAG (1.064μm)	$LiIO_3$	1.95-2.34μm (*DRO*) 3.8-4.2μm (*SRO*)	0.2mJ –	12% –	[32]
Nd^{+3}:YAG (1.833μm)	CdSe	2μm & 9.6μm	860W & 180W (average power)	40%	[33]
Ruby (0.694μm)	$LiIO_3$	1.12-1.83μm	100kW (peak power)	10%	[34]
Argon (0.514μm)	$Ba_2NaNb_5O_{15}$	1.029μm	–	–	[35]
2x Nd^{+3}:YAG (0.532μm)	$Ba_2NaNb_5O_{15}$	–	78mW	52%	[36]
Nd^{+3}:YAG (1.064μm)	$LiNbO_3$	1.5-3.8μm	< 1.8W (average power)	–	[37]
2x Ruby (0.347μm)	$LiIO_3$	0.415-2.1μm	10kW (peak power)	8%	[38]
Nd^{+3}:YAG (1.064μm)	Ag_3AsS_3	1.22-8.5μm	100W (*idler*) (peak power)	–	[39]

Table 1.I. continued

Pump Laser	Crystal	Tuning Range	O/P Power	Efficiency	Refs.
Nd^{+3}:YAG (1.064µm)	LiNbO$_3$	1.51-3.55µm	600W (peak) 6mW (average)	50% 10%	[40]
HF (2.87µm)	CdSe	4.3-4.5µm 8.1-8.3µm	800W (peak power)	15%	[41]
Nd^{+3}:YAG (1.064µm)	LiNbO$_3$	1.4-4.4µm	1mJ	15%	[42]
2x Nd^{+3}:YAG (0.532µm)	CDA	0.854-1.41µm	0.6mJ	6%	[43]
3x Nd^{+3}:YAG (0.355µm)	RD*A	~0.65-0.8µm	1.2MW (peak power)	17%	[44]
Nd^{+3}:YAlO$_3$ (1.08µm)	LiIO$_3$	1.98-2.37µm 3.25-4.05µm	1.1W 50mW (average power)	50% –	[45]
HF (2.87µm)	CdSe	14.1-16.4µm 3.60-3.48µm	100µJ	4%	[46]
Nd^{+3}:YAG (1.064µm)	LiIO$_3$	2.12µm	0.4 J	20%	[47]
2x Nd^{+3}:YAG (0.532µm)	LiIO$_3$	0.63-3.4µm	160kW (peak power)	–	[48]
2x Nd^{+3}:YAG (0.532µm)	KNbO$_3$	0.86-1.4µm	1mW (average power)	5%	[49]
2x Nd^{+3}:YAG (0.532µm)	KNbO$_3$	0.88-1.35µm	12MW (peak) 770mW (average)	32%	[50]
Nd^{+3}:YAG (1.064µm)	AgGaS$_2$	1.40-4µm	0.5mJ	16%	[51]
Nd^{+3}:YAG (1.064µm)	LiIO$_3$	2.5-3.2µm	100mJ	10%	[52]
3x Nd^{+3}:YAG (0.355µm)	Urea	0.5-0.51µm 1.17-1.22µm	91kW (peak) 6mW (average)	20%	[53]
3x Nd^{+3}:YAG (0.355µm)	Urea	0.498-0.640µm 0.79-1.23µm	–	23%	[54]
3x Nd^{+3}:YAG (0.355µm)	β-BaB$_2$O$_4$	0.45-1.68µm	1.4mJ	9.4%	[55]
3x Nd^{+3}:YAG (0.355µm)	β-BaB$_2$O$_4$	0.412-2.55µm	4.7mJ 140mW (average)	24%	[56]

Table 1.I. continued

Pump Laser	Crystal	Tuning Range	O/P Power	Efficiency	Refs.
4x Nd^{+3}:YAG (0.266μm)	β-BaB_2O_4	0.33-1.37μm	–	–	[57]
XeCl excimer (0.308μm)	Urea	0.537-0.720μm	11mJ	66%	[58]-[61]
XeCl excimer (0.308μm)	β-BaB_2O_4	0.354-2.37μm	2mJ	10%	[60]-[62]
XeCl excimer (0.308μm)	β-BaB_2O_4	0.422-0.477μm	0.7mJ	10%	[63]

Optical parametric oscillation in the visible, near infrared, and most recently, the near ultraviolet has been reported in a number of new non-linear crystals using frequency-converted Nd^{+3}:YAG pump lasers. In 1984, Donaldson and Tang [53] constructed the first OPO to use the new organic non-linear crystal, urea. The OPO was pumped at 355nm by Q-switched frequency-tripled Nd^{+3}:YAG pulses and a limited tuning range in the visible and the near infrared was demonstrated. Soon after, Rosker and Tang [54] extended the wavelength coverage of the device and achieved a tuning range in the visible region from 498 to 640nm, with a complementary infrared coverage from 1.230 to 0.790μm. Optical parametric oscillation in β-BaB_2O_4 (BBO) crystal has also been demonstrated using Q-switched frequency-tripled Nd^{+3}:YAG pump lasers. Cheng *et al.* [55] reported a β-BaB_2O_4 OPO that was tunable throughout the range 0.450-1.680μm while Fan *et al.* [56] operated a similar device with improved efficiency (24%, total) and a more extensive tuning range from 0.412 to 2.550μm. More recently, Bosenberg *et al.* [57] demonstrated optical parametric oscillation in β-BaB_2O_4 crystal in the near ultraviolet using the fourth harmonic of a Q-switched Nd^{+3}:YAG laser at 266nm as the pump source. The OPO generated continuously tunable output over the range 0.330-1.370μm. However, the efficiency of the device was limited across its entire tuning range by the need to propagate the 266nm pump light to the far-field, and by damage to OPO optics.

1.3 EXCIMER-PUMPED OPTICAL PARAMETRIC OSCILLATORS

Although, the use of Q-switched, frequency-converted Nd^{+3}:YAG pump lasers for OPO's operating in the visible and near infrared spectral regions has been widespread, the additional frequency conversion processes generally result in significant reductions in overall system efficiencies. In contrast, excimer lasers offer great potential as pumps for OPO's operating throughout the ultraviolet, visible, and infrared spectral regions because of the large number of ultraviolet wavelengths they make available. They are also more efficient and offer the potential for much higher average powers compared with Nd^{+3}:YAG lasers of comparable size and power requirements. The potential spectral coverage of two OPO devices based on urea and β-BaB_2O_4 as the non-linear crystal is shown for a number of excimer pump wavelengths in Figs. 1.3 and 1.4, respectively. The tuning ranges have been calculated by solving the phase-matching equations (1-1) and (1-2) for signal and idler waves at the given pump wavelength, as a function of the internal angle θ between the pump propagation direction and the crystal optic axis. The limit to the operation of these devices beyond the wavelength regions shown, is essentially the infrared absorption in the material. In order to determine these tuning ranges, the dispersion (Sellemeier) equations for the material which are essentially empirical expressions describing the variation in the refractive index with wavelength, must be known. The tuning ranges of the OPO can then be calculated, given the possible phase-matching schemes (type I or type II) that are to be employed. A more detailed discussion of the possible phase-matching techniques in crystals with positive and negative birefringence as well as different tuning methods can be found in chapter 2, section 2.4.1. The exact form the Sellemeier equations for urea and β-BaB_2O_4 together with the detailed form of the calculated OPO tuning curves for the XeCl pump wavelength is given in chapters 5 and 6, respectively. Also, the computer programmes used to determine these tuning curves are documented in appendix A. It can be seen from Figs. 1.3 and 1.4 that extensive spectral regions throughout the near ultraviolet,

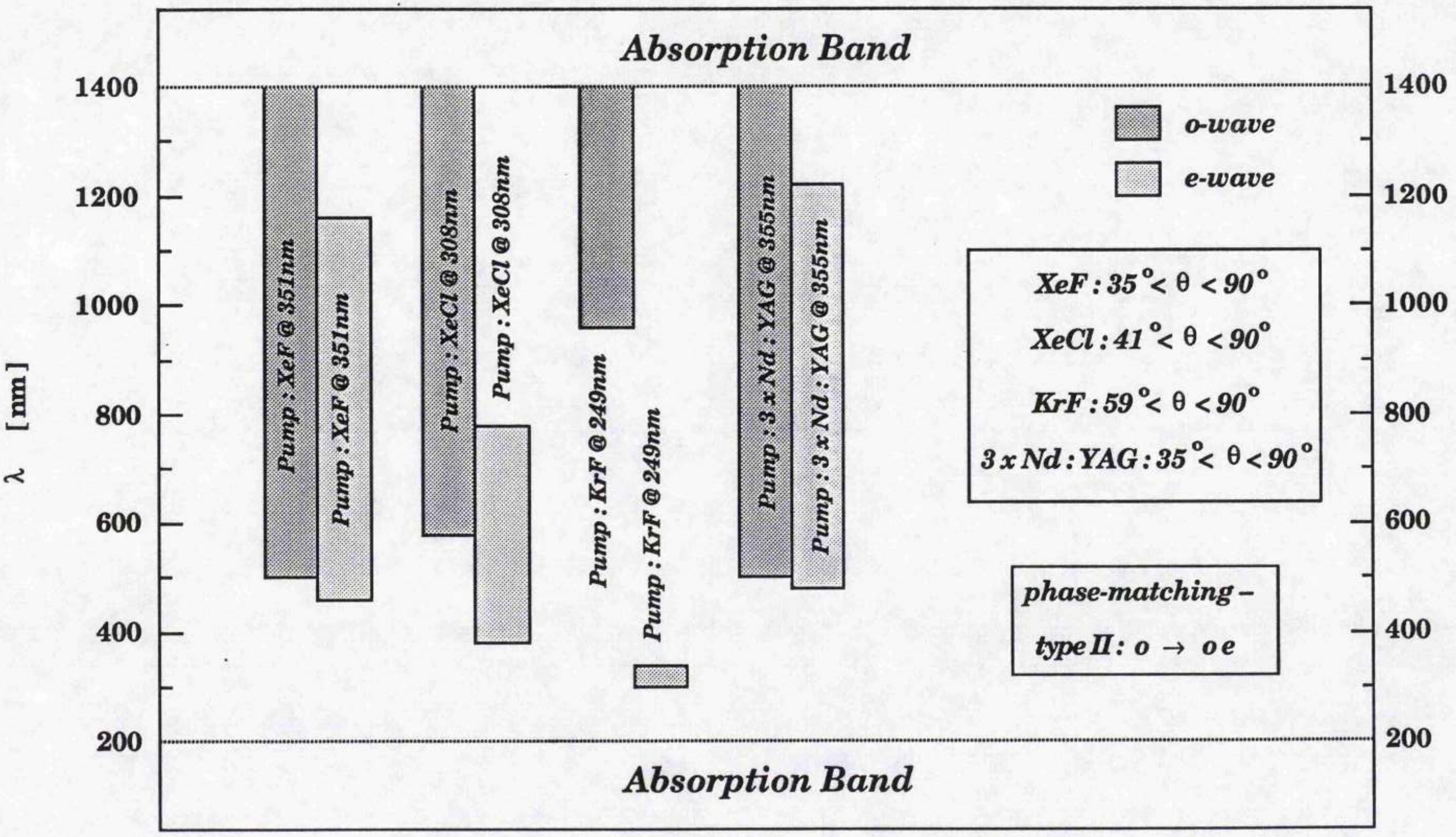

Fig. 1.3. Potential tuning range of urea optical parametric oscillator, with type II phase-matching, for several excimer pump wavelengths.

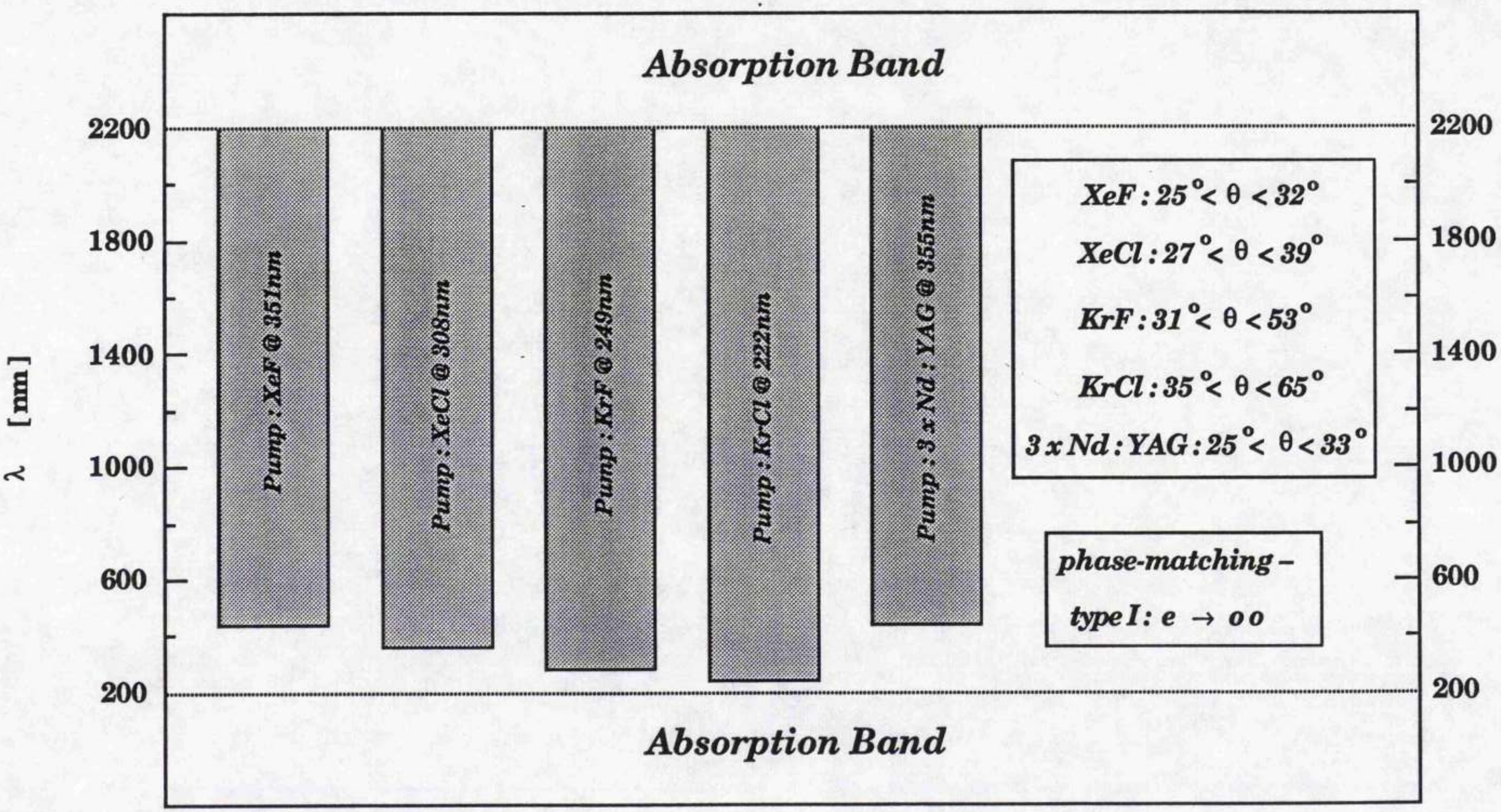

Fig. 1.4. Potential tuning range of BBO optical parametric oscillator, with type I phase-matching, for several excimer pump wavelengths.

visible, and the near infrared may be accessed by utilising XeF, XeCl, KrF, and KrCl excimer lasers to pump OPO's based on urea and β-BaB_2O_4. The ultraviolet and blue/green spectral coverage is particularly important as there are few viable tunable laser sources available in these regions, where many applications including trace element detection (for example, by Resonant Ionisation Spectroscopy), pollution monitoring, underwater communication, and possibly medical therapy may benefit.

Despite the great potential of excimer lasers, their use as pumps for OPO's has previously not been possible because of their poor spatial and spectral coherence. However, the recent development of injection-seeding combined with unstable resonators, and their application to these lasers, has resulted in significant improvements in these parameters, so that the use of excimer lasers as pumps for OPO's is now realistic. The work presented here was the first report on the use of an excimer laser to pump an OPO. This device utilized a urea crystal as the non-linear medium and was pumped at 308nm by an injection-seeded narrow-linewidth XeCl excimer laser. Operation of this device has been described in detail in [58]-[61]. The use of this pump laser was later extended to an OPO based on β-BaB_2O_4 as the non-linear crystal and was reported in [60], [61]. This OPO generated tunable radiation over a broad spectral range from 354nm in the near-UV, throughout the visible, to 2.37μm in the near-IR, with an energy conversion efficiency in excess of 10% over a 500-nm wavelength range from 450 to 960 nm. A more comprehensive characterisation of this device is to appear in [62]. A similar device based on β-BaB_2O_4 , but tunable over a limited range in the visible (from 422-477nm) and near-IR (from 1.14μm-870nm) was also reported by Komine in 1988 [63]. The conversion efficiency of this device was reported as 10.4% at 445nm. This work demonstrates that it is possible to use excimer lasers in conjunction with the new non-linear materials, to provide tunable laser radiation in new regions of the electromagnetic spectrum, particularly in the near ultraviolet and visible that have so far been inaccessible, with relative simplicity and at high efficiency, through optical parametric oscillation. As a result, we expect a revival of interest in such devices for generation of tunable laser radiation and believe that their practical advantages over other competing tunable lasers will lead to their widespread use in a variety of applications.

In the following chapter, we discuss the theory of parametric interaction of electromagnetic fields within optically anisotropic non-linear media and show how this interaction may lead to parametric amplification and oscillation. The design and construction of the pump laser is described in detail in chapter 3. In chapter 4, we present the results of the experiments on spontaneous parametric fluorescence in urea, which are important in the assessment of the properties of the material as well as in determining the OPO tuning curves prior to its construction. An extensive discussion on the operating characteristics of the urea and β-BaB_2O_4 OPO's, together with experimental results on the relevant oscillator parameters are presented in chapters 5 and 6, respectively. Finally, in chapter 7, we summarise the achievements of this work, discuss how further improvements in the performance of these devices may be brought about, and propose a strategy for the future development of excimer-pumped OPO's.

References to Chapter 1.

[1] P. A. Franken *et al.*, Phys. Rev. Lett. 7, 118 (1961)

[2] R. H. Kingston, Proc. IRE 50, 472 (1962)

[3] N. M. Kroll, Phys. Rev. 127, 1207 (1962)

[4] S. A. Akhmanov and R. V. Khokhlov, Sov. Phys. JETP 16, 252 (1963)

[5] J. A. Armstrong *et al.*, Phys. Rev. 127, 1918 (1962)

[6] J. A. Giordmaine and R. C. Miller, Phys. Rev. Lett. 14, 973 (1965)

[7] S. A. Akhmanov *et al.*, JETP Lett. 3, 241 (1966)

[8] J. A. Giordmaine and R. C. Miller, Appl. Phys. Lett. 9, 298 (1966)

[9] R. C. Miller and W. A. Nordland, Appl. Phys. Lett. 10, 53 (1967)

[10] L. B. Kreuzer, Appl. Phys. Lett. 10, 336 (1967)

[11] R. G. Smith *et al.*, Appl. Phys. Lett. 12, 308 (1968)

[12] J. E. Bjorkholm, Appl. Phys. Lett. 13, 53 (1968)

[13] L. B. Kreuzer, Appl. Phys. Lett. 13, 57 (1968)

[14] R. L. Byer *et al.*, Appl. Phys. Lett. 13, 109 (1968)

[15] J. E. Bjorkholm, Appl. Phys. Lett. 13, 399 (1968)

[16] R. G. Smith *et al.*, J. Appl. Phys. 32, 4030 (1968)

[17] A. G. Akhmanov *et al.*, IEEE J. Quantum Electron., QE-4, 828 (1968)

[18] J. Falk and J. E. Murray, Appl. Phys. Lett. 14, 245 (1969)

[19] E. O. Ammann *et al.*, Appl. Phys. Lett. 15, 131 (1969)

[20] Yu. N. Belyaev *et al.*, JETP Lett. 9, 263 (1969)

[21] R. L. Byer *et al.*, Appl. Phys. Lett. 15, 136 (1969)

[22] J. E. Bjorkholm and H. G. Danielmeyer, Appl. Phys. Lett. 15, 171 (1969)

[23] L. B. Kreuzer, Appl. Phys. Lett. 15, 263 (1969)

[24] E. O. Ammann *et al.*, IEEE J. Quantum Electron., QE-5, 356 (1969)

[25] E. O. Ammann and J. M. Yarborough, Appl. Phys. Lett. 17, 233 (1970)

[26] L. S. Goldberg, Appl. Phys. Lett. 17, 489 (1970)

[27] R. W. Wallace, Appl. Phys. Lett. 17, 497 (1970)

[28] E. O. Ammann *et al.*, J. Opt. Soc. Amer. 60, 717 (1970)

[29] C. Laurence and F. Tittel, J. Appl. Phys. 42, 2137 (1971)

[30] D. C. Hanna *et al.*, Appl. Phys. Lett. 20, 34 (1972)

[31] R. L. Herbst and R. L. Byer, Appl. Phys. Lett. 21, 189 (1972)

[32] L. S. Goldberg, IEEE J. Quantum Electron., QE-8, 573 (1972)

[33] R. L. Herbst and R. L. Byer, IEEE J. Quantum Electron.,QE-8, 575 (1972)

[34] A. J. Campillo, IEEE J. Quantum Electron., QE-8, 809 (1972)

[35] J. F. Weller *et al.*, J. Opt. Soc. Amer. 62, 1398 (1972)

[36] R. G. Smith, IEEE J. Quantum Electron.,QE-9, 530 (1973)

[37] J. M. Yarborough and E. O. Ammann, IEEE J. Quantum Electron., QE-9, 702 (1973)

[38] G. Nath and G. Pauli, Appl. Phys. Lett. 22, 75 (1973)

[39] D. C. Hanna *et al.*, Appl. Phys. Lett. 22, 440 (1973)

[40] J. E. Pearson *et al.*, Appl. Opt. 12, 1165 (1973)

[41] J. A. Weiss and L. S. Goldberg, Appl. Phys. Lett. 24, 389 (1974)

[42] R. L. Herbst *et al.*, Appl. Phys. Lett. 25, 520 (1974)

[43] G. A. Massey and R. A. Elliot, IEEE J. Quantum Electron., QE-10, 899 (1974)

[44] K. Kato, IEEE J. Quantum Electron., QE-11, 939 (1975)

[45] E. O. Ammann, IEEE J. Quantum Electron., QE-11, 65D (1975)

[46] R. G. Wenzel and G. P. Arnold, Appl. Opt. 15, 1322 (1976)

[47] A. A. Babin *et al.*, Sov. J. Quantum Electron. 6, 613 (1976)

[48] S. A. Akhmanov *et al.*, Sov. J. Quantum Electron. 7, 1271 (1977)

[49] V. A. D'yakov *et al.*, Sov. J. Quantum Electron. 11, 433 (1981)

[50] K. Kato, IEEE J. Quantum Electron., QE-18, 451 (1982)

[51] Y. X. Fan *et al.*, Appl. Phys. Lett. 45, 313 (1984)

[52] I. I. Ashmarin *et al.*, Sov. J. Quantum Electron. 14, 1237 (1984)

[53] W. R. Donaldson and C. L. Tang, Appl. Phys. Lett. 44, 25 (1984)

[54] M. J. Rosker and C. L. Tang, J. Opt. Soc. Amer. B. 2, 691 (1985)

[55] L. K. Cheng *et al.*, Appl. Phys. Lett. 53, 175 (1988)

[56] Y. X. Fan *et al.*, Appl. Phys. Lett. 53, 2014 (1988)

[57] W. R. Bosenberg *et al.*, Appl. Phys. Lett. 54, 13 (1989)

[58] M. Ebrahimzadeh and M. H. Dunn, in Postdeadline Papers, Conf. Lasers Electro-Opt., Opt. Soc. Amer., Washington, DC, 1988, paper PD30.

[59] M. Ebrahimzadeh and M. H. Dunn, Opt. Commun. 69, 161 (1988)

[60] M. Ebrahimzadeh *et al.*, Opt. Lett. 14, 560 (1989)

[61] M. Ebrahimzadeh and M. H. Dunn, in Tech. Dig., Conf. Lasers Electro-Opt., Opt. Soc. Amer., Washington, DC, 1989, paper FK1.

[62] M. Ebrahimzadeh *et al.*, submitted to IEEE J. Quantum Electron.

[63] H. Komine, Opt. Lett. 13, 643 (1988)

2

Theory of Parametric Interactions

2.0 INTRODUCTION

In this chapter, we discuss the underlying physical principles responsible for parametric interaction of electromagnetic fields in optically anisotropic, non-linear media and derive the equations governing parametric amplification and gain. We also consider, in some detail, the concept of phase-matching and its influence on parametric gain. Finally, we discuss the requirements placed upon the spatial and spectral coherence of pump radiation for maintaining minimum momentum-mismatch (and hence maximum parametric gain), and its implications for successful operation of optical parametric oscillators. We shall adopt MKS units throughout the analysis, as most of the later literature on the subject uses this system of units.

2.1 NON-LINEAR BACKGROUND

When a material is subjected to electromagnetic radiation, the electrons in the medium are polarised with respect to the nuclei. In the case where the electric field **E** associated with the radiation is small, the induced polarisation or the electric dipole moment per unit volume, **P**, of the medium is linearly proportional to the applied field, namely

$$\mathbf{P} = \varepsilon_0 \chi^{(1)} \mathbf{E}\,, \tag{2-1}$$

where $\chi^{(1)}$ is the linear susceptibility of the medium and ε_0 is the permittivity of free space. This is the regime of *linear* optics. The real part of the linear susceptibility $\chi^{(1)}$ is related to the refractive index of the medium, n, by

$$\chi^{(1)} = n^2 - 1 \tag{2-2}$$

and is responsible for the familiar linear optical phenomena of reflection and refraction. In general, $\chi^{(1)}$ is dependent on the frequency, ω, of the optical radiation.

The linear dependence of the induced polarisation on the electric field strength which was assumed as the basis of pre-laser optics is, in fact, only an approximation. In the case when the optical electric field strength is comparable to the intra-atomic electric field, as with laser radiation, the linear relation between **P** and **E** is no longer sufficient and a power series expansion in terms of the field must be used, namely

$$\mathbf{P} = \varepsilon_0 [\, \chi^{(1)} \mathbf{E} + \chi^{(2)} \mathbf{E}^2 + \chi^{(3)} \mathbf{E}^3 + \cdots] \tag{2-3}$$

where $\chi^{(2)}, \chi^{(3)}, \ldots$ are the non-linear susceptibilities of the medium and are, in general, tensors of the third, fourth, and higher ranks, respectively. This is the regime of *non-linear* optics. We note that in writing equations (2-1) and (2-3), we have used a scalar notation on the assumption that the vectors **P** and **E** are parallel, although this is rarely the case when anisotropic media are involved. In such media, **P** and **E** are connected through a tensor relation and are not in general parallel. We will, however, consider these equations in their scalar form in order to simplify the analysis.

Most of the interesting non-linear optical effects arise from the terms of electric polarisation which are quadratic or cubic in the electric field. The quadratic polarisation gives rise to the phenomena of second harmonic generation and d.c. rectification as well as linear electro-optic (Pockel's) effect and parametric generation. The cubic term is responsible for third harmonic generation, stimulated Raman scattering, quadratic electro-optic (Kerr) effect, optical bistability and phase conjugation. In this discussion, we are concerned only with the quadratic non-linear term $\chi^{(2)}$, as this is the term responsible for the parametric interaction that is of interest. This term is usually referred to as the second-order non-linear susceptibility of the medium and is a tensor of the third rank. This tensor is only finite in non-centrosymmetric anisotropic media and is subject to the symmetry conditions of the non-linear material [1]. It may have several components that are zero and in many cases may satisfy further symmetry relations [2].

2.2 PARAMETRIC INTERACTION OF PLANE WAVES

When an electromagnetic field propagates through a *linear* medium, its propagation characteristics are not influenced by its own intensity nor by the presence of other electromagnetic fields. However, different electromagnetic waves can interact when propagating through a *non-linear* medium, with the result that the propagation characteristics of one field can be influenced by the presence of other fields. It is this interaction which is the basis of many of the observed non-linear optical phenomena including parametric generation.

2.2.1 Wave Propagation in Non-Linear Media

In order to derive the equations governing parametric amplification and oscillation, we shall consider the propagation of electromagnetic waves within an anisotropic, non-linear medium. We start by writing down Maxwell's wave equation for a non-conducting dielectric medium containing no free charge, that is

$$\nabla^2\mathbf{E} = \mu\varepsilon\frac{\partial^2\mathbf{E}}{\partial t^2} + \mu\frac{\partial^2\mathbf{P}}{\partial t^2} \tag{2-4}$$

where **E** is the electric field of the electromagnetic field, **P** is the total polarisation of the medium given by (2-3), and $\varepsilon = \varepsilon_0(1+\chi^{(1)})$. In writing (2-4), we have assumed that **P** and **E** are in the same direction. The formalism may now be developed further by separating the total polarisation of the medium, **P**, into two terms; a linear term given by

$$\mathbf{P_L} = \varepsilon_0\chi^{(1)}\mathbf{E} \tag{2-5}$$

and a non-linear term arising from the higher-order susceptibilities in (2-3), namely

$$\mathbf{P_{NL}} = \chi^{(2)}\mathbf{E}^2 + \chi^{(3)}\mathbf{E}^3 + \cdots \tag{2-6(a)}$$

It is important, at this point, to note that within the MKS system of units, as well as the convention used in writing (2-6(a)), a different convention is also frequently used in which the non-linear polarisation is defined in the form

$$\mathbf{P_{NL}} = \varepsilon_0[\chi^{(2)}\mathbf{E}^2 + \chi^{(3)}\mathbf{E}^3 + \cdots] \tag{2-6(b)}$$

Whether one uses the former convention or the latter, determines the units in which $\chi^{(2)}$ and higher-order non-linear susceptibilities are measured. In the present discussion, we use (2-6(a)) to define the relationship between the non-linear polarisation and susceptibility, in which $\chi^{(2)}$ is measured in Coulombs.Volt^{-2}. If, however, the non-linear polarisation is defined through equation (2-6(b)), the units of $\chi^{(2)}$ are metres.Volt^{-1}.

As we are interested in the non-linear polarisation term, we shall be seeking solutions to Maxwell's wave equation (2-4), with $\mathbf{P}_{NL}$ as the source term. Further, to simplify the treatment, we will assume that higher-order terms than $\chi^{(2)}$ in (2-6) can be neglected, so that $\mathbf{P}_{NL}$ may now be written in the reduced form as

$$\mathbf{P}_{NL} \sim \chi^{(2)} \mathbf{E}^2 \tag{2-7}$$

Substituting for $\mathbf{P}$ in (2-4) using the last result, we obtain

$$\nabla^2 \mathbf{E} = \mu\varepsilon \frac{\partial^2 \mathbf{E}}{\partial t^2} + \mu \frac{\partial^2}{\partial t^2} (\chi^{(2)} \mathbf{E}^2) \tag{2-8}$$

This is the equation governing the propagation of electromagnetic fields in an optically anisotropic medium exhibiting second-order non-linear susceptibility $\chi^{(2)}$.

2.2.2 Wave Equation for Three-Wave Mixing

In the case of second-order non-linear processes, we are usually concerned with the interaction of three harmonic waves of frequencies ω_1, ω_2 and ω_3, as they propagate through the non-linear medium (Fig. 2.1), where

$$\omega_3 = \omega_1 + \omega_2 \tag{2-9}$$

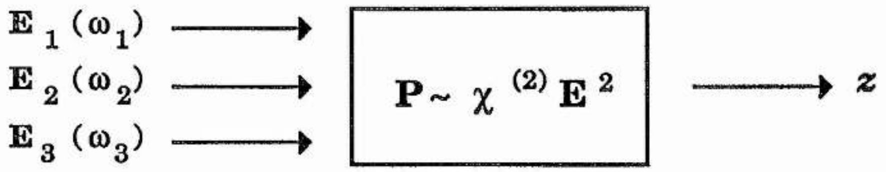

Fig. 2.1. Three-wave mixing in a non-linear medium exhibiting second-order non-linear susceptibility.

We will, therefore, restrict consideration to a total field **E** consisting of three such waves. To simplify the analysis, we assume that the three waves are infinite uniform plane waves propagating in the z-direction, according to

$$\mathbf{E}_1(z,t) = \frac{1}{2}[\,\mathbf{E}_1(z)\, exp\ [i\ (k_1 z - \omega_1 t) + \text{c.c.}] \qquad \textbf{(2-10 (a))}$$

$$\mathbf{E}_2(z,t) = \frac{1}{2}[\,\mathbf{E}_2(z)\, exp\ [i\ (k_2 z - \omega_2 t) + \text{c.c.}] \qquad \textbf{(2-10 (b))}$$

$$\mathbf{E}_3(z,t) = \frac{1}{2}[\,\mathbf{E}_3(z)\, exp\ [i\ (k_3 z - \omega_3 t) + \text{c.c.}] \qquad \textbf{(2-10 (c))}$$

Since the waves at the three different frequencies are interchanging energy through the second-order non-linear polarisation as they propagate through the medium, the respective amplitudes will, in general, vary with position. Hence, the field amplitudes in (2-10) are expressed as functions of z, that is $\mathbf{E}_1(z)$, $\mathbf{E}_2(z)$ and $\mathbf{E}_3(z)$. The total instantaneous field is, therefore, of the form

$$\begin{aligned}\mathbf{E} = {} & \frac{1}{2}\ [\,\mathbf{E}_1(z)\, exp\ [i\ (k_1 z - \omega_1 t) + \text{c.c.}] \\ & + \frac{1}{2}\ [\,\mathbf{E}_2(z)\, exp\ [i\ (k_2 z - \omega_2 t) + \text{c.c.}] \\ & + \frac{1}{2}\ [\,\mathbf{E}_3(z)\, exp\ [i\ (k_3 z - \omega_3 t) + \text{c.c.}]\end{aligned} \qquad \textbf{(2-11)}$$

Since we are dealing with plane waves propagating along the z-axis, the operator ∇^2 in (2-8) can be replaced by $\frac{\partial^2}{\partial z^2}$, and so the wave equation may be written as

$$\frac{\partial^2 \mathbf{E}}{\partial z^2} = \mu\varepsilon \,\frac{\partial^2 \mathbf{E}}{\partial t^2} + \mu \,\frac{\partial^2}{\partial t^2}(\chi^{(2)} \mathbf{E}^2) \tag{2-12}$$

Next we substitute (2-11), using (2-10), into (2-12) and separate the resulting equation into three parts, each containing only terms oscillating at one of the three frequencies. Let us consider that part of the wave equation (2-12) for the field component oscillating at ω_1. Assuming that (2-9) is valid, it can be shown, by manipulating the right-hand side of (2-12), that [3]

$$\frac{\partial^2}{\partial z^2}(\mathbf{E}(\omega_1)) = [-\tfrac{1}{2}(\omega_1^2 \mu\varepsilon\,)\,\mathbf{E}_1(z)\, exp\ [i\ (k_1 z - \omega_1 t) + \text{c.c.}]$$

$$+\ [-\tfrac{1}{2}(\omega_1^2 \mu\, \chi^{(2)}(\omega_1{=}\omega_3{-}\omega_2)\ \mathbf{E}_3(z)\, \mathbf{E}_2^{*}(z)\, exp\ [i\ (k_1 z - \omega_1 t) + \text{c.c.}] \tag{2-13}$$

where $\mathbf{E}_1(z)$, $\mathbf{E}_2(z)$ and $\mathbf{E}_3(z)$ are the field amplitudes at ω_1,ω_2 and ω_3, respectively.

Slowly-Varying Amplitude Approximation Consider the left-hand side of the wave equation (2-12) and let the operator $\frac{\partial^2}{\partial z^2}$ act on the component of the total field $\mathbf{E}$ oscillating at ω_1. Using (2-10), we obtain

$$\frac{\partial^2}{\partial z^2}(\mathbf{E}(\omega_1)) = \frac{1}{2}\,\frac{\partial^2}{\partial z^2}[\ \mathbf{E}_1(z)\ exp\ [i\ (k_1 z - \omega_1 t) + \text{c.c.}]$$

$$= \frac{1}{2}\,\frac{\partial}{\partial z}\,[\frac{\mathrm{d}\mathbf{E}_1(z)}{\mathrm{d}z} + i k_1 \mathbf{E}_1(z)]\ exp\ i\ (k_1 z - \omega_1 t) + \text{c.c.}$$

$$= \frac{1}{2}\,[\ \frac{\mathrm{d}^2\mathbf{E}_1(z)}{\mathrm{d}z^2} + 2ik_1 \frac{\mathrm{d}\mathbf{E}_1(z)}{\mathrm{d}z} - k_1^2 \mathbf{E}_1^2(z)]\ exp\ i\ (k_1 z - \omega_1 t) + \text{c.c.} \tag{2-14}$$

If we assume that the field amplitudes vary only slowly over distances comparable to a wavelength, then

$$\left|\frac{d^2\mathbf{E}_1(z)}{dz^2}\right| << \left|k_1\frac{d\mathbf{E}_1(z)}{dz}\right| \qquad \textbf{(2-15)}$$

and the first term in (2-14) may be neglected. This is also known as *adiabatic approximation* [4]. Equation (2-14) is, thus, reduced to

$$\frac{\partial^2}{\partial z^2}(\mathbf{E}(\omega_1)) \sim \frac{1}{2}\,[\,2ik_1\frac{d\mathbf{E}_1(z)}{dz} - k_1{}^2\mathbf{E}_1{}^2(z)]\; exp\; i\;(k_1 z - \omega_1 t) + \text{c.c.} \qquad \textbf{(2-16)}$$

If we now equate (2-13) and (2-16), and remember that for a freely propagating wave in the medium $k^2 = \omega^2\mu\varepsilon$, then after multiplying all terms by

$$\frac{i}{k_1} exp\;[-\,i\;(k_1 z - \omega_1 t)\,] \qquad \textbf{(2-17)}$$

we obtain

$$\frac{d\mathbf{E}_1(z)}{dz} = -\frac{i\omega_1}{2}\left(\frac{\mu}{\varepsilon_1}\right)^{1/2}\chi^{(2)(\omega_1=\omega_3-\omega_2)}\,\mathbf{E}_3(z)\,\mathbf{E}_2{}^*(z)\; exp\;[i\Delta kz\,] \qquad \textbf{(2-18)}$$

We can readily write down similar equations for each of the other field components at ω_2 and ω_3. The resulting set of equations are the "starting point" in the analysis of a wide range of optical effects involving the second-order non-linear susceptibility $\chi^{(2)}$. For convenience, we write down explicitly the three equations describing three-wave mixing processes satisfying (2-9), namely

$$\frac{d\mathbf{E}_1(z)}{dz} = -\frac{i\omega_1}{2}\left(\frac{\mu}{\varepsilon_1}\right)^{1/2}\chi^{(2)(\omega_1=\omega_3-\omega_2)}\,\mathbf{E}_3(z)\,\mathbf{E}_2{}^*(z)\; exp\;[i\Delta kz\,] \qquad \textbf{(2-19 (a))}$$

$$\frac{d\mathbf{E}_2(z)}{dz} = -\frac{i\omega_2}{2}\left(\frac{\mu}{\varepsilon_2}\right)^{1/2}\chi^{(2)(\omega_2=\omega_3-\omega_1)}\,\mathbf{E}_3(z)\,\mathbf{E}_1{}^*(z)\; exp\;[i\Delta kz\,] \qquad \textbf{(2-19 (b))}$$

$$\frac{d\mathbf{E}_3(z)}{dz} = -\frac{i\omega_3}{2}\left(\frac{\mu}{\varepsilon_3}\right)^{1/2}\chi^{(2)(\omega_3=\omega_1+\omega_2)}\,\mathbf{E}_1(z)\,\mathbf{E}_2(z)\; exp\;[-i\Delta kz\,] \qquad \textbf{(2-19 (c))}$$

where $\Delta k = k_3 - k_2 - k_1$ is the momentum-mismatch between the three optical fields. These equations are also referred to as *coupled amplitude equations* and are the basic equations describing parametric interactions in optically non-linear media. We notice that they are coupled to one another via the second-order non-linear susceptibility $\chi^{(2)}$.

2.3 PARAMETRIC AMPLIFICATION

In any oscillator, some form of gain is required to overcome losses and produce oscillation. In a traditional laser amplifier, the gain is provided by the population inversion between atomic or molecular levels of the active medium. In a parametric amplifier, the gain is the result of interaction between the electromagnetic fields in the non-linear medium, as discussed in the previous section.

In the optical parametric amplification process, a strong, high-frequency radiation field at ω_p interacts, via the non-linear response of the medium, with two lower-frequency electromagnetic waves at ω_s and ω_i. As a result of this interaction, there is a power flow from the strong *pump* wave to the weak *signal* and *idler* fields at ω_s and ω_i and the latter undergo amplification.

We now derive the equations governing parametric amplification and parametric gain in a non-linear medium. In doing so, we will return to the basic equations describing non-linear parametric interactions (2-19), and analyse them for the case of optical parametric amplification.

Formalism

Consider a non-linear medium irradiated by a strong pump field and the three electromagnetic fields, the pump, signal and idler propagating within the medium in the z-direction (as in Fig. 2.2), with frequencies satisfying

$$\omega_p = \omega_s + \omega_i \tag{2-20}$$

Fig. 2.2.

We wish to follow propagation of the weak signal and idler waves through the medium. Let us first assume that the three waves are phase-matched, as this is the condition under which maximum gain occurs. Therefore,

$$\Delta k = k_p - k_s - k_i = 0 \tag{2-21}$$

We shall discuss the situation where there is a non-zero phase-mismatch ($\Delta k \neq 0$) between the coupled waves in section 2.4. Under such condition, a reduction in gain is to be expected with increasing Δk. Equations (2-20) and (2-21) may be regarded as statements of conservation of energy and momentum, respectively.

Let us now return to equation (2-19) and solve it for the propagation of the signal and idler waves. For convenience, we introduce a new field variable defined by

$$A_m \equiv \left(\frac{n_m}{\omega_m}\right)^{1/2} \mathbf{E}_m \qquad m = p, s, i \tag{2-22}$$

so that the power flow per unit area at ω_m can be written as

$$S_m = \frac{1}{2}\left(\frac{\varepsilon_0}{\mu_0}\right)^{1/2} n_m \left|\mathbf{E}_m\right|^2$$

$$= \frac{1}{2}\left(\frac{\varepsilon_0}{\mu_0}\right)^{1/2} \omega_m \left|A_m\right|^2 \tag{2-23}$$

where n_m is the refractive index of the medium at ω_m. Since the photon flux N_m (number of photons per square meter per second) is related to S_m by

$$S_m = N_m \hbar\omega_m = \frac{1}{2}\left(\frac{\varepsilon_0}{\mu_0}\right)^{1/2} \omega_m \left|A_m\right|^2 \tag{2-24}$$

the quantity $\left|A_m\right|^2$ turns out to be proportional to the photon flux at ω_m. We can now rewrite (2-19) for the variable A_m as

$$\frac{dA_s}{dz} = -\frac{1}{2}\, i\ \zeta A_i^{*} A_p \tag{2-25 (a)}$$

$$\frac{dA_i}{dz} = -\frac{1}{2}\, i\ \zeta A_s^{*} A_p \tag{2-25 (b)}$$

$$\frac{dA_p}{dz} = -\frac{1}{2}\, i\ \zeta A_s A_i \tag{2-25 (c)}$$

with

$$\zeta \equiv d_{eff}^{(2)} \left(\frac{\mu}{\varepsilon_0}\right)^{1/2} \left(\frac{\omega_p \omega_s \omega_i}{n_p n_s n_i}\right)^{1/2} \tag{2-26}$$

where $d_{eff}^{(2)}$ is the *effective* second-order non-linear coefficient of the medium [5] coupling the three fields. We emphasize that (2-25) has been derived under phase-match condition $\Delta k = k_p - k_s - k_i = 0$.

Parametric Approximation The exact solution to equation (2-25) has been given for a general set of initial conditions in [6]. However, in a limiting case that demonstrates the essential features of parametric amplification, we make the approximation that the pump wave maintains constant amplitude throughout the interaction region. This is equivalent to assuming that the power drained from the pump at ω_p, by the signal and idler, is negligible compared to the input pump power (i.e. no pump depletion). Hence, we can write

$$A_p(z) \equiv constant \equiv A_p(0) \tag{2-27}$$

With this approximation in mind, we can solve (2-25 (a)) and (2-25(b)) as a pair of coupled linear differential equations of the form [3]

$$\frac{dA_s}{dz} = -\frac{1}{2}\, i\kappa\, A_i^* \tag{2-28 (a)}$$

$$\frac{dA_i}{dz} = -\frac{1}{2}\, i\kappa\, A_s^* \tag{2-28 (b)}$$

where

$$\kappa \equiv \zeta A_p(0) = \left(\frac{\mu}{\varepsilon_0}\right)^{1/2}\left(\frac{\omega_s\omega_i}{n_s n_i}\right)^{1/2} d_{eff}^{(2)}\, \mathbf{E}_p(0) \tag{2-29}$$

The solution of (2-28) subject to the initial conditions

$$A_s(z{=}0) \equiv A_s(0),\, A_i(z{=}0) \equiv A_i(0),\, A_p(0) = A_p^*(0) \tag{2-30}$$

is

$$A_s(z) = A_s(0)\, cosh\, [\tfrac{1}{2}(\kappa z)] - i\, A_i^*(0)\, sinh\, [\tfrac{1}{2}(\kappa z)] \tag{2-31 (a)}$$

$$A_i(z) = A_i(0)\, cosh\, [\tfrac{1}{2}(\kappa z)] - i\, A_s^*(0)\, sinh\, [\tfrac{1}{2}(\kappa z)] \tag{2-31 (b)}$$

which describe exponential growth of the weak signal and idler waves under phase-match condition $\Delta k = 0$. In the case of parametric amplification, the input is assumed to consist of the pump wave at ω_p and one of the other two fields, the signal at ω_s, say. Thus, $A_i(0) = 0$, and noting from (2-24) that,

$$N_m = K\ |A_m|^2 \qquad \text{(2-32 (a))}$$

where the constant K is given by

$$K = \frac{1}{2\hbar}\left(\frac{\varepsilon_0}{\mu_0}\right)^{1/2}, \qquad \text{(2-32 (b))}$$

which is independent of the frequency of the wave and the refractive index of medium.we obtain, from (2-31),

$$N_s(z) = K\ \left|A_s(z)\right|^2 = K\left|A_s(0)\right|^2 cosh^2\left[\tfrac{1}{2}(\kappa z)\right] \qquad \text{(2-33 (a))}$$

$$N_i(z) = K\ \left|A_i(z)\right|^2 = K\left|A_s(0)\right|^2 sinh^2\left[\tfrac{1}{2}(\kappa z)\right] \qquad \text{(2-33 (b))}$$

which, for $\kappa z >> 1$, reduce to

$$N_s(z) \propto \frac{1}{4}\left|A_s(0)\right|^2 exp\ (\kappa z) \qquad \text{(2-34 (a))}$$

$$N_i(z) \propto \frac{1}{4}\left|A_s(0)\right|^2 exp\ (\kappa z) \qquad \text{(2-34 (b))}$$

Therefore, the signal and idler photon fluxes N_s and N_i undergo exponential growth as they propagate through the medium. In particular, the parametric gain experienced by the signal field over the distance z is given by

$$\frac{N_s(z)}{N_s(0)} = \frac{1}{4}\, e^{\kappa z} \qquad \text{(2-35)}$$

It can be shown, using (2-23) together with (2-29), that the gain factor κ, may be written as

$$\kappa = \left(\frac{2\mu\omega_s\omega_i}{c\varepsilon_0{}^2 n_p n_s n_i}\right)^{1/2} d_{eff}^{(2)}\, S_p(0)^{1/2} \qquad \text{(2-36)}$$

which implies that the gain coefficient of the medium depends on the flux of the pump wave S_p incident on the crystal at $z = 0$. In the MKS system of units κ is measured in metres^{-1} and the units of S_p are Watts.metres^{-2}.

Physically, the parametric amplification process can be viewed as the mixing of a strong pump field at ω_p with the wavevector k_p, and an initial (much weaker) signal field at ω_s with the wavevector k_s, through the non-linear response of the medium. Then, as the pump and the signal propagate through the medium, a polarisation wave at $\omega_i = \omega_p - \omega_s$ with wavevector $k_i = k_p - k_s$ will be produced. This oscillating polarisation will then radiate an electromagnetic idler field δE_i at ω_i, which mixes with the pump wave to produce a polarisation at $\omega_s = \omega_p - \omega_i$ which, in turn, generates an incremental field δE_s. Provided that the waves are phased correctly (i.e. $\Delta k \sim 0$), the process will go on leading to simultaneous amplification of the signal and idler fields at the expense of the pump field.

2.4 EFFECTS OF MOMENTUM-MISMATCH ON PARAMETRIC GAIN

In the preceding section, we derived the equations describing parametric amplification and gain on the assumption that the three interacting fields satisfy the phase-match condition $\Delta k = k_p - k_s - k_i = 0$. Let us now consider the parametric process in the case where there is non-zero momentum-mismatch between the three waves, and determine the dependence of parametric gain on the magnitude of Δk. To do this, we return to (2-25(a)) and (2-25(b)) and note that, in the presence of finite momentum-mismatch, these equations take the form

$$\frac{dA_s}{dz} = -\frac{1}{2} i\, \zeta A_i^* A_p\, e^{-i\Delta kz} \qquad \text{(2-37(a))}$$

$$\frac{dA_i}{dz} = -\frac{1}{2} i\, \zeta A_s^* A_p\, e^{-i\Delta kz} \qquad \text{(2-37(b))}$$

which, using (2-27) together with (2-29), can be written as

$$\frac{dA_s}{dz} = -\frac{1}{2} i\kappa\, A_i^*\, e^{-i\Delta kz} \qquad \text{(2-38(a))}$$

$$\frac{dA_i}{dz} = -\frac{1}{2} i\kappa\, A_s^* e^{-i\Delta kz} \qquad \text{(2-38(b))}$$

If we consider the general solution in which both the signal and idler waves are present at the input, we can write $A_s(z{=}0) \equiv A_s(0)$, $A_i(z{=}0) \equiv A_i(0)$ as before. Then, solutions of (2-38) can be shown to be

$$A_s(z)e^{-i(\Delta kz/2)} = A_s(0)\ [cosh(\beta z) - i(\tfrac{\Delta k}{2\beta})\ sinh(\beta z)] - i(\tfrac{\kappa}{2\beta})A_i^*(0)\ sinh(\beta z) \qquad \text{(2-39 (a))}$$

$$A_i(z)e^{-i(\Delta kz/2)} = A_i(0)\ [cosh(\beta z) + i(\tfrac{\Delta k}{2\beta})\ sinh(\beta z)] - i(\tfrac{\kappa}{2\beta})A_s^*(0)\ sinh(\beta z) \qquad \text{(2-39 (b))}$$

where,

$$\beta = \frac{1}{2}[\kappa^2 - (\Delta k)^2]^{1/2} \qquad \text{(2-40)}$$

We notice that the exponential gain factor β depends on the momentum-mismatch Δk and that for the case where $\Delta k = 0$ (i.e. perfect match), equation (2-39) reduces to (2-31), as expected.

Consider the case where we have the pump wave and only one of the other waves present at the input, for example the signal at ω_s. Thus, $A_i(0) = A_i^*(0) = 0$ in (2-39) and the equation is reduced to

$$A_s(z)e^{-i\,(\Delta kz/2)} = A_s(0)\ [cosh(\beta z) - i\ (\tfrac{\Delta k}{2\beta})\ sinh(\beta z)] \qquad \text{(2-41 (a))}$$

$$A_i(z)e^{-i\,(\Delta kz/2)} = -\,i\ (\tfrac{\kappa}{2\beta})\,A_s^*(0)\ sinh(\beta z) \qquad \text{(2-41 (b))}$$

Therefore, the corresponding signal and idler photon fluxes may be written as

$$N_s(z) \propto A_s(z)\,A_s^*(z) = \left|A_s(0)\right|^2 [cosh^2(\beta z) + (\frac{\Delta k}{2\beta})^2 sinh^2(\beta z)] \qquad \text{(2-42 (a))}$$

$$N_i(z) \propto A_i(z)\,A_i^*(z) = \left|A_s(0)\right|^2 (\frac{\kappa}{2\beta})^2\, sinh^2(\beta z) \qquad \text{(2-42 (b))}$$

If we limit consideration to the signal wave at ω_s, it undergoes amplification by a factor

$$G_s = \frac{\left|A_s(z)\right|^2}{\left|A_s(0)\right|^2} = cosh^2(\beta z) + (\frac{\Delta k}{2\beta})^2 sinh^2(\beta z) \qquad \text{(2-43)}$$

Since we are interested in the variation of G_s with Δk, we will consider (2-43) under the following conditions;

i) $\Delta k < \kappa$

In this case the exponential gain coefficient β is real and the solutions for G_s are hyperbolic functions in βz. The signal wave, therefore, undergoes amplification as it propagates through the medium. In particular, in the high-gain regime where $\beta z >> 1$, (2-43) reduces to

$$G_s \sim \frac{1}{4}[\,1+ (\frac{\Delta k}{2\beta})^2\,]\, e^{-2\beta z} \qquad (\beta z >> 1) \qquad \text{(2-44)}$$

so that sustained exponential growth of the signal results. In the low-gain limit where $\beta z << 1$, however, the signal gain becomes

$$G_s \sim 1+ (\beta z)^2 + (\frac{\Delta k}{2\beta})^2 (\beta z)^2 \qquad (\beta z << 1) \qquad \text{(2-45)}$$

which, using (2-40), can be written as

$$G_s \sim 1+\frac{1}{4}\kappa^2 z^2 \qquad (\beta z << 1) \qquad \text{(2-46)}$$

Thus, the signal undergoes amplification by the net amount $\frac{1}{4}\kappa^2 z^2$.

ii) $\Delta k > \kappa$

Under this condition, the gain factor β is imaginary and the hyperbolic *sinh* and *cosh* functions in (2-43) are replaced by sinusoidal functions of the form

$$\cos\left\{ \frac{1}{2}\left[(\Delta k)^2 - \kappa^2 \right]^{1/2} z \right\}$$
$$\sin\left\{ \frac{1}{2}\left[(\Delta k)^2 - \kappa^2 \right]^{1/2} z \right\}$$

respectively, and hence the gain at ω_s oscillates as the signal propagates through the medium along z . Thus, we see that in the case where $\Delta k < \kappa$, the medium exhibits gain at the signal frequency ω_s while for $\Delta k > \kappa$, the gain varies periodically with z, and no sustained growth of the signal is possible. The gain in a parametric amplifier, therefore, varies continuously from a hyperbolic to a sinusoidal function as the condition $\Delta k < \kappa$ to $\Delta k > \kappa$. The condition $\Delta k = \kappa$ which defines the boundary between these two distinct regions has been called the *gain threshold.*

iii) $\Delta k = 0$

This is by far the most important condition and is the key requirement for the existence of non-trivial gain in a parametric amplifier. Under this condition, the gain coefficient becomes

$$\beta = \frac{1}{2}\kappa \qquad \textbf{(2-47)}$$

and the expression for the parametric gain G_s is reduced to

$$G_s = \cosh^2\left(\frac{1}{2}\kappa z\right) \qquad \textbf{(2-48)}$$

resulting in maximum possible gain. In the high-gain limit where $\kappa z >> 1$, the gain factor G_s takes the familiar exponential form, that is

$$G_s \sim \frac{1}{4} e^{\kappa z} \qquad (\kappa z >> 1) \qquad \textbf{(2-49)}$$

We note that the last result is the same as (2-35), as it should be. In the low-gain regime where $\kappa z << 1$, the gain factor becomes

$$G_s \sim 1+\frac{1}{4}\kappa^2 z^2 \qquad (\kappa z << 1) \qquad \textbf{(2-50)}$$

indicating a net gain of $\frac{1}{4}\kappa^2 z^2$ for the signal field. We note that these results apply equally well to the parametric gain G_i at the idler frequency ω_i.

The above analysis clearly indicates the critical dependence of parametric gain on the degree of momentum-mismatch between the coupled waves. In particular, we see that a reduction in parametric gain is to be expected with increasing Δk. Physically, this results from the fact that in the presence of finite momentum-mismatch, the electromagnetic fields and their non-linear polarisation source terms get out of phase as they propagate through the medium. In the case when $\Delta k = 0$, the waves propagate synchronously and constructive interference results in maximum gain. Therefore, it is only in the case of phase-matched interaction ($\Delta k \sim 0$) that one can expect the parametric process to result in significant build-up of generated fields. In practice, however, Δk is non-zero and may be large. The finite magnitude of Δk arises from the dispersion of the medium which causes the fields at different frequencies to propagate with different phase velocities through the material. As a result, unless special precautions are taken, the parametric gain will be small. Several schemes have been realised to compensate for the effects of dispersion. These include the use of birefringence, total internal reflection, interaction in waveguide structures and non-collinear interactions. The most common technique, however, as used in optical parametric amplifier devices is to use the birefringence of the optically anisotropic crystal to offset the dispersion.

2.4.1 Phase-Matching in Parametric Amplification

In general, anisotropic non-linear materials in which parametric processes can occur exhibit the phenomenon of birefringence. In such materials, the index of refraction for a wave at a given frequency depends on the direction of propagation as well as its sense of polarisation. In a uniaxial crystal, the refractive index for an *extraordinary wave* (*e-wave*) propagating at an angle θ to the optic axis is given by

$$\frac{1}{n_e^2(\theta)} = \frac{\cos^2\theta}{n_o^2} + \frac{\sin^2\theta}{n_e^2} \tag{2-51}$$

where n_o and n_e are the principal *ordinary* and *extraordinary* indices, respectively. $n_e(\theta)$ lies between n_o and n_e. The *ordinary wave* (*o-wave*), on the other hand, experiences the same refractive index n_o, independent of its direction of propagation through the crystal, that is

$$n_o(\theta) = n_o \tag{2-52}$$

If we consider the phase-match condition $\Delta k = k_p - k_s - k_i = 0$, and use the relation $k = (\frac{\omega}{c})\, n$, the index of refraction for the pump wave for which collinear phase-matching can occur is given by

$$n_p = (\frac{\omega_s}{\omega_p})\, n_s + (\frac{\omega_i}{\omega_p})\, n_i \tag{2-53}$$

In order to proceed further, consider the particular case where the pump is an *e-wave*, with the signal and idler both *o-waves*. Then the phase-match condition can be satisfied for some angle θ_m according to

$$\begin{aligned} n_e^{\omega p}(\theta_m) &= [\, (\frac{\cos\theta_m}{n_o^{\omega p}})^2 + (\frac{\sin\theta_m}{n_e^{\omega p}})^2 \,]^{-1/2} \\ &= (\frac{\omega_s}{\omega_p})\, n_o^{\omega s} + (\frac{\omega_i}{\omega_p})\, n_o^{\omega i} \end{aligned} \tag{2-54}$$

This is one of the schemes used in a negative uniaxial crystal (for which $n_e < n_o$). In principle, two possible phase-matching schemes can be realised in such a crystal, both involving propagation of the pump as an *e-wave*, with either one or both of the signal and idler as *o-waves*. The case where both the signal and idler are *o-waves*, as in above, is referred to as type I or *parallel* phase-matching. When either one, but not both, is an *e-wave*, the case is referred to as type II or *orthogonal* phase-matching. Thus, for a negative uniaxial crystal, the two possible phase-matching schemes can be summarised, in shorthand notation, as

type I $e \rightarrow o + o$
type II $e \rightarrow o + e$

These two phase-matching schemes are illustrated in Fig. 2.4.

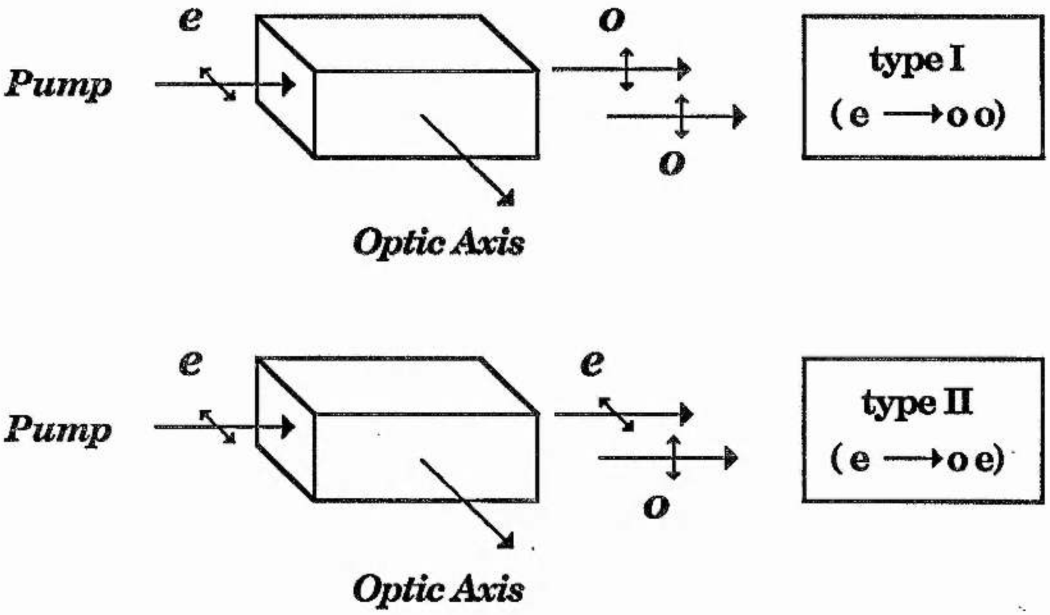

Fig. 2.4. Possible phase-matching schemes in a negative uniaxial crystal.

In a positive uniaxial crystal (for which $n_o < n_e$), the pump must be launched as an *o-wave* and either the signal or the idler or both can be *e-*

waves, resulting in type II or type I phase-matching, respectively. Therefore, for a positive uniaxial crystal we may write the two possibilities as

$$\text{type I} \qquad o \rightarrow e + e$$

$$\text{type II} \qquad o \rightarrow o + e$$

The angle θ_m is usually referred to as the *phase-match* angle. The two possible phase-matching schemes in a positive uniaxial crystal are illustrated in Fig. 2.5.

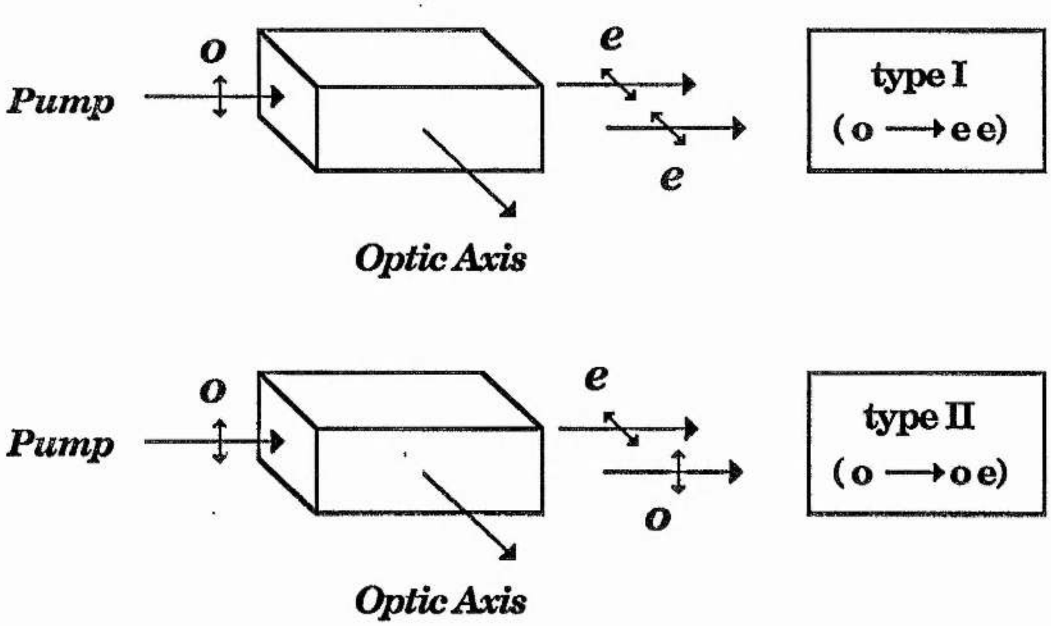

Fig. 2.5. Possible phase-matching schemes in a positive uniaxial crystal.

Whether a given material can be phase-matched, in either type I or type II schemes, depends on the value of its indices of refraction as a function of wavelength, the strength of its birefringence, and the particular combination of wavelengths of the signal and idler fields allowed by the pump wavelength. For a given phase-matching condition, the effective non-linear coefficient $d_{eff}^{(2)}$ is determined by crystal symmetry and direction of propagation within the crystal. In a uniaxial crystal, the locus of phase-matching directions lies on a cone centred about the crystal optic axis, as shown in Fig. 2.6.

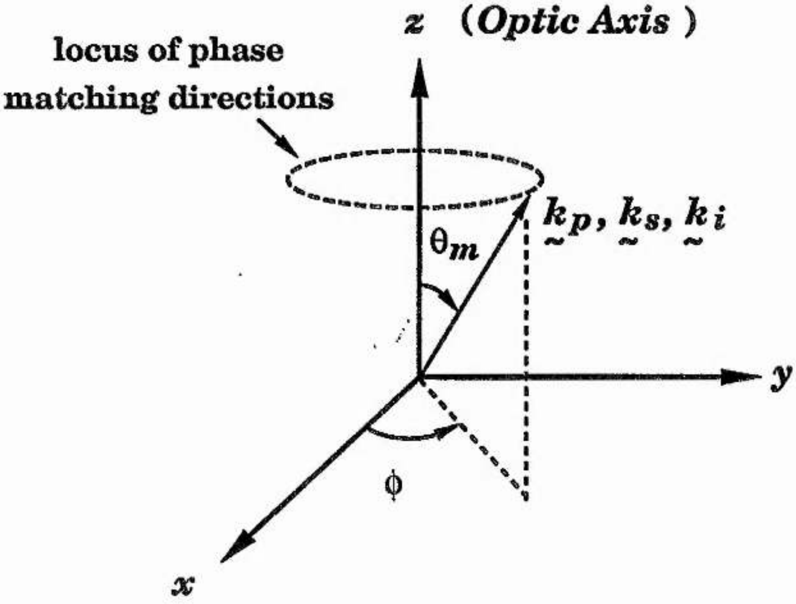

Fig. 2.6. Phase-matching in a uniaxial crystal. The phase-match angle θ_m is defined with respect to the optic axis (z) while the azimuthal angle ϕ is measured in the xy-plane, from x-axis.

For a given phase-match angle θ_m, the azimuthal angle ϕ is chosen in such a way as to maximise the value of $d_{eff}^{(2)}$. For example, in crystal class $\bar{6}2m$ with an interaction involving two *o-waves* and one *e-wave*, the magnitude of the effective non-linear coefficient is given by

$$d_{eff}^{(2)} = d_{22} cos\theta sin3\phi \tag{2-55}$$

Therefore, it is desirable to choose a propagation direction $\theta=\theta_m$ with $\phi=30°$ or $90°$ for maximum $d_{eff}^{(2)}$.

2.4.2 Frequency Tuning in Parametric Amplification

The most important consequence of phase-matching in the parametric amplification process is the ability to tune the frequency of the generated signal and idler fields over an extended spectral range. We have established in the preceding discussion that when $\Delta k = 0$, the gain has a maximum value and as Δk increases, a reduction in gain occurs. We can write this phase-matching condition in a different form as

$$\omega_p n_p = \omega_s n_s + \omega_i n_i \tag{2-56}$$

where we have used the relation $k = (\frac{\omega}{c})\, n$.

In other words, for a given ω_p and θ_m, the phase-match condition selects, out of an infinite number of possible combinations of ω_s and ω_i allowed by (2-20), a single pair of frequencies also satisfying (2-56). Therefore, it is possible to tune the frequencies ω_s and ω_i of the generated signal and idler fields by varying the refractive indices (or the pump frequency ω_p). This can be done by altering the orientation of the crystal relative to the pump beam (*angle tuning*) or the crystal temperature (*temperature tuning*). Other techniques include *pressure tuning* through the photoelastic effects, applying an external electric field to the crystal (*electro-optic tuning*), or altering the angle between the three waves in the case of non-collinear interaction (*non-collinear tuning*). As an example, if we change the crystal orientation, the frequencies ω_s and ω_i will change so as to compensate for the changes in indices and hence the condition (2-56) will be fulfilled for a new pair of frequencies. In general, temperature tuning or angle tuning result in a broader tuning range than pressure or electro-optic tuning.

2.5 OPTICAL PARAMETRIC OSCILLATION

In the discussion of parametric amplification, we demonstrated that a pump wave at ω_p can provide, via the non-linear polarisation of the medium, simultaneous amplification for the signal and idler optical fields at ω_s and ω_i. In general, even for perfect phase-matching ($\Delta k = 0$), the gain in a travelling-wave parametric amplifier is not expected to be large enough to lead to amplification of the signal and idler fields to levels comparable to the pump field. As an example, consider the case of a parametric amplifier using urea as the non-linear crystal and a XeCl excimer laser operating at 308nm as the pump source. We are interested in estimating the magnitude of the gain coefficient κ, using (2-36), for the following data;

$$d_{eff}^{(2)} \sim d_{14} \sim 1.23 \times 10^{-23} \text{ Coulombs.Volt}^{-2}$$
$$\omega_s \sim \omega_i = 5 \times 10^{14} \text{ Hz}$$
$$n_p \sim n_s \sim n_i \sim 1.5$$

where we have assumed $\theta_m = 90°$ (*non-critical* phase-matching). A typical injection-seeded XeCl laser may deliver pulses of 2.5 MW peak power with cross-sectional dimensions of 1 x 2cm. If this beam is compressed to a spot of 2mm^2 cross-section, then the pump power density $S_p(0)$, measured in Watts.m^{-2}, incident on the non-linear crystal will be of the order of 1.25×10^{12} Watts.m^{-2}, that is

$$S_p(0) = 1.25 \times 10^{12} \text{ Watts.m}^{-2}$$

Substituting the data into (2-36) yields

$$\kappa \sim 0.377 \text{ cm}^{-1}$$

Therefore, using (2-48), the net single-pass power gain over a 1-cm-long urea crystal at $\theta_m = 90°$ is only 3.6%. However, an order of magnitude increase in the pump power will result in a ten-fold increase in the net gain to about 40%. This indicates that only at high pump power densities (or for long crystal lengths), the gain in a parametric amplifier is expected to be sufficiently high to lead to macroscopic amplification of the excited fields. It is for this reason that the parametric amplification process is used primarily to obtain oscillation by providing some form of feedback, as in an optical parametric oscillator.

2.5.1 Pump Beam Requirements for Optical Parametric Oscillators

In section 2.4, we established that the gain in a parametric amplifier is critically dependent on the degree of phase-mismatch Δk between the coupled fields. We saw that the maximum gain occurs at $\Delta k = 0$, and a reduction in gain results from an increase in the magnitude of Δk. We also discussed the concept of phase-matching and showed how, in the case where the three waves are propagating collinearly (k_p, k_s, and k_i parallel), the birefringence of the anisotropic medium may be used to offset dispersion, and hence to ensure minimum phase-mismatch ($\Delta k = 0$) and maximum gain. In practice, however, a departure from the ideal phase-match condition ($\Delta k = 0$) is to be expected, because the pump beam exhibits a finite angular divergence and spectral bandwidth, and as such its various angular and spectral components contribute to an increase in Δk. It is, therefore, essential to explore the extent to which the spatial and spectral spread of the pump beam can be tolerated before significant reduction in gain occurs from the resulting phase-mismatch. In order to do this, we return to (2-43), from which the net single-pass power gain over a crystal of length l may be written as

$$g_{(l)} = \frac{|A_s(l)|^2 - |A_s(0)|^2}{|A_s(0)|^2}$$

$$= \kappa^2 l^2 \, \frac{\sinh^2\{[\kappa^2 - (\Delta k/2)^2]^{1/2} l\}}{[\kappa^2 - (\Delta k/2)^2] \, l^2} \qquad (2\text{-}57)$$

where Δk is the phase-mismatch and κ is the gain coefficient, defined by (2-36). From (2-57), the dependence of gain on Δk may be illustrated by obtaining a plot of gain as a function of phase-mismatch. This is shown in Fig. 2.7, where the normalised gain, $g_{(l)}/\kappa^2 l^2$, has been plotted against the quantity $\Delta kl / 2$, for various values of $\kappa^2 l^2$ [15]. We may define the maximum tolerable phase-mismatch $|\Delta k|$ as that value for which the parametric gain $g_{(l)}$ has fallen to half its peak value at $\Delta k = 0$. It can be seen, from Fig. 2.7, that for values of $\kappa^2 l^2$ ranging from 1 to 10, the maximum allowable phase-mismatch (at full-width half-maximum gain) varies between $|\Delta k| \sim 0.99\pi / l$ and $\sim 1.1\pi / l$. Thus, a value of $|\Delta k| \sim \pi / l$ is in practice a good approximation for the maximum allowable momentum-mismatch. This criterion may be used determine the maximum tolerable pump bandwidth and angular divergence in an optical parametric oscillator, before significant reduction in gain occurs.

For a singly-resonant optical parametric oscillator (OPO), with the signal frequency ω_s fixed by the optical cavity, the maximum allowable pump bandwidth (full-width at half-power) giving rise to the momentum-mismatch $|\Delta k| \sim \pi / l$ can be shown to be [16],

$$\Delta \nu_p \ (\text{cm}^{-1}) = \frac{1}{l} \left[(n_p - n_i) + \lambda_i \left(\frac{\partial n_i}{\partial \lambda_i}\right) - \lambda_p \left(\frac{\partial n_p}{\partial \lambda_p}\right)\right]^{-1} \qquad (2\text{-}58)$$

where the indices p and i refer to the pump and the non-resonant idler wave, respectively, and λ is the free-space wavelength. It is seen, from the

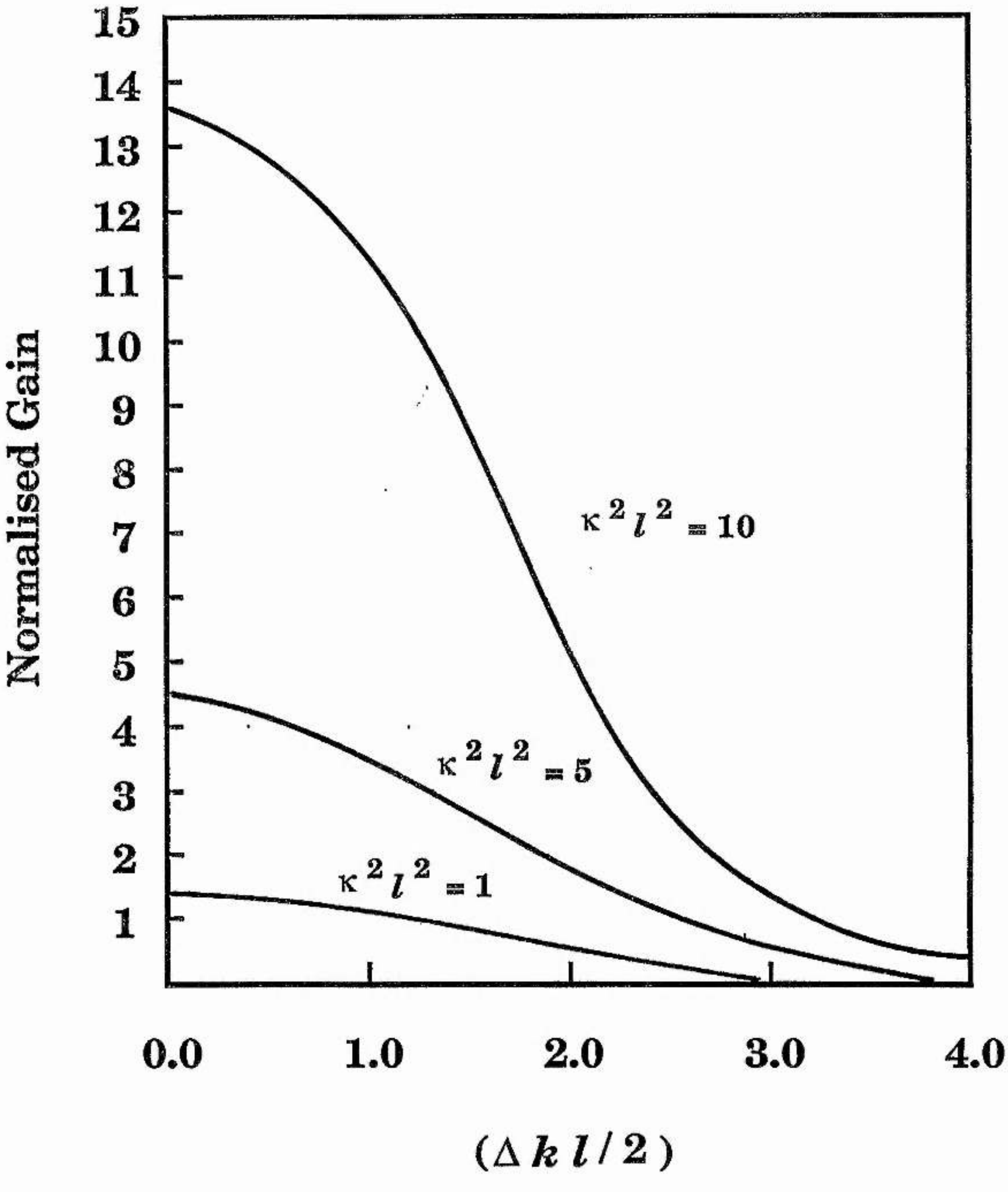

Fig. 2.7. Normalised gain versus $\Delta k\, l / 2$ (after Harris [15]).

expression, that the requirements on pump bandwidth are more stringent for longer crystal lengths. We may use (2-58) to determine the minimum required pump laser bandwidth for successful operation of the urea and β-BaB_2O_4 OPO's. Figs. 2.8(a) and 2.8(b) show the calculated variation in $\Delta\nu_p$ across the tuning range of two singly-resonant OPO's based on urea and β-BaB_2O_4, respectively, and pumped at 308nm by a XeCl excimer laser. The calculations are based on the refractive index data for urea and β-BaB_2O_4 crystals obtained from [19] and [20], respectively. The exact forms of the Sellemeier equations for both materials are given in chapters 5 and 6, respectively. In the case of the urea OPO (Fig. 2.8(a)), the interaction is assumed to be type II phase-matched (i.e. $o \rightarrow oe$, in a positive uniaxial crystal), and the crystal length has been taken as 2.5 cm (the longest crystal used during our experiments). The calculations, in the case of the β-BaB_2O_4 OPO (Fig. 2.8(b)), correspond to a type I phase-matched process (i.e. $e \rightarrow oo$, in a negative uniaxial crystal) in a 1.2 cm crystal used in our experiments. It is clearly seen from the plots that the spectral spread of the pump light must be confined to within a few cm^{-1}, if these oscillators are to be successfully operated across their available tuning ranges. However, the constraint on the allowable pump linewidth $\Delta\nu_p$ is seen to be less severe if resonance is provided for the *e-wave* in the case of urea OPO, and for the lower of the two parametric frequencies (i.e. if $\omega_s < \omega_i$) in the case of β-BaB_2O_4 OPO. Because the spectral linewidth of a free-running XeCl laser oscillator is typically hundreds of cm^{-1}, the use of such a laser as pump source for the described OPO's will not lead to their successful operation. As a result, spectral narrowing techniques have to be utilized to restrict the pump bandwidth to within the limits set by equation (2-58), and shown in Fig. 2.8(a) and 2.8(b). This has been achieved in our experiments by injection-seeding a high-energy "power oscillator" with a low-energy

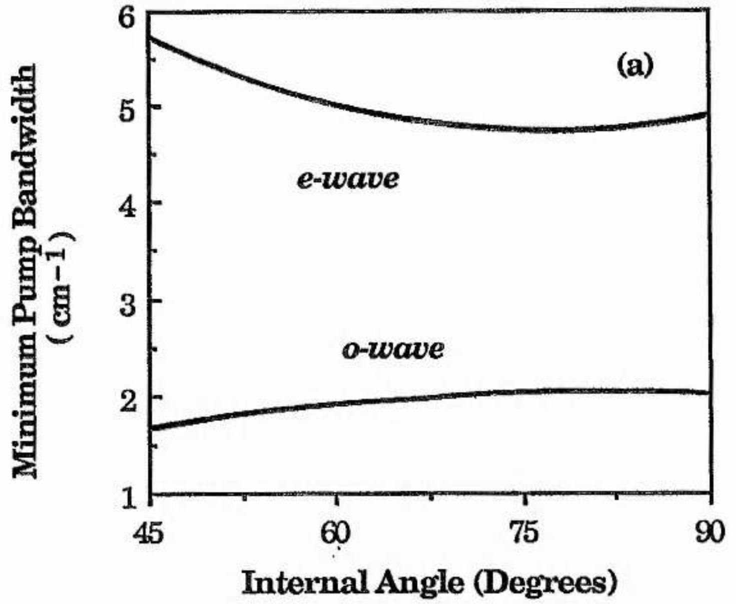

Fig. 2.8 (a). Pump bandwidth requirement (full-width at half-maximum parametric gain) for a singly-resonant urea optical parametric oscillator pumped at 308nm by a XeCl excimer laser, with type II (*o* → *o e*) interaction. ($l = 2.5$ cm).

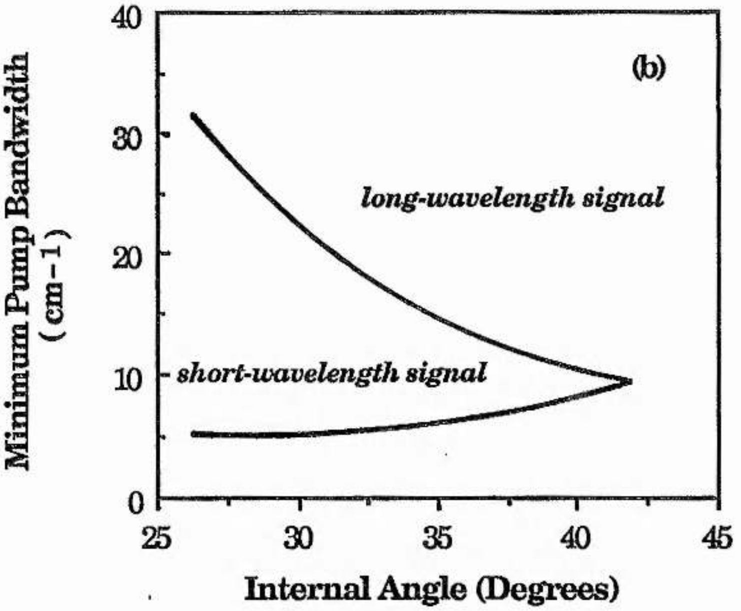

Fig. 2.8 (b). Pump bandwidth requirement (full-width at half-maximum parametric gain) for a singly-resonant β-BaB_2O_4 optical parametric oscillator pumped at 308nm by a XeCl excimer laser, with type I (*e* → *o o*) interaction. ($l = 1.2$ cm).

narrow-line "master oscillator" and will be discussed in greater detail in chapter 3.

The maximum allowable angular divergence in the pump beam may also be obtained in a similar way to spectral bandwidth calculations by considering the maximum tolerable phase-mismatch $|\Delta k| \sim \pi / l$. It can be shown that, for a singly-resonant oscillator with the signal wavelength λ_s fixed by the optical cavity, the maximum allowable pump beam divergence (full-angle), $\Delta\theta_p$, in the phase-match plane giving rise to this momentum-mismatch, under the conditions of critical type II phase-matching in a positive uniaxial crystal (i.e. $o \rightarrow oe$), is given by [17],

$$\Delta\theta_p = 1/l \left[\frac{n_p}{\lambda_p n_i}\left(\frac{\partial n_i}{\partial\theta}\right)\right]^{-1} \qquad \textbf{(2-59)}$$

The subscript p denotes the pump wave, and λ is the wavelength in free space. Under non-critical phase-matching ($\theta = 90°$), where there is a small angular dependence of refractive index, the second-order terms in the expansion of Δk need to be considered, and the maximum allowable pump beam divergence (full-angle) can be shown to be [17]

$$\Delta\theta_p = 2\left[\frac{1}{l}\left(\frac{\lambda_p}{n_p}\right)\right]^{1/2} \qquad \textbf{(2-60)}$$

Equations (2-59) and (2-60), which are applicable to the urea crystal under type II interaction ($o \rightarrow oe$), may be used to predict the minimum required divergence full-angle in the pump beam for optimum OPO operation. The calculated variation in $\Delta\theta_p$ across the tuning range of the XeCl-pumped urea OPO, for a 2.5 cm crystal, is shown in Fig. 2.9(a). It can be seen from the plot that although at angles near the $\theta = 90°$ a high angular divergence in the pump beam may be easily tolerated, in the regions of operation away from non-critical phase-matching the beam divergence must be controlled to better than a few hundred μR, if the entire available tuning range of the device is to be accessed.

In the case of β-BaB_2O_4 OPO, under critical type I phase-matching (i.e. $e \rightarrow oo$, in a negative uniaxial crystal), the minimum required pump beam divergence (full-angle) can be shown to be given by [17]

$$\Delta\theta_p = 1/l \; [\frac{1}{\lambda_p} (\frac{\partial n_p}{\partial\theta})]^{-1} \tag{2-61}$$

Fig. 2.9(b) represents the variation in $\Delta\theta_p$ with the internal phase-match angle, across the tuning range of β-BaB_2O_4 OPO, calculated from (2-61). As before, the oscillator is assumed to be singly-resonant at the signal wavelength, λ_s, and pumped at 308nm by a XeCl excimer laser. The crystal length is taken as 1.2 cm. From the plot, the values of $\Delta\theta_p$ are seen to range between ~ 190 to ~ 230 μR across the OPO tuning bandwidth.

The angular beam divergence of an excimer laser with a conventional plane parallel resonator is typically of the order of a few mR. Therefore, if such a laser is to be used as the pump source for the described OPO's, major steps need to be taken in the design of the optical resonator to ensure sufficient improvements in the spatial beam quality of the laser for successful operation of these devices. This is achieved, in our experiments, by designing the optical cavity of the pump laser as a confocal unstable resonator of the positive branch, and is more fully described in the following chapter.

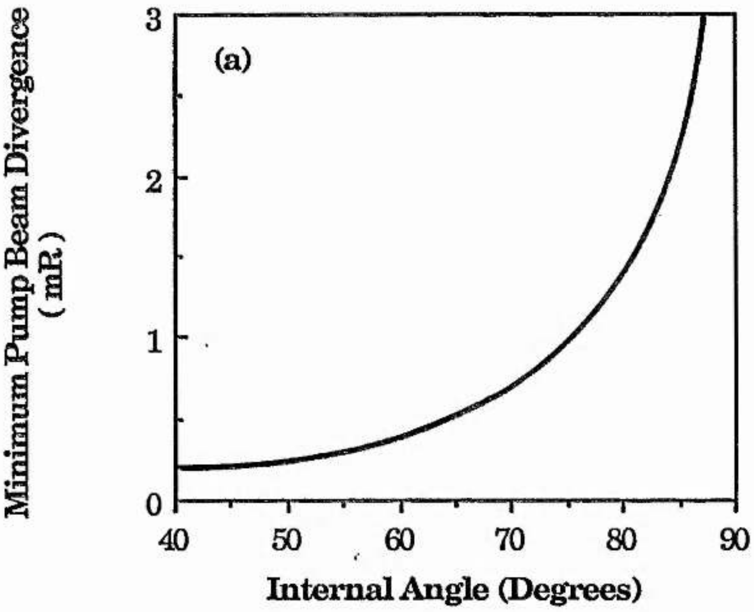

Fig. 2.9 (a). Pump beam divergence requirement (full-angle) for a singly-resonant urea optical parametric oscillator pumped at 308nm by a XeCl excimer laser, with type II ($o \rightarrow o\ e$) interaction. ($l = 2.5$ cm).

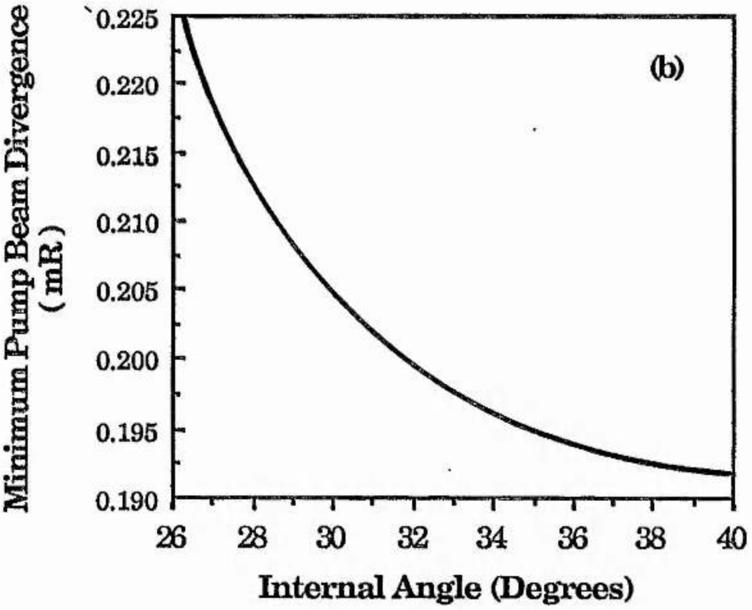

Fig. 2.9 (b). Pump beam divergence requirement (full-angle) for a singly-resonant β-BaB_2O_4 optical parametric oscillator pumped at 308nm by a XeCl excimer laser, with type I ($e \rightarrow o\ o$) interaction. ($l = 1.2$ cm).

References to Chapter 2.

[1] J. F. Nye, "Physical Properties of Crystals," Oxford Univ. Press, New York (1957)

[2] D. A. Kleinman, Phys. Rev. 126, 1977 (1962)

[3] A. Yariv, "Optical Electronics," CBS College Publishing, New York, 3rd Ed., Chapter 8 (1985)

[4] M. H. Dunn, "Introduction to Non-linear Optics," St. Andrews Univ. (1985)

[5] R. G. Smith, "Optical Parametric Oscillators," in *Lasers*, A. K. Levine and A. J. DeMaria, eds., Dekker, New York (1976)

[6] J. A. Armstrong *et al.*, Phys. Rev. 127, 1918 (1962)

[7] R. L. Byer, "Optical Parametric Oscillators," in *Quantum Electronics: A Treatise*, H. Rabin and C. L. Tang, eds. (Academic, New York, 1973), Vol. 1, Pt. B, pp. 587-702.

[8] M. J. Colles and C. R. Pidgeon, Rep. Prog. Phys. 38, 329 (1975)

[9] R. G. Smith, J. Appl. Phys. 41, 4121 (1970)

[10] R. A. Baumgartner and R. L. Byer, IEEE J. Quantum Electron., QE-15, 432 (1979)

[11] J. A. Giordmaine, Sci. Amer. 210, 38 (1964)

[12] M. J. Colles *et al.*, Proc. IEEE 57, 73 (1969)

[13] P. K. Tien, J. Appl. Phys. 29, 1347 (1958)

[14] T. F. Ewanizky, IEEE J. Quantum Electron.,QE-14, 962 (1978)

[15] S. E. Harris, Proc. IEEE 57, 2096 (1969)

[16] J. F. Young *et al.*, J. Appl. Phys. 42, 497 (1971)

[17] N. P. Barnes and V. J. Corcoran, Appl. Opt. 15, 696 (1976)

[18] A. Yariv, "Quantum Electronics," Wiley, New York, 2nd Ed., Chapter 17 (1975)

[19] W. R. Donaldson and C. L. Tang, Appl. Phys. Lett. 44, 25 (1984)

[20] K. Kato, IEEE J. Quantum. Electron, QE-22, 1013 (1986)

3

The Pump Laser

3.0 INTRODUCTION

The laser pump source used in the parametric oscillator experiments was a Transverse-Excitation-Atmospheric (TEA) XeCl excimer laser operating at 308nm. The laser was designed and constructed as part of the research project. In order to ensure simplicity and rapid development, standard electrical discharge techniques were employed in the design of the electrical circuit, although a modification of a standard preionisation scheme was successfully applied to the laser and found to significantly improve the spatial uniformity of the discharge, and thus the optical quality of the output beam. As discussed in the previous chapter, successful operation of an OPO requires a high degree of spectral and spatial coherence in the pump beam. For this reason, it was decided from the outset that the use of a conventional, free-running XeCl excimer laser oscillator with standard plane-parallel optics would not lead to successful OPO operation, because of the excessive spectral linewidth (hundreds of cm^{-1}) and angular divergence (few mR) exhibited by such a laser. Therefore, the primary objective in the development of the pump laser was the attainment of a sufficiently high degree of spectral and spatial coherence in the pump beam. This was achieved by "injection-seeding" a high-energy XeCl "power oscillator" in an unstable resonator configuration by a low-energy, narrow-linewidth "master oscillator". In the development of the injection-seeded system, major emphasis was placed on the choice of optical components, and in particular, the design of the optical resonators and line-narrowing elements. This chapter begins with a brief description of the fundamentals of discharge-pumped excimer lasers and discusses their basic design criteria. The discussion is then followed by a more detailed description of the design and construction of the injection-seeded XeCl laser system, successfully employed in the demonstration of parametric oscillation in urea and β-BaB_2O_4.

3.1 DISCHARGE-PUMPED EXCIMER LASERS

Rare gas halide excimer lasers are pulsed lasers that use a mixture of a noble gas (Ar, Kr, Xe) and a halogen (F, Cl, Br, I) as the active amplifying medium. The term *excimer* refers to molecules that exist only in the excited state, and dissociate in the ground state. Therefore, excimers are ideal laser gain media because of the absence of a ground state population. The laser gas mixture (usually at $P \geq 1$ atm.) contains a small concentration of the halogen and the rare gas in a buffer gas (He, Ne, or Ar). Upon excitation, the halogen and rare gas atoms combine to form a rare gas halide (excimer) molecule. The excited molecules returning to the ground state emit discrete short-wavelength ultraviolet radiation and dissociate into single atoms. The principal interest in excimer lasers is because their emission wavelengths lie in the ultraviolet and vacuum ultraviolet (from 193nm to 351nm) regions of the spectrum, where other laser sources are not readily available, and also because of the relatively efficient production of their excited states, which results in high overall wall-plug to optical output efficiencies (typically $\geq 1\%$).

A variety of pumping techniques have been developed and utilised to achieve efficient excitation of excimer lasers. These include direct electron beam pumping, electron beam sustained discharges, and fast avalanche self-sustained electric discharges. Of these different approaches, fast avalanche electric discharges offer a relatively simple and efficient method for pumping excimer lasers when low to medium output powers are required. Discharges of this type have been used in the past for pulsed N_2 (337nm) and CO_2 (10μm) lasers. In this pumping scheme, the input electrical energy is stored in a capacitor bank and then rapidly transferred, by closure of a switch, into the laser gas mix through an avalanche discharge, initiated between two transverse electrodes which are mounted within the laser chamber. The simplest circuit configuration regularly used in fast transverse discharge excimer lasers is the *c-c transfer* circuit, shown schematically in Fig. 3.1. In the diagram, c_1 denotes the primary energy storage capacitor, s is a high-voltage, high-current switch (spark gap or thyratron), and c_2 is the secondary energy storage or "peaking" capacitor. The electrical energy at high voltage is stored in c_1, and c_2 is initially uncharged. Upon closure of the switch s, voltage gain is achieved across the electrode gap, as charge is rapidly transferred from c_1 to c_2, until the point where gas breakdown voltage is reached and c_2 discharges its stored energy into the laser medium. The inductor L_4 is used to maintain the voltage across c_2 (and hence the electrodes) zero while c_1 is charged, but otherwise does not participate in the circuit dynamics once the switch s is closed. The inductor L_1 serves to isolate the H.V. power supply from the rest of the circuit. The intrinsic self inductances of the primary and secondary circuit loops are represented by L_2 and L_3, respectively. The inductance L_2 determines the voltage rise time in the first loop and hence the voltage at breakdown, while L_3 determines the current rise time in the second loop and hence the rate of energy deposition into the gas [1].

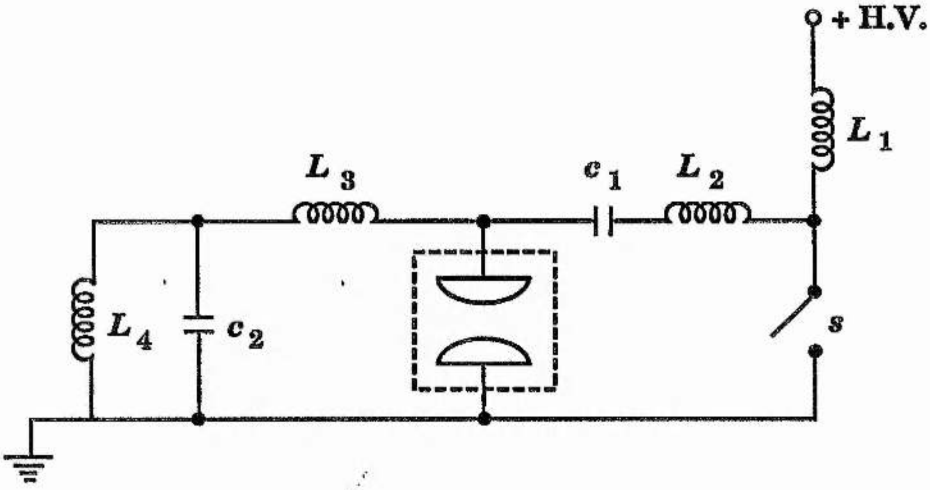

Fig. 3.1. The *c-c* transfer circuit.

The discharge circuits of all excimer lasers are characterised by very low inductance and impedance, very fast voltage and current rise times, and high peak powers. The primary reason for this property is the inherent instability of the electrical discharge in the gas mixes used in these lasers. When electrical breakdown occurs, free electrons which are present in the gas, begin to multiply exponentially through the avalanche process. In low-pressure discharges, the secondary electrons can spread rapidly by diffusion, and effectively homogenise the ionisation within the discharge volume, thus leading to the formation of a uniform glow discharge. At high pressures (such as those used in excimer lasers), however, the ability of these species to diffuse rapidly is significantly reduced. This results in the formation of spatial non-uniformities in the electron distribution which can grow with time and develop quickly into several unstable and constricted arcs, or streamers. The most serious consequence of discharge filamentation is that the resulting inhomogeneous distribution of refractive index can make lasing impossible, or at best, give rise to an output beam of poor optical quality. In this case, discharge pumping becomes very inefficient, due to the large regions of low current density. Even when spatial homogenisation is established, the discharge stability will only last until the formation of arcs and streamers caused by some secondary discharge phenomena, such as hot spots on the electrodes or thermal instabilities, which usually develop over longer time scales (> 40 ns). Because of this phenomenon, the useful electrical pulse length of lasers with no external stabilisation is usually limited to ≤ 30 ns at low pressures (≤ 0.5 atm.) and proportionally less at higher pressures. For these reasons, it is essential to minimise the inductance of the discharge circuit and to keep the current and voltage pulse fast-rising and short in duration (≤ 30 ns at $P \leq 0.5$ atm.), so that more of the stored electrical energy can be dumped into the laser medium before the inherent instabilities in the discharge set in and terminate the lasing process. In practice, this may be achieved by, for example, replacing the lumped inductive circuit elements by distributed versions, by careful component arrangement, and by compact physical design of the laser assembly itself. All these provisions can lead to major reductions in the various loop inductances and result in a more efficient excitation of the gas and a superior optical quality in the output beam. The formation of arcs and streamers in the discharge may in turn be significantly reduced or forestalled by utilising electrodes of smooth profiles to eliminate any strong localised electric field gradients at the surfaces, and by *preionisation* of the gas prior to the initiation of the discharge. Here, some form of volume ionisation is used to "flood" the inter-electrode region with electrons, from which the main discharge can avalanche uniformly into a glow discharge rather than degenerating prematurely into arcs and streamers. Several methods of preionisation have been successfully applied to excimer lasers. A simple and yet effective technique frequently employed, is to irradiate the laser gas mix by a flux of ultraviolet radiation, immediately before the initiation of the main discharge (commonly known as *UV preionisation*). The flux of UV radiation can be generated by means of, for example, a short corona discharge pulse [3], [4], or a spark array distributed along the length of the laser [5]-[8]. In any preionising configuration, however, it is important to use a geometry that produces uniform preionisation through the discharge volume and not only in the regions close to the preionising elements. Because of the small penetration depth of UV radiation in the gas mixes used in these lasers, it is advantageous to locate the preioniser as close to the discharge volume as practically possible and to produce the UV radiation within the laser chamber. When large discharge volumes are involved, the more penetrating effect of X-rays may be utilised to preionise the gas (*X-ray preionisation*). This technique has been successfully applied to large-bore excimer lasers [9], although the size and complexity of the overall system is considerably increased.

3.2 THE XeCl EXCIMER LASER ; – General Considerations

The criteria for the design of the XeCl excimer laser were set primarily by the requirements on the pump beam (in terms of output pulse energy, duration, linewidth, and output beam divergence) for successful operation of an OPO based on urea as the non-linear crystal. Thus, as an initial step it was necessary to carry out a study of the previously reported OPO devices based on this material and pumped at 355nm with the third harmonic of Nd^{+3}:YAG lasers, using the available literature [10]-[12]. From these studies, it was concluded that a XeCl laser suitable for pumping such an OPO should be capable of delivering output pulses of between 10 to 100 mJ in energy with 10 to 50 ns pulse length, in an output beam with a divergence close to the diffraction limit. In the interest of simplicity and cost-effectiveness, a low-repetition-rate system (of ≥ 1Hz) was favoured. This option eliminated the need for expensive and elaborate gas circulation systems that would have been necessary for high-repetition-rate operation, and meant that a spark gap rather than a thyratron could be used as the switch. The use of a spark gap was also considered advantageous because of its lower inductance, which would lead to a more efficient laser pumping. Other important considerations in the design and engineering of the pump laser included reliability, compactness, a simple (yet effective) preionisation scheme, and suitable choice of material for the mechanical and optical components for long life and optimum laser performance.

3.3 THE XeCl EXCIMER LASER ;– Electrical Design

Illustrated in Fig. 3.2 is a schematic of the electrical circuit used for excitation of the XeCl pump laser. The circuit was a fast avalanche transverse discharge of the simple *c-c* transfer type. The circuit employed an automatic UV preionisation scheme which eliminated the need for an auxiliary preionisation circuit. This was achieved by "breaking" the main discharge circuit and allowing the peaking capacitors c_2 to charge up through a series of 45 preionising pins which were located within, and equally-spaced in two rows on either side, along one of the electrodes (Photograph 3.1), in the vicinity of the discharge. The sparks produced between the pins and the body of the electrode provided the source of UV radiation necessary for preionisation of the gas while the voltage across the gap rose to the breakdown voltage and the main discharge was

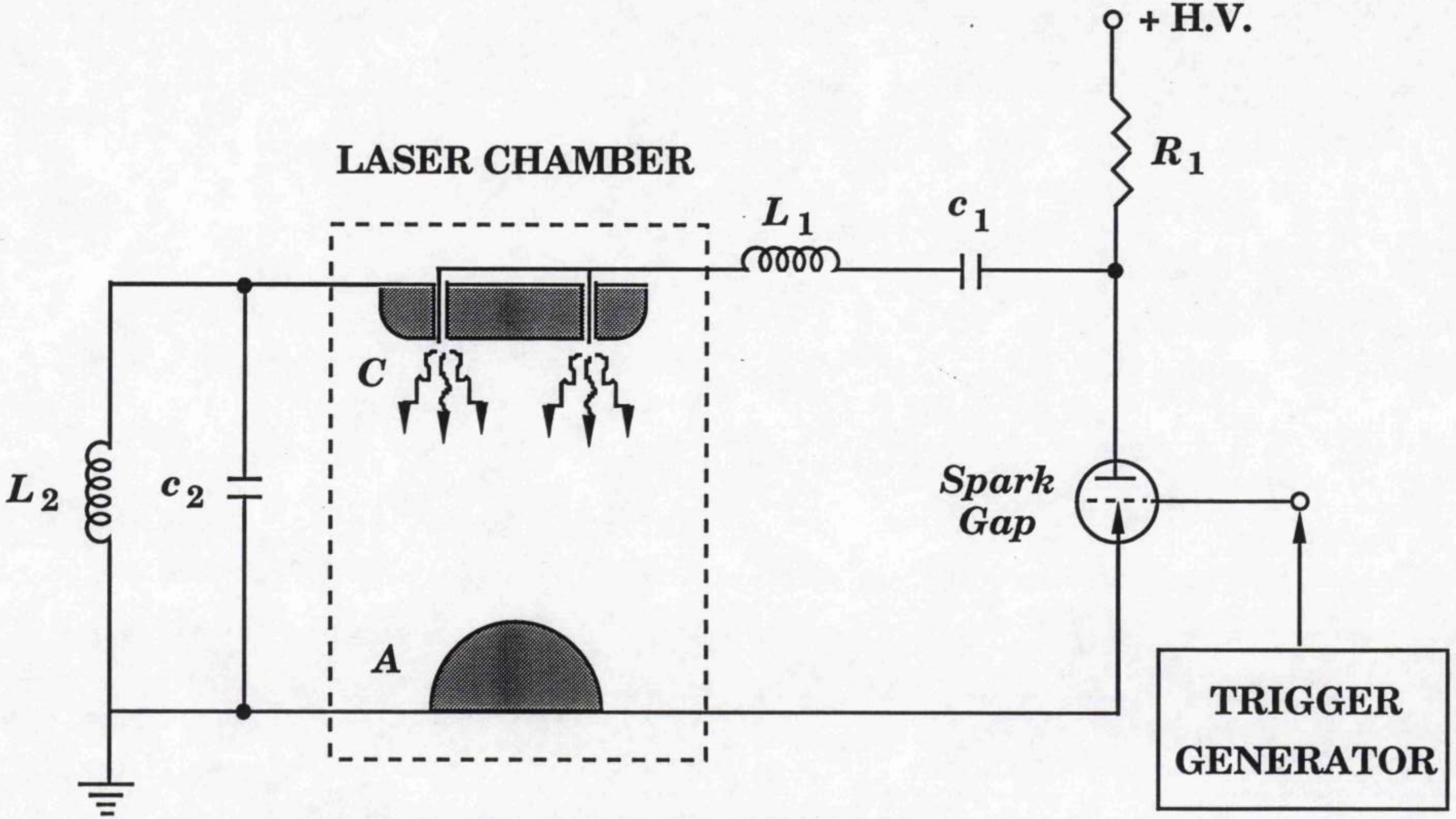

Fig. 3.2. Schematic diagram of the automatic UV-preionised transverse electrical discharge XeCl excimer circuit.

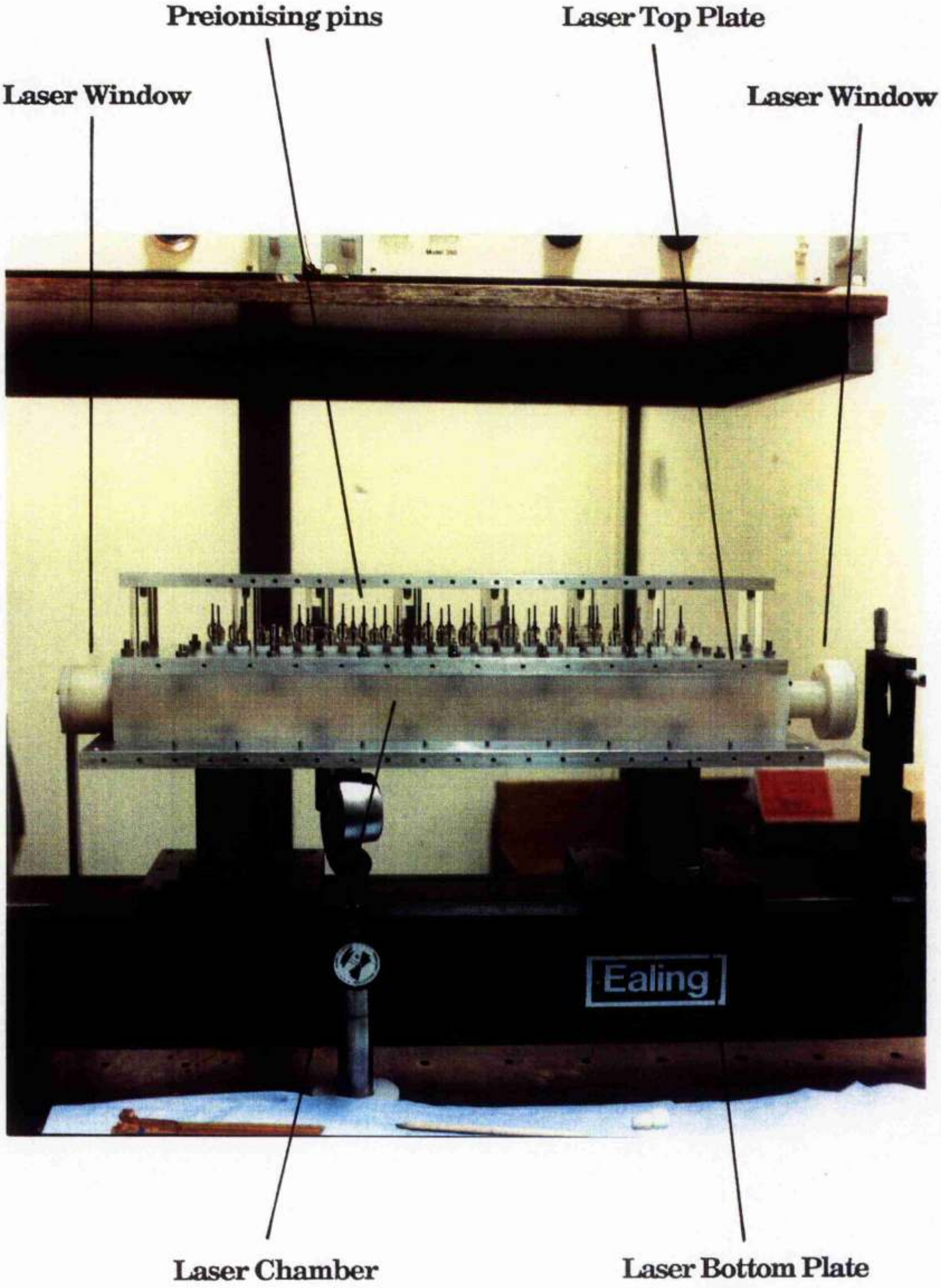

Photograph 3.1. Side view of the XeCl laser assembly.

initiated. In this way, UV preionisation began some time before the main discharge and persisted until the self-breakdown of the gas, allowing sufficient time for formation of a uniform glow discharge, without the need for an additional delay circuitry. The pins were also individually ballasted by a series of inductors, in order to maintain uniform illumination along the discharge volume. The total inductance of the parallel combination is represented by L_1 in the Fig. 3.2, while the self-inductance of the loops has been eliminated for convenience. The choice of this particular preionisation scheme was governed primarily by its relative simplicity of design and by the ease with which future modifications and adjustments could be implemented if deemed necessary. A second preionisation configuration based on mesh cathode and two rows of preionising pins behind the electrode was also considered. However, this option was not favoured because of the difficulties anticipated in manufacturing a mesh of uniform surface flatness. Any non-uniformities in surface flatness in this case could lead to a non-uniform preionisation along the volume of discharge because of the resulting variations in the separation between the preionising pins and the surface of the mesh electrode. The use of a mesh electrode was also considered to be a disadvantage in that the "shadow" of the electrode could appear in the discharge region and give rise to an output beam of inferior optical quality than would be the case with a solid electrode, as used here. In addition, any future modifications to the preionisation geometry with the mesh electrode were considered to be more difficult to implement than the preionisation scheme used here.

Initial observations of the discharge in pure Ne, with the preionising pins located within the cathode electrode, revealed several filamentary arcs originating from the pins and terminating at the edges of the anode electrode. The resulting discharge consisted of a "hollow" central region with constricted arcs and streamers on either side. These non-uniformities were observed to be even more pronounced in the presence of the appropriate laser gas mix, indicating a highly inefficient laser pumping and a corresponding degradation of output beam quality and pulse energy. This was attributed to ineffective preionisation of the discharge volume by the arrangement used. Several experiments were performed with the aim of significantly improving the uniformity of the discharge. These included, the use of He instead of Ne as the buffer gas, operating the laser with several different gas mix ratios and at different overall pressures, as well as utilising anode electrodes of different profiles and examining various pin-electrode assembly geometries. However, no one of these measures were found to be successful in significantly enhancing the spatial uniformity of the discharge. As a final attempt towards improving the preionisation, the cathode and anode electrodes were interchanged by the simple reversal of polarity on the H.V. power supply (from +ve to –ve). This modification seemed reasonable, since in the resulting configuration the preionising pins would be located within the anode electrode, enabling a more efficient UV irradiation of the cathode surface region, thus leading to a more uniform discharge [13]. In addition, the problem of "tracking" from the pins to the edges of the anode electrode, which was predominant in the original geometry, was expected to be largely eliminated because in the new configuration the discharge would originate from the electrode not incorporating the preionising pins. In the new arrangement, the preionising sparks would also be located well away from the cathode electrode, thus greatly reducing filamentation of the discharge [14]. Observations of the discharge with the modified preionisation geometry revealed major improvements in its uniformity, with little or no evidence of filamentation or tracking from the individual pins, observed previously. The discharge also appeared uniform over the entire inter-electrode region, with no sign of the hollow central region previously present. These observations indicated a more effective preionisation scheme and an efficient UV penetration to the cathode region, leading to an output beam of superior optical quality.

Choice of Component Values ;

3.3.1 Storage Capacitor c_1 :

The magnitude of the storage capacitor c_1 was determined primarily by the amount of electrical energy that was required to be stored in the system to ensure sufficient laser output. For output optical pulses of up to 100 mJ in energy, and assuming a typical (but pessimistic) laser wall-plug efficiency of 0.5%, an input electrical energy of 20 J was required for storage in c_1. Therefore, the magnitude of c_1 could be calculated using

$$E = \frac{1}{2} c_1 V^2 \tag{3-1}$$

where, E is the stored electrical energy and V is the input voltage. For a typical input voltage of 25 kV, we obtain $c_1 = 64$ nF. A second important criterion in the choice of c_1, however, was the amount of "stored capacitance per unit length of the discharge". This parameter which is a measure of the total electrical energy available per unit volume of the discharge, is an important yardstick in determining the correct value of c_1, for a given electrode spacing, width, and length, to give the necessary output pulse energy. An extensive survey of the available literature revealed no conclusive preferred value for this parameter, and the obtained values varied for different laser systems depending on the choice of gas mixture, pressure, size, and other operating conditions. However, for lasers of similar operating characteristics and discharge dimensions to the device discussed here, a typical value of ~1 nF/cm was commonly typical. This value was found to compare very favourably with that used here, since the laser electrodes were 52cm in length, yielding a value of 1.23 nF/cm for this parameter, given a storage capacitance value of c_1 = 64nF.

Having determined the magnitude of the total storage capacitance c_1, an important consideration in the choice of suitable capacitors was to ensure low inductance in the charging circuit for fast voltage rise time on the electrodes, and hence efficient transfer of electrical energy to the laser gas mixture. This consideration implied the need for keeping the storage capacitance c_1 as distributed as possible. For this reason, a series of commercially available compact, high-voltage, high-performance, "door-knob" ceramic capacitors (Murata DHS60 New Series, M-40) were selected. Each capacitor was capable of withstanding a test d.c. voltage of up to 60kV, and a working d.c. voltage of 40kV, well above the projected 25kV input voltage required for the operation of the laser. Thirty-two such capacitors, each 2000 pF in value (with an O.D.= 60mm), were distributed in two rows, each containing sixteen capacitors (two sets of eight capacitors placed back-to-back), along the 52-cm length of the discharge, as shown in Photograph 3.2. This combination resulted in a total storage capacitance of c_1 = 64nF, with eight current "nodes" located at equal intervals of 64 mm along the laser length, ensuring as low an inductance in the charging loop as practically possible.

Photograph 3.2. Inside view of the XeCl laser assembly.

3.3.2 Peaking Capacitor c_2:

The choice of the peaking capacitors c_2 is largely dependent on the value of the storage capacitance c_1, as the ratio c_1/c_2 determines the extent of voltage amplification and/or charge transfer from c_1 to c_2 [15]. In the special case where $c_1 = c_2$, charge and hence energy transfer from c_1 to c_2 is complete. For large values of c_1/c_2 ($\geq \sim 3$), high voltage amplification can result across the gap ($\geq \sim 1.5$ times), but only at the expense of a smaller charge transfer from c_1 to c_2, and thus a lower energy transfer efficiency to the gas mix ($\leq \sim 75\%$). Conventional wisdom in excimer circuit design has been to use large values of c_1/c_2 in order to maximise voltage gain, so that the gas breakdown voltage is reached more rapidly during the charging cycle, before the inherent instabilities in the discharge set in. However, although such an approach may improve certain aspects of laser performance, the inefficient transfer of energy from c_1 to c_2 in general leads to shorter component lifetime and poor reliability. This is because the fraction of the energy originally stored in c_1, but not used for laser oscillation (due to inefficient transfer) is deposited in other discharge components, with the consequent damaging effects on the lifetime and performance of the circuit. For this reason, a moderate value of $c_1/c_2 \sim 2$, corresponding to a voltage gain of ~1.35, and an energy transfer efficiency of of ~90% [15] was chosen. However, in order to compensate for the relatively low voltage magnification, a relatively small electrode gap of ~25mm was favoured and major efforts were expended in ensuring an effective preionisation scheme. Both these provisions were considered to be important in relaxing the constraint on the low voltage gain. The smaller electrode spacing leads to a higher electric field gradient across the gap, thus leading to a smaller breakdown voltage, while efficient preionisation of the gas delays the formation of arcs and streamers and results in a more efficient pumping. Further, as discussed previously, the inductance of the discharge loop can also play an important role in the efficient operation of the laser, as it determines the rise time of the discharge current and the rate of energy deposition into the laser gas mix. Hence, as with the storage capacitors, the peaking capacitors were chosen in such a way as to maintain the total capacitance as distributed as possible. With this in mind, and given the practical design limitations, a series of twenty high-performance, door-knob, ceramic capacitors (Murata DHS52 New Series, M-40), each 1300 pF in value (O.D.= 52mm), were selected. The capacitors were mounted external (but as close as possible) to the laser chamber, and were distributed in two rows of ten, on either side of the laser head, as shown in Photograph 3.2. This resulted in a total peaking capacitance of $c_2 = 26\text{nF}$, yielding a capacitance ratio of $c_1/c_2 \sim 2.5$, which is close to the design figure of 2. This value corresponds to a voltage gain of ~1.4 and an energy transfer efficiency of ~85% [15].

3.3.3 Power Supply:

The first criterion in the choice of a suitable power supply for the discharge circuit was obviously the ability to deliver a charging voltage of up to 25 kV to the capacitor bank c_1. More importantly, however, the power supply had to be capable of pulse charging the storage capacitors at the repetition rate of interest. In other words, the "energy rating" of the power supply was the important parameter for successful operation of the circuit. Since, high average power laser operation was not of primary interest, a repetition rate of 1 Hz was considered adequate. Therefore, we were interested in a high-voltage power supply capable of pulse charging $c_1 = 64$ nF up to 25 kV, at a 1 Hz repetition rate. In other words, the power supply was required to repetitively deliver 25 kV to the storage capacitors

c_1 in time intervals of ≤ 1 second. The amount of energy stored in c_1, in each pulse charging cycle is given by equation (3-1). With $c_1 = 64$ nF, and V= 25kV, we obtain E = 20 Joules. Therefore, the power supply must be able to deposit this amount of energy in the storage capacitors in ≤ 1 second. The corresponding required energy rating for the power supply may thus be calculated as

$$W = dE\,/\,dt = 20\ \text{J. second}^{-1} \tag{3-2}$$

Therefore, we chose a high-voltage Hartley Measurements Limited (HML, Model 411 series) capacitor charging unit with an energy rating of 100 J/s, and capable of delivering charging voltages of up to 30 kV, safely above the required charging voltage for successful laser operation. Another useful advantage of this unit was the inclusion of a "dump switch" to discharge the storage capacitors of any residual charge subsequent to shut-down.

3.3.4 Charging Resistor R_1:

The purpose of including the resistor element R_1 in the discharge circuit is two-fold. First, to protect the power supply against any transients that may be produced and fed back into the power supply when the storage capacitor bank is discharged and, second, to prevent the charging unit from exceeding its maximum "current rating" by attempting to deliver excessive current into the short circuit which occurs on the closure of the switch. Although the Model 411 HML power supply incorporated additional protective and current limiting circuits to ensure satisfactory operation under normal circumstances, it was decided, as a precautionary measure, to include the resistor R_1 in the circuit (an inductor element would be equally suitable), between the power supply and the capacitor bank c_1. This is because in the case where the capacitor values c_1 and c_2 differ (as is the case here), and the charge transfer from c_1 to c_2 is incomplete, the remaining charge on c_1 rings the discharge circuit until the (time-varying) gas impedance damps oscillations. However, as the impedance of excimer laser circuit is typically quite low (a fraction of an ohm), the damping time can be several complete cycles [15]. This may cause the voltage across the capacitor c_1 to oscillate with such an amplitude in the negative direction that the current surge back into the power supply may be large enough to cause damage to the unit. These considerations, therefore, indicated the need to include a resistive element between the power supply and the storage capacitor bank. With the particular power supply used here, it is recommended that if a voltage reversal in excess of 30% is anticipated, the unit must be connected through a resistance of ≥1kΩ [16]. However, we chose a higher value of $R_1 = 50$ kΩ. This resulted in a time constant of $R_1 c_1 = 3.2$ ms for the charging circuit, and thus did not limit operation of the device at the required 1 Hz repetition rate.

3.3.5 Spark Gap Switch:

As well as the high-voltage capability, an important parameter in the choice of a suitable spark gap switch is its "current rating". Once the switch is triggered, the charge initially stored on c_1 is transferred, through the spark gap, to c_2 in a time scale typically of the order of 100ns [9]. For $c_1 = 64$ nF and V= 25 kV, and assuming 100% charge transfer efficiency (unrealistic, but safe), the total amount of charge passing through the switch during the transfer cycle is

$$Q = c_1 \mathrm{V} = 1.6 \times 10^{-3} \text{ coulombs} \tag{3-3}$$

This charge "leaks away" through the spark gap in approximately 100 ns, yielding a maximum current through the switch of

$$I_{max.} = Q / \tau = \frac{(1.6 \times 10^{-3})}{(100 \times 10^{-9})} = 16 \text{ kAmps.} \qquad \textbf{(3-4)}$$

Therefore, the spark gap switch was required to have a minimum current rating of 16 kA. We chose a Tachisto demountable spark gap switch (model SG 301) with a peak current rating of 200 kA, and an operating voltage range over 8-40 kV, depending on the pressure of the nitrogen gas (oil-free or zero-grade) flowing through the gap. The use of a spark gap switch instead of a thyratron, as well as the lower inductance, had the additional advantage in that the voltage polarity of the device could be readily reversed without any adverse effect on its performance. The switch was repetitively triggered by means of 300 V output pulses derived from a trigger unit (HML, model 350) in conjunction with a pulse transformer (HML, model 531-0030).

3.3.6 Ballast Inductors L_1:

The value of the individual ballast inductors that give rise to a total parallel combination represented by L_1 in Fig. 3.2, can be calculated by considering the rate of change of current through the inductors during the transfer of charge from c_1 to c_2. We consider one individual inductor L_i and assume that it attempts to draw the maximum available current of ~16 kA, once the spark gap switch is closed. This current flows through the inductor in ~ 100 ns, yielding a current flow rate of

$$\frac{dI}{dt} = -16 \times 10^{10} \text{ Amps.s}^{-1} \qquad \textbf{(3-5)}$$

The corresponding voltage developed across L_i is given by

$$V_L = -L_i \frac{dI}{dt} = (16 \times 10^{10}) L_i \qquad \textbf{(3-6)}$$

This voltage opposes the change that produced it in the first instance. If, for example, one pin attempts to draw all the available current, the voltage V_L developed across it will oppose the flow of current through it and thus prevent it from drawing the entire current. In this way, the individual pins are prevented from "starving" the remaining pins of current and all pins will draw equal share of the available current. This leads to simultaneous and uniform sparking of all pins, and thus a uniform preionisation of the gas along the discharge. A reasonable design value for V_L would be ~ 25 kV (i.e. the supply voltage), so that L_i ~ 0.16 μH. We chose 45 such inductors, each 0.17μH in value (Cirkit, MC107). The inductors were attached to the individual pins and were distributed in two rows on either side, along the length of the discharge. The total inductance (L_1 in Fig. 3.2) resulting from the parallel combination of 45 such inductors was, therefore, ~3.7 nH. The total voltage drop across L_1 can be calculated using (3-6). This yields V_L (total) = ~ 555 Volts (for a 100 ns charge transfer time), which is only a small fraction (~ 2.2%) of the total supply voltage of 25 kV. Hence, the loss in the available input voltage arising from the inclusion of ballast inductors was negligible, and a high percentage (~98%) of the input voltage could still be efficiently used for pumping the laser.

3.3.7 Discharge Inductor L_2:

The primary purpose of including the inductor L_2 in the discharge circuit was to ensure that the peaking capacitors c_2 were completely discharged in between successive charging cycles. In choosing a correct value for L_2, two important factors needed to be taken into consideration. First, the magnitude of L_2 has to be large enough (compared with the discharge impedance) not to draw any current during the discharge cycle, so that all the available current flows through the electrode gap. Second, the inductance value L_2 has to be small enough not to limit operation of the laser at the required repetition rate, by prolonging the charging cycle due to a high inductance value. A 20 μH inductor element was formed by winding the inner conductor of a BNC cable around a piece of plastic piping (~25 cm long, and ~2.5 cm in diameter). With the inductor L_2 in place, we performed experiments to determine the voltage pulse profile across the electrode gap during the charge/discharge cycle. This was achieved by attaching a high-voltage probe to the laser top plate and monitoring the voltage pulse-form on an oscilloscope. The charging cycle was observed to last for ~ 80 ns, with the gas breaking down at a voltage of ~ 17 kV, while the discharge cycle was observed to occur in ~ 30 ns (see Trace 3.1).

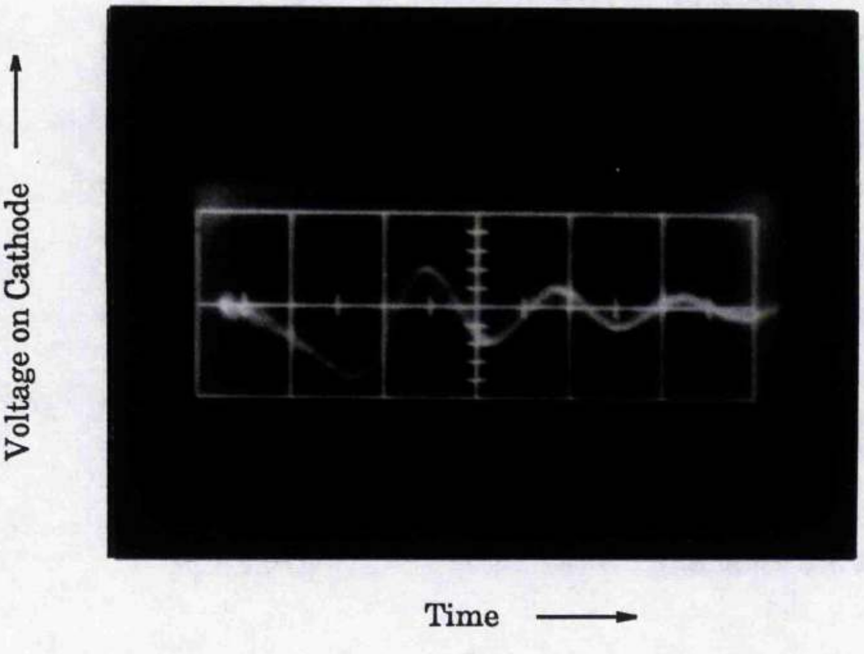

Trace 3.1. Voltage waveform on the cathode electrode.
Vertical scale: 20 kV / major division; Horizontal scale: 50 ns / division.

The impedance of the inductor element ($Z = \omega_{disch.} L_2$) during the discharge cycle was, therefore, calculated to be ~ 4.2 kΩ (for τ = 30 ns), much greater than that of the electrode gap (a few Ω), as required. The charging time of 80 ns was also seen to be much smaller than the period of the charging cycle corresponding to the required 1 Hz repetition rate. Therefore, the choice of the particular value of L_2 = 20 μH was expected to lead to an efficient laser pumping at the required repetition rate.

Since the XeCl excimer laser was to be used in an injection-seeded configuration, it was necessary to provide two discharge circuits, one for the master oscillator and one for the power oscillator. This was achieved by simply placing two such circuits back-to-back, as shown in Fig. 3.3. The circuits shared a common spark gap switch, trigger unit, and charging resistor R_1. To obtain the required time-delay between the breakdown of the gap in the master oscillator and initiation of the discharge in the power oscillator, which is necessary for efficient injection-seeding (see section 3.4), the electrode spacing in the master oscillator was made adjustable. Several electrode separations were examined, but the best results were obtained with a master oscillator electrode separation of 17mm and a power oscillator electrode gap of 25mm (see section 3.7 for more details).

3.4 THE XeCl EXCIMER LASER ; –
Optical Design – General Considerations

As discussed earlier, the key to successful and efficient operation of an OPO lies in the attainment of a high degree of spectral and spatial coherence in the pump light. In addition, the pump light must be of sufficiently high intensity (typically ≥ 100 $MW.cm^{-2}$) for the OPO to reach oscillation threshold. In practice, the simultaneous achievement of all these requirements using a single excimer laser is difficult. Although

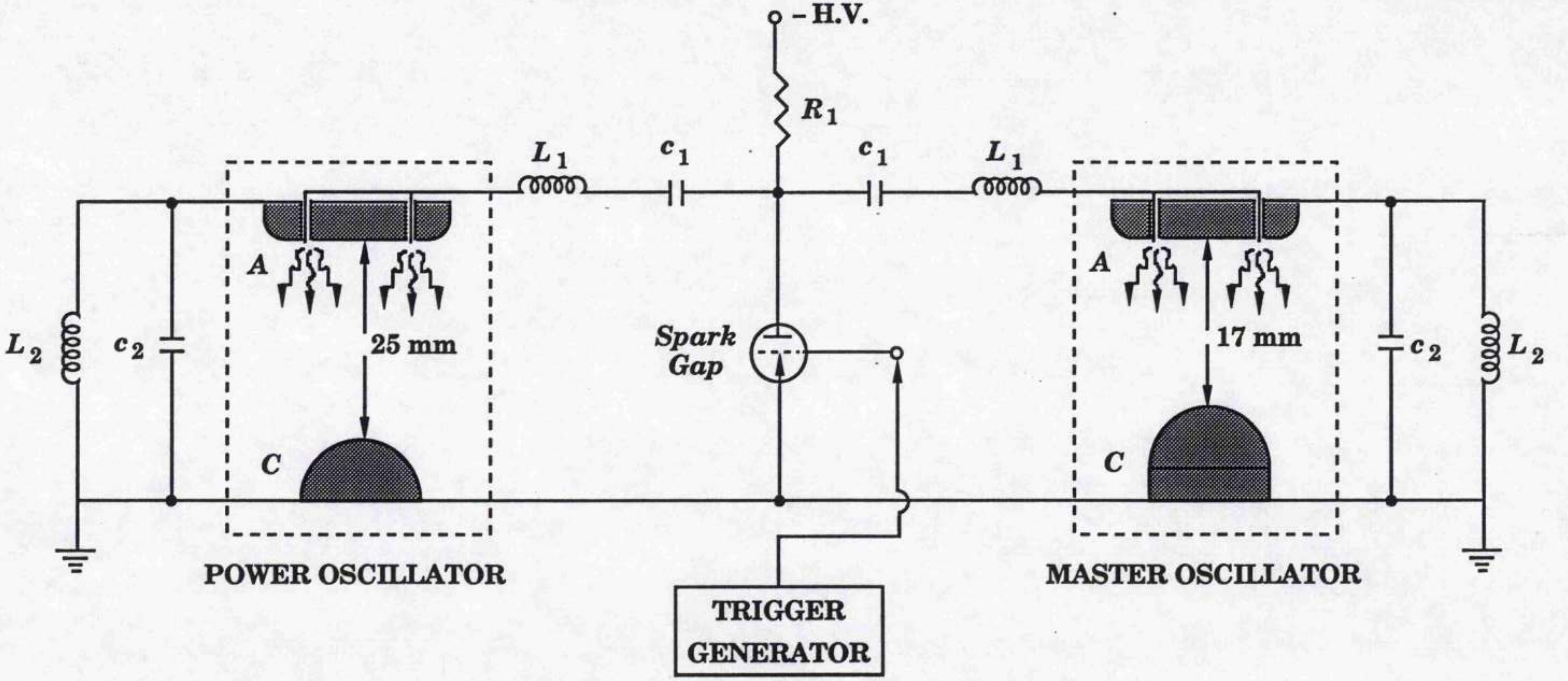

Fig. 3.3. Schematic diagram of the transverse electrical discharge injection-seeded XeCl excimer circuit.

typical single-headed excimer lasers with simple plane-parallel cavity configurations are capable of delivering intense output pulses, the angular divergence and focusability of the output beam is in general relatively poor and the linewidth is broad (hundreds of cm^{-1}). The former is due to the short pulse duration in such lasers (typically 10-20 ns) which is detrimental to the establishment of any particular low-order transverse mode, because of the small number of round-trips available over the duration of optical gain. In addition, the plane-parallel resonator geometry regularly used in these lasers has the lowest mode discrimination of all stable resonators, and as such can support simultaneous oscillation of several independent spatial modes. As a result, the output beam from such lasers is highly multimode, with a full-angle of divergence ~ 5-10mR (many times the diffraction limit), leading to a highly uncollimated phasefront and a diffuse focal spot when focused. The multimode nature of the output beam and the excessive angular beam divergence can be somewhat alleviated by the use of more effective stable resonator geometries (e.g. employing spherical mirrors). However, this solution is, in practice, not favoured because it leads to a significant loss in the output power by confining the laser oscillation to only a small region of the available gain volume (close to resonator axis), thus resulting in a reduction in the overall efficiency. The problem can be overcome by the use of an unstable resonator configuration [17], which can successfully reduce the output beam divergence without a significant sacrifice in the output power. With an unstable optical cavity, the higher-order transverse modes suffer much greater losses than the lower-order modes and as such there is a high degree of discrimination in favour of the lowest-order modes. This solution particularly favours excimer lasers because of their high gain (~10% per cm) and large mode volumes. In this way, one can simultaneously achieve a high degree of spatial coherence and a high output intensity, both necessary requirements for successful operation of an OPO. However, the use of an unstable resonator excimer laser alone, to pump an OPO, will not lead to successful operation of the device, because of the inherently broad spectral linewidth still exhibited by such a laser. Therefore, additional line-narrowing techniques have to be applied to such a laser to confine the spectral bandwidth within the calculated limits set by equation (2-58), chapter 2, for the particular OPO device. In a stable optical resonator, this is most simply achieved by incorporating additional frequency-selective elements (e.g. birefringent filters, etalons, etc.) within the cavity, or by the use of gratings in various configurations, as feedback elements or laser mirrors. In an unstable resonator, on the other hand, incorporation of such elements is more difficult because of the spherical nature of the phasefronts, and the large mode volumes involved. Recently, these techniques have been applied to novel unstable resonator cavities and narrow linewidth radiation has been extracted from a single-headed excimer laser [30]. However, the output intensities attainable from such lasers is generally low, because of the additional insertion loss introduced by the incorporation of intracavity frequency-selective elements. Further, the output beam divergence in such lasers is relatively poor compared with the best divergence that can be achieved in a confocal unstable resonator. This is due to the departure from confocal resonator configurations to the more novel unstable cavity geometries, that are necessary to enable narrow-linewidth operation.

The most successful approach that has regularly been adopted in line-narrowing excimer lasers when narrowest attainable linewidth and highest attainable beam quality are paramount, without great sacrifice in output intensity, is "injection-seeding" of an unstable resonator by a stable resonator [21]-[24], [28]-[29]. In this approach, the output radiation from a high-quality (narrow-bandwidth, low-order transverse mode), low-energy "master oscillator" (MO) is used to "seed" the gain medium of a high-energy "power oscillator" (PO) of otherwise broad linewidth. Provided, the power level of the radiation injected (or "seeded") into the PO cavity exceeds the level of the spontaneous emission (noise) present in the cavity, the stimulated emission at the frequency of the injected radiation will "win" the competition in setting up oscillations in the active PO cavity, and the PO bandwidth will be reduced to the narrow bandwidth of the MO as the resonator modes evolve. As an additional advantage, injection-seeding further reduces the output beam divergence, particularly in the early part of the pulse, before the full benefit of the unstable resonator has been fully exploited. This technique allows the simultaneous attainment of the three necessary requirements in the pump beam for successful OPO operation, namely, a narrow linewidth, a low beam divergence, and a sufficiently high output intensity.

In order to achieve effective line-narrowing and efficient mode discrimination in the PO, the injected reference signal should be made to match, as closely as possible, the fundamental transverse mode of the unstable PO cavity, with regard to both phasefront profile and propagation direction. In other words, the two resonators should be "mode-matched". In addition, it is important to provide a time-delay between the initiation of laser oscillation in the PO and that in the MO, so that the injection signal "fills" the mode volume in the PO cavity before laser action occurs. In this way, the initial rise of gain in the PO is made to coincide with a cavity-filling pass of the MO beam, enabling most of the gain volume in the PO cavity to be seeded by the injected beam and the laser oscillation in the PO to be initiated from a coherent optical signal with maximum efficiency. The timing between the two lasers is particularly critical in the case where short pulse durations are involved, as here. In the design of the injection-seeded XeCl laser system, the time-delay between the MO and PO cavities was facilitated by adjustment of the electrode separation in the MO laser chamber, and will be discussed in more detail in section 3.7. Further, in order to provide a large number of round-trips over the short duration of optical gain, both lasers were designed with a view to maintaining the cavity lengths as short as possible. We now describe the optical design of the injection-seeded XeCl excimer laser.

3.5 MASTER OSCILLATOR ; – Optical Design

The MO cavity consisted of a concave spherical mirror and a planar output coupler, forming a stable resonator, as shown in Fig. 3.4.

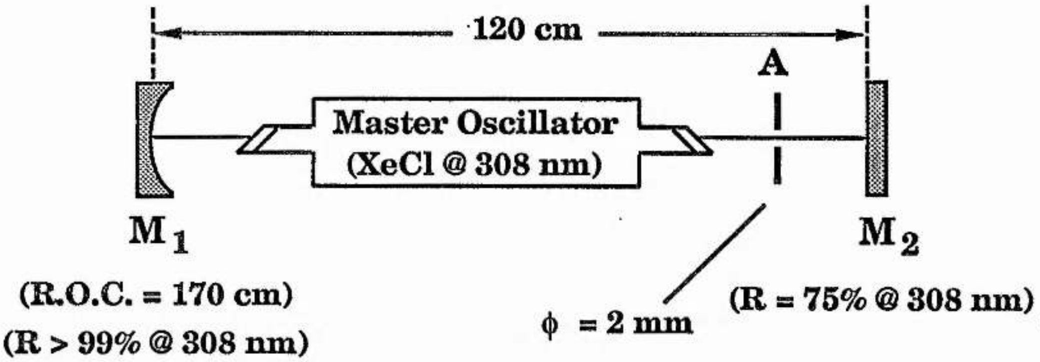

Fig. 3.4. Schematic of the master oscillator cavity configuration (side view).

This particular cavity configuration was chosen, because it was desirable to obtain a beam waist at the output mirror of the laser in order to simplify mode-matching. The mirrors were separated by 120 cm to accommodate line-narrowing etalons and a spatial filter (A in Fig. 3.4). The rear concave mirror M_1 had a reflectivity $R > 99\%$ at 308 nm and the plane output coupler M_2 was a partial reflector with $R = 75\%$ at 308nm/0°, and was antireflection-coated on its rear surface for 308nm. This relatively low output coupling of 25% (or large feedback of 75%) was considered to be necessary in order to achieve oscillation in the MO, given the high insertion loss introduced by the additional intracavity elements and the large reduction in the available gain volume anticipated from the incorporation of the spatial aperture into the laser cavity. The concave rear mirror M_1 had a radius of curvature (R.O.C.) of 170 cm which, from standard Gaussian beam optics, yields a beam waist radius at the output mirror of [18]

$$W_0 = \sqrt{\frac{\lambda}{\pi}\,[z\,\{R(z) - z\}]^{1/2}} \sim 0.3 \text{ mm} \qquad (3\text{-}7)$$

where, $R(z)$ is the mirror curvature, z is the cavity length, and λ is the wavelength. As a preliminary attempt to achieve laser action in the fundamental Gaussian mode, a circular aperture was placed within the MO cavity close to the output mirror M_2. The aperture diameter (~0.5 mm) was chosen to closely match the Gaussian spot size at the location of the pinhole (~10 cm from the beam waist), and a He-Ne laser was used for alignment of the cavity. However, after several attempts at different gas pressures and with various gas mixture ratios, it was found not to be possible to achieve laser oscillation. Thus, it seemed necessary to enlarge the pinhole diameter to provide more gain, and hence facilitate laser action, but at the expense of a departure from the desired fundamental TEM_{00} beam quality. After several experiments with various pinhole sizes, and with the intracavity etalons in place, laser action was achieved with a pinhole, 2mm in diameter, located at a distance of ~10 cm within the cavity, from the output plane mirror. Since, the pump light for the

OPO had to be linearly polarised to achieve parametric oscillation, the MO chamber was designed to incorporate windows at Brewster's angle (see section 3.8 for details of mechanical design). In this way, the "seed" radiation from the MO was strongly linearly polarised, thus resulting in a linearly polarised output from the PO. The windows were 10mm thick (with ≤ 2 minutes of arc parallelism), to withstand differential pressures of up to a few atmospheres. The windows and mirror substrates were all made of fused silica (Suprasil, optical 4000, $\lambda/10$ both surfaces) and were 2" in diameter.

3.5.1 Line-Narrowing

Several techniques have been frequently employed in line-narrowing excimer lasers. These include the use of dispersing prisms for relatively coarse frequency-selection, and diffraction gratings in various configurations as well as Fabry-Perot etalons for ultra-narrow operation. The choice of the particular line-narrowing technique in our case was determined by the need to achieve a very narrow pump bandwidth ($\leq 1\text{cm}^{-1}$), safely below the limit set by equation (2-58) in chapter 2 (and shown in Figs. 2.8(a) and 2.8(b)), for successful OPO operation. For this reason, the option of using dispersing prisms as line-narrowing elements was ruled out in favour of gratings and etalons. In order to ensure simplicity and flexibility of incorporating additional elements in the future for further bandwidth reduction, the use of etalons rather than gratings was favoured. As an initial step towards the choice of appropriate etalons for line-narrowing, it was necessary to obtain details of the spectral structure of the free-running XeCl MO. In order to do this, the output beam from the free-running MO (Fig. 3.4) was directed onto a calibrated monochromator, with its entrance and exit slits set for maximum resolution. The monochromator was scanned near 308nm and the spectrum, which was detected by a photomultiplier tube, was displayed on an XY-plotter. Illustrated in Fig. 3.5 is a typical spectrum obtained from the free-running laser, exhibiting two main peaks separated by 2.73Å (28.8 cm^{-1}), and two additional weaker spectral components on either side. The observed spectrum was found to be consistent with those previously reported in the literature for a XeCl excimer laser [19], [20]. The four distinct laser lines correspond to the (0,0), (0,1), (0,2), and (0,3) vibrational bands of the $^2\Sigma^+_{1/2}$–$^2\Sigma^+_{1/2}$ transition of XeCl, with most of the laser power concentrated in the two spectral components (0,1) at 307.9 nm, and (0,2) at 308.2 nm [20]. As a first step, it was necessary to choose an etalon of appropriate free spectral range (F.S.R.) to select only one of the main spectral features (preferably, the stronger of the two), and eliminate the second peak. For example, a suitable etalon would be one with a F.S.R. greater than the separation of the two main peaks. Hence, we selected a 70μm thick solid etalon (F.S.R.= 48 cm^{-1}, finesse = 25). The etalon, 1" in diameter, was sandwiched around its perimeter between layers of PTFE, to prevent damage, and then mounted in a plastic holder. The holder was then placed in an adjustable gimbal mount to facilitate angular rotation of the etalon. Both intracavity and extracavity configurations were examined and were observed to reduce the MO bandwidth, although the intracavity option was found to be more effective, as expected. Thus, the latter option was favoured. In order to obtain the best results, the etalon was placed inside the MO cavity and was "calibrated" by recording the laser spectrum for various values of the angle ψ_1 between the etalon and the laser axis (Fig. 3.6(a)). A He-Ne laser and a pinhole were used to aid precise measurements of the angle ψ_1. Several spectra for a range of values of ψ_1 ($0^\circ < \psi_1 < 7^\circ$), showing a systematic tuning across the spectrum with the change in ψ_1, in a manner consistent with the F.S.R. of the etalon. At an angle $\psi_{1_0} = 6.2^\circ$, the

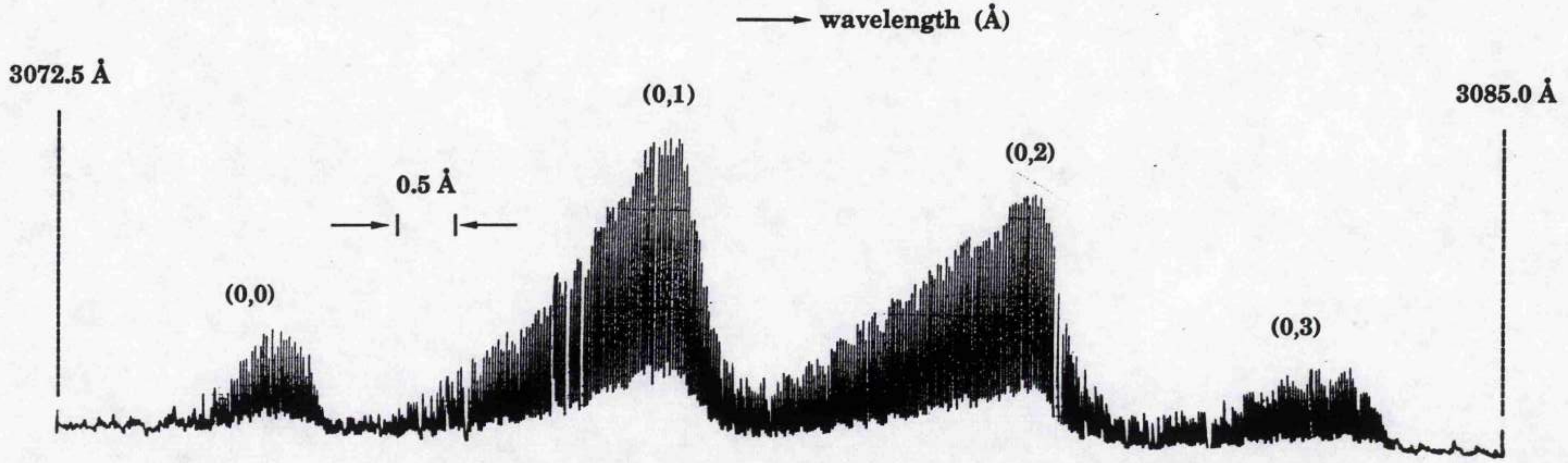

Fig. 3.5. Free-running spectrum of the XeCl master oscillator, showing the distinct vibrational transitions (0,0), (0,1), (0,2), and (0,3).

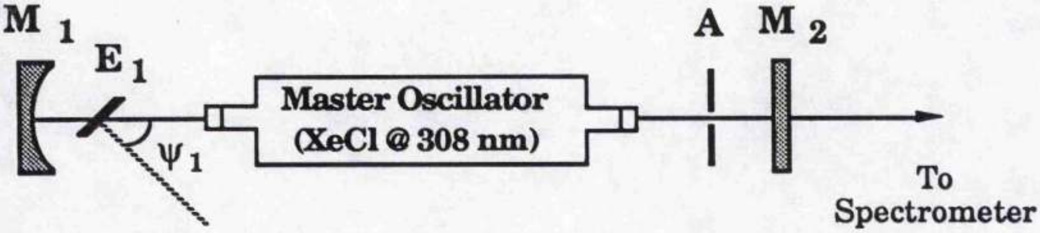

Fig. 3.6(a). Narrow-linewidth XeCl master oscillator (top view); E_1 : 70 μm solid etalon (F.S.R.= 48 cm^{-1}, finesse = 25).

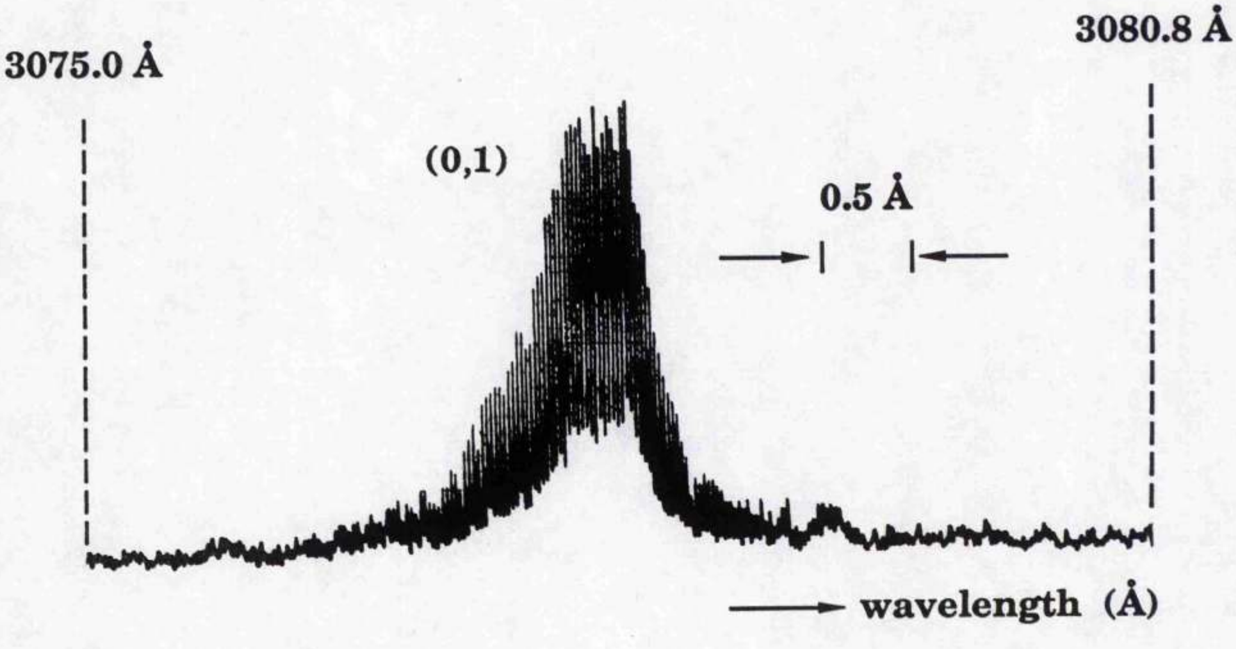

Fig. 3.6(b). Spectrum of the line-narrowed XeCl master oscillator with the 70 μm intracavity solid etalon at an angle $\psi_1 = \psi_{1o} = 6.2^o$.

spectrum was observed to collapse to a single primary peak with no other spectral components present, as shown in Fig. 3.6(b). The spectral width (FWHM) of this component was measured to be only about 0.7-0.8 Å (~ 7-8 cm^{-1}), somewhat close to, but not safely below, the pump laser bandwidth required for OPO operation. Therefore, it was necessary to achieve further bandwidth reduction by incorporating an additional etalon into the MO cavity. A 500μm thick solid etalon (F.S.R.= 6.7 cm^{-1}, finesse = 25) was selected and placed inside the MO resonator, as shown in Fig. 3.7(a). With the 70μm etalon set at its optimum angle ($\psi_{1_o} = 6.2^o$), the 500μm etalon was calibrated in a manner similar to the 70μm, by recording several spectra for various values of the angle ψ_2 between the etalon and the laser axis. At an angle $\psi_{2_o} = 2.5^o$, the MO bandwidth was reduced to ~ 0.2Å (~ 2 cm^{-1}), as shown Fig. 3.7(b). Although the obtained bandwidth was sufficiently narrow for OPO operation, it was found to be an order of magnitude broader than that expected from the etalon F.S.R. and finesse (i.e. ~ 0.2 cm^{-1}). In fact, incorporation of the additional 500μm etalon into the cavity resulted only in a 3 to 4-fold reduction in the MO bandwidth. This was soon attributed to the resolution limit of the monochromator and indicated the need for a more accurate measurement of linewidth. We, therefore, attempted to monitor the linewidth with the use of a number of etalons as interferometers. However, this proved not to be possible because of the low output power available from the MO. This technique was, however, successfully used for accurate measurements of the linewidth of the final output beam from the injection-seeded system, because of the far greater output intensities available from the PO, and the relevant experiments will be described in more detail in section 3.7. The observed spectrum was found to be consistently reproducible over periods of several hours and many days. The experiments were also performed with degraded gas

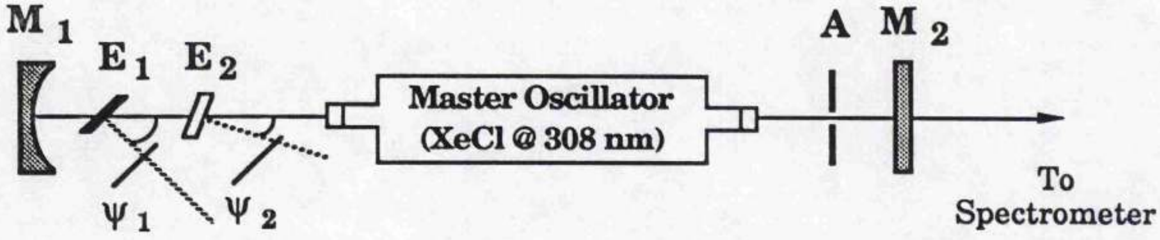

Fig. 3.7(a). Narrow-linewidth XeCl master oscillator (top view);
E_1 : 70 μm solid etalon (F.S.R.= 48 cm^{-1}, finesse = 25),
E_2 : 500 μm solid etalon (F.S.R.= 6.7 cm^{-1}, finesse = 25).

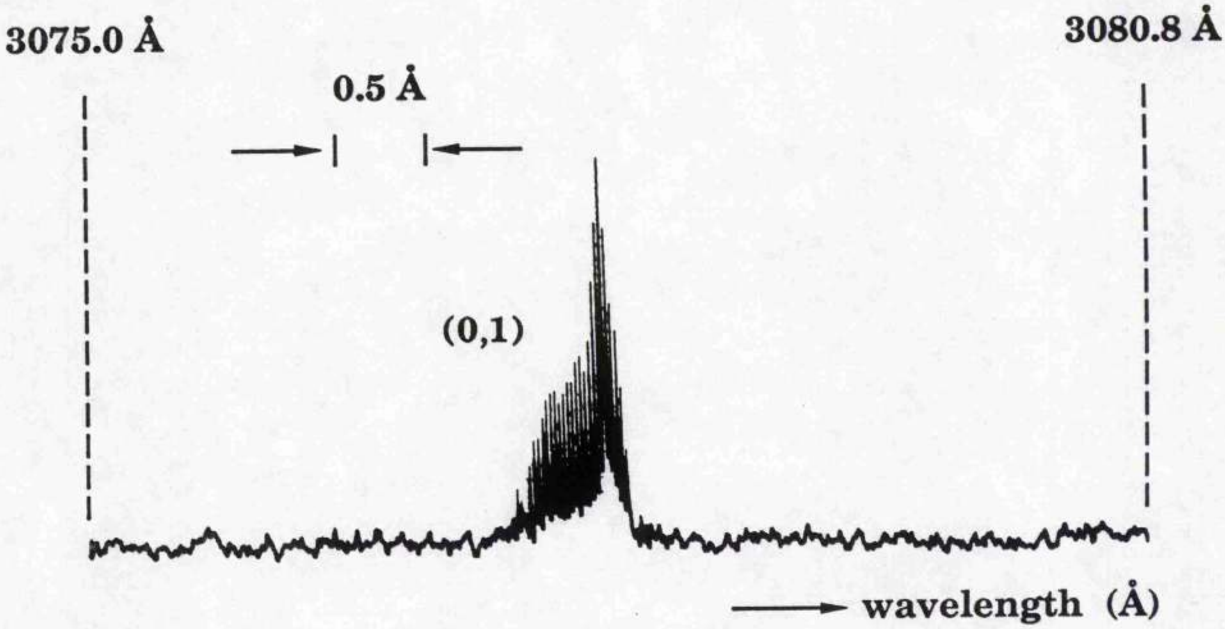

Fig. 3.7(b). Spectrum of the line-narrowed XeCl master oscillator with the 70 μm and 500 μm intracavity solid etalons at an angle $\psi_1 = \psi_{1o} = 6.2^o$ and $\psi_2 = \psi_{2o} = 2.5^o$, respectively.

mixtures and in all cases the same spectrum was obtained with excellent reproducibility.

3.6 POWER OSCILLATOR ;- Optical Design

The PO cavity was designed as a confocal unstable resonator, formed by a concave high-reflector rear mirror and a zero-power convex/concave quartz meniscus as the output coupler (Fig. 3.8).

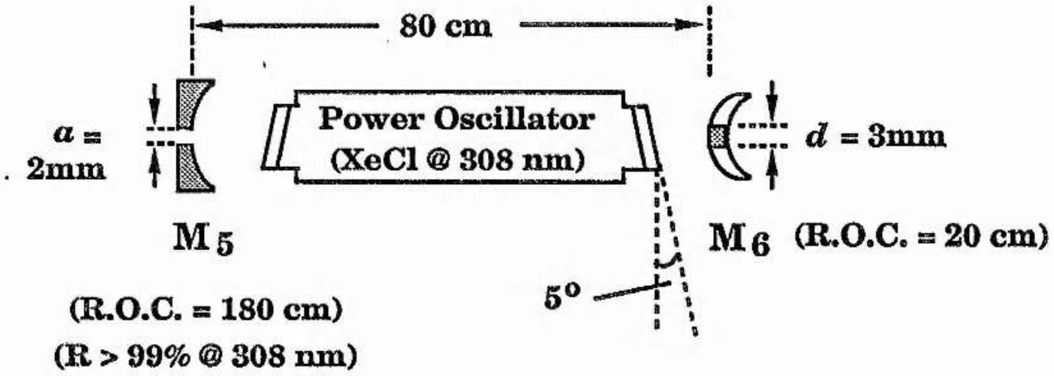

Fig. 3.8. Schematic of the power oscillator cavity configuration (side view).

A positive-branch unstable cavity configuration was favoured to avoid an intracavity focus and possible optical breakdown within the PO cavity. The rear mirror M_5 had a reflectivity $R > 99\%$ at 308nm, with a circular hole at the centre, to allow entrance of the injection signal into the PO cavity. The meniscus output coupler M_6 was antireflection-coated on both surfaces for 308nm, and a high-reflector ($R > 99\%$ at 308nm) spot was located at the centre of the convex face to form the unstable resonator output mirror. The output from the unstable resonator was, thus, "diffraction-coupled", with the emerging output beam exhibiting a hole at the centre, resulting from the high-reflector spot. An important consideration in the design of the PO cavity was the choice of resonator magnification M, since this parameter determines the amount of feedback and/or output coupling from the PO. In order to allow rapid build-up of the resonator mode during the short duration of optical gain, it was desirable to use a resonator of high geometrical magnification. However, it was equally important that the value of M be small enough to provide sufficient feedback to maintain laser oscillation in the PO. After an extensive study of the available literature [21]-[27], a value of $M \sim 10$ was favoured. Further, it was considered advantageous to design the PO cavity as a confocal unstable resonator to yield a collimated output beam with minimum angular divergence. Therefore, the mirror curvatures were chosen so as to form an unstable resonator with a geometrical magnification $M \sim 10$, while maintaining confocal condition over the shortest cavity length practically possible, determined by the physical length of the laser assembly (75cm). The concave mirror had a radius of curvature $R_5 = 180$ cm and the meniscus output coupler had a curvature radius $R_6 = 20$ cm, yielding a geometrical magnification for the PO cavity of

$$M = \frac{|R_5|}{|R_6|} = 9 \tag{3-8}$$

which is close to the design figure of $M \sim 10$. This magnification resulted in a geometrical output coupling

$$\Gamma = 1 - \frac{1}{M^2} \sim 98\% \tag{3-9}$$

corresponding to a feedback of only ~ 2%. This relatively small feedback was, however, considered adequate in maintaining laser oscillation well above the threshold level, given the high-gain nature of the excimer medium. In order to obtain a confocal resonator, the two mirrors had to be separated by a distance L, where

$$L = \frac{1}{2}\,(\mathrm{R}_5 - \mathrm{R}_6) = 80 \text{ cm}, \tag{3-10}$$

which is just sufficient to accommodate the laser assembly. The meniscus output coupler was 2" in diameter, with a high-reflector spot deposited at the centre of the convex face. The diameter d of the spot was calculated according to

$$d \sim \frac{D}{M} \tag{3-11}$$

where D is the larger discharge dimension. With $D = 25$ mm, we obtain a high-reflector spot diameter $d \sim 2.8$ mm. Therefore, a high-reflector spot, 3mm in diameter, was coated at the centre of the meniscus on the convex surface. In choosing a suitable meniscus for the PO cavity, particular attention was paid to the optical damage threshold of the coating material for the high-reflector spot. This was considered to be important, since the injection beam from the MO would be directly incident on this spot, and could lead to optical damage of the component over long periods of irradiation. Possible back-reflections from the OPO mirrors or other optical components could also result in optical damage to this high-reflector spot. The rear PO concave mirror was also 2" in diameter to provide feedback over the useful discharge aperture (measuring 1 x 2.5 cm in cross-section). A hole was drilled through the centre of the mirror to facilitate injection into the PO. The diameter of this hole should, ideally, be large enough (≥ 3mm, say) to produce a 3mm-diameter Gaussian beam waist at the high-reflector spot on the PO output meniscus. However, the hole size should, at the same time, be small enough to keep the cavity losses (due to the hole itself) low. Therefore, we chose a hole diameter of 2mm, with a corresponding cavity loss of only 1.2%, much below the geometric output coupling of 98%, from the PO cavity. However, small deviations from this hole size were not considered to be too critical in affecting the efficiency of injection-seeding, except in the case where very low MO powers are involved. The windows on the PO laser chamber were 3" in diameter so as not to restrict the available discharge aperture, and 10mm thick to withstand differential pressures of a few atmospheres. In order to avoid competing cavity effects, the windows were tilted with their normal at 5° to the laser axis. The window surfaces were also wedged by ≤ 10 seconds of arc. All window materials and mirror substrates were made of fused silica (Suprasil, optical 4000, $\lambda/10$ both surfaces).

3.7 INJECTION-SEEDING

As pointed out earlier, in order to achieve efficient injection-seeding, it is important to provide a time-delay between the initiation of laser oscillation in the PO and that in the MO. Since the two lasers shared a common spark gap switch and trigger circuit, the required time-delay could not be obtained by preferential triggering of the MO before the PO, and alternative options had to be explored. Several other methods have been regularly used in achieving this time-delay. These include changing the gas pressure or composition, altering the electrode separation, or modifying the various circuit inductances. Of these, the latter is the most difficult to implement, as it involves extensive alteration to the electrical or mechanical design of the laser assembly. Thus, this option was dismissed in favour of the first two. For this reason, the MO was designed with an adjustable electrode gap to provide a variable time-delay. As an initial step, it was necessary to gain an insight into the temporal behaviour of the two laser pulses. In order to do this, the optical pulses from the MO and

PO were directed onto two separate photodiodes (BPX 65/UV) and monitored on two channels of a 275 MHz analog storage oscilloscope (Hewlett-Packard 1727A). A schematic of the experimental set-up is shown in Fig. 3.9. The output beams from the two lasers were attenuated by means of uncoated quartz flats and neutral-density UV filters to prevent saturation of the photodiodes, and thus produce a true picture of the optical pulse shapes and durations on the oscilloscope. Further, in order to ensure accurate measurements of the time-delay between the two laser pulses, the photodiodes were located at exactly equal distances from the output mirrors of the MO and PO, and equal lengths of BNC cable were used to connect the two detectors to the oscilloscope. The cables were also wound around ferrite cores, located immediately before the connection points to the oscilloscope, so as to reduce the effects of EMI noise radiated from the cables. The oscilloscope itself was placed inside an earthed screening metal box and was connected to the mains, via HF mains filters and earth-line choke filters, to prevent radiative as well as electrical interference from the various noise sources. These provisions were found to be very useful in significantly reducing the level of EMI interference, and greatly improving the ease and accuracy with which the time-delay measurements could be performed. Since, it was considered desirable for the initial rise of gain in the PO to coincide with the cavity-filling pass of the trailing edge of the MO injection pulse, it was important to monitor the MO pulse duration and, from considerations of the cavity lengths and the distance between the two lasers in the final injection-seeding arrangement (~ 4' between M_2 and M_5 in Fig. 3.10), to determine the appropriate time-delay. With a laser gas mixture of HCl/He:Xe:Ne (50:30:1950 mbar) at 2 atmospheres of pressure, the MO pulses were found to have a Gaussian-like profile, with a duration of ~20 ns, and were consistently reproducible. Observations of the PO pulses, on the other hand, revealed pulse lengths of

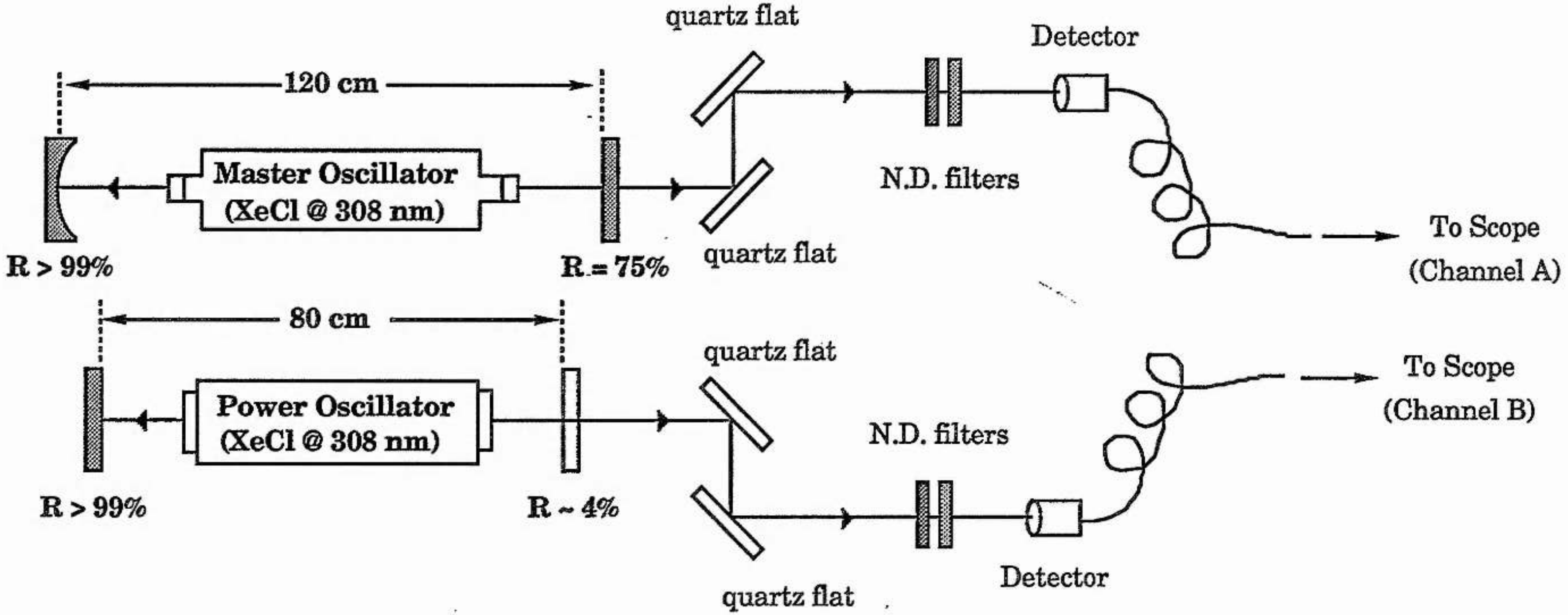

Fig. 3.9. Schematic of the experimental configuration for measurements of time-delay between the master oscillator and power oscillator optical pulses. (top view).

the order of ~10-15 ns, with a gas mix composed of HCl/He:Xe:Ne (20:30:1970 mbar) at 2 atmospheres of pressure, and with a similar quasi-Gaussian pulse shape. These observations, together with the geometrical considerations, indicated that a peak separation τ of 15-20 ns between the MO and PO pulses would constitute an appropriate time-delay. However, simultaneous observation of the two laser pulses revealed that the PO pulses consistently occurred prior to the MO pulses by approximately 5-10 ns. This was attributed to possible minor variations in the inductance of the two discharge circuits, the difference in gas composition, as well as the different build-up time for the two resonators. This time-delay was also observed to be strongly dependent on the gas pressure and composition. For example, a two-fold reduction in the total gas pressure in the MO (from 2 to 1 atmosphere) resulted in a decrease in the time-delay by a factor of ~1/2. However, in order to maintain maximum injection power, it was decided to operate the MO at a total gas pressure of 2 atmosphere, with the optimum gas mixture HCl/He:Xe:Ne (50:30:1950 mbar), and obtain the required time-delay by reducing the electrode separation in the MO chamber. This was achieved by simply inserting additional metal spacers between the cathode electrode and the laser bottom plate in the MO cavity (Fig. 3.3), while maintaining a fixed gap in the PO. The required time-delay (τ ~15 ns) between the two laser pulses was observed to occur when the electrode separation in the MO was reduced from 25 mm to 17mm, with the corresponding electrode gap in the PO fixed at 25 mm. We investigated the variations in the time-delay over several hundred shots and observed excellent shot-to-shot reproducibility, with little or no jitter in τ, and no significant variation in the pulse profiles.

Having achieved the required time-delay between the MO and PO, the two lasers were placed, in series, at the pre-determined distance corresponding to τ ~15ns. Fig. 3.10 shows a schematic of the injection-seeding configuration.

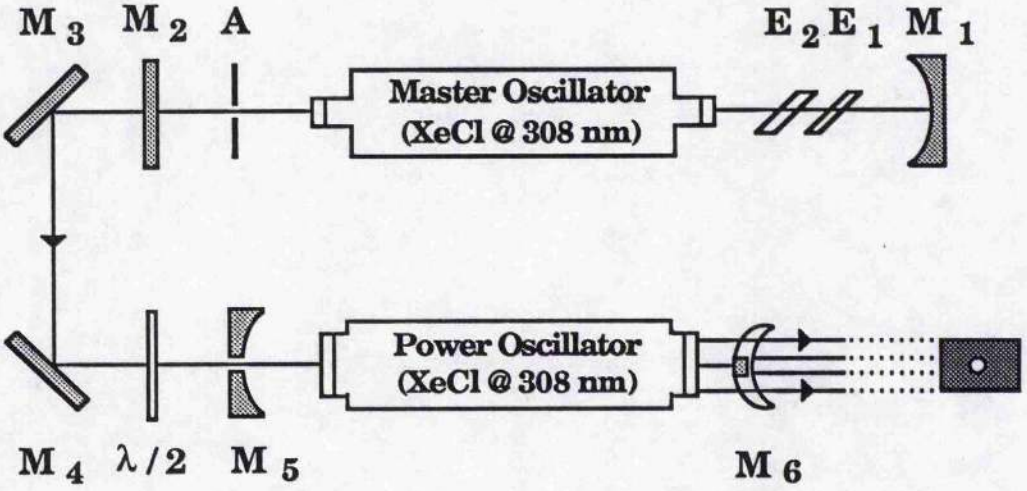

Fig. 3.10. Schematic of the injection-seeding arrangement (top view);
E_1: 70 µm thick solid etalon (F.S.R. = 48 cm^{-1}, finesse = 25),
E_2: 500 µm thick solid etalon (F.S.R. = 6.7 cm^{-1}, finesse = 25).

The injection signal from the MO was directed into the PO cavity by means of two beam-steering mirrors (M_3 and M_4), with reflectivities $R > 99\%$ at 308nm/45° (*s*-polarisation). A He-Ne laser was used for alignment purposes. A half-wave plate was inserted between the MO and PO cavities to facilitate rotation of the plane of polarisation of the injection-signal, and hence of the output pump beam from the PO. This was considered useful in providing some degree of flexibility in the choice of more favourable phase-matching geometries in the OPO experiments. The output beam emerging from the injection-seeded laser was found to have a rectangular cross-section with dimensions 10 x 25 mm (width x height), with a 3mm-hole at the centre due to the high-reflector spot on the PO output mirror. A pyroelectric energy meter (scientech 362) was utilised for measurements of output pulse energy. With the optimum gas mixtures in each laser, and at a pressure of 2 atmosphere, typical pulse energies of the order of 25 to 30 mJ were measured for a working input voltage of around 18 to 22 kV. The output beam divergence was determined by propagating the beam over several meters and recording the burn patterns on thermal paper, at different distances from the laser output mirror. The beam divergence was optimised by fine-adjustment of the PO cavity length, and a minimum divergence half-angle of 30μR was measured near the confocal condition ($L \sim 80$ cm). This figure was found to be about 3 times the diffraction half-angle $\alpha = \lambda / D$ which, for a discharge of dimension $D = 25$mm, is around 12μR. In order to examine the effectiveness of injection-seeding, the spectral linewidth of the output beam was determined in the absence and presence of the injection-signal. Two sets of experiments were performed. In the first set, a "stop" was inserted between the MO and PO cavities to prevent entrance of the injection-beam into the PO cavity. The output beam from the PO was then focused onto the entrance slit of a high-resolution monochromator and displayed on a chart-recorder. Fig. 3.11(a) shows the obtained spectrum, clearly identical to the broad-band spectrum obtained with the free-running MO (Fig. 3.5). In the second set of experiments, the "stop" was removed to allow injection-seeding of the PO to occur. The spectrum in this case was observed to collapse to a single peak (Fig. 3.11(b)), clearly indicating the effectiveness of this technique. Measurements of the sub-angstrom bandwidth of the output beam was, however, found to be limited by the resolution of the monochromator. Therefore, a 5mm thick solid etalon (F.S.R.= 0.66 cm^{-1}, finesse = 25) was utilised for more accurate measurements of the linewidth. In this case, a negative lens was used to diverge the output beam from the PO, before it was incident on the etalon. A screen was used beyond the etalon for observation of the fringes. With this set-up, we were able to obtain sharp fringes on the screen with a finesse ~3. These observations implied that the linewidth

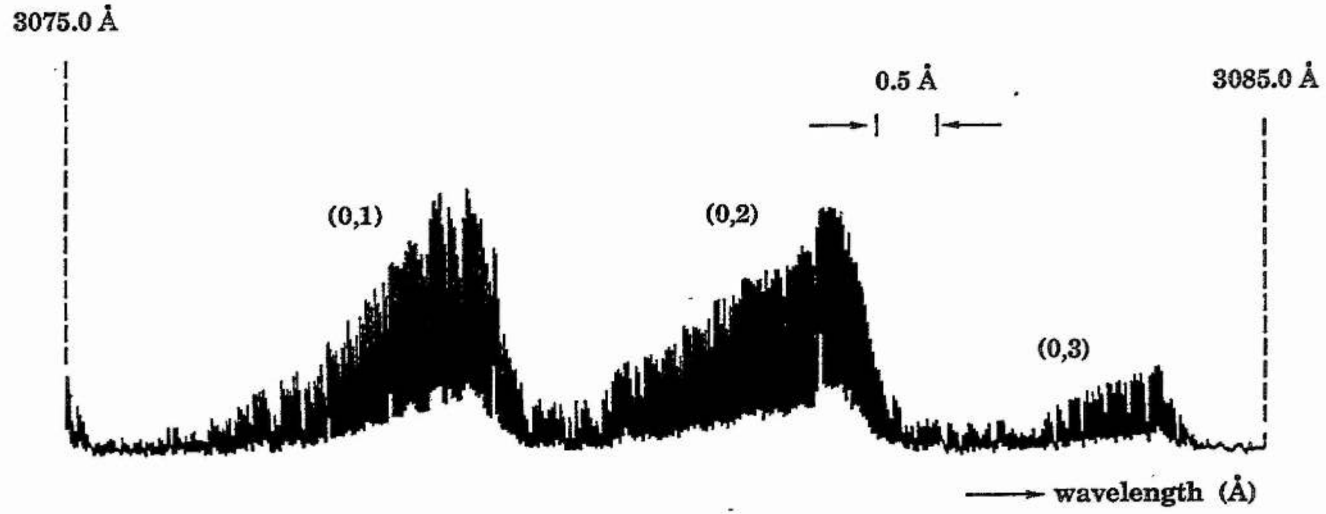

Fig. 3.11(a). Spectrum of the unseeded XeCl power oscillator.

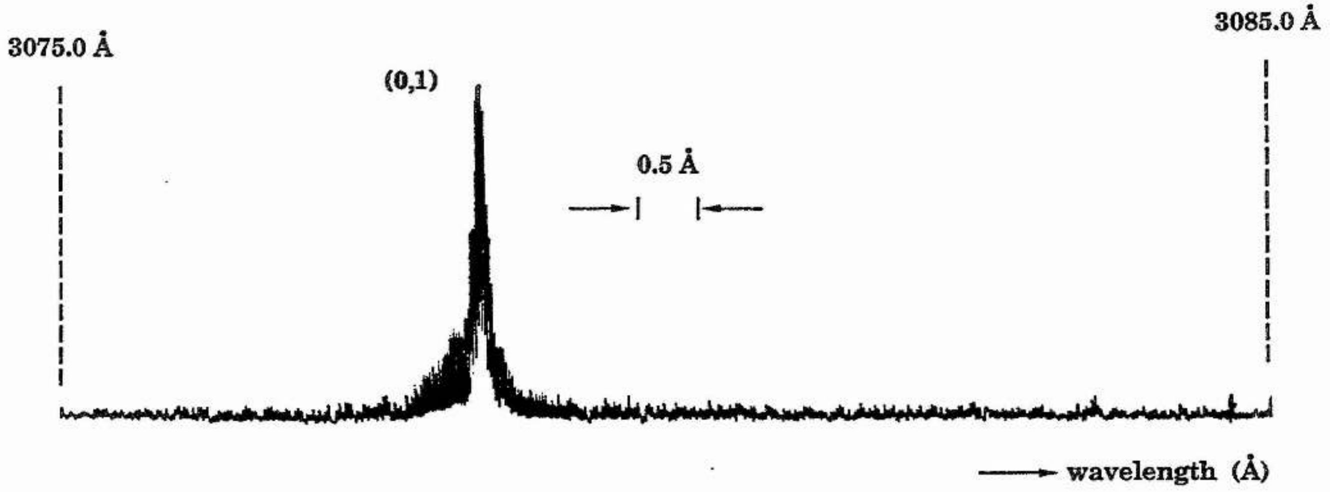

Fig. 3.11(b). Spectrum of the injection-seeded XeCl power oscillator.

was no more than ~ 0.2 cm^{-1} (consistent with the value expected from the F.S.R. and finesse of the 500μm etalon), and thus safely below the required pump linewidth for successful OPO operation. They also indicated the effectiveness of the intracavity etalons in line-narrowing, despite the small number of round-trips of the 120cm MO cavity (~1-2) available over the short duration of the laser pulses. The linear polarisation of the output beam was also measured by recording the output energy in the two orthogonal states, using a Glan-Foucault prism. The result of these measurements indicated a linear polarisation better than 95%, and in the same orientation as that of the injection signal. All these observations indicated the success of the injection-seeding technique in providing a pump beam of required spatial and spectral coherence as well as sufficiently high intensity to achieve successful operation of urea and β-BaB_2O_4 OPO's.

It is, however, important to note that although, in injection-seeding the PO, we were able to exploit the full potential of the technique in obtaining the narrowest possible output linewidth (for the given etalons), we were not able to achieve the minimum beam divergence (i.e. the diffraction-limit) attainable with such a technique. This may be attributed to the departure, by the injection beam, from a Gaussian spatial profile, to a multimode profile, due to the incorporation of a larger aperture within the MO than that necessary for a TEM_{00} beam size. It may also be due to the small departure of the injection signal from a plane phasefront to a spherical phasefront (of R.O.C. ~ 2.5 m) over the 3mm-diameter high-reflector spot, on the output meniscus of the PO. It should, therefore, be possible to improve the output beam divergence by spatial filtering the injection signal (after emergence from the MO, and before entrance into the PO) to obtain a TEM_{00} beam, or by spatial mode-matching of the two resonators to yield a plane phasefront at the output mirror of the unstable PO cavity. As such, these may well be the areas where further improvements may be effected.

3.8 THE XeCl EXCIMER LASER ;– Mechanical Design

The major considerations in the mechanical design of the XeCl laser assembly included simplicity, reliability, compactness, and a degree of flexibility for future modifications. The laser chamber itself was of a simple box-type design, with the laser cavity sandwiched between top and bottom plates (Photograph 3.3). The choice of material for the laser body was set primarily by its suitability to operate in a high-voltage, high-pressure environment, in the presence of UV radiation, and under constant exposure to toxic HCl. We selected polyvinylidene fluoride (PVDF), because of the excellent chemical, physical, and mechanical properties of this material, as well as its easy machineability. A series of blind holes were tapped on the side walls of the laser head to accommodate studs, and thus enable attachment to the laser top and bottom plates (Photograph 3.4). The exact geometry of the laser body, together with a specification of various dimensions is shown in Fig. 3.12. The laser top and bottom plates (Photographs 3.5 and 3.6) were made of stainless steel to avoid corrosion due to the presence of HCl. For the same reason, the material for the O-rings was chosen to be Viton. Schematic drawings of the top and bottom laser plates are illustrated in Figs. 3.13 and 3.14, respectively. A series of blind holes were tapped on the sides of the top plate to provide side terminals for connections to the peaking capacitors c_2. The discharge electrodes were mounted directly onto the top and bottom

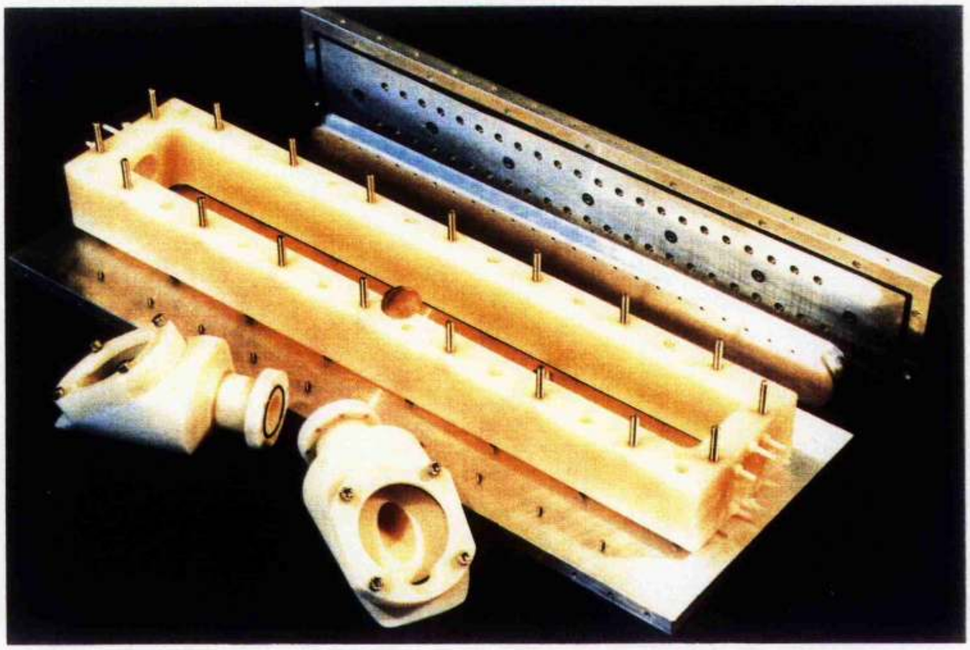

Photograph 3.3. The XeCl laser chamber configuration.

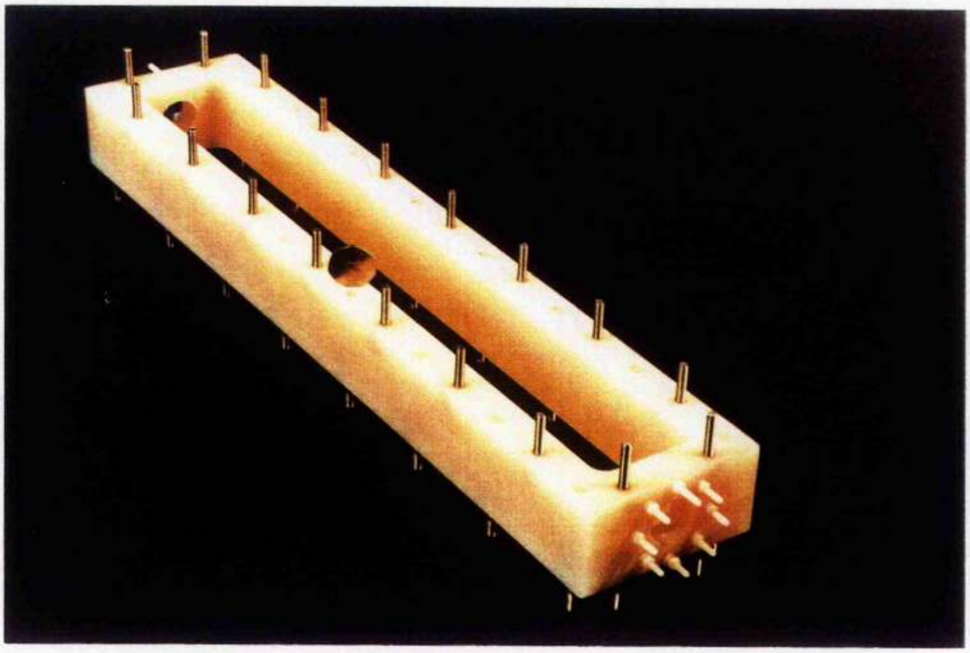

Photograph 3.4. Structure of the XeCl laser body.

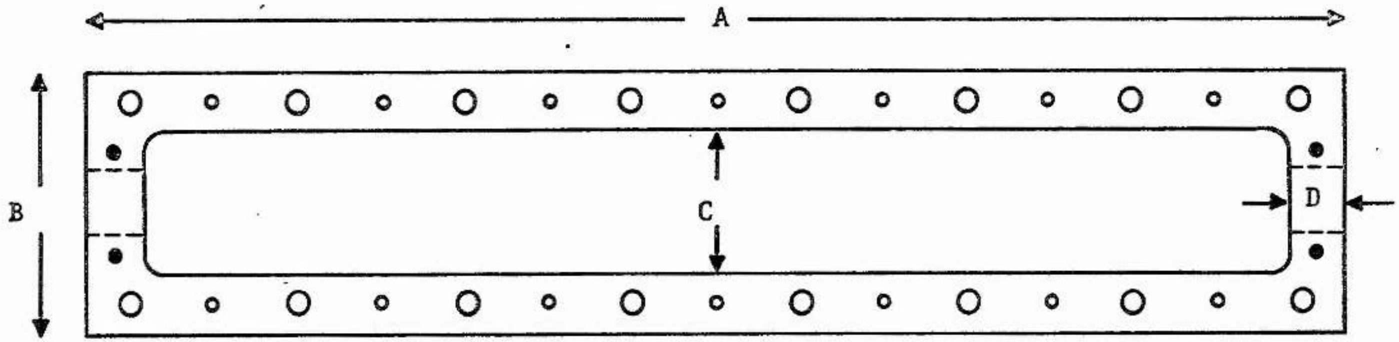

Fig. 3.12

Top view of the laser body.

A=600mm, B=122mm, C=70mm, D=26mm.

○ 6mm tapped hole, 20mm deep, counterbored ø=10mm.
◯ 10mm blind hole, 40mm deep, countertapped ø=6mm.
● 6mm blind hole, 20mm deep.

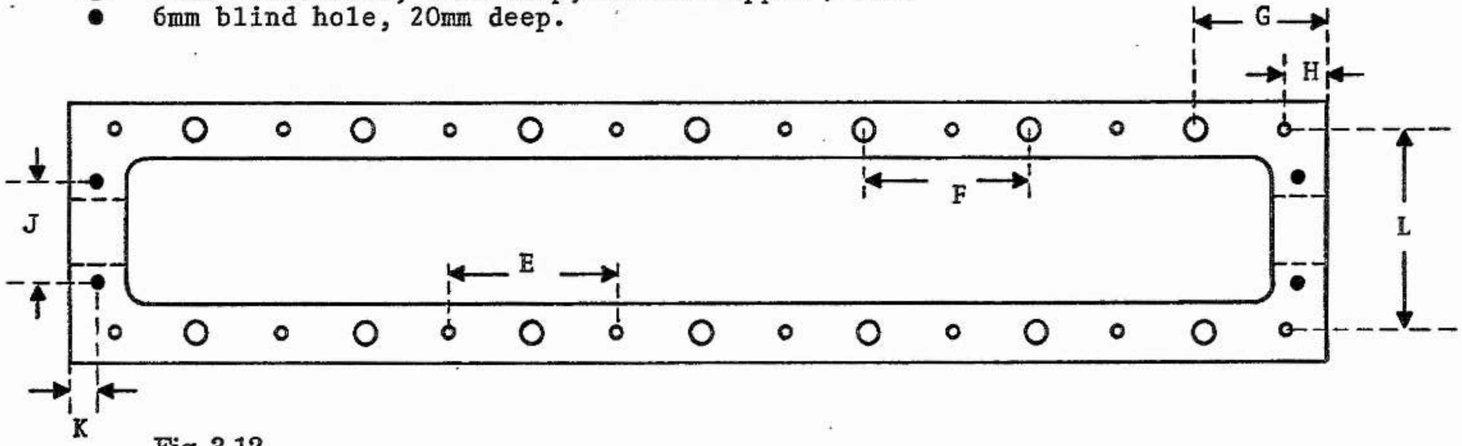

Fig. 3.12

Bottom view of the laser body.

E=80mm, F=80mm, G=60mm,
H=20mm, J=60mm, K=10mm,
L=101mm.

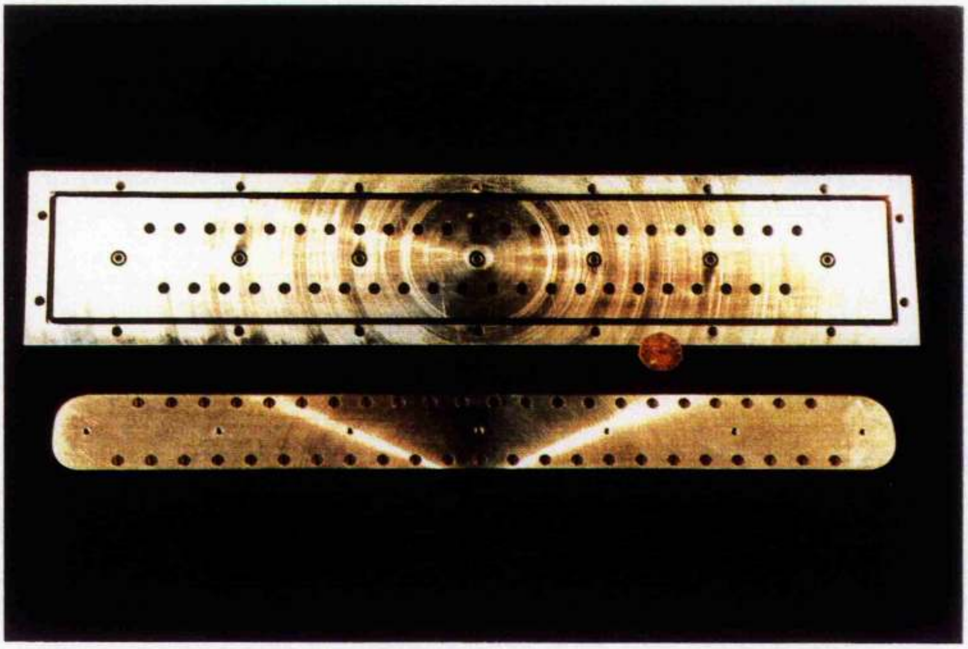

Photograph 3.5. Laser top plate and the anode electrode.

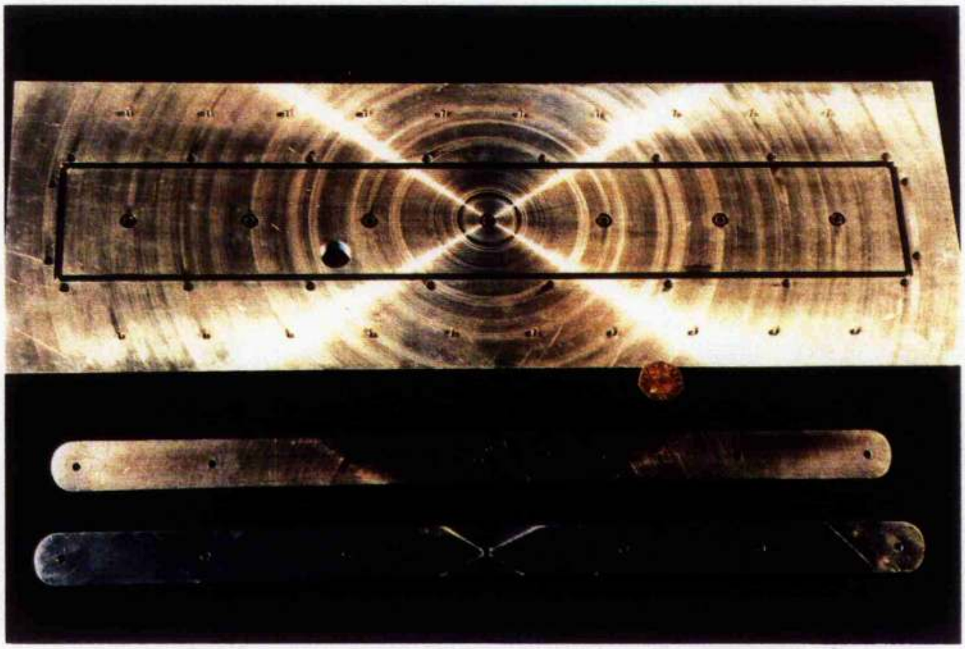

Photograph 3.6. Laser bottom plate and cathode electrodes.

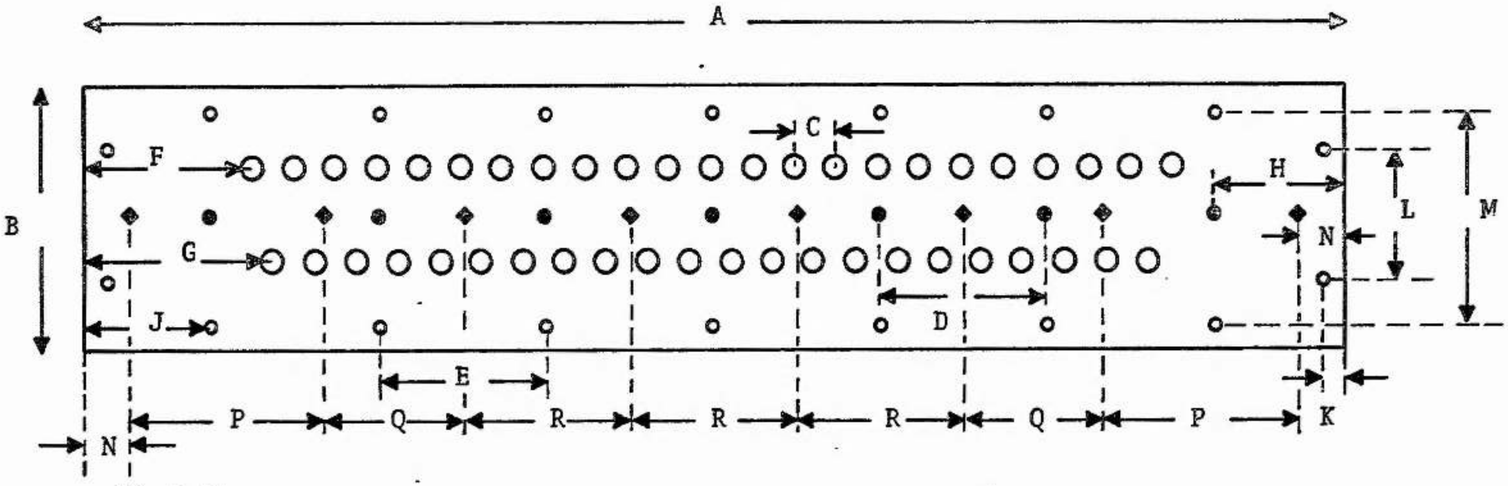

Fig. 3.13

Top view of the laser top plate.

- ○ 6mm clearance holes.
- ● 5mm clearance holes.
- ◆ 5mm blind tapped holes, 8mm deep.
- ○ 12.6mm (O.D.) tapped holes, 10mm deep (approx.), counterbored ø=6.4 — for exact details see Fig.

A=600mm, B=122mm, C=20mm, D=80mm,
E=80mm, F=80mm, G=90mm, H=60mm,
J=60mm, K=10mm, L=60mm, M=101mm,
N=20mm, P=93mm, Q=67mm, R=80mm.

Fig. 3.13

Side view of the laser top plate.
4mm blind tapped holes, 6mm deep.

S=40mm, T=15mm, W=40mm=S.

Fig. 3.14

Top view of the bottom plate of the laser.

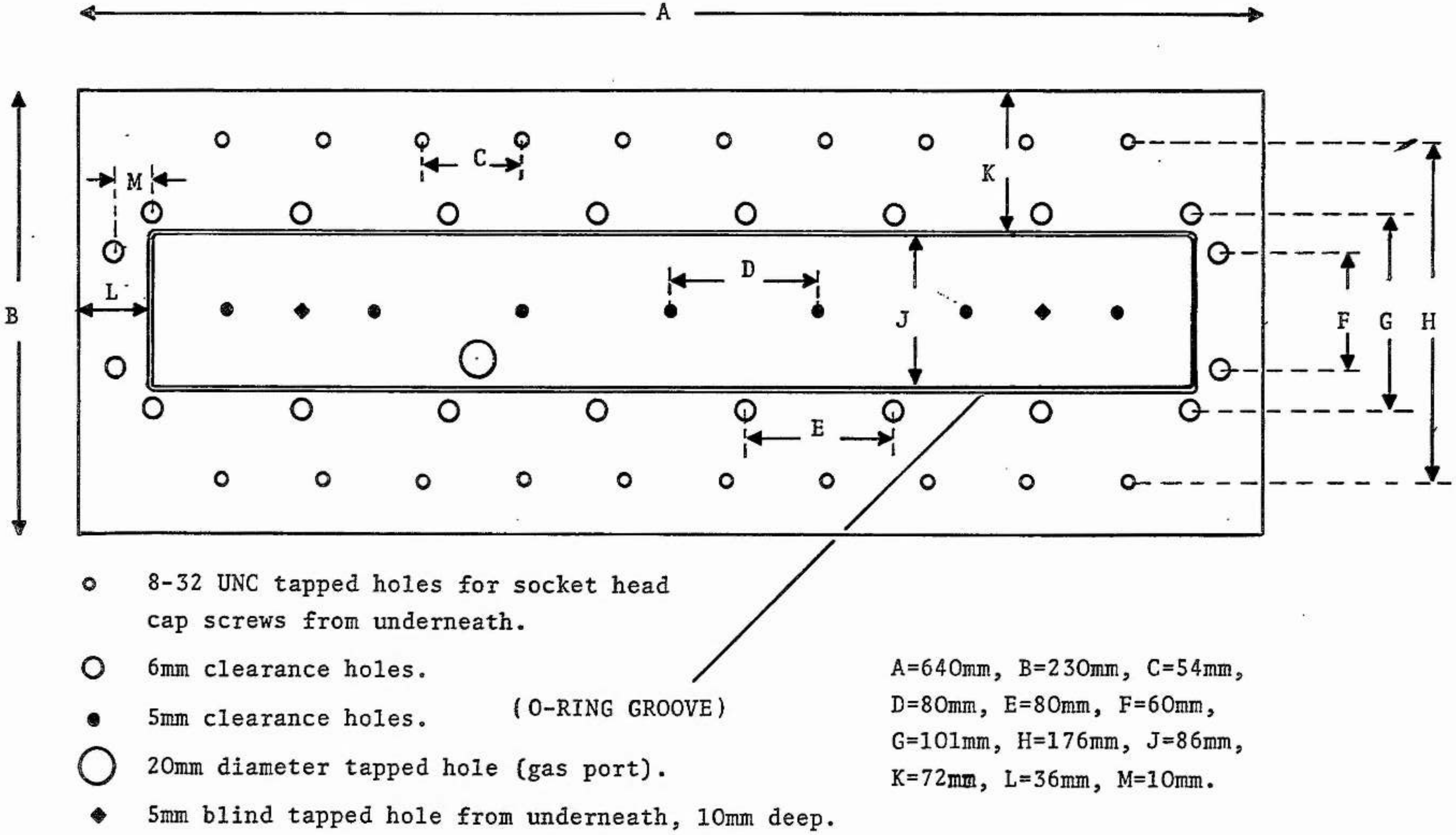

- ○ 8-32 UNC tapped holes for socket head cap screws from underneath.
- ◯ 6mm clearance holes.
- ● 5mm clearance holes.
- ◯ 20mm diameter tapped hole (gas port).
- ◆ 5mm blind tapped hole from underneath, 10mm deep.

A=640mm, B=230mm, C=54mm,
D=80mm, E=80mm, F=60mm,
G=101mm, H=176mm, J=86mm,
K=72mm, L=36mm, M=10mm.

plates. The anode electrode was made of aluminium, with a series of clearance holes in two rows on either side, to accommodate preionisation pins, as can be seen from Photograph 3.7. The exact dimensions of the anode electrode are shown in Fig. 3.15. Although, aluminium is not an ideal metal for maintaining gas purity, its use as the electrode material does not pose any serious difficulties due to the formation of a relatively passive chloride layer on its surface after the initial exposure to the halogen donor gas. A total of 4 different cathode electrode profiles were examined to achieve the best discharge quality (Fig. 3.16). Of these, the best results were obtained with a "pure radius" stainless steel electrode (4th electrode in Fig. 3.16). The laser chamber and electrodes, when fully assembled, defined a total discharge volume of approximately 500 x 10 x 25 mm^3 (length x width x height) in the case of PO, and 500 x 10 x 18 mm^3 in the case of MO. The preionising pins were made of solid ground tungsten rods (diameter = 1.5mm) encapsulated in quartz capillary tubing to provide insulation (Photograph 3.8). Tungsten was chosen as the spark pin material for its physical hardness and its resistance to corrosion. The pins were located inside threaded plastic casings and then screwed onto the laser top plate, and thus the anode electrode. The structure of the preionising pin geometry and the relevant dimensions are shown in Fig. 3.17. The window mounts on the MO and PO chambers were also manufactured of PVDF. They were bolted on the laser head by means of plastic screws and studs, and sealed with Viton O-rings. The windows on the MO chamber was of Brewster design (Photograph 3.9), while those on the PO were tilted at 85^{o} to the laser axis (Photograph 3.10). In order to maintain low circuit inductance, and thus efficient discharge pumping, the current paths were made as distributed as possible by using copper sheeting, in a strip-line configuration. We also used layers of melinex (or mylar) sheet (ICI, type 226, 250 μm thick), to provide electrical insulation

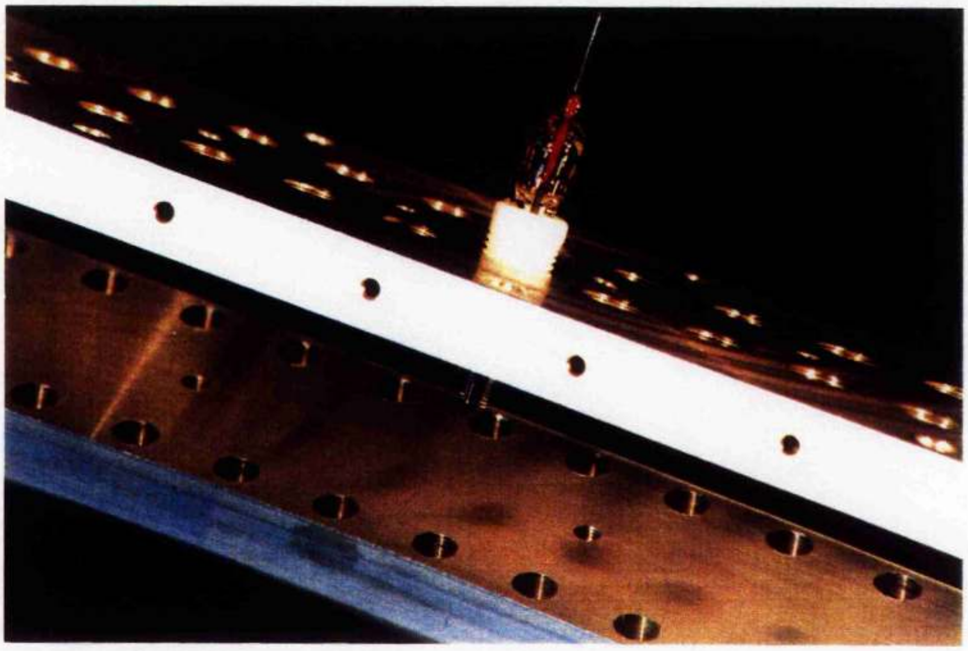

Photograph 3.7. The preionisation arrangement, showing the laser top plate, the preionising pin, and the anode electrode.

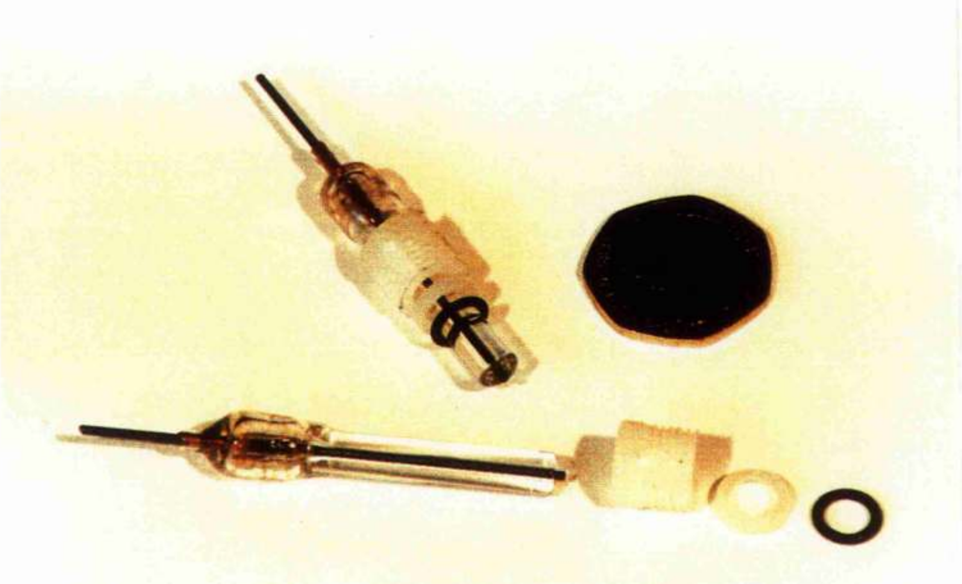

Photograph 3.8. Structure of the preionising pins.

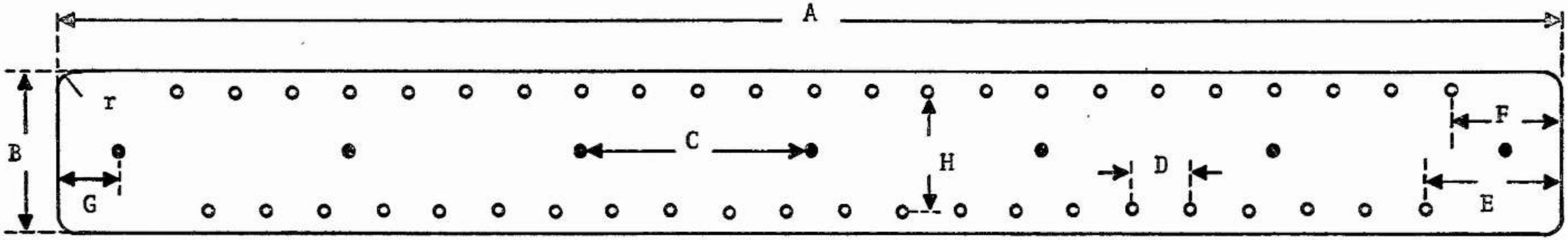

Fig. 3.15

Bottom view of the anode electrode.

- ○ 6.5mm clearance hole, 16mm deep, counterbored ϕ=3mm.
- ● 5mm tapped blind hole, 10mm deep.

A=520mm, B=54.2mm, C=80mm,
D=20mm, E=50mm, F=40mm,
G=20mm, H=42mm.

r: arbitrary

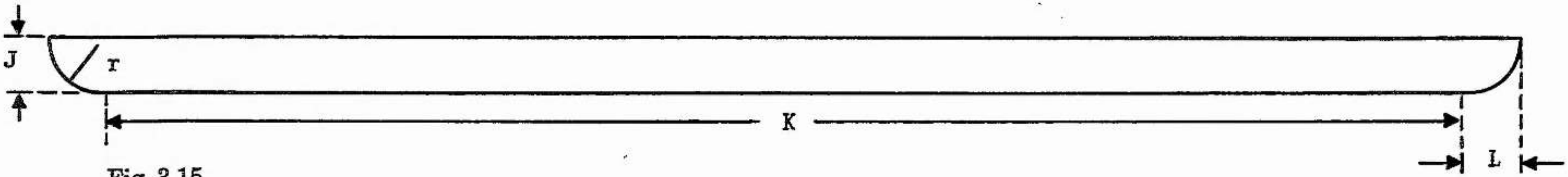

Fig. 3.15

Side view of the anode electrode.

J=18mm, K=470mm, L=25mm.

r: arbitrary

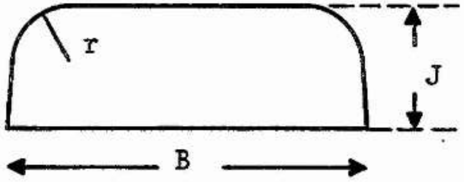

Fig. 3.15

End view of the anode electrode.

r=4mm (approx.)

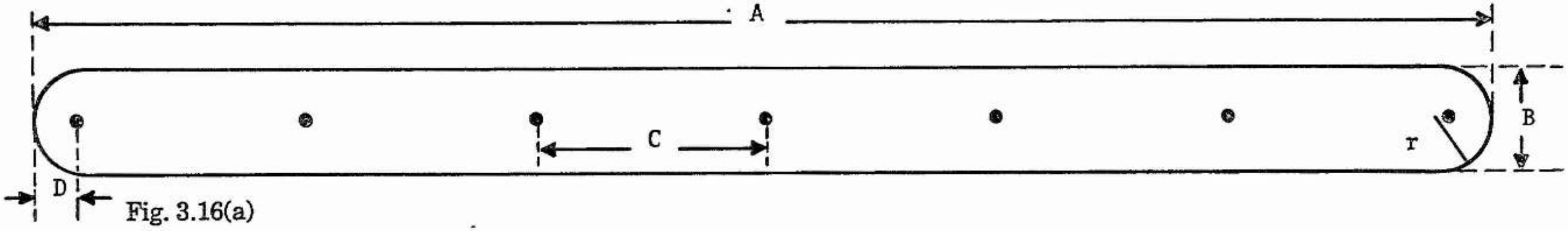

Fig. 3.16(a)

Schematic of the cathode electrode geometry
(Bottom view, 1st electrode).

● 5mm tapped blind hole, 10mm deep.

A=510mm, B=32mm,
C=80mm, D=15mm,
r=16mm (5/8") approx.

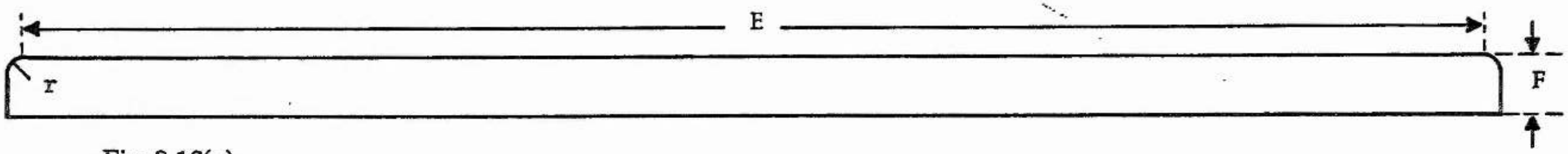

Fig. 3.16(a)

Schematic of the cathode electrode geometry
(Side view, 1st electrode).

E=500mm, F=18mm,
r: arbitrary.

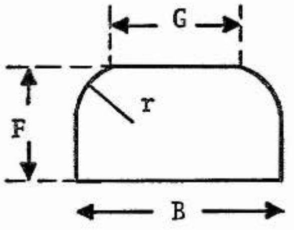

Fig. 3.16(a)
Schematic of the
cathode electrode geometry
(End view, 1st electrode).

r=6.35mm (1/4"),
G=24mm (approx.).

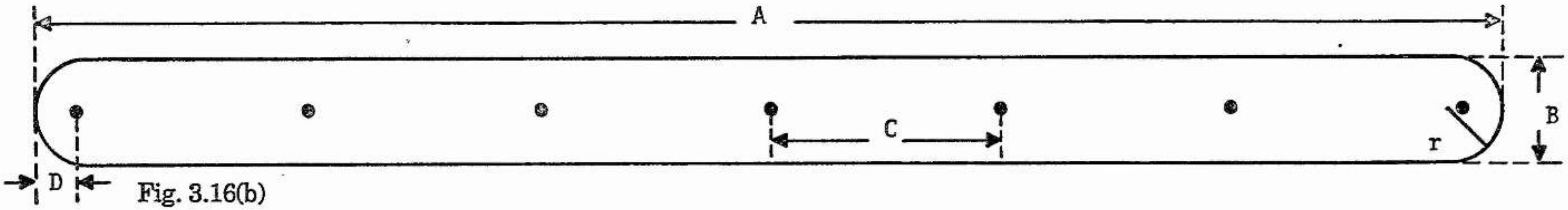

Fig. 3.16(b)

Schematic of the **cathode** electrode geometry
(<u>Bottom view</u>, 2nd and 3rd electrodes).

● 5mm tapped blind hole, 10mm deep.

A=510mm, B=32mm,
C=80mm, D=15mm,
r=16mm (5/8") approx.

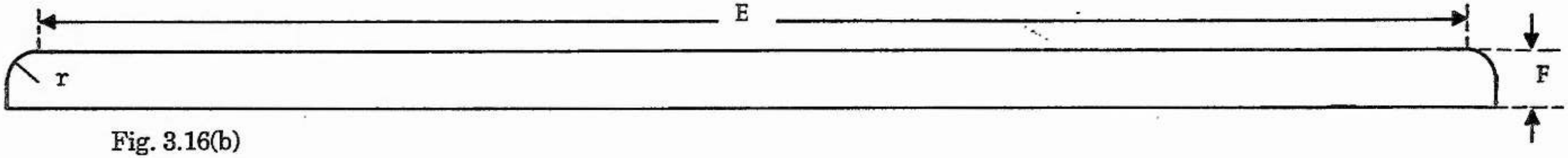

Fig. 3.16(b)

Schematic of the **cathode** electrode geometry
(<u>Side view</u>, 2nd and 3rd electrodes).

E=490mm, F=18mm,
r: arbitrary.

Fig. 3.16(b)
<u>End view,</u>
2nd electrode.

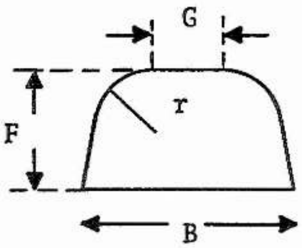

r=16mm (approx.),
G=10mm (approx.).

Fig. 3.16(b)
<u>End view,</u>
3rd electrode.

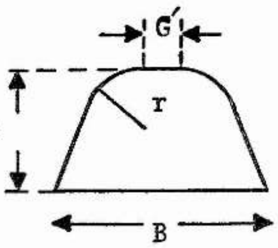

r=16mm,
G'=5mm (approx.).

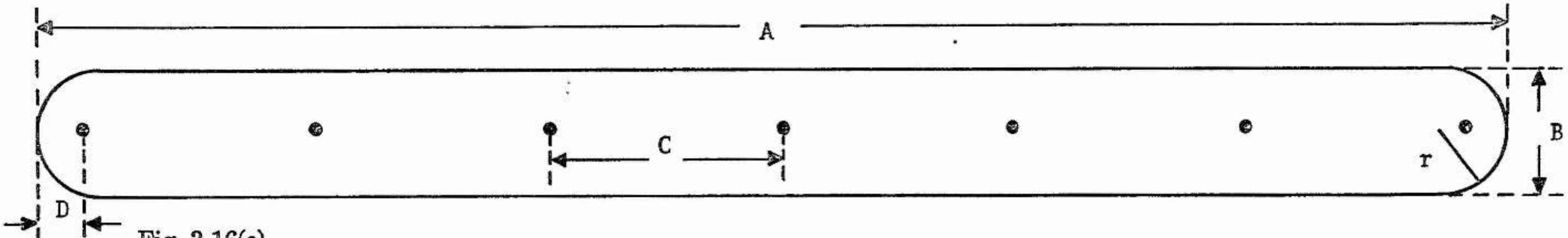

Fig. 3.16(c)

Schematic of the cathode electrode geometry (Bottom view, 4th electrode).

- ● 5mm tapped blind hole, 10mm deep.

A=510mm, B=38mm,
C=80mm, D=15mm,
r: arbitrary.

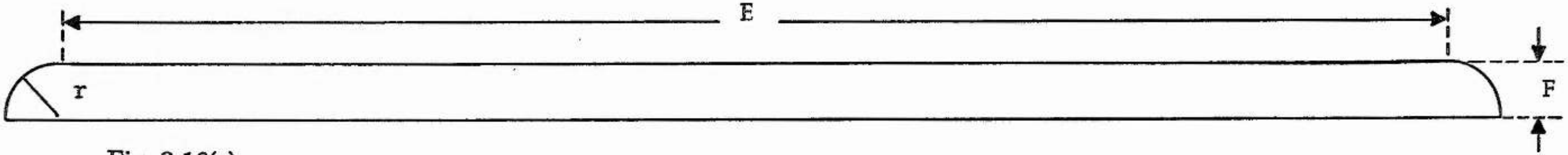

Fig. 3.16(c)

Schematic of the cathode electrode geometry (Side view, 4th electrode).

E=500mm, F=18mm,
r: arbitrary.

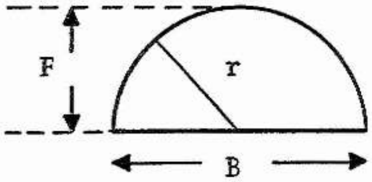

Fig. 3.16(c)

Schematic of the cathode electrode geometry (End view, 4th electrode).

r=19mm (3/4")

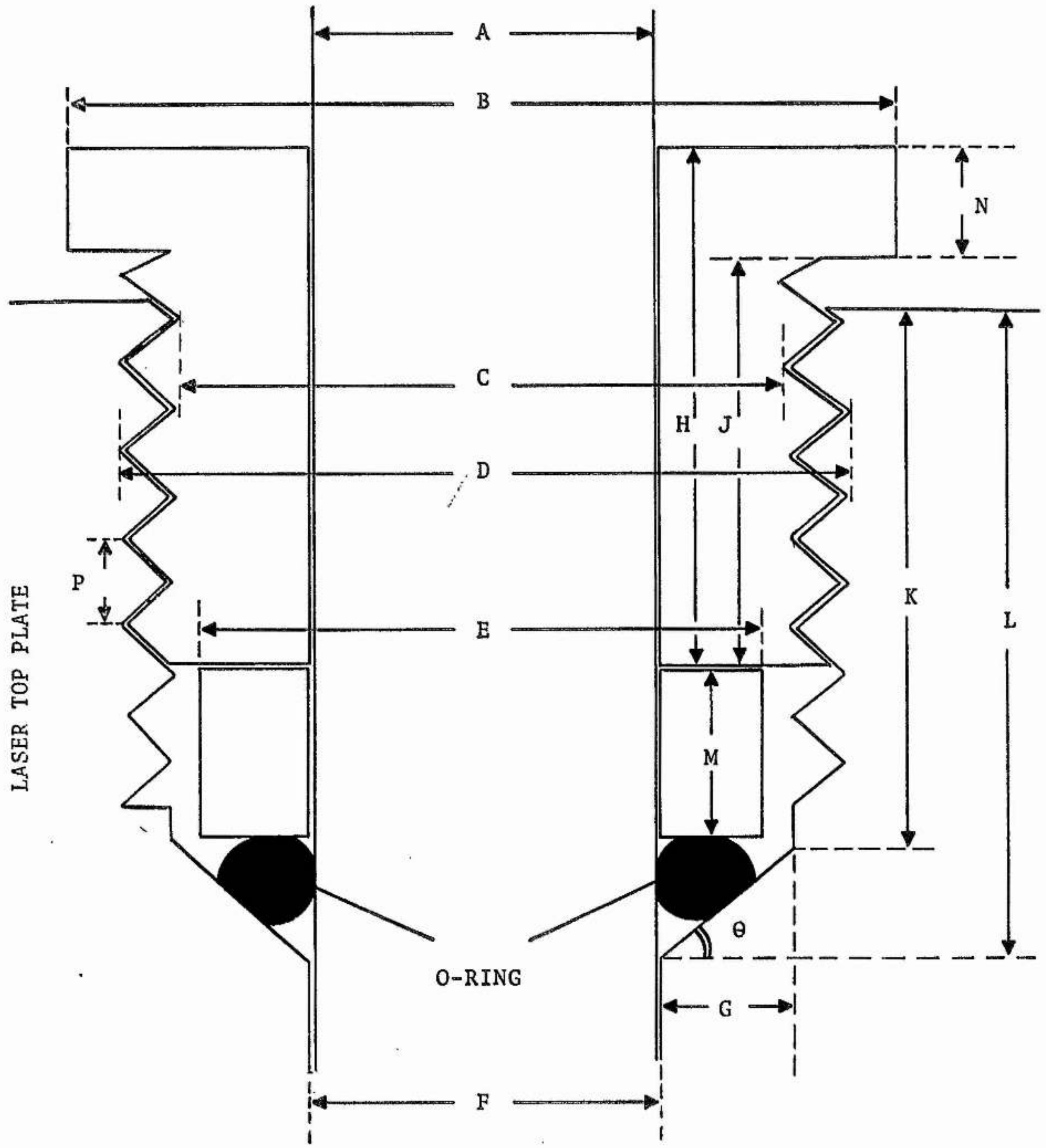

Fig. 3.17

Schematic diagram showing the structure of preionising pin arrangement.

A=6.25, B=14.8, C=11.10, D=12.6, E=10.0, F=6.4, G=2.3, H=9.5, J=7.5, K=9.7, L=12.0, M=3.0, N=2.0, P=1.588, Θ=45°.

(All Dimensions in mm)

Photograph 3.9. Window mounts for master oscillator laser chamber (at Brewster's angle).

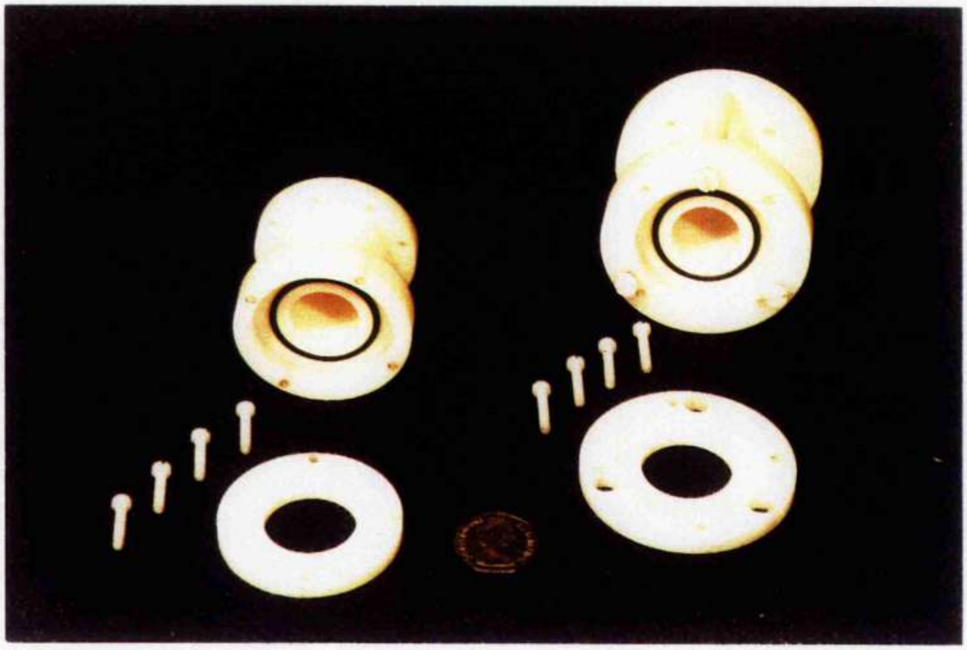

Photograph 3.10. Window mounts for power oscillator laser chamber (with normal at 5° to the laser axis).

between the various high- and low-voltage components, throughout the laser assembly. As a final step, before operation of the laser could begin, the two cavities were successfully tested for any possible leaks, under both vacuum and high pressure of up to 5 atmospheres, safely above the working pressure of 2 atmospheres.

3.4 THE XeCl EXCIMER LASER ; – Vacuum and Gas Handling System

Illustrated in Fig. 3.18, is the XeCl laser vacuum and gas handling system. The entire system employed stainless steel components, piping, and Viton O-rings, to prevent corrosion due to the presence of HCl. All the regulators on the gas cylinders, were also made of stainless steel. The piping was predominantly 1/4" O.D., with Swagelok couplings, although 1" piping was used between the laser heads and the rotary pump, to enable rapid pumping of the two chambers. Stainless steel bellows valves (Nupro, model M-4BK) were used throughout the system, except for the connection between the rotary pump and the laser heads, where a Speedivalve with Viton diaphragm (Edwards, SP 25K) was used. Clamping rings and co-seals were used to connect the various components. In order to monitor the gas pressure inside the laser chambers, two pressure gauges (Air Products, G-402-SS) were connected directly to the two cavities. A similar gauge was installed in the piping system for measurement of gas mixture ratios. In addition, a higher-sensitivity gauge (Leybold-Heraeus, Diavac K) was used for accurate delivery of low partial pressures of HCl and Xe. A Pirani Gauge head (PRM 10 KCR) together with a controller (Pirani, 503) were employed to monitor the vacuum level. The rotary pump (Edwards, two-stage, model EM25) was fitted with an inlet chemical trap (Edwards,

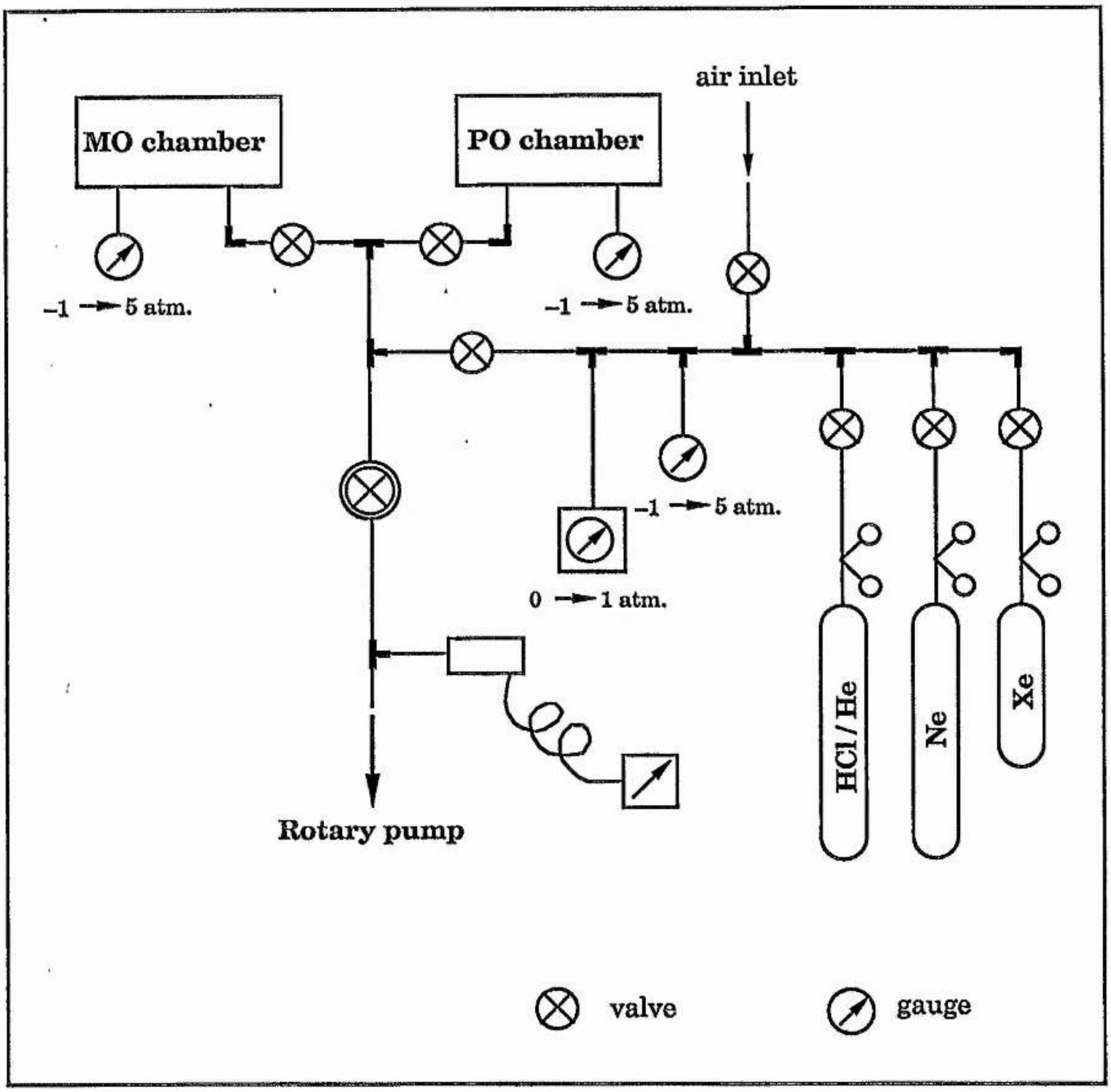

Fig. 3.18. Schematic of the XeCl laser gas handling and vacuum system.

model TC 20) and outlet mist (MF 20 HS/AE) and odour (OF 20) filters, as well as a magnetic isolation valve (PV 25 EK). Rubber isolators and flexible stainless steel bellows were used to minimise vibration noise during operation.

As a final conclusion to this chapter, we summarise the parameters of the injection-seeded narrowband XeCl excimer laser in table 3.I. The output pulse profile is also shown in Trace 3.2. The pulse is observed to be modulated in its structure at a period corresponding to the round-trip time in the PO cavity. In the next chapter, we shall discuss spontaneous parametric fluorescence and will present the results of experiments in urea crystal, using the described XeCl excimer laser as the pump source.

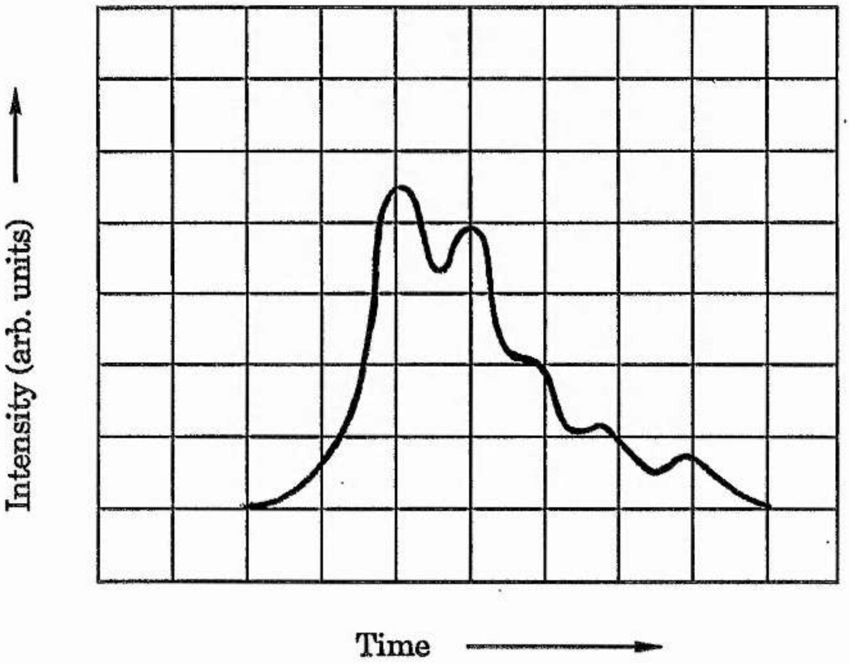

Trace 3.2. Waveform of the output pulse from the injection-seeded, narrowband XeCl excimer laser. Horizontal Scale: 5ns /div.

Table 3.I. Summary of the final performance parameters and operating characteristics of the injection-seeded XeCl excimer laser.

Pulse Energy	~ 30 mJ
Pulse Duration	~ 10 ns (FWHM)
Pulse Repetition Rate	1 Hz
Linewidth	~ 0.2 cm^{-1}
Divergence	~ 30 μR (half-angle)
Polarisation	> 95% (linear)
Output Beam Cross-section	10 x 25 mm (horizontal x vertical)
Discharge Dimension	50 x 10 x 17 mm (length x width x height) – MO 50 x 10 x 25 mm (length x width x height) – PO
Operating Voltage	~ 20 kV (typical)
Working Gas Pressure	2 atmospheres (MO and PO)
Gas Mixture	HCl/He:Xe:Ne = 50:30:1950 mbar (MO) HCl/He:Xe:Ne = 20:30:1970 mbar (PO)

References to Chapter 3.

[1] R. C. Sze and P. B. Scott, Rev. Sci. Instrum. 49, 772 (1978)

[2] Ch. A. Brau, in *Excimer Lasers, Topics in Applied Physics,* Ch. K. Rhodes, ed. (Springer-Verlag, Berlin, 1979), Chapter 4.

[3] R. Burnham *et al.*, Appl. Phys. Lett. 29, 30 (1976)

[4] T. S. Fahlen, IEEE J. Quantum Electron., QE-15, 311 (1979)

[5] A. J. Andrews *et al.*, Opt. Commun. 20, 265 (1977)

[6] T. J. McKee *et al.*, IEEE J. Quantum Electron., QE-15, 332 (1979)

[7] E. Armandillo *et al.*, Opt. Commun. 42, 63 (1982)

[8] A. J. Kearsely *et al.*, Opt. Commun. 31, 181 (1979)

[9] A. J. W. Brown, PhD thesis, St. andrews University (1988)

[10] W. R. Donaldson and C. L. Tang, Appl. Phys. Lett. 44, 25 (1984)

[11] M. J. Rosker and C. L. Tang, J. Opt. Soc. Amer. B. 2, 691 (1985)

[12] M. J. Rosker *et al.*, IEEE J. Quantum Electron., QE-21, 1600 (1985)

[13] K. Miyazaki *et al.*, Rev. Sci. Instrum. 56, 201 (1985)

[14] I. Park, private communication.

[15] Technical notes, *Questek Excimer Lasers* (1983)

[16] Hartley Measurements Limited, instruction manual, HV capacitor charging unit, model 411 series.

[17] A. E. Siegman, Proc. IEEE 53, 277 (1965); Appl. Opt. 13, 353 (1974);

[18] A. Yariv, "Optical Electronics," CBS College Publishing, New York, 3rd Ed., Chapter 4 (1985)

[19] T. J. McKee, Can. J. Phys. 63, 214 (1985)

[20] V. N. Ishchenko *et al.*, Opt. Commun. 21, 30 (1977)

[21] I. J. Bigio and M. Slatkine, IEEE J. Quantum Electron., QE-19, 1426 (1983)

[22] T. J. McKee *et al.*, J. Appl. Phys. 56, 2170 (1984)

[23] R. S. Hargrove *et al.*, IEEE J. Quantum Electron., QE-15, 1228 (1979)

[24] R. G. Caro *et al.*, J. Phys. D: Appl. Phys. 15, 767 (1982)

[25] D. James *et al.*, IEEE J. Quantum Electron., QE-15, 335 (1979)

[26] A. A. Isaev *et al.*, Sov. J. Quantum Electron. 7, 746 (1977)

[27] T. J. McKee *et al.*, Appl. Phys. Lett. 30, 278 (1977)

[28] J. Goldhar *et al.*, IEEE J. Quantum Electron., QE-16, 235 (1980)

[29] C. J. Buczek *et al.*, Proc. IEEE 61, 1411 (1973)

[30] D. Cooper *et al.*, in Tech. Dig., Conf. Lasers Electro-Opt., Opt. Soc. Amer., Washington, DC, 1988, paper TUH2.

4

Spontaneous Parametric Fluorescence

4.0 INTRODUCTION

In deriving the equations governing parametric amplification and gain in chapter 2, we established that even in the absence of an idler field at the input to a non-linear crystal and for an input consisting of only the pump wave at ω_p , and a signal wave at ω_s , one can expect parametric amplification for both the signal and idler fields. In fact, it can be shown that [1] in the absence of any inputs at ω_s and ω_i , the non-linear crystal, when irradiated by the pump wave at ω_p, will *spontaneously* emit radiation at the signal and idler frequencies ω_s and ω_i , where $\omega_p = \omega_s + \omega_i$ and $k_p = k_s + k_i$. This phenomenon, which is predicted quantum-mechanically but not classically, is variously referred to as *spontaneous parametric emission*, *spontaneous parametric scattering*, *optical parametric noise* and *optical parametric fluorescence*. In an optical parametric oscillator starting from noise, this is the process responsible for the presence of the small signal (or idler) field at the input to the non-linear crystal, which together with the strong pump field at ω_p, results in parametric amplification at ω_s and ω_i. Spontaneous parametric fluorescence in an optical parametric oscillator is somewhat analogous to the spontaneous emission of radiation from the gain medium in a conventional laser. Above threshold, the emission from an optical parametric oscillator is stimulated by the presence of the signal and idler fields, while below threshold, and even in the absence of an optical resonator, there is spontaneously-emitted radiation at both the signal and idler frequencies. However, the underlying physical principle responsible for the parametric fluorescence process is entirely different from the spontaneous emission arising from transitions in atomic media. Viewed quantum-mechanically, in the parametric scattering process the incident photon spontaneously breaks up, through the non-linear polarisation of the medium, into a pair of photons with wavevectors k_s and k_i within the non-linear medium and satisfying the energy and momentum conservation $\omega_p = \omega_s + \omega_i$ and $k_p = k_s + k_i$. In other words, with an incident pump photon at ω_p, scattered photons at frequencies ω_s and ω_i with wavevectors k_s and k_i appear spontaneously without any corresponding input. In the semi-classical picture, the parametric scattering process can be regarded as the mixing of the incident pump photon of frequency ω_p, with the quantum-mechanical zero-point energy of the electromagnetic radiation at ω_i leading to a polarisation at $\omega_s = \omega_p - \omega_i$ through the non-linear response of the medium, which in turn leads to scattered light at ω_s. One can think of the zero-point energy of the electromagnetic modes of the quantising volume of the crystal as providing an effective input field at ω_i, with an intensity corresponding to one *photon per mode*. The polarisation so generated will attempt to radiate at all frequencies and in all directions. However, the ability to do so is constrained by the phase-match condition, namely $k_s + k_i = k_p$. In general, all pairs of signal and idler waves that satisfy the energy and momentum conservation will be excited. In other words, *non-collinear* as well as *collinear* interactions are possible (Fig. 4.1). The spontaneous parametric fluorescence is, therefore, emitted in the forward direction and within a cone of typically a few degrees in solid angle. This is shown, in the case of urea, in Fig. 4.2.

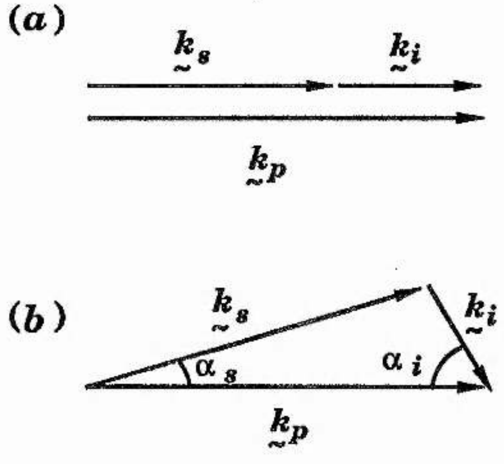

Fig. 4.1. (a) Collinear, and (b) Non-collinear phase-matching.

4.1 THE SPONTANEOUSLY-EMITTED POWER

The total power radiated into the acceptance angle α_s, where $\Omega_s = \pi\alpha_s^2$ (see Fig. 4.2), integrated over all signal frequencies contained within the solid angle Ω_s, measured within the crystal, is given by [4]

$$\text{(C.G.S.)} \qquad P_s^{sp} = \frac{16\pi P_p h [d_{eff}^{(2)}]^2 n_s \omega_s^4 \omega_i l \alpha_s^2}{b n_p n_i c^5} \tag{4-1}$$

where P_p is the total pump power, l is the length of the non-linear crystal, ω_s and ω_i are the collinear frequencies, h is Planck's constant, b is the *dipersion parameter* defined as [4]-[6]

$$b = \frac{\partial k_s}{\partial \nu_s} - \frac{\partial k_i}{\partial \nu_i} \tag{4-2}$$

and other symbols have their usual meaning. It should be noted that (4-1) has been derived under the phase-match condition Δk=0.

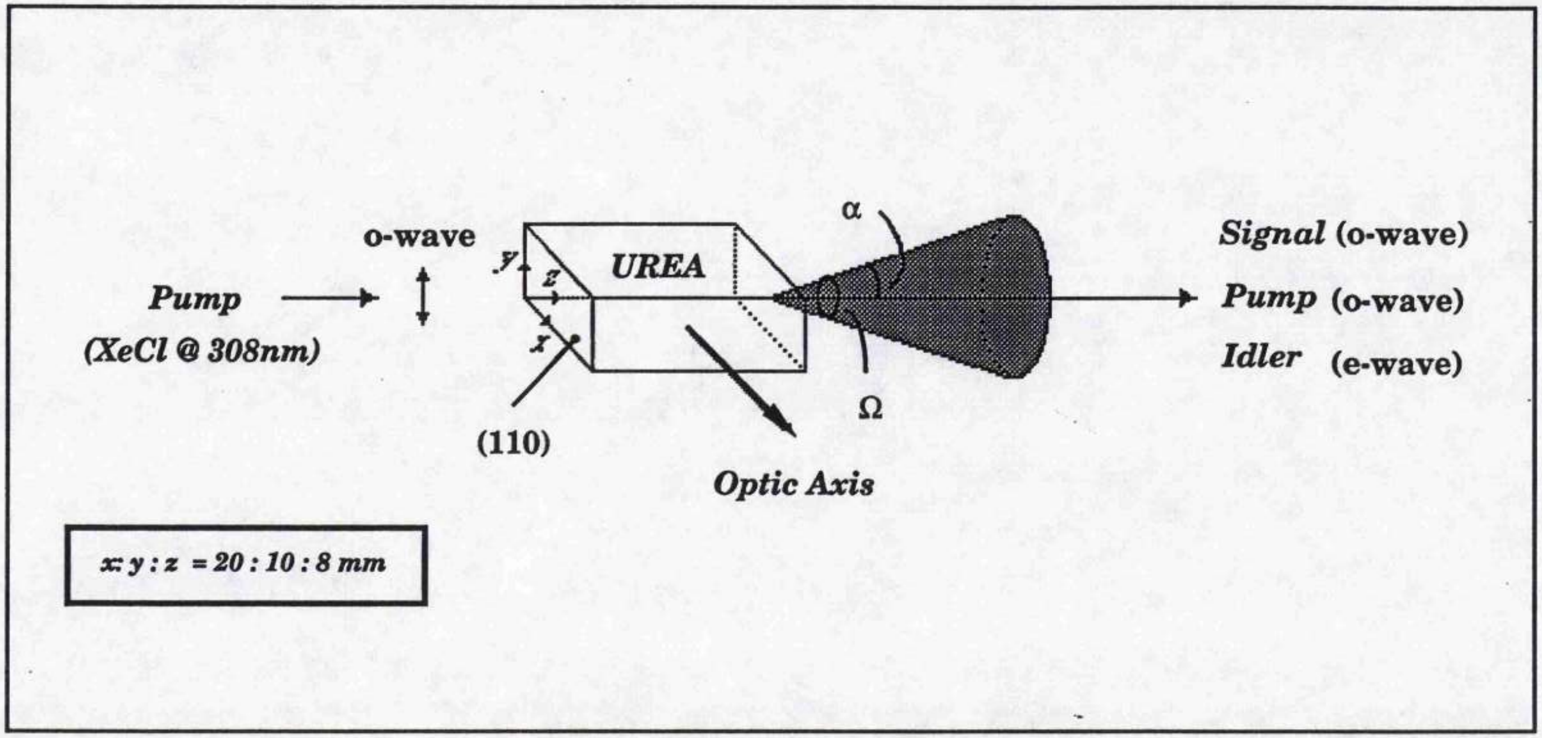

Fig. 4.2. Spontaneous parametric fluorescence in urea. The pump light is incident on the crystal as an o-wave, suitable for type II interaction (o → o + e), and the spontaneously-scattered radiation is emitted from the crystal in a cone of solid-angle Ω. The wavelength of emission varies depending on the angle of view α, and orientation of the crystal optic axis relative to the pump propagation direction.

It can be seen, from (4-1), that the emitted spontaneous power is linearly proportional to the incident pump power, the length of the non-linear crystal, the square of the second-order non-linear susceptibility, and the fourth power of the frequency of the scattered radiation. As an example, let us estimate the magnitude of the spontaneously-scattered signal power in the case of a urea crystal irradiated by a pump wave at 308nm. We can assume that the interaction is phase-matched, with the pump and the generated signal both *o-waves* and the idler as an *e-wave* (i.e. type II phase-matching). Also, we can take the phase-match angle $\theta_m = 90^o$ (i.e. *non-critical* phase-matching). Using the following data

$$P_p = 2.5\ \mathrm{MW}$$
$$l = 1.2\ \mathrm{cm}$$
$$d_{eff}^{(2)} \sim d_{14} = 1.23 \times 10^{-23}\ \mathrm{Coulombs.Volt}^{-2}$$
$$\alpha_s = 10^o$$
$$\omega_s = 3.2 \times 10^{15}\ \mathrm{Hz}$$
$$\omega_i = 2.8 \times 10^{15}\ \mathrm{Hz}$$
$$n_s \sim n_i \sim n_p \sim 1.5$$

Using the appropriate dispersion equations for urea (see chapter 5), the value of the dispersion parameter b can be estimated and shown to be

$$b = 4.79 \times 10^{-12}\ \mathrm{cm}^{-1}.\mathrm{s}$$

Substitution into (4-2) yields

$$P_s^{sp} \sim 0.503\ \mathrm{Watts}$$

Therefore, the fraction of the total pump power converted to the signal power emitted spontaneously is

$$\eta = \frac{P_s^{sp}}{P_p} \sim 2 \times 10^{-7}$$

This indicates that only a very small fraction of the input pump power is scattered into the signal (or idler) power.

4.2 APPLICATIONS

The spontaneous parametric process has some useful applications. Since the tuning characteristics of both spontaneous and stimulated parametric emission are based on the same energy and momentum conservation conditions, the tuning curves of an optical parametric oscillator can be directly determined, prior to the construction of the oscillator itself, from the spectrum of spontaneous parametric emission. The technique is particularly useful as its requirements on the spatial, spectral and temporal properties of the pump beam are far less severe than is the case with stimulated parametric fluorescence which leads to parametric amplification and oscillation. This technique is routinely used in parametric oscillator work. Also, since the total parametric noise is insensitive to the degree of focusing of the pump beam and (on average) to the fluctuations in pump intensity, it is a superior technique to optical second harmonic generation for measurement of the magnitude and dispersion of the non-linear coefficient. This is because second harmonic generation is sensitive to the spatial and temporal characteristics of the fundamental input wave [2]. We now discuss the results of experiments on spontaneous parametric fluorescence in urea.

4.3 PARAMETRIC FLUORESCENCE EXPERIMENTS

In order to characterise the urea crystal and deduce the type II phase-matching tuning curves experimentally, a study of parametric fluorescence was carried out using the XeCl pump wave at 308nm. Fig. 4.3 shows a schematic of the experimental set-up. The polarised pump beam was compressed through a x10 collimating telescope and then passed through a pair of dispersing prisms to separate any fluorescence from the laser discharge (mainly in the visible) from the UV pump beam. Apertures were used for spatial filtering of the pump beam and for blocking any amplified spontaneous emission. The pump beam, once separated from the discharge fluorescence, was passed through a third pinhole and then launched onto the non-linear crystal in the absence of an optical resonator. To facilitate observation of the spontaneously emitted radiation, a "stop" was used to block the strong pump light emerging from the crystal and the signal and idler spectra were separated by means of a polariser. The parametric fluorescence spectrum was then measured by translating a small monochromator across the emitted cone of fluorescence in the plane containing the crystal optic axis and pump propagation vector. The spontaneous parametric fluorescence was easily observable with the unaided eye. Figs. 4.4 (a) and 4.4 (b) show the obtained parametric fluorescence spectra for the *o-wave* and the *e-wave*, respectively. For each external propagation angle ϑ between the pump beam and the crystal optic axis, the wavelength of fluorescence was measured as a function of the angle of view α. The collinear phase-matched spectral components corresponding to values of $\alpha = 0^o$ are those which give rise to on-axis oscillation in the OPO. In Fig. 4.5, the measured wavelength of the collinear spectral components (at $\alpha \sim 0^o$) is plotted as a function of the internal propagation angle θ. The solid curves represent the calculated type II phase-matching tuning curves for the oscillator deduced from the published Sellemeier equations for urea. From the plot, good agreement is found, within the experimental error, between the parametric fluorescence measurements and the theoretical predictions.

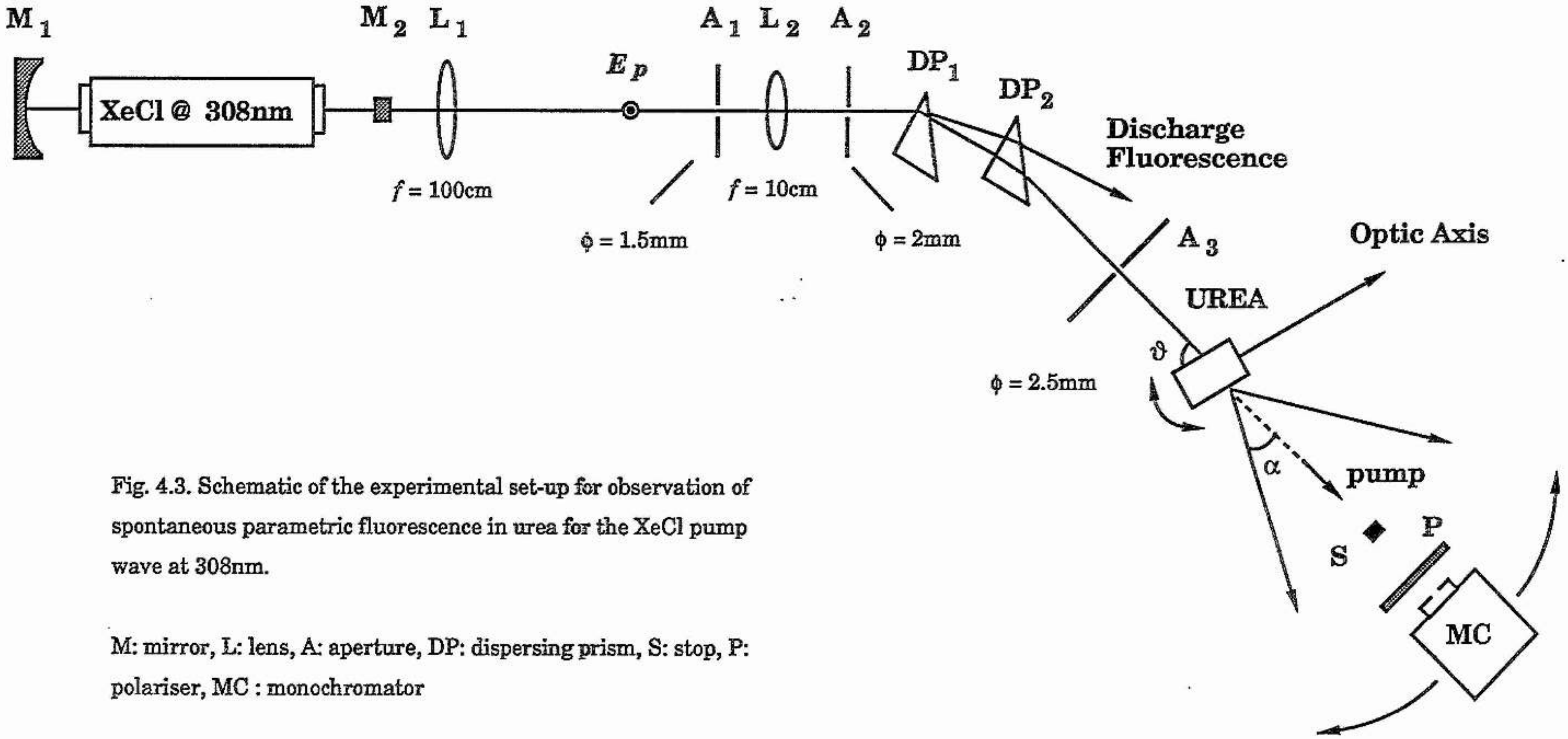

Fig. 4.3. Schematic of the experimental set-up for observation of spontaneous parametric fluorescence in urea for the XeCl pump wave at 308nm.

M: mirror, L: lens, A: aperture, DP: dispersing prism, S: stop, P: polariser, MC : monochromator

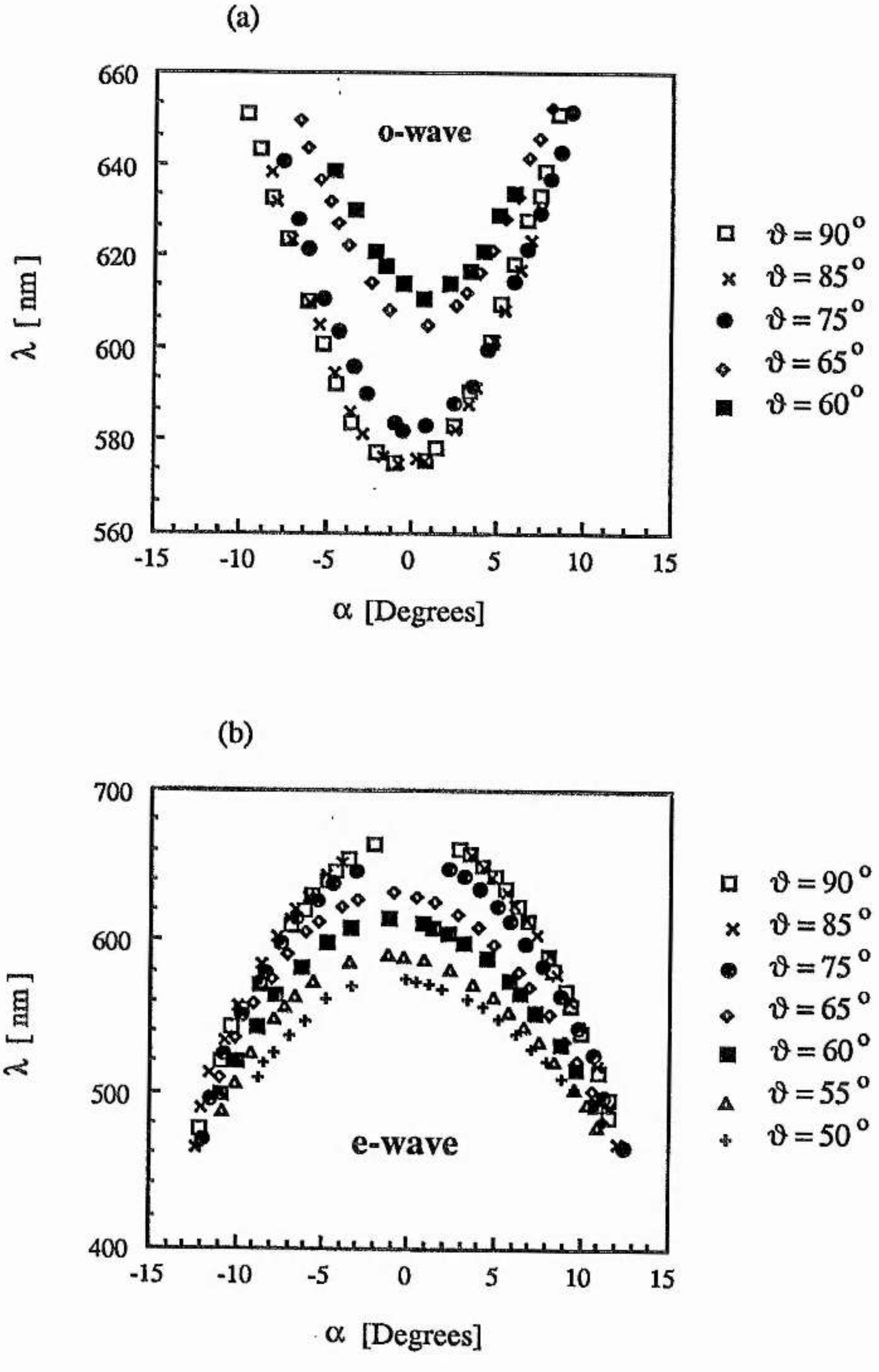

Fig. 4.4. Spectrum of spontaneous parametric fluorescence in urea for a XeCl pump wave at 308nm with type II interaction (o → oe).

Therefore, this technique can be regarded as a useful yardstick for assessment of the properties of the crystal by confirming the oscillator tuning range prior to its construction.

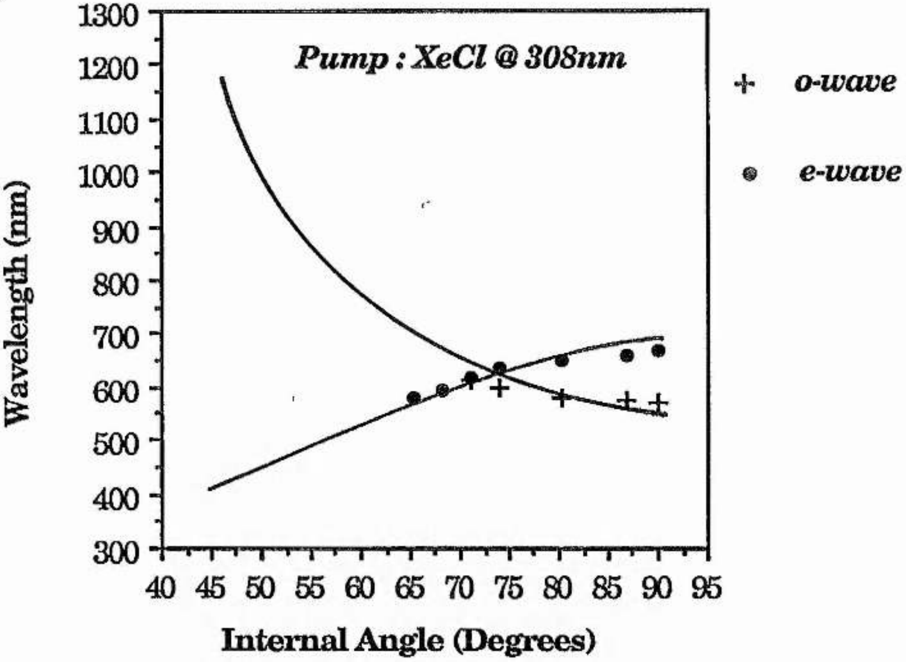

Fig. 4.5. Measured wavelength of the collinear phase-matched spectral components (at $\alpha \sim 0^{o}$) in the parametric fluorescence process (experimental points), and the calculated tuning curves for urea optical parametric oscillator pumped at 308nm by a XeCl excimer laser, under type II phase-matching ($o \rightarrow oe$).

References to Chapter 4.

[1] A. Yariv, "Quantum Electronics," Wiley, New York, 2nd Ed., Chapter 17 (1975)

[2] C. L. Tang, "Spontaneous and Stimulated Parametric Processes," in *Quantum Electronics: A Treatise*, H. Rabin and C. L. Tang, eds. (Academic, New York, 1973), Vol. 1, Pt. A, pp. 419-447.

[3] D. A. Kleinman, Phys. Rev. 174, 1027 (1968)

[4] R. L. Byer and S. E. Harris, Phys. Rev. 168, 1064 (1968)

[5] A. Hordvik *et al.*, Appl. Phys. Lett. 18, 448 (1971)

[6] J. E. Pearson *et al.*, Appl. Opt. 12, 1165 (1973)

[7] R. G. Smith, "Optical Parametric Oscillators," in *Lasers*, A. K. Levine and A. J. DeMaria, eds., Dekker, New York (1976)

[8] S. E. Harris, Proc. IEEE 57, 2096 (1969)

[9] D. Magde and H. Mahr, Phys. Rev. 171, 393 (1968)

[10] R. G. Smith *et al.*, Appl. Phys. Lett. 12, 97 (1968)

[11] T. G. Giallorenzi and C. L. Tang, Appl. Phys. Lett. 12, 376 (1968)

[12] J. P. Budin *et al.*, IEEE J. Quantum Electron, QE-4, 831 (1968)

[13] J. S. Kruger and T. J. Gleason, J. Appl. Phys. 41, 3903 (1970)

[14] S. E. Harris *et al.*, Phys. Rev. Lett. 18, 732 (1967)

[15] A. J. Campillo and C. L. Tang, Appl. Phys. Lett. 16, 242 (1970)

[16] D. Magde and H. Mahr, Phys. Rev. Lett. 18, 905 (1967)

[17] D. Magde *et al.*, Appl. Phys. Lett. 11, 381 (1967)

5

Urea Optical Parametric Oscillator

5.0 INTRODUCTION

In this chapter, we discuss the design and operating characteristics of a pulsed singly-resonant optical parametric oscillator (OPO) based on urea as the non-linear crystal and pumped at 308nm by the injection-seeded XeCl excimer laser described in chapter 3. We begin with a description of some of the properties that make urea a suitable material for incorporation into such an OPO. We then describe the design and construction of the OPO, and present experimental results on several oscillator parameters including tuning range, spectral bandwidth, oscillation threshold, and energy conversion efficiency. The experimental findings are also compared, and found to agree favourably, with the predictions of theoretical analysis.

5.1 MATERIAL PROPRTIES

Urea is an organic non-linear material belonging to the space group class $\bar{4}2m$, the same space group as the KDP and ADP isomorphs. It was the first organic material to be successfully used as the non-linear medium in an OPO, as first reported by Donaldson and Tang in 1984 [1]. Like ADP and related materials, urea is grown from solution. It is a positive uniaxial crystal ($n_o < n_e$), for which both type I ($o \rightarrow ee$) and type II ($o \rightarrow oe$) phase-matching are possible. The effective non-linear coefficient in each case is given by [2]

$$|d_{eff}| = d_{14} sin2\theta cos2\phi \qquad \text{(type I)} \qquad (5\text{-}1)$$

$$|d_{eff}| = d_{14} sin\theta sin2\phi \qquad \text{(type II)} \qquad (5\text{-}2)$$

where θ is the internal phase-match angle (i.e. the internal angle between the direction of propagation of the pump beam and the crystal optic axis), and ϕ is the azimuthal angle, as defined in Fig. 2.6, chapter 2. It is seen from (5-2) that the maximum non-linear coefficient in urea, and thus the peak gain in the parametric generation process, occurs at ($\theta = 90^o$, $\phi = 45^o$) for the type II interaction. This characteristic is of great importance in the design of an angle-tuned OPO, since it allows non-critical phase-matching ($\theta = 90^o$) to occur with maximum parametric gain. The importance of non-critical phase-matching is that the parametric generation process, in this case, is less sensitive to angular deviations and, more significantly, the interacting waves do not suffer from Poynting vector walk-off due to crystal double-refraction, thus ensuring maximum interaction over the available crystal length. This is to be contrasted with the case of BBO, discussed in the next chapter, where non-critical phase-matching can not occur. It can also be seen from (5-1) that for a type I process in urea, the effective non-linear coefficient vanishes at non-critical phase-matching ($\theta = 90^o$); the maximum gain in this case occurring for ($\theta = 45^o$, $\phi = 0^o$). Thus, the use of type II ($o \rightarrow oe$) phase-matching in urea generally leads to lower oscillation thresholds, and hence higher OPO conversion efficiencies than is the case with the type I ($o \rightarrow ee$) interaction. Fig. 5.1 shows a typical geometry of the urea crystal used under type II phase-matching ($o \rightarrow oe$).

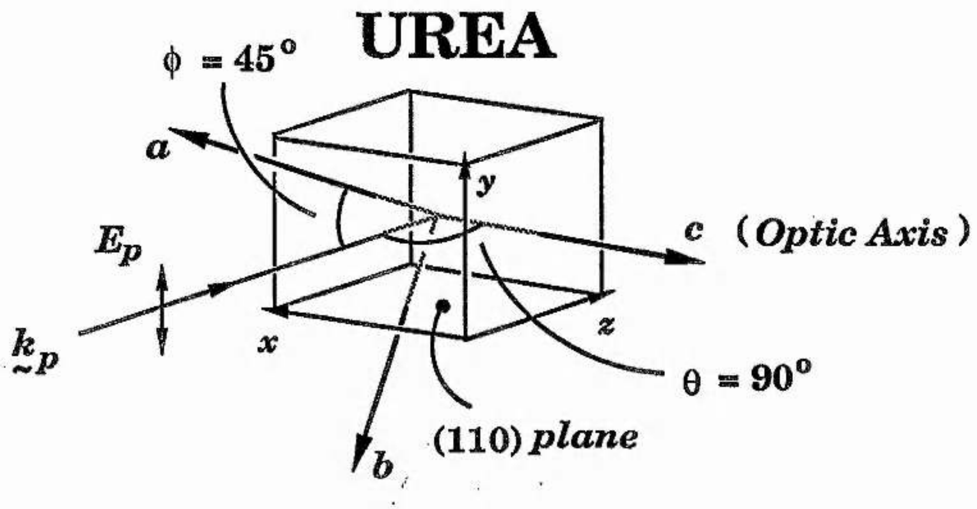

Fig. 5.1. Crystal geometry and pump wave polarisation for parametric oscillation in urea with type II interaction ($o \rightarrow oe$). The pump beam is launched as an *o-wave*, with its electric vector, E_p, as shown. The diagram corresponds to non-critical phase-matching ($\theta = 90^{\circ}$), with the pump beam propagating normal to the (110) crystallographic planes. Angle-tuning of the OPO is achieved by altering the internal angle θ between the pump beam and crystal optic axis, while maintaining $\phi = 45^{\circ}$ for maximum gain.

The natural growth morphology of urea is along the (110) crystallographic direction, which is the normal to the (110) cleavage planes. The azimuthal angle φ, which is the angle between the projection of this direction onto the crystal plane *ab* and the *a*-axis is equal to 45°. This is very useful, particularly in the situation where the crystal is used with type II ($o \rightarrow oe$) interaction, since maximum d_{eff} occurs at $\phi = 45^{\circ}$. Hence, by propagating the pump beam normal to the natural (110) crystal faces, one can conveniently ensure maximum gain without the need for further cutting the crystal subsequent to its growth. In addition, because the crystal optic axis (*c*) is at 90° to the (110) direction, pump propagation at right-angles to the crystal faces automatically sets $\theta = 90^{\circ}$, thus ensuring non-critical phase-matching as well as maximum d_{eff}. Other properties that make urea suitable for use in an OPO include its large non-linear coefficient (d_{14} = 1.4 pm/V), which is about 2.5 times that of ADP [3], and its wide transparency range throughout most of the visible and the near infrared (~ 0.2 - 1.4 μm), which allows OPO operation in these spectral regions. In addition, it exhibits a relatively large birefringence ($(n_e - n_o)$ / n_o = 6.6 x 10^{-2}), considerably greater than that of ADP (~ 3.1 x 10^{-2}). This enables phase-matching, and hence OPO tunability, over much broader wavelength regions, particularly in the visible and the near ultraviolet, not accessible by many other non-linear crystals. However, perhaps the most important property of urea that has made its use as an OPO medium possible is its high optical damage threshold, which has been reported to be at least an order of magnitude greater than that of $LiNbO_3$ [3], and as high as 1.4 GW.cm^{-2} at 355 nm (single-shot) [4]. Our studies have shown this damage threshold to be considerably lower at the XeCl pump wavelength of 308 nm, but still at least a few hundred MW.cm^{-2}, greater than that of many of the classical non-linear crystals. Indeed, in most part, it is this high damage capability of urea and other new non-linear materials (such as BBO and LBO) coupled with their large non-linear coefficient that has led to a resurgence of interest in the OPO for the generation of tunable laser radiation in new regions of the optical spectrum. The recent advances in material science and crystal technology have also made possible the growth of sizeable non-linear crystals of high optical quality. The use of crystals of long optical path lengths and high optical quality, as well as leading to higher OPO efficiencies, also has the advantage of relaxing the somewhat severe constraint on damage to the crystal and other optical components. In the case of urea, large crystals of geometrical path lengths ≥ 20 mm are routinely grown and are readily available. In our own laboratory at St.Andrews, we have been able to grow urea crystals of up to 15 mm in optical length and > 10 x 10 mm in aperture. Some of these crystals have been successfully used in this study to achieve parametric oscillation in the visible spectrum, with energy conversion efficiencies as high as 37% (in a 15-mm-long crystal) at $\theta = 90^{\circ}$. We have also performed experiments in commercially available urea crystals of larger optical path lengths, and have obtained exceptionally high conversion efficiencies of up to 66% (in a 25-mm-long crystal) under conditions of non-critical phase-matching. These experiments are described in detail in section 5.3. However, it is also important to point out that, due to its relative softness and some undesirable mechanical and chemical properties, urea is in general a difficult material to polish, although polishing of the crystal faces to optical quality of better than a few wavelengths has been reported to be possible, with no great difficulty [3]. In addition, since urea is hygroscopic, its exposure to normal atmospheric conditions can cause surface degradation, due to absorption of water vapour, and thus limit the optical quality of the crystal. Both these problems can, however, be alleviated by immersion of the crystal in an index-matching fluid with compatible chemical and optical properties. As well as protecting the crystal faces against surface degradation and significantly improving its optical quality, the use of index-matching fluid can also greatly reduce any Fresnel reflection losses within the OPO cavity, thus resulting in lower OPO oscillation threshold and higher conversion efficiency.

5.2 OPO DESIGN AND CONSTRUCTION

The OPO consisted of a single urea crystal enclosed between a pair of dichroic mirrors, forming the optical cavity. The crystal was located inside a cell containing *n*-hexane as index-matching fluid (IMF). The choice of this particular IMF was governed by its high UV transparency (which we measured to be ≥ 85% @ 308nm for a 10mm fluid path length), its relative chemical inertness, and a comparable index of refraction ($n \sim 1.4$) to that of urea. Several OPO cells were used during these experiments, as were several urea crystals. The cells were fabricated of nylon or perspex, and incorporated uncoated quartz windows (thickness = 2 mm, diameter = 1", ≤ 2 minutes of arc wedge) . O-rings were used to seal the structure. Nylon and perspex were favoured as the cell material, because experiments with cells manufactured of some metals (aluminium, brass) revealed unacceptable levels of IMF contamination over relatively short periods (a few hours) of IMF enclosure within the cell. In particular, in the case of brass, this was found to lead to a serious degradation in the UV transparency of the IMF, resulting in strong absorption of the pump light (at 308 nm) before it was incident on the urea crystal. The OPO cavity was of a simple plane-parallel design, and was formed by two flat mirrors. The mirrors were both highly reflecting at the wavelength of the signal wave to be resonated, and had high transmittance at the idler wavelength. They were also highly transmitting at the pump wavelength and were mostly AR-coated on their rear surfaces at 308 nm. The high pump transmission of the OPO mirrors is particularly important, since any absorption of the pump light by the mirrors could lead to serious optical damage to the coatings, given the high pump power levels involved, and prevent OPO operation. The rear surfaces of the mirrors were also wedged to avoid competing cavity effects. All mirrors were 1" in diameter, with 1/4" thickness, and were placed inside adjustable gimbals to enable cavity alignment. The OPO cavity length was maintained as short as possible to provide a maximum number of round-trips of the resonated signal wave over the 10-ns duration of the pump pulse, and thus ensure adequate parametric gain to reach oscillation threshold. The cell structures were also designed with minimum thickness to accommodate this short cavity length. An XY-translation stage was used for precise location of the urea crystal within the OPO cavity and a miniature rotation mount was used to allow angle-tuning of the crystal as well as to enable accurate measurements of the phase-match angle θ. Location along the axis of the optical system (i.e. along z) could be adjusted by translation of the entire OPO assembly along the optical bench. A He-Ne laser beam propagated through pinholes, along the pump beam direction, was used for alignment of the OPO cavity.

5.3 OPO EXPERIMENTS

We used a total of three samples of urea during our studies. Initial experiments were performed in a relatively short crystal grown in our own laboratory from methanol solution, using a seed-growth technique. The crystal measured 8mm in physical length (along z in Fig. 5.1) and 20mm x 10mm ($x \times y$) in aperture. In order to verify the orientation of the optic axis, a polarising microscope was used to obtain the characteristic Maltese-cross patterns that can be observed when a uniaxial crystal is viewed along its optic axis [6]. These observations confirmed the expected orientation of the optic axis in the direction shown in Fig. 5.1. The surface quality of the crystal was greatly improved by polishing the (110) entrance and exit faces. During the polishing process special care was taken to ensure that the two faces were maintained very nearly parallel. An approximate measure of the degree of parallelism is the level of birefringence exhibited by the crystal when viewed at right-angles to these faces. Alternatively, the back-reflections of a He-Ne beam from the two surfaces could be used for this purpose. The optical quality of the crystal (bulk and surface) was examined by using a He-Ne beam, and observing the beam profile after transmission through the crystal. The described crystal was successfully used to demonstrate, for the first time, optical parametric oscillation in the visible spectrum (from 572 to 667 nm) using an excimer laser as the pump source [7], [8]. The conversion efficiency of this OPO, however, was limited to 2.5%, due to the short length of the crystal. The tuning range of this device was soon extended to 537 to 720 nm, and its efficiency was greatly improved (to as high as 37% at $\theta = 90^o$) by utilising a second home-grown crystal, 15mm in geometrical length (z), and 12mm x 10mm (x x y) in aperture [9], [10]. Finally, in an effort to achieve even higher conversion efficiencies, experiments were performed in a 25-mm-long commercially available urea crystal (supplied from the Fujian Institute of Research on the Structure of Matter, People's Republic of China), and OPO efficiencies of up to 66% (at $\theta = 90^o$) were obtained, with evidence of even higher levels of pump depletion [9], [11]. A schematic of the experimental design predominantly used throughout our studies is shown in Fig. 5.2. The narrowband pump beam from the injection-seeded XeCl excimer laser is compressed through a x 8 Galilean telescope, before being launched into the OPO. The telescope consisted of two uncoated, non-best-form, quartz lenses; a plano-convex lens of focal length $f = 2$ m, and a plano-concave lens of focal length $f = -25$ cm, separated by ~ 1.75 m. Initial experiments in the 8-mm-long crystal were performed using a x 10 astronomical telescope, with the compressed pump beam further focused into the crystal using a positive lens ($f = 25$ cm), as shown in Fig. 5.3. The telescope in this case was formed by two plano-convex quartz lenses of focal lengths $f = 1$ m and $f = 10$ cm, separated by ~ 1.1 m, and a pinhole was used at the telescope focus for spatial filtering of the beam. The lenses were again uncoated and non-best-form. The greater beam compression

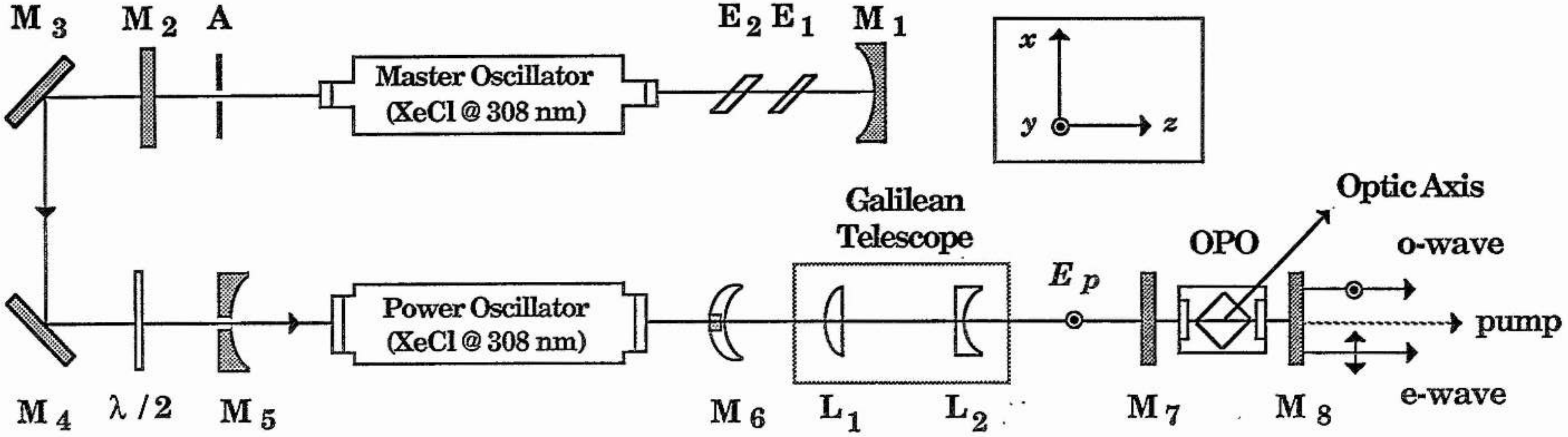

Fig. 5.2. Schematic of the urea optical parametric oscillator pumped by an injection-seeded, narrowband XeCl excimer laser at 308 nm, with type II interaction, using a Galilean beam compressor (top view). M's: mirrors; E's: etalons; A: aperture; L's: lenses.

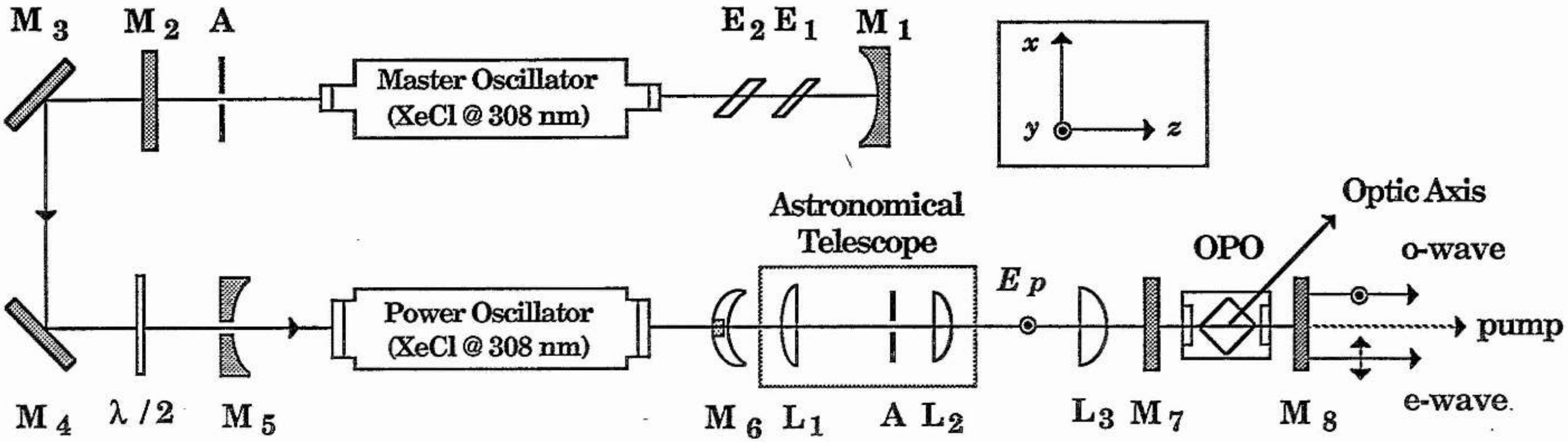

Fig. 5.3. Schematic of the urea optical parametric oscillator pumped by an injection-seeded, narrowband XeCl excimer laser at 308 nm, with type II interaction, using an astronomical beam compressor (top view). M's: mirrors; E's: etalons; A: aperture; L's: lenses.

and additional focusing in this case were considered necessary to obtain the higher pump power densities required to reach oscillation threshold, due to the relatively short crystal length. In subsequent experiments with the 15-mm and 25-mm crystals, however, the x 10 astronomical telescope was replaced by a x 8 Galilean telescope, with no additional focusing optics. The use of a Galilean telescope had the advantage of avoiding a real focus for the pump beam, which was found to lead to air breakdown as well as distortions in the pump beam after compression. A smaller beam compression was also favoured in this case, in order to prevent the serious optical damage to the OPO mirrors and the crystal, observed during the initial experiments in the 8-mm urea sample. The smaller pump power densities in this case were compensated for by the longer crystal path lengths. Throughout these experiments, we used type II interaction ($o \rightarrow oe$) to maximise parametric gain and to enable non-critical phase-matching. The pump beam was launched into the OPO as an *o-wave*, with its electric vector (E_p) as shown in Fig. 5.2, and the parametric waves emerged with their electric vectors in orthogonal *o*- and *e*- polarisations. The OPO mirrors provided feedback for the signal, but were highly transmitting at the idler and pump wavelengths. The oscillator was, thus, singly-resonant over its entire tuning range. Wavelength tuning of the OPO was accomplished by altering the internal phase-match angle θ between the pump propagation direction (along z) and the crystal optic axis (Fig. 5.2). In the following sections, we describe the results of these experiments in detail.

5.3.1 *Tuning Range*

The oscillator tuning range was experimentally determined by focusing the OPO output onto the entrance slit of a calibrated grating monochromator (Rank Hilger, monospek 1000), with the slit widths set for maximum resolution, and measuring the signal and idler wavelengths for various values of the internal phase-match angle θ. Two UV high reflector mirrors were used to block the undepleted portion of the pump beam emerging from the OPO.

(i) 8-mm-long crystal :

In the case of the 8-mm urea crystal, the OPO consisted of a rear high-reflector mirror (R > 95%) in the visible (M_7 in Fig. 5.2) with a UV transmission > 75% at 308 nm. The output coupler (M_8) was a partial reflector (R ~ 40%) over the range 400-700 nm, and had a UV transmission of ~ 60% at the pump wavelength. The mirrors were separated by 5.5 cm. The crystal, measuring 20 x 10 x 8mm (x x y x z), was located inside a perspex cell with uncoated quartz windows and containing n-hexane as the IMF. Angle-tuning of the OPO was accomplished by rotation of the cell assembly in the xz-plane relative to the pump propagation direction (z). Fig. 5.4 shows the calculated tuning curves for the urea OPO pumped at 308nm by a XeCl excimer laser, with type II interaction (solid curves). The curves have been calculated using the appropriate Sellemeier equations for urea, namely [1]

$$n_o^2(\lambda) = 2.1548 + \frac{0.0131}{(\lambda^2 - 0.0318)} \tag{5-3 (a)}$$

$$n_e^2(\lambda) = 2.5527 + \frac{0.01784}{(\lambda^2 - 0.0294)} + \frac{0.0288\,(\lambda - 1.50)}{[(\lambda - 1.50)^2 + 0.03371]} \tag{5-3 (b)}$$

where λ is in microns. The computer programmes used for these calculations are provided in appendix A. It can be seen from Fig. 5.4 that the OPO is potentially tunable from 395nm in the near UV to 1.4μm in the near IR, by angle-tuning the urea crystal between $\theta = 90^o$ and $\theta = 40^o$. The limit to OPO operation beyond this wavelength range is the IR absorption cut-off in urea, which has been reported to set in at about 1.4μm [4]. Our inspection of several home-grown as well as commercial crystal samples, however, revealed an additional strong absorption band, centred at around 1.03μm, and approximately 150nm wide. This absorption line coincides with that of the O–H band. Also shown in Fig. 5.4, is the observed tuning range in the signal and idler waves (experimental points). The *o-wave* was tuned from 572 to 646nm by altering the internal angle θ from 90^o to 69^o. The corresponding range for the *e-wave* was found to be from from 667 to 589nm. The OPO was, therefore, continuously tunable over a 95-nm wavelength range in the visible, from 572 to 667nm. It can be seen from Fig. 5.4 that the observed tuning range is in good agreement, within the experimental error, with the calculated tuning curves. Angle-tuning of the OPO below $\theta = 69^o$ was not possible because of the dimensions of the cell, and the reflectivity bandwidth of the rear high-reflector mirror. The OPO was operating as a *SRO* over the observed tuning range, since there was clear evidence of the expected Poynting vector walk-off between signal (*o-wave*) and idler (*e-wave*) beams within the crystal, restricting alignment of the cavity (and hence oscillation) only to the *o-wave*. Hence, even in the wavelength regions close to degeneracy (at 616nm) the OPO was acting as a *SRO*. The linewidth of the *o-wave* was measured at different points across the tuning range. It was found to be 10-15 cm^{-1} wide at 90^{o} phase-matching and approximately independent of the phase-match angle θ. We also observed the expected increase in the linewidth with the increase in pumping strength.

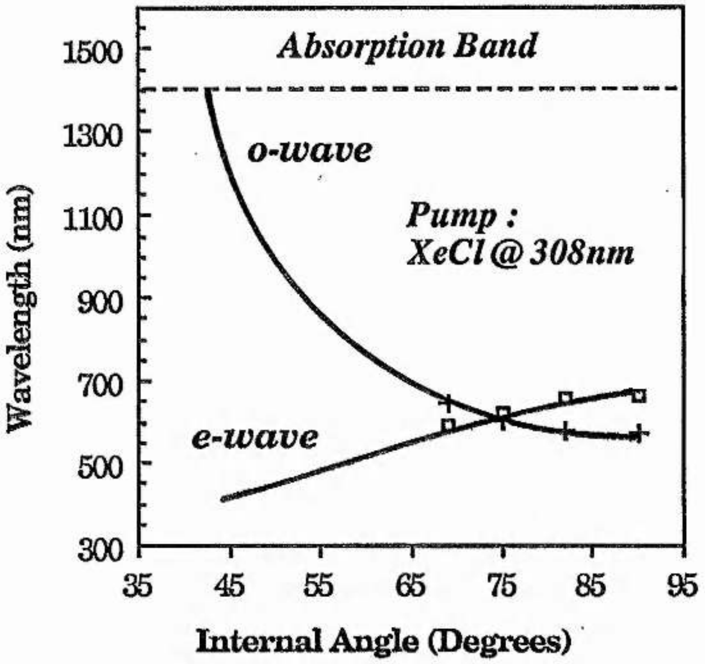

Fig. 5.4. Potential tuning range of urea OPO pumped at 308nm by a XeCl excimer laser, with type II phase-matching ($o \rightarrow oe$). The solid curves represent the calculated tuning range based on the Sellemeier equations (5-3), while the observed tunable output from the oscillator in the two polarisations is indicated by the experimental points. (crystal length = 8mm).

(ii) 15-mm-long crystal :

The observed OPO tuning range was soon extended by utilising a longer home-grown urea crystal, measuring 15 x 12 x 10 mm (x x y x z). In order to reduce the Fresnel reflection loss from the cell windows during angle-tuning of the OPO, the cell assembly was designed in such a way as to enable rotation of the crystal within a fixed cell. The cell in this case was fabricated of nylon, and as with the 8-mm crystal was filled with *n*-hexane as the IMF. The OPO employed identical mirrors at each end of the cavity. Both mirrors were highly reflecting (R >95%) over the range of 500-600nm, with a rapid fall in the reflectivity outside this range. The mirrors were also highly transmitting (T > 95%) and AR-coated on the rear surface at 308nm. The mirrors were also wedged to avoid "etaloning" effects. The physical length of the OPO cavity was 5.5 cm. Fig. 5.5 shows the obtained tuning range with this oscillator. The *o-wave* was tuned from 570 to 720nm for a change in the internal angle from $\theta = 90^o$ to $\theta = 63^o$. The corresponding tuning range for the *e-wave* was measured to be from 670 to 537nm. The OPO was, thus, continuously tunable over the spectral range 537-720nm, with a single set of dichroic mirrors. The linewidths of the signal and idler waves were also measured at different points across the tuning range and were found to be typically 10 cm^{-1} wide. The limit to OPO operation at angles below $\theta = 63^o$ was the cell thickness, which prevented further rotation of the crystal within the fixed cell. As in the previous case, this OPO was also operating as a *SRO* over its entire tuning range. Although the reflection coefficients of the OPO mirrors had approximately the same magnitude ($R \sim 40\%$) for both the signal and the idler in the regions close to wavelength degeneracy, an angular separation between the two waves of about 2^o limited oscillation to one of the waves only. Furthermore, because of the reflectivity bandwidth of the mirrors, the OPO cavity was resonant for the *o-wave* in the regions close to $\theta = 90^o$, while at angles near $\theta = 63^o$ the *e-wave* was resonated.

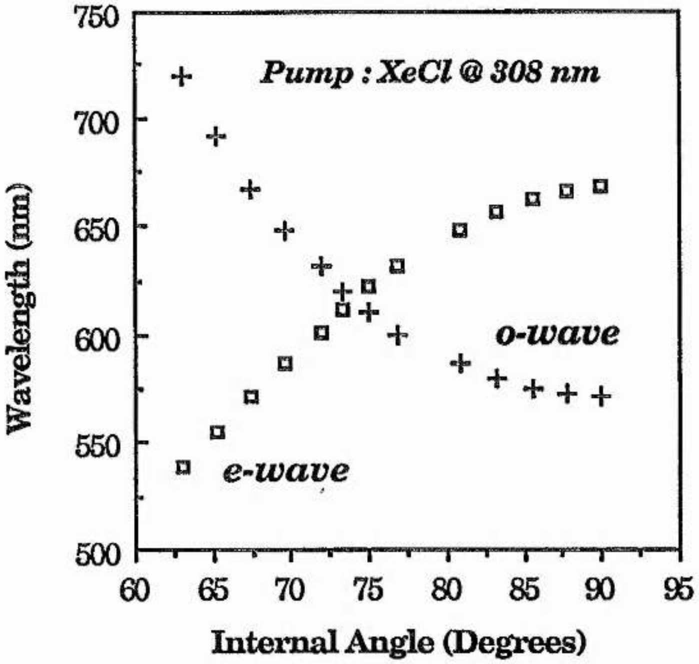

Fig. 5.5. The observed OPO tuning range in the 15-mm-long urea crystal pumped at 308nm by a XeCl excimer laser, with type II interaction ($o \rightarrow oe$).

(iii) 25-mm-long crystal :

In the case of the 25-mm commercially available crystal, the OPO cavity was identical to that used with the 15-mm crystal, above. However, since the primary objective during these experiments was the attainment of high energy conversion efficiencies (see section 5.3.3 (*iii*)), operation of OPO was confined to the region of 90° non-critical phase-matching. For this reason, only the two discrete wavelengths corresponding to $\theta = 90°$ (i.e. 570nm (signal) and 670nm (idler)) were obtained from the OPO.

5.3.2 *Oscillation Threshold*

The OPO oscillation threshold was measured at $\theta = 90^\circ$ by attenuating the pump beam using UV neutral density filters and recording the pump beam energy and spot size at which oscillation could just occur. A pyroelectric energy meter (Scientech 362) was used for measurements of pump pulse energy. The pump spot sizes were recorded on thermal paper and accurately measured under a travelling microscope.

(i) 8-mm-long crystal :

In this case, the OPO threshold was reached by translating the 25-cm focal length lens (see Fig. 5.3) along the pump propagation direction (z) until the peak pump intensity inside the urea crystal was sufficiently high to initiate oscillation. The OPO cavity consisted of a high reflector ($R >$ 99%) at the signal wavelength and a partial reflector ($R \leq 45\%$) output coupler, separated by 5.5 cm. The threshold energy fluence (energy per unit area), deduced from measurements of pump pulse energy and spot size, was 1.7 J.cm^{-2}, corresponding to a threshold pump power density at the non-linear crystal of 170 MW.cm^{-2}, given the 10 ns duration of the pump pulse.

The OPO oscillation threshold may be predicted from the theoretical model of Brosnan and Byer [12]. The model is valid for a pulsed singly-resonant oscillator utilising a negative uniaxial crystal, with type I phase-matching ($e \rightarrow oo$). The pump light is also assumed to be Gaussian in its spatial profile and the effects of Poynting vector walk-off are included in the model. In this analysis, the generated signal wave is assumed to be amplified from an initial parametric noise power to a detectable level, as it makes consecutive transits through the OPO cavity. The oscillation threshold is defined as the point at which the signal energy (after n round-trips) has reached 100μJ, corresponding to a threshold signal power to noise power ratio of $ln\ (P_n\ /\ P_0) = 33$. Although not strictly applicable to an OPO based on a positive uniaxial crystal under type II ($o \rightarrow oe$) interaction (as here), the model may be successfully used to predict threshold of the urea OPO under non-critical phase-matching ($\theta = 90^o$), where there is no walk-off between the interacting waves. We have used this model to predict the OPO threshold at $\theta = 90^o$. In our calculations, however, the Gaussian spatial profile assumed for the coupled waves has been replaced by a "top hat" profile which is more appropriate for the XeCl pump beam used in these experiments. For this case, the signal and idler fields may be assumed to have the same profile as their driving polarisations, that is $W_s = \overline{W}_s$ and $W_i = \overline{W}_i$, where W is the beam radius. Therefore, the spatial mode coupling coefficient, defined in [15] as

$$g_s = 2\,\overline{W}_s^{\,2}\ (W_s^{\,2} + \overline{W}_s^{\,2})^{-1} \qquad \text{(5-4)}$$

is equal to unity. Further, since under non-critical phase-matching there is no beam walk-off due to the absence of crystal double-refraction, the effective parametric gain length £ (eqn. (5) in [12]) is equal to the crystal length l, so that the coupled amplitude equations (B-8) and (B-9) in [12], in our case, are simplified to

$$\frac{dE_s}{dz} + \alpha_s E_s = j\,\xi_s\,E_p\,E_i^{*}e^{j\Delta kz} \qquad \text{(5-5 (a))}$$

$$\frac{dE_i}{dz} + \alpha_i E_i = j\,\xi_i\,E_p\,E_s^{*}e^{j\Delta kz} \qquad \text{(5-5 (b))}$$

where

$$\xi_m = \frac{\omega_m\, d_{eff}}{n_m\, c} \qquad \text{(5-6)}$$

The coupled equations (5-5) may be solved to yield the threshold energy fluence

$$J_0 = \frac{2.25}{\delta l^2}\tau\left[\frac{L}{2\tau c}\ln\frac{P_n}{P_0} + 2\alpha l + \ln\frac{1}{\sqrt{R}} + \ln 2\right]^2 \qquad (5\text{-}7)$$

where τ is the $1/e^2$ intensity half-width of the pump pulse, L is the cavity length, α is the absorption coefficient, R $(= R_1 R_2)$ is the effective mirror reflectivity, and δ is defined by

$$\delta = \frac{2\omega_s\,\omega_i\,{d_{eff}}^2}{n_s n_i n_p \varepsilon_0\,c^3} \qquad (5\text{-}8)$$

Equation (5-7) may be used to obtain a theoretical value for the OPO oscillation threshold with the 8-mm-long crystal at 90° phase-matching. Assuming $d_{eff} = d_{14} = 1.4$ pm/V, and substituting the various oscillator parameters into (5-7), we obtain a value $J_0 = 2.1$ J.cm^{-2}. This value is close to, but somewhat larger (~1.2 times) than, the measured threshold fluence of 1.7 J.cm^{-2}. In fact throughout our experiments with urea crystals of various lengths, the measured OPO threshold values were found to be consistently lower, in all cases, than the calculated values based on the theoretical model (see sections (*ii*) and (*iii*), below). This behaviour, which has also been reported by other investigators [1], [13], could be due to the fact that the model is strictly applicable to single-frequency pump and single-frequency signal. In the case of multi-mode pump and signal, as here, equation (5-7) should be used for qualitative estimates of threshold and not for quantitative measurements of the non-linear coefficient.

(*ii*) *15-mm-long crystal :*

For this case, we measured the OPO oscillation threshold (at $\theta = 90°$) to be 4-5 mJ per pulse, for a cavity consisting of a high reflector ($R > 95\%$) and a partial reflector ($R \sim 40\%$) output coupler, and separated by 5.5 cm. The pump beam in this case measured 1 x 2.5 mm^2 (x x y in Fig. 5.2) at the entrance to the non-linear crystal. Therefore, the corresponding threshold energy fluence for the OPO was 0.16 - 0.2 J.cm^{-2}. Given the 10 ns pump pulse duration, this value corresponds to a pump power density of between 16 and 20 MW.cm^{-2} at the non-linear crystal. We also observed reliable oscillation with this crystal even with the high reflector rear mirror (M_7 in Fig. 5.2) completely removed, thus indicating that the residual feedback from the rear cell window in this case was sufficient to maintain OPO oscillation. From equation (5-7) and using $d_{eff} = 1.4$ pm/V, we obtain a value $J_0 = 0.61$ J.cm^{-2} for the threshold energy fluence, which is again considerably higher (~3.5 times) than the observed threshold fluence of 0.16 - 0.2 J.cm^{-2}.

We also performed experiments to determine the dependence of OPO oscillation threshold on the oscillator cavity length L and effective mirror reflectivity R_1R_2. The result of these experiments is shown in Figs. 5.6 (a) and 5.6 (b), where the measured threshold energy fluence J_0 is plotted against cavity length and mirror reflectivity product, respectively. The threshold dependence on OPO cavity length was investigated for a range of cavity lengths from 55 to 150 mm, while maintaining a fixed mirror reflectivity product of 38% ($R_1 = 95\%$, $R_2 = 40\%$). Similarly, the variation in threshold with effective mirror reflectivity was investigated for a constant cavity length of 55 mm, for mirror reflectivity products (R_1R_2) ranging from 9% to 90%. The solid curves in each case represent the calculated threshold fluence for a range of values of d_{eff}, and are derived from (5-7). It is seen from Figs. 5.6 (a) and 5.6 (b) that the observed values of threshold energy fluence are consistently lower than those calculated from (5-7), for a range of values of d_{eff} from 1.4 to 3.4 pm/V. However, it can also be seen that the OPO oscillation threshold follows the trend predicted by the theoretical model of Brosnan and Byer. The decrease in OPO cavity length

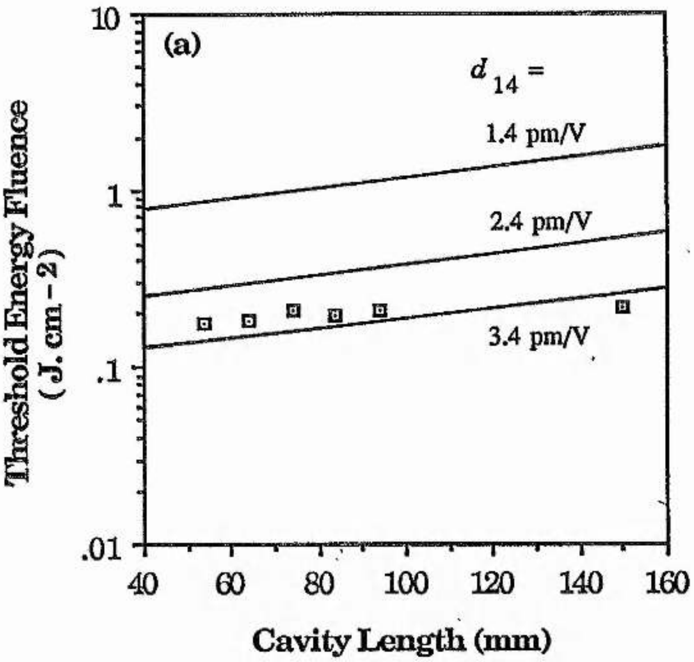

Fig. 5.6(a). The dependence of OPO oscillation threshold on cavity length. The solid lines represent the calculated variation, derived from equation (5-7), for different values of the d_{14} coefficient. $R_1 = 95\%$, $R_2 = 40\%$.

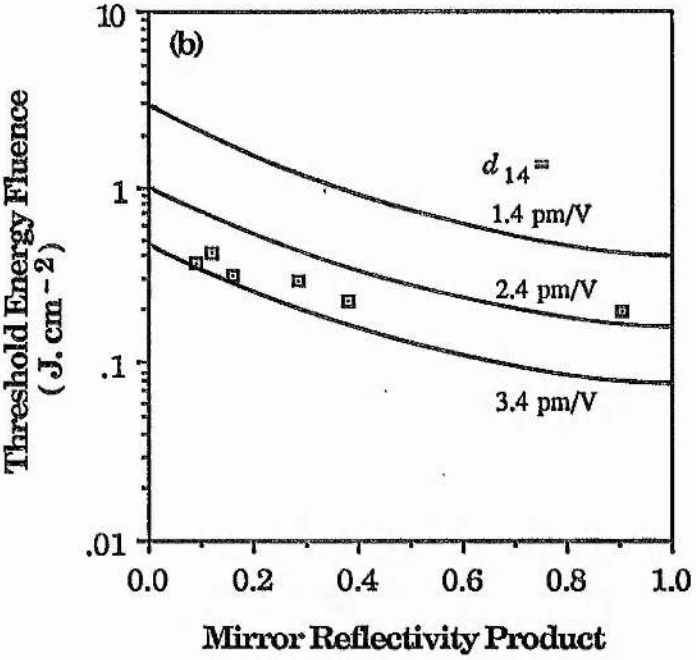

Fig. 5.6(b). The dependence of OPO oscillation threshold on the effective mirror reflectivity. The solid curves represent the calculated variation, derived from equation (5-7), for different values of d_{14} coefficient. $L = 55$ mm.

results in an increase in the number of round-trips of the resonated wave over the duration of the pump pulse, while the increase in mirror reflectivity increases the net gain per round-trip at the signal wavelength, both resulting in a reduction in oscillation threshold.

(iii) 25-mm-long crystal :

The OPO oscillation threshold in this case was found to be as low as 0.84 mJ per pulse at 90° phase-matching, corresponding to a threshold energy fluence of only 0.023 J.cm^{-2} (1.2 x 3.1 mm^2 spot size). The associated pump power density at the crystal was, therefore, only 2.3 MW.cm^{-2}. The OPO cavity parameters in this case were identical to that used with the 15-mm-long crystal (see section 5.3.2 (*ii*), above). Parametric oscillation was also observed in the absence of the OPO optical cavity, indicating an adequately high level of gain for superfluorescent parametric emission from the crystal to occur. Substituting the OPO parameters, with d_{eff} = 1.4 pm/V, into (5-7), we obtain a theoretical value J_0 = 0.23 J.cm^{-2}, which is an order of magnitude greater than the measured threshold fluence of 0.023 J.cm^{-2}.

The results of OPO oscillation threshold experiments with the three crystals is summarised in Fig. 5.7, where the measured threshold fluence is plotted for the three different crystal lengths. The calculated fluence values corresponding the range of values of d_{eff} from 1.4 to 3.4 pm/V are represented by the solid curves.

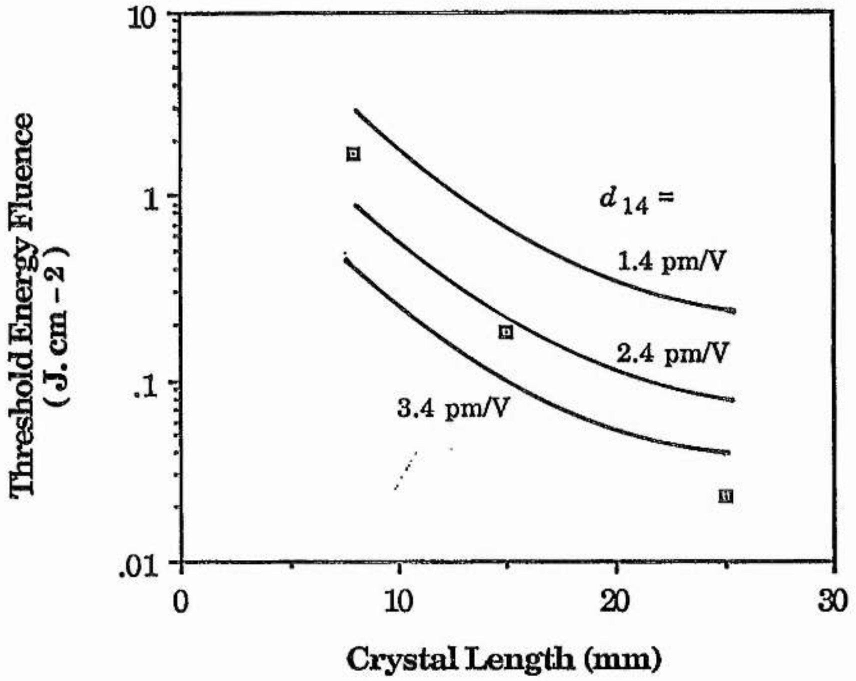

Fig. 5.7. The dependence of OPO oscillation threshold on the length of the non-linear crystal. The solid curves represent the predicted dependence, based on (5-7). L = 55 mm, R_1= 95%, R_2= 40%.

5.3.3 *Energy Conversion Efficiency*

The energy conversion efficiency of the OPO, which we define as the ratio of the total output energy in the parametric waves to the input pump energy, was determined by measuring the output pulse energy in the signal and idler waves for a given input pump pulse energy, using a pyroelectric energy meter (Scientech 362). The maximum OPO conversion efficiency during our experiments was limited primarily by the optical damage to OPO mirrors and cell windows.

(i) 8-mm-long crystal :

The relatively short crystal length in this case prevented operation of the OPO well above threshold, since at input pump intensities above ~ 200 MW.cm^{-2} (~1.2 times threshold pump intensity of 170 MW.cm^{-2}) severe damage to the OPO mirrors and cell windows was observed to occur. At the maximum pump power density of 200 MW.cm^{-2}, the OPO generated 0.25 mJ of output pulse energy in the signal and idler waves at $\theta = 90^o$ for an input pump pulse energy of 10 mJ, indicating a total energy conversion efficiency of 2.5%. Although there was no evidence of single-shot optical damage to the urea crystal itself at pump power densities exceeding 200 MW.cm^{-2}, over long periods of irradiation (several thousand shots) at this pump intensity we observed significant bulk optical damage, in the form of cloudy tracks, within the urea crystal itself. Therefore, the OPO efficiency was limited not only by the single-shot damage to the OPO mirrors, but also by the long-term damage to the urea crystal itself.

(ii) 15-mm-long crystal :

The OPO energy conversion efficiency in this case was found to be significantly higher than the 2.5% attained in the 8-mm-long crystal. The longer crystal length here greatly reduced the oscillation threshold of the device, which meant that the OPO could be operated at many times the oscillation threshold, while still maintaining the pump intensities well below the damage threshold of the optical components. Measurements of energy conversion efficiency in this case were performed by recording the output pulse energy in the signal wave and inferring the energy in the corresponding idler wave using the ratio of the two photon energies. In order to maximise efficiency, a flat partial reflector (R ~ 40%) was used as the OPO output mirror to improve output coupling from the device. While this was found to be successful in increasing the OPO output energy in the regions close to $\theta = 90^o$, at angles near $\theta = 63^o$ this mirror had to be replaced by high-reflector output coupler ($R > 95\%$) to maintain oscillation. At 90^o phase-matching, where the OPO oscillation threshold is lowest (4-5 mJ) owing to an absence of beam walk-off, 3.4 mJ of energy was measured in the signal wave (at 570nm) for an input pump pulse energy of 19 mJ (~ 4 times the oscillation threshold). This corresponds to a total conversion efficiency of 32%, if the energy in the idler wave at 670nm (2.9 mJ) is also included. The OPO efficiency was limited by the optical damage to the OPO mirrors and cell windows. We were also able to improve the conversion efficiency by double passing the pump beam through the OPO cavity. In this configuration, a UV high-reflector mirror ($R > 99\%$ @ 308nm) was used to return the portion of the pump beam transmitted through the OPO cavity back into the non-linear crystal. In this way, the output energy in the signal wave was increased to 3.8 mJ, corresponding to a rise in the OPO efficiency to as high as 37% at $\theta = 90^o$. We did not observe any evidence of optical damage to the urea crystal or the OPO optics in the single-pass-pump configuration, even after sustained OPO operation at the peak pump power density of 76 $MW.cm^{-2}$ required for the maximum efficiency of 32%. In the double-pass-pump geometry, however, significant bulk damage to the urea crystal itself was observed to occur at this pump intensity, over relatively short periods of irradiation (a few hundred shots).

Although parametric gain in urea under type II phase-matching is expected to be angle-independent [1], [13], and thus OPO efficiency is expected to remain constant across the tuning range, in practice a reduction in OPO output power results from the walk-off of the *e-wave* from the pump beam and the *o-wave* as the crystal is angle-tuned away from $\theta = 90^\circ$. We measured the variation in OPO conversion efficiency across the tuning range, for a fixed input pump pulse energy of 19 mJ, as the crystal was angle-tuned away from the 90° phase-match condition. This variation is shown in Fig. 5.8, where the total energy conversion efficiency is plotted as a function of the internal phase-match angle θ. The solid curve represents the calculated variation in the crystal double-refraction angle ρ across the OPO tuning range.

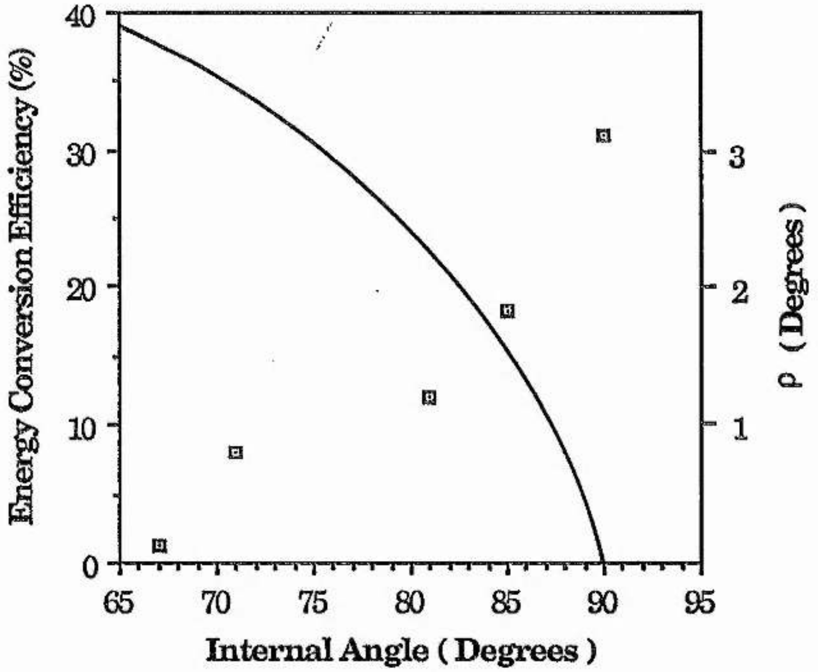

Fig. 5.8. Measured OPO energy conversion efficiency as a function of the internal phase-match angle, θ. The solid curve represents the variation in the crystal double-refraction angle, ρ, across the tuning range of the oscillator. $L = 55$ mm, $R_1 = 95\%$, $R_2 = 40\%$, $l = 15$ mm.

The angle ρ is a measure of the magnitude of *e-wave* walk-off within the non-linear crystal and is given by

$$tan\,(\rho + \theta) = \left(\frac{n_o^2}{n_e^2}\right)\, tan\theta \tag{5-9}$$

where n_o and n_e are the principal refractive indices at the wavelength corresponding to the *e-wave* and are obtained from the Sellemeier equations (5-3). It is clearly evident from the plot that a major consequence of the increase in the magnitude of ρ associated with the decrease in the value of θ is the fall in OPO conversion efficiency.

(iii) 25-mm-long crystal :

The very low oscillation threshold of only 0.023 $J.cm^{-2}$ in this case enabled OPO operation at several times threshold. This meant that high conversion efficiencies could be obtained at relatively modest levels of pump power, comfortably below the damage threshold of OPO optics or the crystal itself. The energy conversion efficiency was measured at 90° phase-matching, for an OPO cavity consisting of a high-reflector rear mirror (R = 95%) and a partial reflector as the output coupler (R = 40%). For an input pump pulse energy of 16.7 mJ (~ 20 times threshold), the OPO generated 6mJ in the signal wave (at 570 nm) and 5.1mJ in the idler wave (at 670 nm). This corresponds to a peak conversion efficiency of 66%, which is exceptionally high for an OPO operating in the visible region. We also investigated the level of pump depletion due to parametric conversion, by monitoring the transmitted pump pulse through the OPO, with the aid of a fast photodiode and an analog storage oscilloscope. The observed pulse shapes corresponding to the transmitted pump beam are shown in Traces 5.1(a)-(d), where the increasing level of pump depletion with increasing OPO cavity Q is clearly demonstrated. In order to obtain these traces, the input pump pulse energy was maintained at a constant value of 16.7 mJ, while the OPO cavity alignment was progressively improved (from (a) to (d)). It can be seen that, with the OPO cavity optimally aligned, the pump pulse is depleted by as much as 85%. This indicates an even higher peak

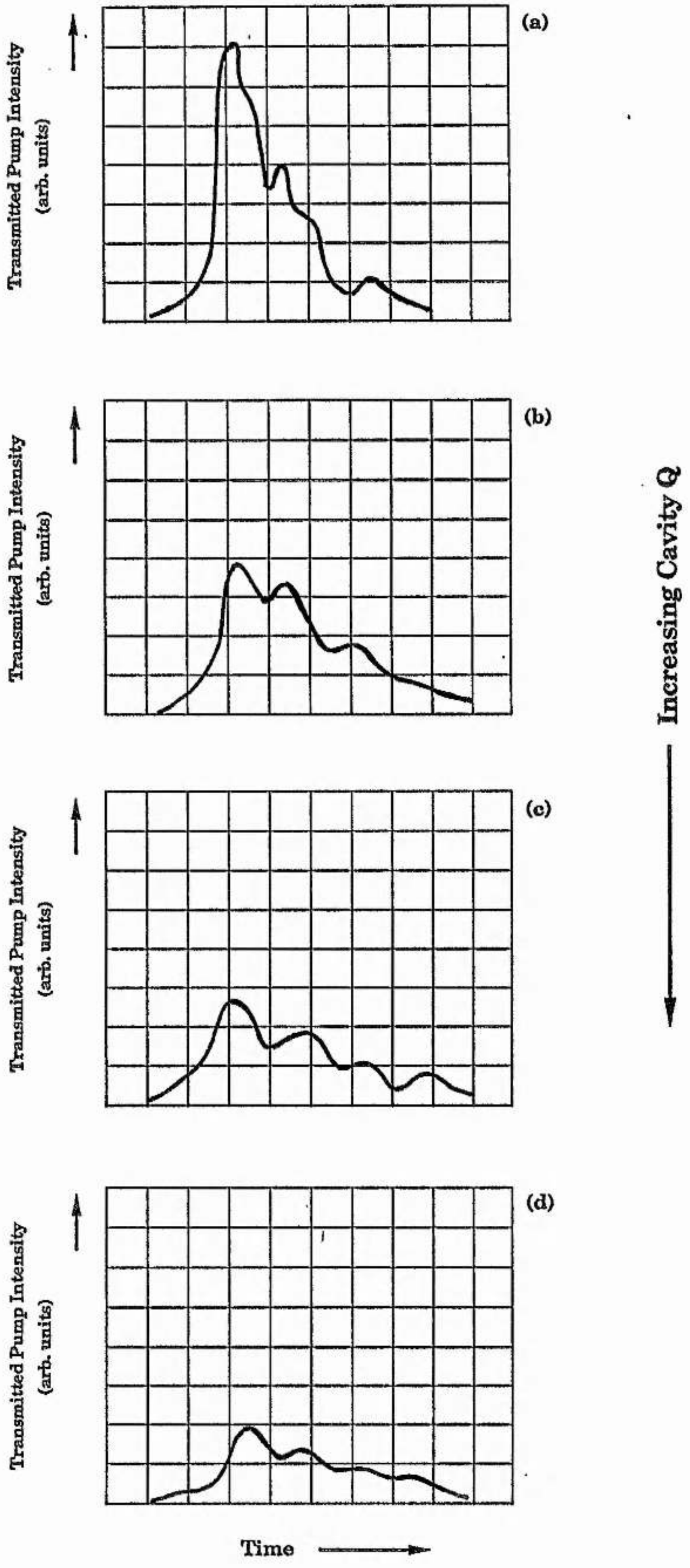

Trace 5.1(a)-(d). Pump depletion in the urea optical parametric oscillator at 90° phase-matching. Crystal length = 25 mm.
Time-scale: 5ns/div.

internal conversion efficiency than the maximum value of 66% measured external to the OPO cavity in the signal and idler waves. This difference may be accounted for by the presence of other losses within the OPO cavity in addition to the mirror transmission loss (e.g. absorption and scattering within the crystal, Fresnel loss from the cell windows, etc.), which lead to the loss of parametric power from the cavity to other than the extracted signal and idler beams. It is also evident that significant pump depletion sets in only over the trailing edge of the pump pulse, after the OPO rise-time to oscillation threshold has elapsed.

It should be noted that during our experiments in this crystal, there was no evidence of any single-shot optical damage to the urea crystal (or the OPO optics) at the pump power levels of 40-45 MW.cm^{-2}, necessary for the maximum conversion efficiency of 66%. However, over long periods of operation (several thousand shots) at this pumping intensity we observed localised damage in the form of cloudy tracks within the crystal. These observations clearly indicate that, although the single-shot optical damage threshold of urea may be as high as a few hundred MW.cm^{-2} at 308 nm, the multiple-shot damage for the material is considerably lower (possibly by as much as an order of magnitude) than this value. Our observations are also consistent with the estimated multiple-shot damage threshold for this material which has been reported by other investigators to be about 40 MW.cm^{-2} for pumping at 355 nm [14].

5.3.4 *Temporal Behaviour*

In the case of the 15-mm-long crystal, the temporal variation of the OPO resonated wave was monitored at $\theta = 90^{o}$ (λ_s = 570nm) with the use of a fast vacuum photodiode (ITL, 800 ps rise-time) and an analog storage oscilloscope (Hewlett-Packard 1727A, 1.3 ns rise-time). For an OPO cavity composed of the 95% rear mirror and the 40% output coupler, the observed pulse profiles were typically 4-5 ns in duration, with a 2-3 ns rise-time, as shown in Trace 5.2. In contrast to the 10-ns pump pulses which were observed to be modulated in their structure at a period corresponding to the round-trip time in the XeCl power oscillator cavity, the OPO pulses were of smooth Gaussian-like profiles.

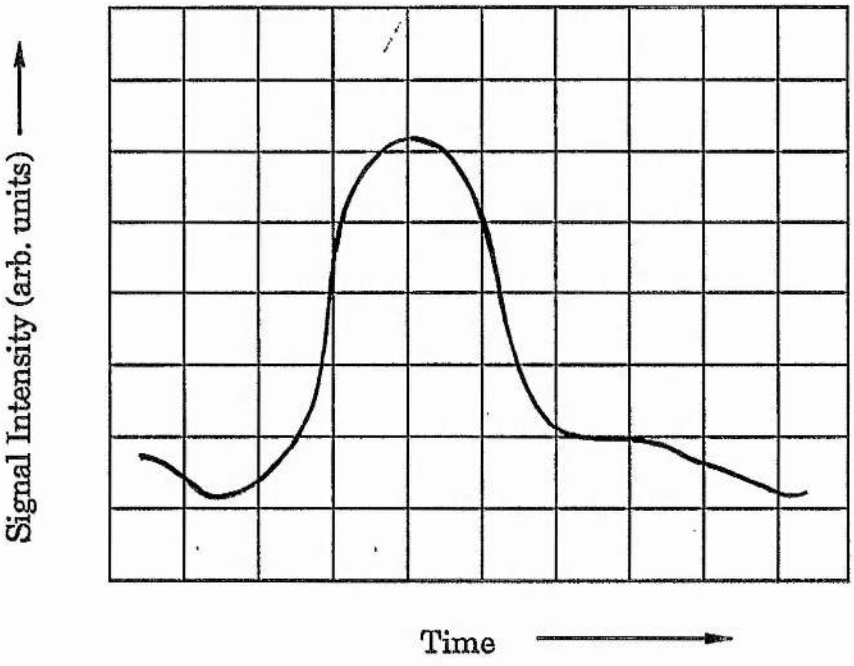

Trace 5.2. Temporal variation of the resonated signal wave at 570 nm ($\theta = 90^o$). $R_1 = 95\%$, $R_2 = 40\%$, $l = 15$ mm, $L = 55$ mm.
Time-scale: 2ns/division.

References to Chapter 5.

[1] W. R. Donaldson and C. L. Tang, Appl. Phys. Lett. 44, 25 (1984)

[2] R. G. Smith, "Optical Parametric Oscillators," in *Lasers*, A. K. Levine and A. J. DeMaria, eds., Dekker, New York (1976)

[3] M. J. Rosker *et al.*, IEEE J. Quantum Electron., QE-21, 1600 (1985)

[4] J-M Halbout *et al.*, IEEE J. Quantum Electron., QE-15, 1176 (1979)

[5] C. Cassidy *et al.*, Opt. Commun. 29, 243 (1979)

[6] F. D. Bloss, "An Introduction to the Methods of Optical Crystallography," Holt, Rinehart and Winston, New York (1961)

[7] M. Ebrahimzadeh and M. H. Dunn, in Postdeadlind Papers, Conf. Lasers Electro-Opt., Opt. Soc. Amer., Washington, DC, 1988, paper PD30.

[8] M. Ebrahimzadeh and M. H. Dunn, Opt. Commun. 69, 161 (1988)

[9] M. Ebrahimzadeh and M. H. Dunn, in Tech. Dig., Conf. Lasers Electro-Opt., Opt. Soc. Amer., Washington, DC, 1989, paper FK1.

[10] M. Ebrahimzadeh *et al.*, Opt. Lett. 14, 560 (1989)

[11] A. J. Henderson *et al.*, submitted to J. Opt. Soc. Amer. B.

[12] S. J. Brosnan and R. L. Byer, IEEE J. Quantum. Electron., QE-15, 415 (1979)

[13] M. J. Rosker and C. L. Tang, J. Opt. Soc. Amer. B 2, 691 (1985)

[14] G. C. Catella *et al.*, IEEE J. Quantum. Electron., QE-24, 1201 (1988)

[15] S. E. Harris, Proc. IEEE 57, 2096 (1969)

6

Beta Barium Borate Optical Parametric Oscillator

6.0 INTRODUCTION

In this chapter, we describe the design, construction, and operating characteristics of a pulsed singly-resonant beta barium borate (β-BaB_2O_4, or BBO) optical parametric oscillator (OPO) pumped at 308nm by the injection-seeded XeCl excimer laser described in chapter 3. This OPO is capable of generating widely tunable radiation over the entire spectral range from 354nm in the near ultraviolet to 2.370μm in the near infrared using a single β-BaB_2O_4 crystal, and energy conversion efficiencies in excess of 10% are demonstrated over a substantial portion of the tuning range in a 12-mm-long crystal. We first discuss some of the properties of β-BaB_2O_4 crystal and describe the design and construction of the OPO. We then present experimental results on the characterisation of the OPO with regard to its tuning range, spectral bandwidth, oscillation threshold, energy conversion efficiency, and spatial as well as temporal behaviour, and compare the experimental findings with the predictions of theory.

6.1 MATERIAL PROPRTIES

Barium borate (BaB_2O_4) is an inorganic material, which has been in existence for half a century. It was discovered by Levin and McMurdie as early as 1949 [1]. The material exists in two distinct solid phases ; a low-temperature β phase and a high-temperature α phase. The transition from the β to α phase occurs at a temperature of 925 ± 5° [2], while the melting point of the material is 1095 ± 3° [3]. The material is grown from melt using the flux growth technique and was first produced in crystalline form in 1968 [4]. The high-temperature α phase of the barium borate crystal is centrosymmetric and therefore does not exhibit any second-order non-linear properties. The low-temperature β phase, on the other hand, does not possess an inversion symmetry in its crystalline structure, and thus can exhibit second-order non-linear susceptibility. This is the phase commonly referred to as beta barium borate, β-BaB_2O_4, or BBO, and is the material used as the OPO medium in this work. It is a negative uniaxial crystal ($n_e < n_o$), for which both type I ($e \rightarrow oo$) and type II ($e \rightarrow oe$) interactions are possible. The effective non-linear coefficient in each case is given by [3], [5]-[7]

$$|d_{eff}| = d_{31} sin\theta + (d_{11} cos3\phi - d_{22} sin3\phi)\, cos\theta \qquad \text{(type I)} \qquad \textbf{(6-1)}$$

$$|d_{eff}| = (d_{11} sin3\phi + d_{22} cos3\phi)\, cos^2\theta \qquad \text{(type II)} \qquad \textbf{(6-2)}$$

where θ is the internal phase-match angle measured from the crystal optic axis, and ϕ is the azimuthal angle, as defined in Fig. 2.6, chapter 2. The definition of the angle ϕ depends on the choice of the co-ordinate system with respect to the crystallographic axes, which also determines the relative magnitude of the *d*-coefficients in (6-1) and (6-2). We follow the convention adopted in [6] and [7], whereby the *abc* co-ordinate system is chosen in such a way that the *c*-axis lies along the crystal optic axis, and the *a*-axis is perpendicular to the crystallographic mirror plane. The azimuthal angle ϕ is then defined as the angle between the projection of the wave normal vector ($\underset{\sim}{k}_p$) onto the *ab*-plane, and the *a*-axis, as illustrated in Fig. 6.1. The figure, as drawn, corresponds to $\phi = 0$. With this convention, it turns out that $d_{22} \sim d_{31} \leq 0.05\, d_{11}$, so that the effective non-linear coefficient is reduced to

$$|d_{eff}| = d_{31} \sin\theta + d_{11} \cos 3\phi \cos\theta \qquad \text{(type I)} \qquad (6\text{-}3)$$

$$|d_{eff}| = d_{11} \sin 3\phi \cos^2\theta \qquad \text{(type II)} \qquad (6\text{-}4)$$

Therefore, in order to maximise d_{eff} for a given phase-match angle θ, we must set $\phi = 0°$ (or $60°$) if type I interaction ($e \rightarrow oo$) is to be utilised, and $\phi = 30°$ (or $90°$) if the crystal is to be used with type II ($e \rightarrow oe$) phase-matching.

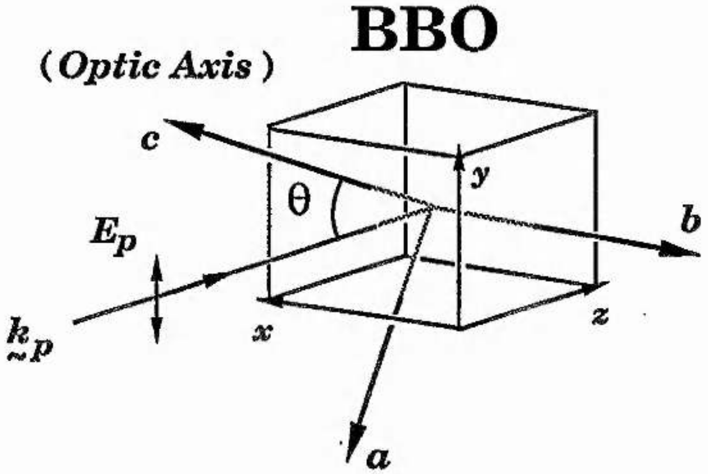

Fig. 6.1. The geometry of β-BaB$_2$O$_4$ crystal, with laboratory axes *xyz* and crystallographic axes *abc* illustrated. The azimuthal angle ϕ, which is the angle between the projection of the wave normal of the pump beam (k_p) onto the *ab*-plane and the *a*-axis, is set to $\phi = 0°$ for maximum gain. The pump beam is launched as an *e-wave*, suitable for type I interaction ($e \rightarrow oo$), at an internal phase-match angle θ to the optic axis (*c*-axis).

We see, from (6-3) and (6-4), that for a given phase-match angle θ, the effective non-linear coefficient in β-BaB$_2$O$_4$ crystal is greater under type I than type II interaction. In the former case, the magnitude of d_{eff} is linearly dependent on $\cos\theta$, while in the latter case the dependence is quadratic. Therefore, the use of type I phase-matching in this crystal will in general be expected to lead to higher parametric gains, lower OPO oscillation thresholds, and thus higher conversion efficiencies than is the case with type II interaction. In addition, although d_{eff} vanishes at non-critical phase-matching ($\theta = 90°$) under type II interaction (see (6-4)), under type I phase-matching a finite component of d_{eff} (first term in (6-3)) remains at $\theta = 90°$. However, this component is proportional to the weak d_{31} coefficient and, as such, results only in very small gains. The only reported case of 90° phase-matching in β-BaB_2O_4 crystal, to the author's knowledge, is that of type I ($oo \rightarrow e$) SHG of a pulsed dye laser output (at 409.6nm) to 204.8nm [7]. However, the conversion efficiency of the process was limited to 4%, but was increased to 17% when the SHG wavelength was tuned away from $\theta = 90°$ to 205.8nm. This increase in efficiency was attributed to the additive contribution of the term involving the d_{11} coefficient, which vanishes at $\theta = 90°$ (see (6-3)). However, in most other applications, including optical parametric oscillation, non-critical phase-matching in this crystal is in general not possible, which implies that in all such processes a finite crystal double-refraction, and hence beam walk-off between the coupled waves, is present. In the case of XeCl-pumped β-BaB_2O_4 OPO discussed here, the double-refraction angle, ρ, is typically 4-5° across the oscillator tuning range (see Fig. 6.4, section 6.3). Hence, in order to ensure maximum gain over the available crystal length (and thus high OPO efficiency), it is important to use a pumping geometry that minimises the effects of Poynting vector walk-off within the crystal. This is achieved by, for example, propagating the pump beam with its longer dimension in the walk-off plane, and is discussed in more detail in section 6.3.

Because of the difficulties associated with the growth of β-BaB_2O_4, production of sizeable single crystals has, up until recently, not been possible. The material was first grown in large sizes (76 mm in diameter, 15mm thick) by Chen and colleagues at the Fujian Institute of Research on the Structure of Matter, People's Republic of China [8]. The crystal was grown from melt, below the phase-transition temperature 925 ± 5^o, using a flux growth technique, and was subsequently characterised for non-linear optical applications. Unlike urea, β-BaB_2O_4 is chemically stable and non-hygroscopic. As such, it does not present any special handling problems. It is mechanically hard, which means that the crystal faces may be easily polished to optical quality and cleaned, and dielectric coatings may be directly applied to the surfaces. The transmission range of the material has been measured by a number of investigators [3], [6], [7], and has been reported to be at least 200nm-2.6μm. The material also possesses a large d_{11} non-linear coefficient of 2.6 pm/V (4.1 times d_{36} in KDP, and 1.8 times d_{14} in urea) [3], [9], although many conflicting estimates of this value exist in the literature. Our measurements of OPO oscillation threshold (see section 6.3.3), however, indicate that the magnitude of this coefficient may in fact be even larger than this figure and possibly as high as ~4 pm/V. The material also exhibits an exceptionally high optical damage threshold. The single-shot threshold for optical damage has been reported to be as high as 13.5 GW.cm^{-2} for 1-ns pulses at 1.064μm, and 7 GW.cm^{-2} at 532nm [3]. The material also appears to have a good high average power capability. At no time during our OPO experiments, did we observe any sign of surface or bulk damage to the β-BaB_2O_4 crystal itself, even after long periods of irradiation (several thousand shots) at pump power densities of a few hundred MW. cm^{-2} (at 308nm).

6.2 OPO DESIGN AND CONSTRUCTION

The OPO consisted of a commercially available single crystal of β-BaB_2O_4 enclosed by a pair of flat dichroic mirrors separated by 28mm, and forming a simple plane-parallel optical cavity. The crystal was purchased from the Fujian Institute of Research on the Structure of Matter, People's Republic of China. It measured 12 mm in geometrical path length (along z in Fig. 6.1), with a 6x8 mm^2 (x x y) aperture, and was cut for type I ($e \rightarrow oo$) phase-matching at a nominal internal angle of θ= 32° to the optic axis. It had polished, but uncoated faces, and was placed inside a perspex holder with no windows. In order to prevent premature optical damage to the crystal (e.g. as a result of mechanical stress, etc.), the location of crystal within the holder was secured by means of a spring-loaded PTFE plunger (rather than a screw). The structure of the crystal holder is shown in Fig. 6.2.

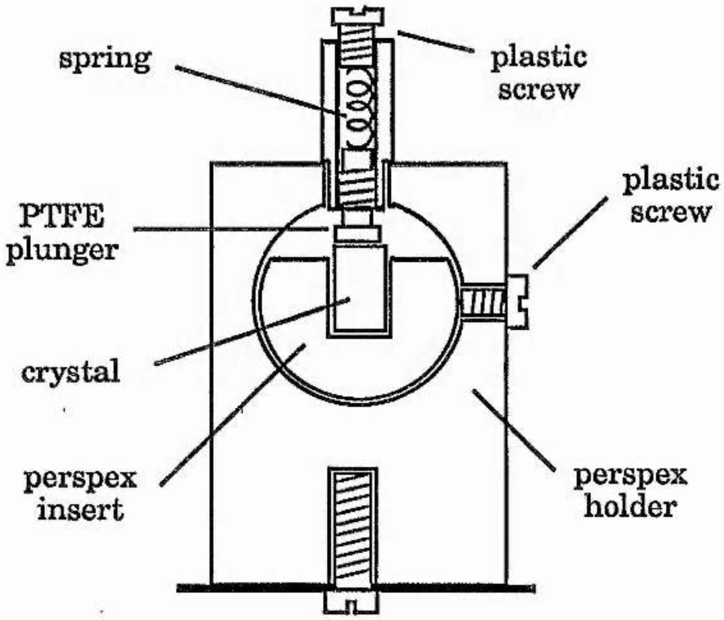

Fig. 6.2. Schematic structure of the β-BaB_2O_4 crystal holder.

The OPO mirrors were identical, and both highly reflecting (R>95%) at the signal wavelength, and had high transmittance (T>95%) at the idler wavelength, thus ensuring singly-resonant oscillation. The rear surfaces of mirrors were also mostly AR-coated at 308nm, and wedged to avoid "etaloning" effects. The pump transmission of the OPO mirrors was greater than 95%, except for the mirror set used to cover the UV regions of OPO tuning range; in this case, the mirror transmittance at 308nm was about 60%. All mirrors were 1" in diameter, with 1/4" thickness, and were placed inside adjustable gimbals to enable cavity alignment. The OPO cavity length was maintained as short as possible (28mm) to provide a maximum number of round-trips for the resonated signal wave over the 10-ns duration of the pump pulse. The crystal holder was also designed with minimum OPO cavity length in mind. An XY-translation stage was used for precise location of the crystal within the OPO cavity and a miniature rotation mount was used to allow angle-tuning of the crystal as well as to enable accurate measurements of the phase-match angle θ. Location along the axis of the optical system (i.e. along z) could be adjusted by translation of the entire OPO assembly along the optical bench. A He-Ne laser beam propagated through pinholes, along the pump beam direction, was used to assist in alignment of the OPO cavity.

6.3 OPO EXPERIMENTS

Figure 6.3 shows a schematic of the experimental design. The pump beam, 1 x 2.5 cm (x x y) in cross-section, was compressed through a x 8 Galilean telescope to a 1.2 x 3 mm spot size, before being launched into the non-linear crystal. The telescope was identical to that used in the case of the urea OPO described in chapter 5, and consisted of two uncoated, non-

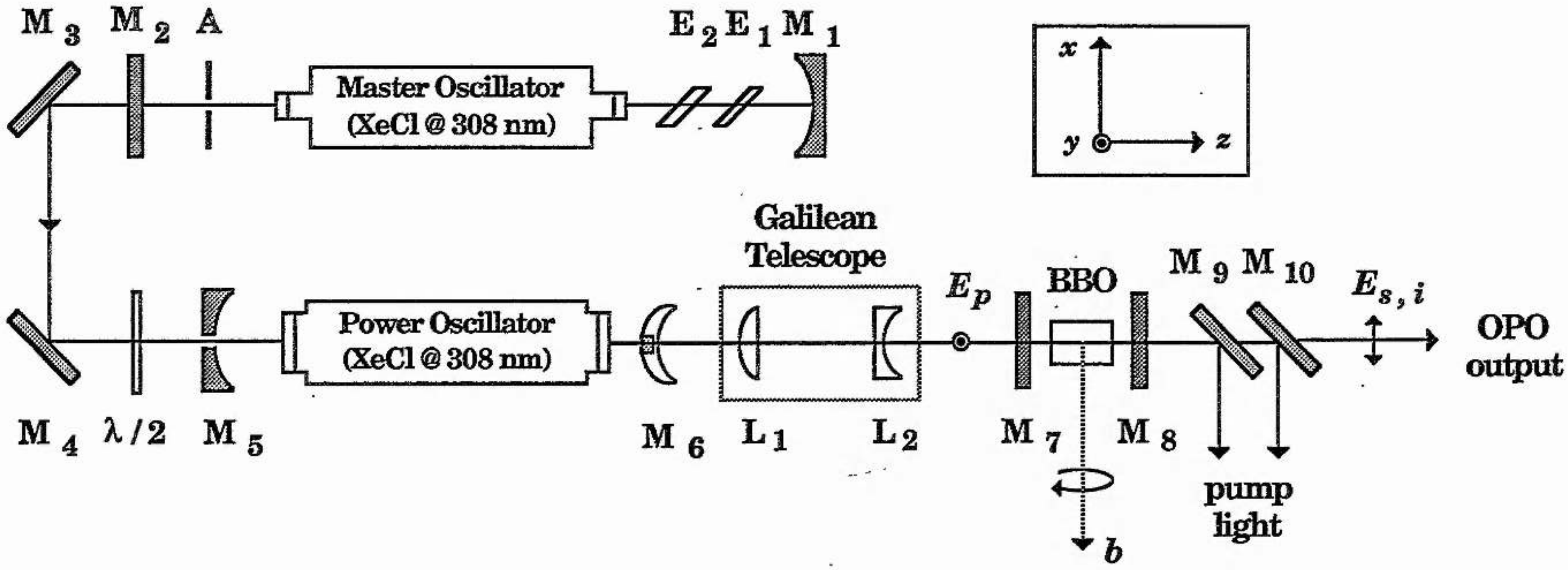

Fig. 6.3. Schematic of the BBO optical parametric oscillator pumped by an injection-seeded, narrowband XeCl excimer laser at 308 nm, with type I interaction (top view).
M's: mirrors; E's: etalons; A: aperture; L's: lenses.

best-form, quartz lenses; a plano-convex lens of focal length $f = 2$m, and a plano-concave lens of focal length $f = -25$ cm, separated by ~1.75 m. From geometrical considerations, the eight-fold compression of the pump beam should result in an increase in its angular spread from 60μR (full-angle) to approximately 0.5mR, in the phase-match (yz) plane. However, the measured full-angle of divergence of the compressed pump beam in this plane was found to be about twice this value and approximately 1mR. This excessive angular divergence, which may be due to aberrations introduced by the compression optics, is some 4 to 5 times larger than the calculated angular acceptance angles for the β-BaB_2O_4 crystal across the oscillator tuning range (see Fig. 2.9 (b), chapter 2), and as such may lead to a significant increase in the OPO oscillation threshold. Therefore, major enhancement in OPO performance may be brought about by more careful design of the beam compression optics, and this may well be an area where further improvements may be effected.

The pump beam was launched into the OPO as an *e-wave* (suitable for type I phase-matching) with its electric vector (E_p) as shown in Figs. 6.1 and 6.3, and the parametric waves emerged as *o*-waves. In view of walk-off of the pump (*e wave*) from the parametric waves (*o waves*) within the non-linear crystal, which occurs in the plane containing the pump wavevector k_p and the crystal optic axis (yz-plane), it is desirable to choose a phase-matching geometry which results in maximum possible interaction over the available length of the non-linear crystal. For this reason, the plane of polarisation of the pump beam was adjusted to yield an electric vector along the larger cross-sectional dimension of the pump beam (along y), thus minimising the effects of beam walk-off for the given phase-matching geometry and crystal orientation used in these experiments. Fig. 6.4 shows the calculated variation in the double-refraction angle ρ and the corresponding aperture length l_a for a 3mm pump spot size (diameter), across the tuning range of the β-BaB$_2$O$_4$ OPO. The calculations are based on the published Sellemeier equations for the β-BaB$_2$O$_4$ crystal, namely [7]

$$n_o^2(\lambda) = 2.7359 + \frac{0.01878}{(\lambda^2 - 0.01822)} - 0.01354\,\lambda^2 \qquad \textbf{(6-5 (a))}$$

$$n_e^2(\lambda) = 2.3753 + \frac{0.01224}{(\lambda^2 - 0.01667)} - 0.01516\,\lambda^2 \qquad \textbf{(6-5 (b))}$$

with λ in microns, and are valid for a an OPO pumped at 308nm under type I phase-matching scheme ($e \rightarrow oo$). As can be seen from the plots, the effective walk-off length l_a ranges from approximately 3.3 to 4.0 cm across the entire OPO tuning range. These values are typically 3 to 4 times greater than the 1.2 cm full length of the β-BaB$_2$O$_4$ crystal used here and imply that the effective crystal length, and thus parametric gain, is not limited by the Poynting vector walk-off of the pump from the signal and idler waves. Further, the pump beam geometry used in our experiments to minimise the effects of walk-off has an additional advantage in that the smaller angular divergence is now in the phase-match plane (yz-plane), because of the larger cross-sectional dimension along y, and as such it more closely approaches the the constraint given by equation (2-61), and shown in Fig. 2.9(b), chapter 2. This ensures a lower oscillation threshold across the OPO tuning range than would be the case with the alternative pump beam geometry. The OPO mirrors were highly reflecting at the signal wavelength, but were highly transmitting at the idler and pump wavelengths. The OPO was, therefore, singly-resonant over its entire tuning range. Wavelength tuning of the OPO was accomplished by altering the internal phase-match angle θ through rotation of the crystal

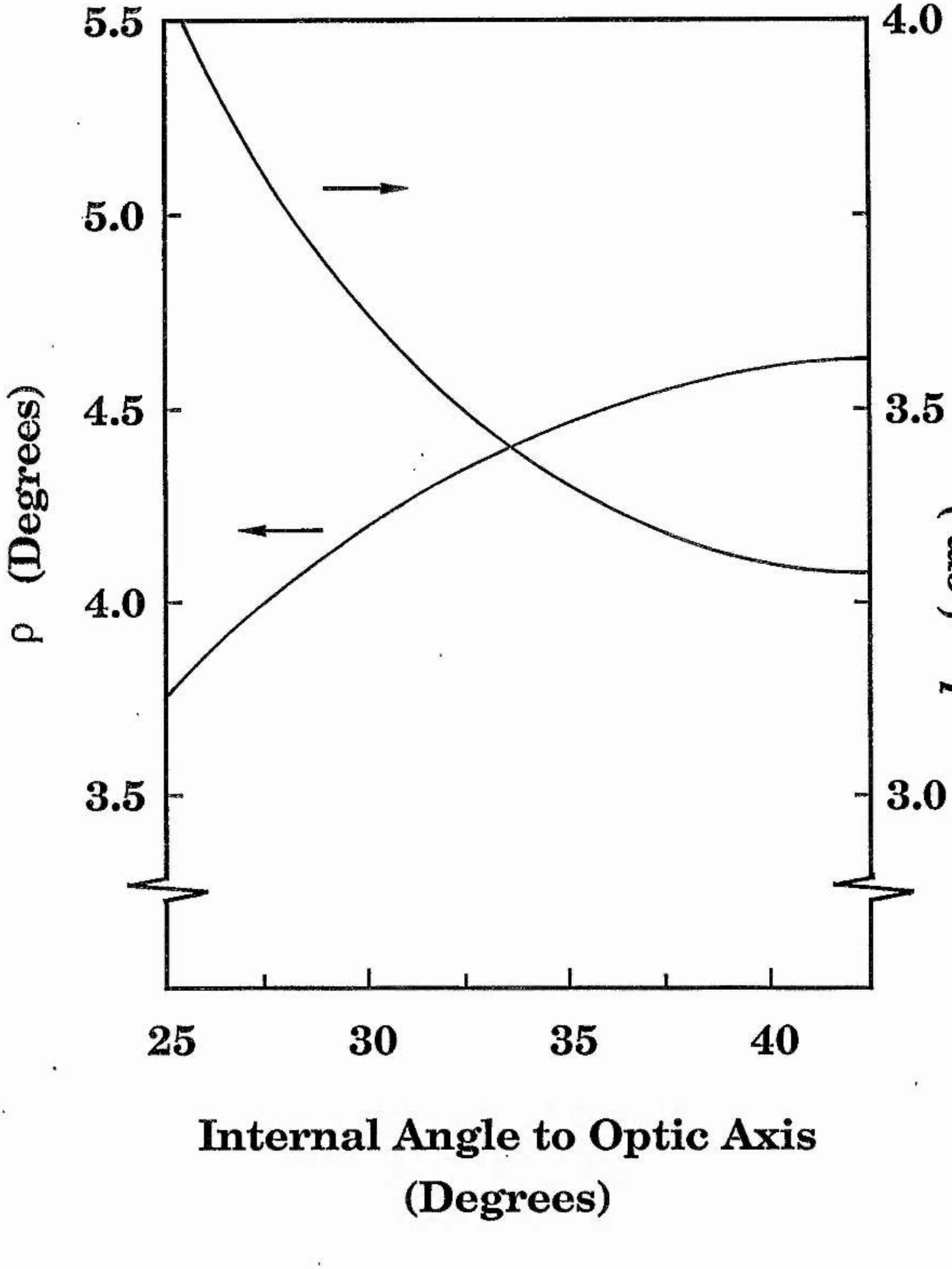

Fig. 6.4. Crystal double-refraction angle, ρ, and the walk-off length, l_a, for a 3mm pump spot size (diameter), across the tuning range of the BBO optical parametric oscillator.

about the *b*-axis (Figs. 6.1 and 6.3). In the following sections, we describe the results of these experiments in detail.

6.3.1 *Tuning Range*

The tuning range of the β-BaB_2O_4 OPO was determined by directing the generated output from the oscillator onto the entrance slit of a calibrated high-resolution monochromator (Rank Hilger, Monospek 1000). The residual pump light emerging from the OPO was separated from the parametric waves by a pair of narrowband UV high reflectors ($R > 90\%$ at 308nm), as shown in Fig. 6.3. The calculated tuning curve together with the experimental results are shown in Fig. 6.5. An expanded version of the high-frequency branch of the tuning curve is further illustrated in Fig. 6.6. For each value of the phase-match angle θ, the wavelength of the UV/visible component was experimentally determined and the corresponding IR/visible wavelength was inferred from this value. The OPO could be tuned from 354nm in the near ultraviolet, throughout the visible, to 2.370μm in the near infrared by altering the internal phase-match angle between $\theta=26.5^o$ and $\theta=39^o$. The tuning was continuous over the entire wavelength range, except for a small gap from 372nm to 398nm in the ultraviolet, with a corresponding infrared gap from 1.790μm to 1.362μm, due to a lack of available mirrors. We foresee no difficulty in covering this remaining wavelength region by utilising mirrors of appropriate reflectivity profile. We believe the observed tuning range was limited, not by the ultraviolet reflectivity of the available mirrors, but by the infrared absorption cut-off in β-BaB_2O_4 crystal which occurs at approximately 2.3μm [6]. This is because the reflectivity bandwidth of the available mirrors extended well beyond the measured 354nm limit in the ultraviolet,

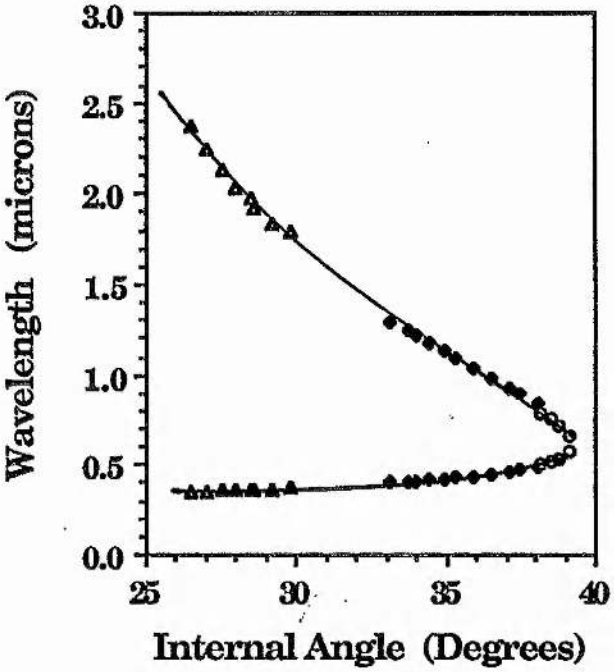

Fig. 6.5. Tuning range of the β-BaB_2O_4 optical parametric oscillator pumped at 308 nm, with type I interaction ($e \rightarrow oo$). The solid curve represents the calculated tuning curve based on the Sellemeier equations (6-5), while the output from the oscillator is indicated by the experimental points. The different symbols correspond to the three sets of mirrors used in these experiments; triangle: $R_1 = R_2$~90% @ 320-370 nm; diamond: $R_1 = R_2$~95% @ 420-480 nm; circle: $R_1 = R_2$~95% @ 500-600 nm.

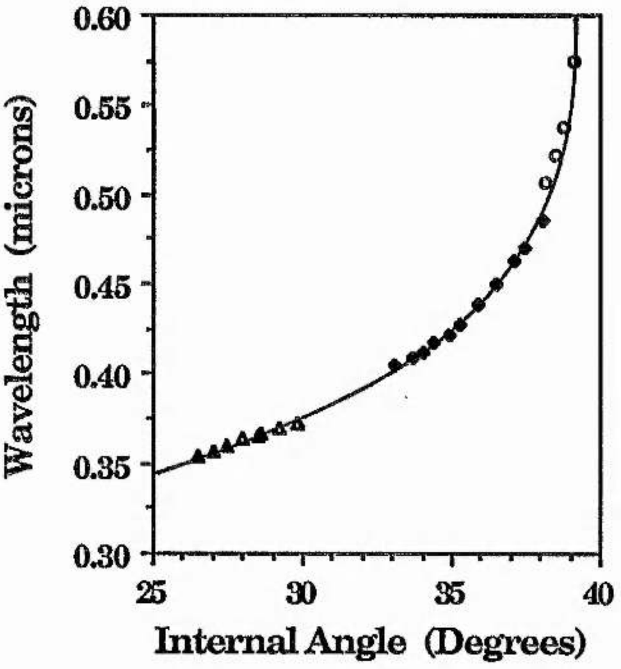

Fig. 6.6. The short-wavelength coverage of the β-BaB_2O_4 optical parametric oscillator, from 354 nm in the near UV to ~616 nm (degeneracy). All conditions as in Fig. 6.5.

to 320nm. Three sets of dichroic mirrors were used to cover the observed OPO tuning range. In each case, the mirror pairs were identical and highly reflecting at the signal wavelength, with high transmittance at the idler wavelength, thus ensuring singly-resonant oscillation. The first set of mirrors had high reflectance (R=95%) at 500-600nm, and were also highly transmitting (T=95%) at 308nm. The second set had coatings with 95% reflectivity at 420-480nm, and 95% transmittance at the pump wavelength. The rear surfaces of both sets of mirrors were also antireflection-coated at 308nm. The third set of mirrors had greater than 90% reflectance for signal wavelengths over the range 320-370nm. However, the transmittance of these mirrors at the pump wavelength was only 60%, with no antireflection coating on their rear surfaces, at 308nm. The reflectivity bandwidth of the available OPO mirrors provided oscillation at signal wavelengths in the ultraviolet and visible branch of the tuning curve up to wavelength degeneracy, with the non-resonant idler component covering the corresponding infrared and visible portions. Although, the restrictions placed upon the allowable pump bandwidth $\Delta\nu_p$ indicate that it is advantageous to resonate the longer wavelength of the two parametric waves (see Fig. 2.8 (b), chapter 2), in practice this would require more sets of mirrors than used here, to maintain oscillation throughout the available tuning range. In contrast, coverage of the short-wavelength portion of the tuning curve, as here, requires relatively few sets of mirrors and as such is a more practical option, provided the pump laser bandwidth lies comfortably within the corresponding limits of $\Delta\nu_p$, as is the case here.

6.3.2 *Spectral Linewidth*

In general, the spectral linewidth of the OPO is set primarily by the oscillator gain bandwidth which is, in turn, determined by crystal birefringence, dispersion, and length. From equation (2-57) and Fig. 2.7, chapter 2, the full-width half-power gain bandwidth for the OPO can, for small gains ($1< \kappa^2 l^2 < 10$), be defined by the condition $|\Delta k \sim \pi / l$ [10], [11]. The signal linewidth (full-width at half-maximum power gain) arising from this gain bandwidth may thus be shown to be

$$\Delta\nu_{s1} = \frac{c}{l} \; [(n_i - n_s) + \lambda_s (\frac{\partial n_s}{\partial \lambda_s}) - \lambda_i (\frac{\partial n_i}{\partial \lambda_i})]^{-1} \qquad (6\text{-}6)$$

where the subscripts *s* and *i* denote the signal and idler, respectively, and λ is the free-space wavelength. In practice, the angular and spectral spread of the pump beam may also lead to significant broadening of OPO bandwidth. This contribution can be determined by considering the extent of the departure from the ideal phase-matching conditions ($\Delta k = 0$), due to the finite angular divergence and spectral spread of the pump beam. The component of signal linewidth resulting from the angular divergence of the pump beam can be shown, under critical phase-matching conditions, to be given by

$$\Delta\nu_{s2} = \frac{1}{2} \frac{c}{\lambda_p} (\frac{\partial n_p}{\partial \theta}) \, \delta\theta_p \; [(n_s - n_i) + (\lambda_i \frac{\partial n_i}{\partial \lambda_i} - \lambda_s \frac{\partial n_s}{\partial \lambda_s})]^{-1} \qquad (6\text{-}7)$$

where $\delta\theta_p$ is the divergence full-angle of the pump beam. Similarly, the pump bandwidth contribution to signal linewidth may be obtained from

$$\Delta\nu_{s3} = \Delta\nu_p \; [(n_p - n_i) + (\lambda_i \frac{\partial n_i}{\partial \lambda_i} - \lambda_p \frac{\partial n_p}{\partial \lambda_p})] \; [(n_s - n_i) + (\lambda_i \frac{\partial n_i}{\partial \lambda_i} - \lambda_s \frac{\partial n_s}{\partial \lambda_s})]^{-1} \qquad (6\text{-}8)$$

where $\Delta\nu_p$ is the pump bandwidth (full-width at half-maximum). In writing (6-7) and (6-8), we have ignored the second and higher-order terms in the expansion of Δk. The idler bandwidth is also defined by similar expressions to (6-6), (6-7), and (6-8), with the subscripts s and i interchanged. In general, the pump bandwidth contribution to OPO linewidth is expected to be small, given the restrictions placed upon $\Delta\nu_p$ for optimum OPO operation (see section 2.5.1, chapter 2). Hence, the signal and idler linewidths are primarily determined by the oscillator gain bandwidth and pump beam divergence.

The spectral bandwidth of the constructed oscillator in both parametric waves was measured at different points on the tuning curve. The result of these measurements is shown in Figs. 6.7 and 6.8, where the obtained signal and idler linewidth values for a given value of the internal phase-match angle θ are plotted against their respective wavelengths. All experimental data were taken for a constant set of OPO cavity and pump beam parameters. The observed spectra in each case exhibited a weak secondary peak in their structure in addition to the strong primary spectral component. One possible explanation for this behaviour may be the presence of the secondary maximum in the oscillator gain lineshape [10], [11]. This component may become significant at pump power levels well above threshold, where high parametric gain can be expected. The linewidth values shown in Figs. 6.7 and 6.8, correspond to the main spectral feature. Also shown in the figures is the predicted linewidth for the oscillator calculated from equations (6-6), (6-7), and (6-8), using $\Delta\nu = \Delta\nu_1+\Delta\nu_2+\Delta\nu_3$, but expressed in wavelength units (nm). The calculations are based on the appropriate Sellemeier equations for β-BaB_2O_4 crystal (equations (6-5), above) and correspond to a crystal of length $l = 1.2$ cm. The pump beam full-angle of divergence is taken as $\delta\theta_p = 1$mR. It is seen from

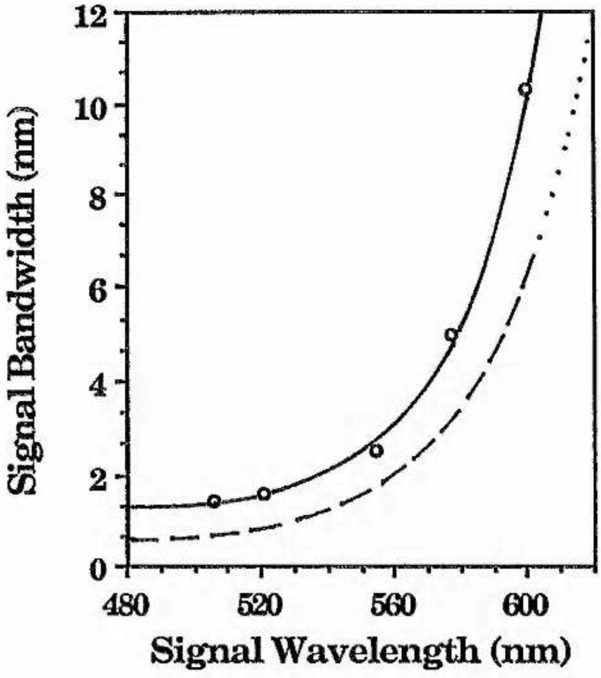

Fig. 6.7. The variation in signal linewidth across the oscillator tuning range. The solid curve represents the best fit to the experimental data, while the total predicted linewidth in wavelength units (nm), obtained from (6-6), (6-7) and (6-8), is represented by the dashed curve. The dotted curve represents those regions of the tuning range (near degeneracy), where the first-order approximations in the bandwidth calculations may not be valid, and higher-order terms in the expansion of Δk may have to be taken into account. OPO cavity parameters: $R_1 = R_2 \sim 95\%$, $L = 28$ mm; pump pulse energy: 15 mJ.

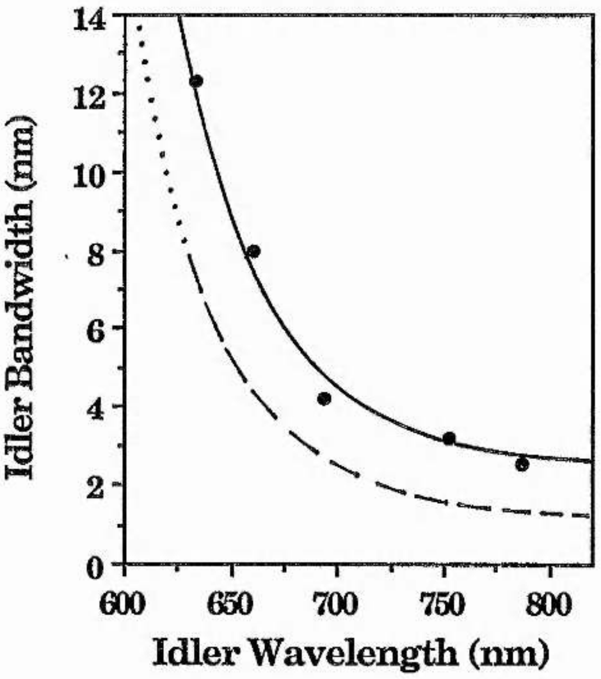

Fig. 6.8. The variation in idler linewidth across the OPO tuning range. All conditions as in Fig. 6.7.

the plots that the measured linewidths of the signal wave (ranging from ~1.5 to ~10.5nm) in wavelength units (nm) are somewhat smaller than the corresponding idler linewidths (ranging from ~2.5 to ~12.5nm) across the oscillator tuning range. However, for each internal phase-match angle θ, the two linewidths when expressed in frequency units (Hz or cm^{-1}) are, within the experimental error, equal, as expected. Further, in both cases the linewidth increases as the oscillator is tuned towards wavelength degeneracy (at 616nm). These observations are in favourable agreement with the predicted variation in OPO linewidth across the tuning range, although the measured linewidths for both parametric waves are consistently higher than those expected from the theoretical calculations, at all points on the tuning curve. This may be due to operation well above (~ 2-3 times) the oscillation threshold.

6.3.3 *Oscillation Threshold*

The OPO oscillation threshold was measured at several points across the tuning range by attenuating the pump beam using UV neutral density filters and recording the pump pulse energy at which oscillation could just be maintained. All measurements were performed for a fixed set of oscillator parameters including a constant cavity length (L = 28mm) and mirror reflectivities ($R_1 = R_2 \sim 95\%$). The threshold pump pulse energy, corrected for the pump transmission of the OPO input mirror (M$_7$ in Fig. 6.3), was found to vary from approximately 10mJ at a signal wavelength of 354nm in the ultraviolet, to about 4.5mJ at 590nm in the visible. The corresponding threshold energy fluence for oscillation varied between 0.28 and 0.125 J.cm^{-2} over this wavelength range, with an associated threshold pump power density at the non-linear crystal ranging from 28 to

12.5 MW.cm^{-2}, respectively. These values are far below the expected single-shot UV damage threshold for β-BaB_2O_4 crystal, which we estimate to be of the order of a few hundred MW.cm^{-2} at 308nm. Our estimates are based on the previously observed damage threshold figures for the material which reportedly range from about 120 MW.cm^{-2} at 266nm [12] to $>$ 400 MW.cm^{-2} at 355nm [13]. As a result, even after sustained OPO operation at pump power levels 3 to 4 times the threshold power density, there was no evidence of any surface or bulk damage to the β-BaB_2O_4 crystal itself. In Fig. 6.9, the obtained values of threshold energy fluence (in J.cm^{-2}) are plotted for various signal wavelengths. It is important to note that the measured threshold values correspond to an oscillator that is singly-resonant over its entire tuning range, even in the regions close to wavelength degeneracy (at 616nm). The rapid fall in the reflectivity of the available mirrors beyond 600nm prevented access to wavelength degeneracy where doubly-resonant oscillation, and thus a significant reduction in the oscillation threshold can be expected. Although, reliable parametric oscillation was obtained at wavelengths as close to degeneracy as 610nm (with a corresponding component at 622nm), the reflection coefficient of the OPO mirrors was typically several times smaller for the longer wavelength than the corresponding shorter wavelength. Therefore, even in the wavelength regions close to degeneracy, oscillation was confined only to the shorter wavelength component and the OPO was acting as a singly-resonant oscillator.

The threshold energy fluence for the OPO may be calculated using the theoretical model of Brosnan and Byer [14], which was described in chapter 5. This model, which is valid for a pulsed singly-resonant OPO under type I phase-matching in a negative uniaxial crystal ($e \rightarrow oo$), may be directly applied to the β-BaB_2O_4 OPO discussed here. In our calculations, however, the Gaussian spatial distribution assumed for the coupled fields in [14] has been replaced by a "top hat" intensity profile which is more appropriate for the XeCl pump beam used in these experiments. For this case, the signal coupling coefficient (equation (B-3) in [14]) in the presence of walk-off can be shown, for small walk-off angles, to be given by

$$c_s = \frac{1}{1+\frac{\rho z}{2W_y}} \qquad \textbf{(6-9)}$$

where ρ is the double-refraction angle and W_y is the beam radius in the walk-off (yz) plane. The coupled amplitude equations (B-8) and (B-9) in [14] are then modified to

$$\frac{dE_s}{dz}+\alpha_s E_s = j\,\xi_s \frac{1}{1+\frac{\rho z}{2W_y}}\, g_s E_p E_i^* e^{j\Delta kz} \qquad \textbf{(6-10 (a))}$$

$$\frac{dE_i}{dz}+\alpha_i E_i = j\,\xi_i \frac{1}{1+\frac{\rho z}{2W_y}}\, E_p E_s^* e^{j\Delta kz} \qquad \textbf{(6-10 (b))}$$

where, we have assumed that the idler beam has the same dimension as the signal and equal to that of the pump beam. The factor g_s is the spatial mode coupling coefficient in the absence of beam walk-off, defined by (5-4), and ξ_m is the interaction coefficient, defined by (5-6), in chapter 5. All other variables are as defined in [14]. Assuming the signal and idler fields have the same profile as their respective driving polarisations, that is $W_s = \overline{W}_s$ and $W_i = \overline{W}_i$, the modified coupled amplitude equations (6-10) may be solved to yield the OPO threshold energy fluence as

$$J_0 \simeq \frac{2.25}{\delta \mathcal{L}'^2}\tau\left[\frac{L}{2\tau c}\ln\frac{P_n}{P_0} + 2\alpha l + \ln\frac{1}{\sqrt{R}} + \ln 2\right]^2 \qquad \textbf{(6-11)}$$

where the parameter δ is defined by eqn. (5-8), chapter 5, and the modified effective parametric gain length $\mathcal{L}'$ (cf equation (5) in [14]) is given by

$$\mathcal{L}' = \frac{2W_y}{\rho}\ln\left(1+\frac{\rho l}{2W_y}\right) \qquad \textbf{(6-12)}$$

Also shown in Fig. 6.9, is the theoretical variation in the threshold energy fluence J_0 across the tuning range of the oscillator, calculated from (6-11). The calculations have been performed for several values of the non-linear coefficient d_{11} for β-BaB_2O_4 crystal, as there appears to be some uncertainty regarding the magnitude of this coefficient. The value of d_{11} has been variously reported by several investigators as ranging from ~1.6pm/V [6] to ~2.6pm/V [9], and possibly higher [3].

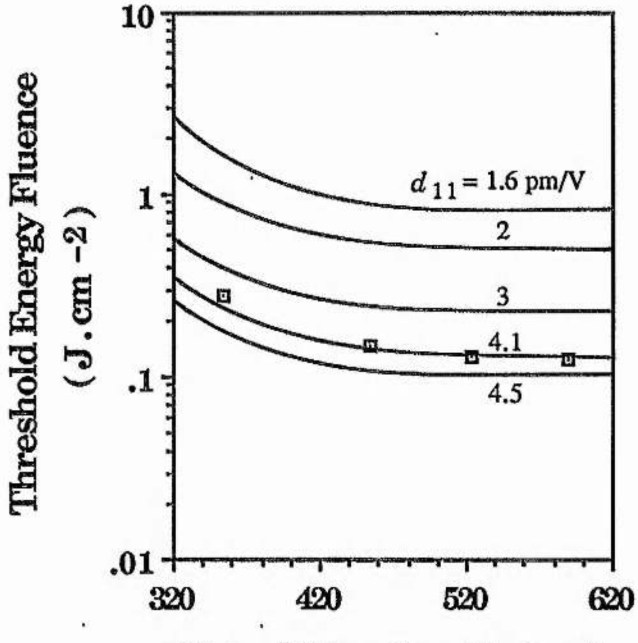

Fig. 6.9. The variation in the threshold energy fluence across the tuning range of the β-BaB_2O_4 OPO. The solid curves represent the predicted fluence for the described OPO, for various values of the non-linear coefficient d_{11}, and are derived from (6-11).

It is seen from Fig. 6.9, that the OPO oscillation threshold follows the same trends as predicted by the theoretical model. However, the observed threshold energy fluence values for the oscillator are low compared with the predictions of the model, for the range of values of d_{11} already reported in the literature. This discrepancy may be explained by noting that equation (6-11) is strictly applicable to a single-frequency pump and single-frequency signal oscillation. In the case of a multi-mode pump source ($\Delta\nu_p$ ~ 0.2 cm^{-1}) and multi-mode signal oscillation (several nm), as here, the model should be used only for qualitative estimates of oscillation threshold and not for quantitative measurements of the non-linear coefficient.

The dependence of oscillation threshold on OPO cavity parameters was also investigated at a signal wavelength of 454nm by measuring the threshold energy fluence for various values of cavity length and mirror reflectivities. The result of these measurements is shown in Figs. 6.10 and 6.11, where the expected reduction in the oscillation threshold with decreasing cavity length and increasing cavity Q is clearly demonstrated. The solid curves, in each case, represent the calculated dependence, predicted by the theoretical model for several values of d_{11}. The decrease in OPO cavity length results in an increase in the number of round-trips of the resonated wave over the duration of the pump pulse, while the increase in mirror reflectivity increases the net gain per round-trip at the signal wavelength, both resulting in a lower oscillation threshold.

6.3.4 *Energy Conversion Efficiency*

The energy conversion efficiency of the β-BaB_2O_4 OPO was measured at different points across the oscillator tuning range. The measurements were performed by recording the output pulse energy in the signal and

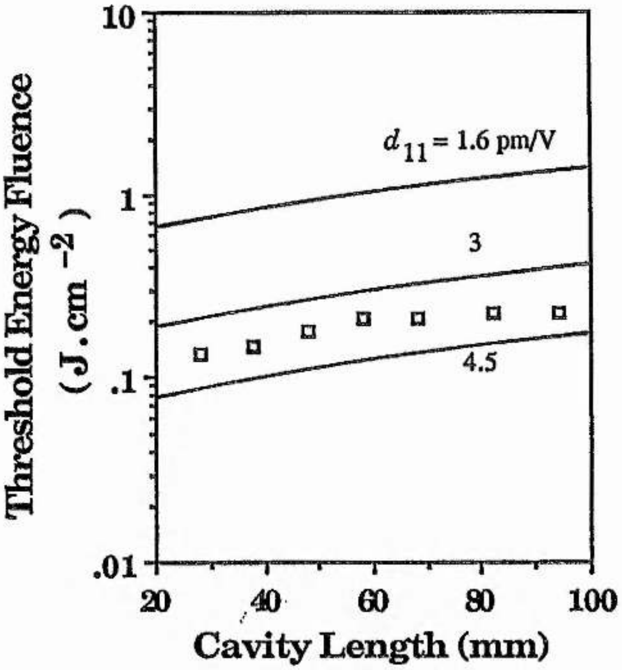

Fig. 6.10. The calculated and measured dependence of OPO oscillation threshold on cavity length, at a signal wavelength of 454 nm. The solid curves corresponding to different values of the d_{11} coefficient, are derived from (6-11).

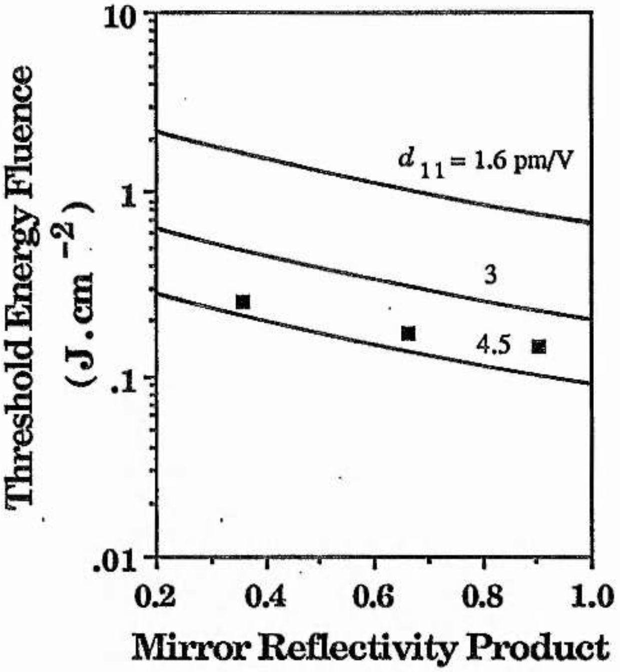

Fig. 6.11. The calculated and measured dependence of OPO oscillation threshold on output coupling, at a signal wavelength of 454 nm. The solid curves corresponding to different values of the d_{11} coefficient, are derived from (6-11).

idler waves for a fixed input pump pulse energy, on a pyroelectric detector (Scientech 362). In each case, the output pulse energy in the two waves was monitored from one end of the oscillator and then doubled to allow for the symmetry in the output coupling from the OPO cavity, to yield the total output. Fig. 6.12 shows the measured overall energy conversion efficiency in both the signal and idler waves for a range of signal wavelengths from 354 to 590nm (corresponding to an idler wavelength range from 2.370μm to 644nm). The experimental data correspond to an input pump pulse energy of 17.5mJ and represent the fraction of input pump energy converted to useful optical output in the two parametric waves. It is seen from the plot that over a significant wavelength range in the visible from about 454 to 590nm (corresponding to an idler band from approximately 958 to 644nm) conversion efficiencies exceeding 10% can be maintained, and output energies approaching 2mJ per pulse can be obtained from the OPO. The peak efficiency in these experiments was limited by the low optical damage threshold of OPO mirrors (~ $50MW.cm^{-2}$), which prevented OPO operation at pump power intensities above ~ 3 to 4 times the oscillation threshold. This limitation was particularly severe in the UV regions of the tuning curve, where the poor pump transmittance of the mirrors resulted in lower-than-expected damage threshold (~ $35MW.cm^{-2}$). Therefore, in these regions the OPO could only be operated at approximately 1.25 times above threshold and the energy conversion efficiency was found to be low. The use of OPO mirrors of improved optical damage threshold and pump transmission properties should enable operation of the device at pump power intensities well above the oscillation threshold, where much higher conversion efficiencies may be expected. The constraint on damage to OPO optics may, in turn, be eased by the use of crystals of larger geometrical path lengths or by employing other cavity configurations such as that used in [12].

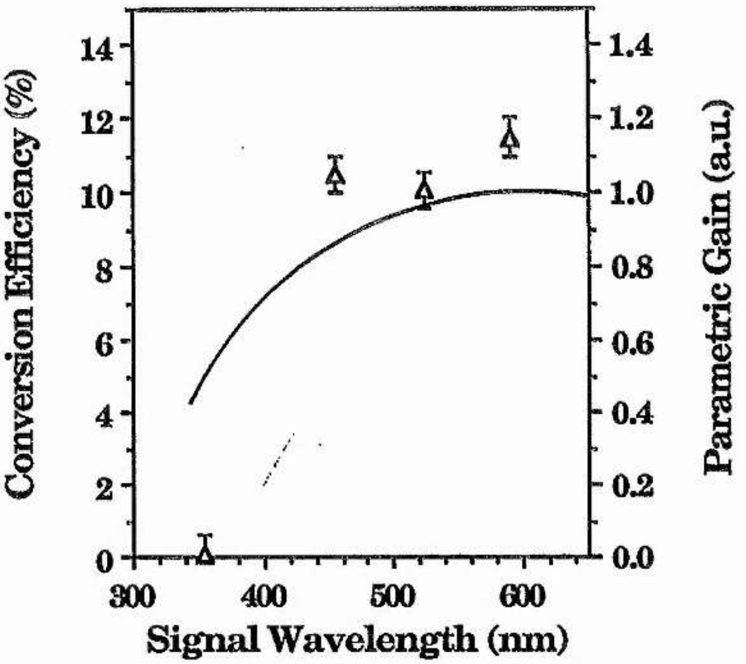

Fig. 6.12. The variation in the overall energy conversion efficiency of the β-BaB_2O_4 OPO in the signal and idler waves, across the tuning range of the oscillator. The solid curve represents the predicted variation in parametric gain, in terms of the quantity $|d_{eff}|^2(1-\Delta^2)$, and has been obtained from eqn. (2-36), chapter 2.

For a given input pump power, the energy conversion efficiency of the oscillator at a given wavelength is also expected to be strongly dependent on the variation in the parametric gain across its tuning range. This variation may be seen by rewriting the gain factor (eqn. (2-36), chapter 2), as

$$\kappa^2 = \frac{2\mu\omega_0^2(1-\Delta^2)\ |d_{eff}|^2\, S_p(0)}{n_p\, n_s\, n_i\, c\varepsilon_0^2} \qquad (6\text{-}13)$$

The quantity $(1-\Delta^2)$ is the "degeneracy factor", defined by

$$\omega_s = \omega_0(1-\Delta) \quad , \quad \omega_i = \omega_0(1+\Delta) \quad , \quad \omega_s\,\omega_i = \omega_0^2(1-\Delta^2) \qquad \textbf{(6-14)}$$

where $\omega_0 = \frac{1}{2}\omega_p$ is the degenerate frequency. It is clearly seen from (6-13), that the parametric gain, and thus conversion efficiency of the OPO, is largely dependent on the degeneracy factor $(1-\Delta^2)$. This variation is also shown in Fig. 6.12, in terms of the quantity $|d_{eff}|^2(1-\Delta^2)$ across the wavelength coverage of the device, where we have assumed that the change in the refractive indices n_p , n_s , and n_i over the oscillator tuning range can be neglected. It is clearly seen from the plot that the maximum gain occurs at, and in the regions close to, wavelength degeneracy (at 616nm) and a fall in gain, and thus conversion efficiency, is to be expected as the OPO is tuned away from degeneracy. Therefore, considerations of parametric gain alone indicate a lower conversion efficiency in the ultraviolet spectral regions of the tuning curve. This variation in gain may also account for the relatively high UV oscillation threshold (28MW.cm^{-2}) observed at 354nm.

The energy conversion efficiency of the OPO was also measured as a function of the pumping intensity at a signal wavelength of 454nm. The result of these measurements is shown in Fig. 6.13, where the total energy conversion efficiency in the signal and idler waves is plotted against the number of times above threshold. The threshold pump pulse energy at this signal wavelength, and for a cavity composed of two high reflectors (R_1 = R_2 = 95%), was about 5mJ. When pumping at approximately 3 to 4 times above oscillation threshold, the conversion efficiency reached 10.5%, with 1.25mJ of output pulse energy in the signal wave and 0.6mJ of output in the corresponding idler wave at 958nm.

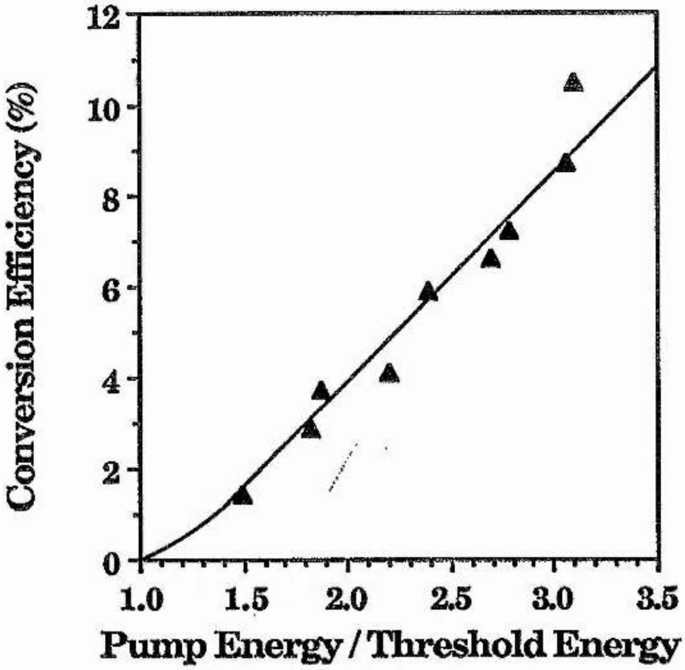

Fig. 6.13. The energy conversion efficiency of the β-BaB$_2$O$_4$ OPO as a function of the pumping strength. The line represents the best fit to the experimental data. Signal wavelength: 454 nm; OPO cavity: $R_1 = R_2 \sim 95\%$.

6.3.5 *Spatial and Temporal Characteristics*

We measured the output beam divergence of the OPO in the signal wave at 454nm, by recording the spot sizes at several distances from the oscillator. The full-angle of divergence of the output beam was found to be approximately 1mR, which is of the same order as that of the compressed pump beam. The output beam profile in both parametric waves was also found to be the same as the pump spatial profile at the entrance to the OPO. These observations may indicate a good spatial coupling between the pump and the parametric waves. Although, the measured OPO beam divergence is relatively high, significant improvements in this parameter may be brought about by a more careful design of the optical resonator. The plane-parallel OPO cavity configuration used in our experiments is inherently poor in discriminating between the various spatial modes, and as such leads to multimode operation of the oscillator, particularly given the pulsed nature of OPO operation. The output beam divergence may, therefore, be significantly improved by employing curved cavity mirrors for the OPO to confine oscillation to the lowest-order, on-axis transverse modes. Further improvements in the pump beam divergence through the use of superior beam compression optics could, in turn, result in a significant reduction in the angular spread of oscillator output.

The temporal variation of the OPO output pulses was monitored at a signal wavelength of 454nm with the aid of a fast photodiode and an analog storage oscilloscope with a combined rise time of 1.3ns. The OPO cavity during these experiments consisted of two high reflectors ($R_1 = R_2 =$ 95% @ 500-600nm). The pulses exhibited a small modulation in their structure at a period corresponding to the round-trip time of the XeCl power oscillator cavity, but were otherwise nearly symmetrical and on average had a smooth Gaussian-like profile. The pulse durations were observed to increase from approximately 4-5ns (FWHM) at ~1.5 times above threshold to about 10-12ns when pumping at ~3 times the oscillation threshold, as shown in Traces 6.1(a)-(c). This behaviour is to be expected, given that the OPO oscillation threshold (as defined in the Brosnan and Byer model) is reached at an earlier time in the pump pulse and thus the duration of the output pulses from the OPO is increased in time.

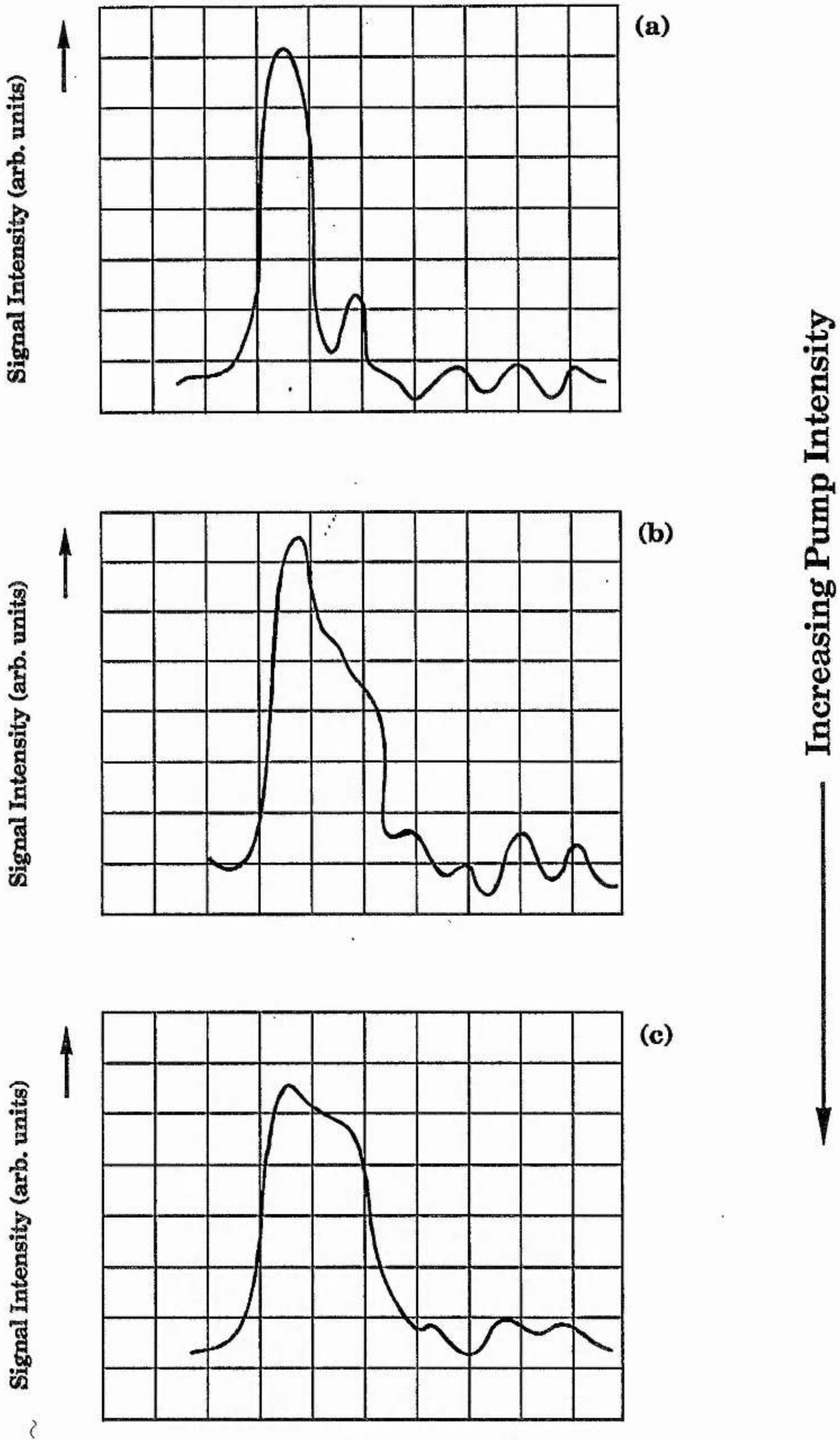

Trace 6.1(a)-(c). Pulse waveforms of the OPO resonated wave at a signal wavelength of 454 nm. OPO cavity: $R_1 = R_2 = 95\%$. Time-scale: 5 ns / division.

References to Chapter 6.

[1] E. M. Levin and A. F. McMurdie, J. Amer. Cer. Soc. 32, 99 (1949)

[2] K. H. Huber, Nueus Jahrb Mineral Monatsh 335 (1969)

[3] C. Chen *et al.*, in Proc. SPIE 681, 12 (1986)

[4] L. H. Brixner and K. Babcock, Mat. Res. Bull. 3, 817 (1968)

[5] R. S. Adhav *et al.*, Laser Focus, Sept. 1987, pp. 88-100.

[6] D. Eimerl *et al.*, J. Appl. Phys. 62 1968 (1987)

[7] K. Kato, IEEE J. Quantum. Electron., QE-22, 1013 (1986)

[8] Laser Focus, Dec. 1986, p. 10.

[9] Y. X. Fan *et al.*, Appl. Phys. Lett. 53, 2014 (1988)

[10] S. E. Harris, Proc. IEEE 57, 2096 (1969)

[11] R. L. Byer, "optical parametric oscillators," in *treatise in Quantum Electronics,* H. Rabin and C. L. Tang, Eds., Academic, New York, 1975, Vol. I, Part B, pp. 587-702.

[12] W. R. Bosenberg *et al.*, Appl. Phys. Lett. 54, 13 (1989)

[13] L. K. Cheng *et al.*, Appl. Phys. Lett. 53, 175 (1988)

[14] S. J. Brosnan and R. L. Byer, IEEE J. Quantum Electron., QE-15, 415 (1979)

7

Conclusions

This study has demonstrated the feasibility of use of excimer lasers as pump sources for optical parametric oscillators (OPO's) based on new non-linear materials, and operating throughout the near ultraviolet, visible, and the near infrared. The vital criterion for successful operation of these devices has been shown to be a high degree of spectral and spatial coherence in the pumping radiation. As such, the use of conventional single-headed and free-running excimer lasers for pumping these OPO's may be ruled out, because of the broad spectral bandwidth and large beam divergence exhibited by such lasers. In this work, we used the technique of injection-seeding to achieve a sufficiently narrow linewidth (0.2 cm^{-1}) and a near-diffraction-limited divergence (60μR, full-angle) in the pump beam, for successful operation of these devices. In the case of the urea OPO, we demonstrated external (optical-to-optical) conversion efficiencies as high 66% (in a 25-mm-long crystal) and a tuning range in the visible region from 537 to 720nm, with a single (15-mm-long) crystal. We also demonstrated an extensive tuning range in the β-BaB_2O_4 OPO from 354nm in the near ultraviolet to 2.370μm in the near infrared, using a single crystal, and achieved energy conversion efficiencies in excess of 10% (in a 12-mm-long crystal) over a significant portion of the tuning range from 450 to 960nm. The conversion efficiencies and tuning ranges of these OPO's easily rival those of the more widely-established tunable laser sources, including the dye laser, where typical efficiencies of ~10-20% can be expected across the tuning range of a single dye, with a much narrower wavelength coverage. As well as the tuning range and energy conversion efficiency, we also characterised the constructed OPO's with regard to oscillation threshold and spectral linewidth. The thresholds for oscillation in both devices were found to be typically 0.1 to 0.2 J.cm^{-2}, for crystals 10-15 mm long, although the observed values were consistently lower than those predicted from the theoretical analysis, possibly because of the possession by urea and β-BaB_2O_4 of higher non-linear coefficients than those reported in the literature. The measured oscillation threshold of the urea OPO with the 25-mm-long crystal, however, was as low as 0.023 J.cm^{-2} at 90° phase-matching. This very low oscillation threshold opens up the possibility of use of alternative lower-power, but more compact, laser sources, e.g. the doubled output of a diode-laser-pumped Nd^{3+}:YAG laser, to pump such an OPO, and thus provide an all-solid-state, compact, tunable laser source in the visible and the near infrared. The linewidths of the OPO's were also investigated and were found to be typically 0.4-0.8nm wide across the tuning range of the urea OPO, and 5-10nm wide across the tuning range of the β-BaB_2O_4 OPO, with the linewidth in this case increasing towards degeneracy. A major contributing factor to these relatively large linewidths is the excessive angular divergence exhibited by the compressed pump beam. This is possibly due to aberrations introduced by the compression optics and, as such, major reduction in OPO linewidths may be brought about by more careful design of the telescope, and by the use of aberration-free optics. Therefore, this is a major area where future improvements may be implemented. The reduction in pump beam divergence is also expected to significantly enhance OPO efficiency, by resulting in lower oscillation thresholds. In addition, the signal and idler linewidths may be further reduced by applying standard spectral narrowing techniques to these devices. These include the use of dispersing cavities (e.g. using gratings as feedback elements) or incorporating line-narrowing elements within the present OPO cavity. However, in doing so, it is important to choose a scheme in which the shortest cavity length and the minimum amount of loss are mintained. Further improvements in the performance of these devices may also be brought about by the use crystals of longer interaction length, higher damage threshold optics, mirrors of more appropriate reflectivity-wavelength profiles, and pump pulses of longer temporal duration. Given the present crystal growth and mirror coating technology, as well as the commercial availability of narrowband excimer lasers of high spectral, spatial, and temporal coherence, realisation of any of these improvements should not pose any serious difficulties. The use of more refined OPO cavity configurations (e.g. with cylindrical mirrors) and anamorphic optics is also expected to lead to major enhancement in OPO performance in the presence of beam walk-off, particularly where longer crystal lengths are involved.

The future potential of this approach with the use of other excimer lasers such as XeF (at 351nm), KrF (at 249nm), and KrCl (at 222nm) to pump similar devices based on urea, β-BaB_2O_4, and other new non-linear materials, e.g. Lithium tri-Borate (LBO), will open up the possibility of generation of tunable laser radiation in new regions of the optical spectrum, particularly in the near ultraviolet, with relative simplicity and high efficiency. We have so far explored one such possibility, in collaboration with the Rutherford Appleton Laboratory, by pumping a urea OPO, based on the 25-mm-long crystal, with a narrowband commercial KrF excimer laser (Lambda Physik EMG150), to provide ultraviolet radiation at 354nm, at 90° phase-matching. However, the efficiency of this device was limited by the relatively low optical damage threshold of the material at this pumping wavelength (10-20MW.cm^{-2}), which resulted in significant bulk damage to the crystal over relatively short periods of irradiation (few hundred shots). Thus, the potential of this material may be best realised by the use of longer-wavelength excimer lasers such as XeCl, as used here, and XeF, with the latter offering new non-critical wavelength regions (near 500nm) where high efficiencies can be expected. However, the use of KrF, and possibly the shorter-wavelength excimer lasers, to pump OPO's based on β-BaB_2O_4 and LBO should not pose such difficulties, because of the much higher damage thresholds exhibited by these crystals. We have carried out an extensive survey of the potential spectral coverage of new OPO devices based on these materials, and pumped at 249nm by a KrF excimer source. The results of this survey indicate the potential for generation of continuously tunable radiation from about 280nm in the near ultraviolet to 2.4μm in the near infrared by utilising β-BaB_2O_4, and wavelength regions further into the ultraviolet by utilising LBO as the OPO medium. Although, LBO does not offer the potential for broad tunability, one can attain relatively high conversion efficiencies because of the possibility of non-critical phase-matching in this crystal in several regions of OPO operation. Further, the high average power capability of excimer lasers coupled with the high optical damage threshold of β-BaB_2O_4 and LBO should enable generation of high-power tunable radiation in new regions of the optical spectrum. An experimental programme is currently underway to exploit the full potential of these materials by the use of a commercially available, narrowband excimer laser, with higher average-power capability than the pump laser used during this work, and capable of providing three excimer wavelengths (XeF at 351nm, XeCl at 308nm, and KrF at 249nm). The exceptionally broad tuning bandwidths, ease of operation, high conversion efficiency, and the potentially high output powers attainable from these OPO's, should make them practical and competitive alternatives to many of the well-established tunable laser sources, and devices of great utility for a variety of scientific applications.

Appendix A

Computer Programmes Used to Determine the Tuning Ranges of the Urea and β-BaB$_2$O$_4$ Optical Parametric Oscillators :

1) Urea : type I ($o \rightarrow e\,e$)

```
 10INPUT "PUMP WAVELENGTH",P
 20INPUT "SIGNAL WAVELENGTH LOWER LIMIT",LL
 30INPUT "SIGNAL WAVELENGTH UPPER LIMIT",UL
 40PRINT "ANGLE","SIGNAL","IDLER"
 50FOR S=LL TO UL STEP 0.01
 60I=P*S/(S-P)
 70NOP=SQR(2.1548+0.0131/(P^2-0.0318))
 80NOS=SQR(2.1548+0.0131/(S^2-0.0318))
 90NOI=SQR(2.1548+0.0131/(I^2-0.0318))
100X1=2.5527
110Y1=0.01784/(S^2-0.0294)
120Z1=0.0288*(S-1.5)
130T1=Z1/((S-1.5)^2+0.03371)
140NES=SQR(X1+Y1+T1)
150X2=2.5527
160Y2=0.01784/(I^2-0.0294)
170Z2=0.0288*(I-1.5)
180T2=Z2/((I-1.5)^2+0.03371)
190NEI=SQR(X2+Y2+T2)
200A=((NOP/P)^4)*(((NOS^2)-(NES^2))^2)*(((NOI^2)-
(NEI^2))^2)
210B1=((NOP/P)^2)*((NOS^2)-(NES^2))*((NOI^2)-(NEI^2))
220B2=((NOP/P)^2)*((NOS^2)-(NES^2))*(NEI^2)
230B3=((NOP/P)^2)*((NOI^2)-(NEI^2))*(NES^2)
240B4=(((NOS*NES)^2)/(S^2))*((NOI^2)-(NEI^2))
250B5=(((NOI*NEI)^2)/(I^2))*((NOS^2)-(NES^2))
260B=2*B1*(B2+B3-B4-B5)
270C11=((NOP/P)^2)*((NOS^2)-(NES^2))*(NEI^2)
280C12=((NOP/P)^2)*((NOI^2)-(NEI^2))*(NES^2)
290C13=(((NOS*NES)^2)/(S^2))*((NOI^2)-(NEI^2))
300C14=(((NOI*NEI)^2)/(I^2))*((NOS^2)-(NES^2))
310C1=(C11+C12-C13-C14)^2
320C21=((NOP/P)^2)*((NOS^2)-(NES^2))*((NOI^2)-(NEI^2))
330C22=((NOP/P)^2)*(NES^2)*(NEI^2)
340C23=(((NOS*NES)^2)/(S^2))*(NEI^2)
350C24=(((NOI*NEI)^2)/(I^2))*(NES^2)
360C2=2*C21*(C22-C23-C24)
370C31=(((NOS*NES)^2)/(S^2))*((NOI^2)-(NEI^2))
380C32=(((NOI*NEI)^2)/(I^2))*((NOS^2)-(NES^2))
390C3=4*C31*C32
400C=C1+C2-C3
410D11=((NOP/P)^2)*(NES^2)*(NEI^2)
```

```
420D12=(((NOS*NES)^2)/(S^2))*(NEI^2)
430D13=(((NOI*NEI)^2)/(I^2))*(NES^2)
440D14=((NOP/P)^2)*((NOS^2)-(NES^2))*(NEI^2)
450D15=((NOP/P)^2)*((NOI^2)-(NEI^2))*(NES^2)
460D16=(((NOS*NES)^2)/(S^2))*((NOI^2)-(NEI^2))
470D17=(((NOI*NEI)^2)/(I^2))*((NOS^2)-(NES^2))
480D1=2*(D11-D12-D13)*(D14+D15-D16-D17)
490D21=(((NOS*NES)^2)/(S^2))*((NOI^2)-(NEI^2))
500D22=(((NOI*NEI)^2)/(I^2))*(NES^2)
510D2=4*D21*D22
520D31=(((NOS*NES)^2)/(S^2))*(NEI^2)
530D32=(((NOI*NEI)^2)/(I^2))*((NOS^2)-(NES^2))
540D3=4*D31*D32
550D=D1-D2-D3
560E11=((NOP/P)^2)*(NES^2)*(NEI^2)
570E12=(((NOS*NES)^2)/(S^2))*(NEI^2)
580E13=(((NOI*NEI)^2)/(I^2))*(NES^2)
590E1=(E11-E12-E13)^2
600E2=4*E12*E13
610E=E1-E2
620FOR W=0 TO 0.99 STEP 0.01
630M=FNPOLY (W,A,B,C,D,E)
640K=SQR(((W)+(W+0.01))/2)
650ANGLE=DEG(ASN(K))
660@%=131850
670IF FNPOLY (W,A,B,C,D,E)*FNPOLY (W+0.01,A,B,C,D,E)<0
THEN PRINT ANGLE,S,I
680NEXT W
690NEXT S
700END
710DEF FNPOLY
(T,F,G,H,I,J)=F*(T^4)+G*(T^3)+H*(T^2)+(I*T)+J
```

2) Urea : type II ($o \rightarrow o\, e$)

```
 10INPUT "PUMP WAVELENGTH",P
 20INPUT "SIGNAL WAVELENGTH LOWER LIMIT",LL
 30INPUT "SIGNAL WAVELENGTH UPPER LIMIT",UL
 40PRINT "ANGLE","SIGNAL","IDLER"
 50FOR S=LL TO UL STEP 0.01
 60I=P*S/(S-P)
 70NOP=SQR(2.1548+0.0131/(P^2-0.0318))
 80NOS=SQR(2.1548+0.0131/(S^2-0.0318))
 90NI=(NOP/P-NOS/S)*I
100NOI=SQR(2.1548+0.0131/(I^2-0.0318))
110X=2.5527
120Y=0.01784/(I^2-0.0294)
130Z=0.0288*(I-1.5)
140T=Z/((I-1.5)^2+0.03371)
150NEI=SQR(X+Y+T)
160A=SQR((1/(NI^2)-1/(NOI^2))/(1/(NEI^2)-1/(NOI^2)))
170ANGLE=DEG(ASN(A))
180@%=131850
190PRINT ANGLE,S,I
200NEXT S
```

3) BBO : type I ($e \rightarrow o\,o$)

```
 10INPUT "PUMP WAVELENGTH",P
 20INPUT "SIGNAL WAVELENGTH LOWER LIMIT",LL
 30INPUT "SIGNAL WAVELENGTH UPPER LIMIT",UL
 40PRINT "ANGLE","SIGNAL","IDLER"
 50FOR S=LL TO UL STEP 0.01
 60I=P*S/(S-P)
 70NOS=SQR(2.7359+(0.01878/(S^2-0.01822))-(0.01354*S^2))
 80NOI=SQR(2.7359+(0.01878/(I^2-0.01822))-(0.01354*I^2))
 90NP=(NOS/S+NOI/I)*P
100NOP=SQR(2.7359+(0.01878/(P^2-0.01822))-(0.01354*P^2))
110NEP=SQR(2.3753+(0.01224/(P^2-0.01667))-(0.01516*P^2))
120A=SQR((NEP^2)*((NOP^2)-(NP^2))/((NP^2)*((NOP^2)-
(NEP^2))))
130ANGLE=DEG(ASN(A))
140@%=131850
150PRINT ANGLE,S,I
160NEXT S
```

4) BBO : type II ($e \rightarrow o\,e$)

```
 10INPUT "PUMP WAVELENGTH",P
 20INPUT "SIGNAL WAVELENGTH LOWER LIMIT",LL
 30INPUT "SIGNAL WAVELENGTH UPPER LIMIT",UL
 40PRINT "ANGLE","SIGNAL","IDLER"
 50FOR S=LL TO UL STEP 0.01
 60I=P*S/(S-P)
 70NOP=SQR(2.7359+(0.01878/(P^2-0.01822))-(0.01354*P^2))
 80NOI=SQR(2.7359+(0.01878/(I^2-0.01822))-(0.01354*I^2))
 90NOS=SQR(2.7359+(0.01878/(S^2-0.01822))-(0.01354*S^2))
100NEP=SQR(2.3753+(0.01224/(P^2-0.01667))-(0.01516*P^2))
110NEI=SQR(2.3753+(0.01224/(I^2-0.01667))-(0.01516*I^2))
120A=((NOS/S)^4)*(((NOI^2)-(NEI^2))^2)*(((NOP^2)-
(NEP^2))^2)
130B1=((NOS/S)^2)*((NOI^2)-(NEI^2))*((NOP^2)-(NEP^2))
140B2=((NOS/S)^2)*((NOI^2)-(NEI^2))*(NEP^2)
150B3=((NOS/S)^2)*(NEI^2)*((NOP^2)-(NEP^2))
160B4=(((NOI*NEI)^2)/(I^2))*((NOP^2)-(NEP^2))
170B5=(((NOP*NEP)^2)/(P^2))*((NOI^2)-(NEI^2))
180B=2*B1*(B2+B3-B4-B5)
190C11=((NOS/S)^2)*((NOI^2)-(NEI^2))*(NEP^2)
200C12=((NOS/S)^2)*((NOP^2)-(NEP^2))*(NEI^2)
210C13=(((NOI*NEI)^2)/(I^2))*((NOP^2)-(NEP^2))
220C14=(((NOP*NEP)^2)/(P^2))*((NOI^2)-(NEI^2))
230C1=(C11+C12-C13-C14)^2
240C21=((NOS/S)^2)*((NOI^2)-(NEI^2))*((NOP^2)-(NEP^2))
250C22=((NOS/S)^2)*(NEI^2)*(NEP^2)
260C23=(((NOI*NEI)^2)/(I^2))*(NEP^2)
270C24=(((NOP*NEP)^2)/(P^2))*(NEI^2)
280C2=2*C21*(C22-C23-C24)
290C31=(((NOI*NEI)^2)/(I^2))*((NOP^2)-(NEP^2))
300C32=(((NOP*NEP)^2)/(P^2))*((NOI^2)-(NEI^2))
```

```
310C3=4*C31*C32
320C=C1+C2-C3
330D11=((NOS/S)^2)*(NEI^2)*(NEP^2)
340D12=(((NOI*NEI)^2)/(I^2))*(NEP^2)
350D13=(((NOP*NEP)^2)/(P^2))*(NEI^2)
360D14=((NOS/S)^2)*((NOI^2)-(NEI^2))*(NEP^2)
370D15=((NOS/S)^2)*((NOP^2)-(NEP^2))*(NEI^2)
380D16=(((NOI*NEI)^2)/(I^2))*((NOP^2)-(NEP^2))
390D17=(((NOP*NEP)^2)/(P^2))*((NOI^2)-(NEI^2))
400D1=2*(D11-D12-D13)*(D14+D15-D16-D17)
410D21=(((NOI*NEI)^2)/(I^2))*((NOP^2)-(NEP^2))
420D22=(((NOP*NEP)^2)/(P^2))*(NEI^2)
430D2=4*D21*D22
440D31=(((NOI*NEI)^2)/(I^2))*(NEP^2)
450D32=(((NOP*NEP)^2)/(P^2))*((NOI^2)-(NEI^2))
460D3=4*D31*D32
470D=D1-D2-D3
480E11=((NOS/S)^2)*(NEI^2)*(NEP^2)
490E12=(((NOI*NEI)^2)/(I^2))*(NEP^2)
500E13=(((NOP*NEP)^2)/(P^2))*(NEI^2)
510E1=(E11-E12-E13)^2
520E2=4*E12*E13
530E=E1-E2
540FOR W=0 TO 0.99 STEP 0.01
550M=FNPOLY (W,A,B,C,D,E)
560K=SQR(((W)+(W+0.01))/2)
570ANGLE=DEG(ASN(K))
580@%=131850
590IF FNPOLY (W,A,B,C,D,E)*FNPOLY (W+0.01,A,B,C,D,E)<0
THEN PRINT ANGLE,S,I
600NEXT W
610NEXT S
620END
630DEF FNPOLY
(T,F,G,H,I,J)=F*(T^4)+G*(T^3)+H*(T^2)+(I*T)+J
```